

# STUDY OF TURBULENT FLOW AND CONJUGATE HEAT TRANSFER OF PLANE WALL AND OFFSET JETS

*A Thesis*  
*submitted in partial fulfillment of the*  
*requirements for the Degree of*  
**Doctor of Philosophy**

*by*

**Elaprolu Vishnuvardhanarao**



DEPARTMENT OF MECHANICAL ENGINEERING

Indian Institute of Technology Guwahati

GUWAHATI

NOVEMBER-2008

# CERTIFICATE

It is certified that the work contained in the thesis entitled **Study of Turbulent Flow and Conjugate Heat Transfer of Plane Wall and Offset Jets** by Elaprolu Vishnuvardhanarao, has been carried out under my supervision and that this work has not been submitted elsewhere for a degree.

Dr. Manab Kumar Das

Associate Professor

Department of Mechanical Engineering

I.I.T. Guwahati-781039

Assam, India

Present Address:

Dr. Manab Kumar Das

Associate Professor

Department of Mechanical Engineering

I.I.T. Kharagpur-721302

West Bengal, India



Dedicated to

my Parents, sister Sarada  
&  
Sirisha

# ACKNOWLEDGEMENT

I express my sincere gratitude and hearty thanks to my guide Dr. Manab Kumar Das, for his invaluable guidance and constant encouragement. I am deeply inspired by not only his rich experience and knowledge but the way of approaching a problem, immense patience and utmost care. I am highly indebted to him for his untiring devotion and willingness. During my project work, he provided me with the most invaluable ideas, books and journals that are incorporated in the thesis played most important role in completing the thesis successfully. I enjoyed each and every moment working under his supervision and learnt a lot many things from him, which will be an asset for my future research.

I express my sincere gratitude and hearty thanks to my administrative guide Dr. P. Muthukumar who agreed to take care of the official matters and provided me help in the final phase of thesis submission. I am thankful to my doctoral committee members Dr. M. Pandey, Dr. M. K. Nandy and Dr. P. Muthukumar for giving their valuable suggestions and encouragement which helped to shape my self to meet the requirement of a successful researcher. I would like to express my sincere thanks to Prof. U. S Dixit (H.O.D Mechanical Engineering Department) for providing all the facilities needed during my Project work. I take this opportunity to thank all the faculty members for valuable suggestions and cooperation during my course work. I specially thank Mr. Amal Kalita for providing good facilities in CAD lab and providing me a separate computer for my research work.

I am sincerely thankful to the institute for providing me the sufficient funds and grants to have this research work done successfully. I am thankful to staff of Computer Center who have provided me the computational facilities. I am thankful to other faculty members and staff directly or indirectly motivated me to complete the thesis work.

I would like to express my sincere gratitude to my parents whose blessings and never ending support is the real impetus that continuously motivates me to produce my best.

I am sincerely thankful to Dr. P. Rajesh Kanna for providing me help and sending me useful journal papers. I express my sincere and hearty thanks to Mr. Amaresh Dalal for providing the help during my research work. I specially thank Mr. Vijay Kumar Pantangi, who has given his immense help by allowing his note book to use during my thesis writing. I am very much grateful to Mr. Atal Bihari Harichandan for providing accommodation in IIT Kharagpur, otherwise it could have been very difficult for me. I am thankful to Mr. Falguni Patnaik whose companion at IIT Kharagpur made a pleasant one. I would like to thank Mr. B. Rama Raju, with whom I shared my personal feelings has provided his continuous help during my entire stay in IIT Guwahati. I am very much thankful to G. V. D. Prasad who provided constant encouragement during my research period. I am thankful to Mr. D. Santhosh Kumar, Mr. L. Lakshmanan, D. A. Perumal and Mr. Sateesh with whom I had a healthy discussion and provided financial help whenever I am in need during my stay in IIT Guwahati. I am thankful to Mr. D. Siva Krishna Reddy who has provided the required journal papers. Finally I would like to thank my friends Mr. Ravi Kiran Purama and Mr. Veera Baburao Kavala for their support and making my stay at IIT Guwahati a pleasant one.

## Abstract

When a fluid is ejected from a nozzle, it forms a jet. A jet can be classified as free jet or bounded jet. If the effect of wall is negligibly small, then it is called a free jet; otherwise it is bounded jet. Bounded jets can be classified into three types: (a) wall jet where the fluid is discharged at the wall (b) offset jet where the fluid is discharged at an offset and parallel to wall and (c) impinging jet aimed towards the boundary. The present study aimed to understand the flow and conjugate heat transfer characteristics of the wall jet, offset jet and combined jet flows.

Glauert [1] has defined a plane wall jet as a stream of fluid blown tangential along a plane wall. The wall jet consists of an inner region and an outer region. It is a combination of boundary layer flow over flat plate at inner region and plane free jet at outer region. The velocity profile has a point of inflexion. The surrounding medium of wall jet may be quiescent or co-flow or counter-flow depending upon the applications.

Offset jet flow occurs when fluid is discharged from a slot in a vertical wall into the ambient near a horizontal solid boundary parallel to the inlet jet direction. The asymmetric entrainment on both side of the jet causes the flow to deflect towards the wall. This is called the Coanda effect [2]. The offset jet contains different flow features which are different in various regions. The region very close to the jet is dominated by the properties of the free jet. At the reattachment region, the jet can be partly described as impingement jet and in the far downstream, the jet attains the characteristics of the wall jet.

A dual-jet or a combined jet flow is formed by a plane wall jet and a parallel offset jet. The low pressure zone in the downstream region between the jets causes to deflect each other and merge together at some down-stream distance, where mean velocity is zero, and referred to as merging point ( $x_{mp}$ ). The region up to

the merging point from the nozzle exit is called the converging region. Downstream of the merging point is combined point ( $x_{cp}$ ), where the mid-part of the  $U$  profile disappears. The region between the merging point and the combined point is called the merging region. The region beyond the combined point is called the combined region.

Wall jet and offset jet commonly represent the flows like heat exchangers, fluid injectors, environmental dischargers, combustion chambers, cooling systems and many others. The understanding of the flow behavior of wall bounded jet is important in engineering practices. If attachment is not desired for more mixing, a knowledge of calculation and design is required to prevent it. For a case where attachment is desirable, study of the involved variables is required so that a precise location of the attachment point and the containment of the flow can be established.

In the present study, the flow and non-conjugate and conjugate heat transfer study of wall jet, offset jet and combined jet flow is investigated. The wall jet and offset jet at different offset ratios are studied for development of the self-similarity, wall pressure, shear stress on the wall and different flow and heat transfer characteristics are observed under the adiabatic impingement surface. The Reynolds number ( $Re$ ) equal to 15000 is considered for all the computations. The standard  $k-\epsilon$  model has been used for the turbulence modeling. It is observed that pressure distribution along the wall remains nearly constant for wall jet and at a distance of approximately 60, the velocity profile for wall jet and other three offset ratio (OR) cases overlap with each other implying that a wall jet situation arises in far downstream for all the cases. The computed temperature profiles are compared with the experimental results.

The conjugate heat transfer involving the cooling of a heated slab by a turbulent plane wall jet has been numerically solved. The bottom of the solid slab is maintained at a hot uniform temperature whereas the wall jet temperature is equal

to the ambient temperature. The Reynolds number considered is 15000 because it has already been experimentally found and reported that the hydrodynamic solution becomes fully turbulent and is independent of the Reynolds number. The high Reynolds number two-equation model ( $k-\epsilon$ ) has been used for the turbulence modeling. The parameters chosen for the study are the conductivity ratio of the solid-fluid ( $K$ ), the solid slab thickness ( $S$ ) and the Prandtl number ( $Pr$ ). The range of parameters are:  $K=1-1000$ ,  $S=1-10$  and  $Pr=0.01-100$ . It is demonstrated clearly that local Nusselt number ( $Nu_x$ ) increases with  $Pr$  because of the thinning of the thermal boundary layer. It is observed that for the range of  $K$  and  $S$ , the  $Nu_x$  distribution superimposes with each other suggesting that it is independent of both  $K$  and  $S$ . Results for the solid-fluid interface temperature, local Nusselt number, local heat flux distribution at the interface, average Nusselt number and average heat transfer have been presented and discussed. Similar parametric study is carried out when the bottom of the solid slab subjected to uniform heat flux condition. Since the side walls of the slab are adiabatic, it is ensured that heat applied at the bottom of the solid block and at the interface are equal.

The conjugate heat transfer involving a turbulent plane offset jet is considered. The bottom wall of the solid block is maintained at an isothermal temperature higher than the jet inlet temperature. The parameters considered are the offset ratio ( $OR=3,7$  and  $11$ ), the conductivity ratio ( $K=1-1000$ ), the solid slab thickness ( $S=1-10$ ) and the Prandtl number ( $Pr=0.01-100$ ). High Reynolds number  $k-\epsilon$  is used for modelling the turbulence. The local  $Nu_x$  decreases with the increase in  $OR$ . It increases with the increase in  $Pr$ . However,  $Nu_x$  remains nearly unaffected by the variation of  $K$  and  $S$ . Investigation is carried out for the solid-fluid interface temperature, local Nusselt number, local heat flux at the interface, average Nusselt number and average heat transfer have been discussed in detail. Similar parametric study is done when the bottom of the solid slab is maintained at uniform heat flux. As the side walls of the slab are adiabatic, it is ensured that heat applied at the

bottom of the solid block and at the interface are equal.

A two-dimensional, steady, incompressible, turbulent flow of combined jets consisting of a wall jet and an offset jet has been solved numerically. Streamline curvature modification to the  $k - \epsilon$  is used. The Reynolds number is considered as 20000 for all computations because the flow becomes fully turbulent. Parametric study by varying the wall jet and offset jet velocities has been carried out. It is observed that pressure on the wall is almost constant along the wall and it increases when one of the jet velocity is increased keeping the other constant. Several important flow features like self-similarity, pressure and shear stress on the wall, maximum velocity decay and spreading rate in the downstream direction are investigated for different combinations of the wall jet and the offset jet velocities.

The fluctuations of the velocities and other parameters have been noticed near the jet issuing location for equal wall and offset jet velocities. At some downstream locations, these fluctuations disappear. However, for unequal jet velocities, the flow remains fairly steady even close to the jet issue location. The domains for these kind of flow features have been identified and reported. The applicability of steady state solution is discussed.

The heat transfer study of a combined wall jet and offset jet flow with different wall jet and offset jet flow velocities are considered. The Reynolds number is varied from  $10^4$  to  $4 \times 10^4$  and  $Pr=0.71$  is taken for all computations. Constant wall temperature and constant wall heat flux boundary conditions are considered on the wall. It is observed that  $Nu_x$  increases with mass flow rate, i.e, by increasing either the wall jet or offset velocity keeping the other constant. The results are presented in the form of local Nusselt number, local heat flux, surface temperature in case of constant heat flux condition, average Nusselt number and total heat transfer.

# Contents

<b>1</b>	<b>Introduction</b>	<b>1</b>
1.1	Introduction and Literature review . . . . .	1
1.2	Aim of the present work . . . . .	10
1.3	Contents of the thesis . . . . .	11
<b>2</b>	<b>Mathematical Formulation</b>	<b>12</b>
2.1	Introduction . . . . .	12
2.2	Governing Equations . . . . .	13
2.3	Non-dimensionalization . . . . .	15
2.4	The Standard $k - \epsilon$ model . . . . .	16
2.5	Streamline curvature modification . . . . .	16
2.6	Numerical Procedure . . . . .	17
2.7	Validation Study . . . . .	18
<b>3</b>	<b>Computation of Mean Flow and Thermal Characteristics of In-</b>	
	<b>compressible Turbulent Offset Jet Flows</b>	<b>20</b>
3.1	Introduction . . . . .	20
3.1.1	Boundary Conditions . . . . .	21
3.1.2	Code Validation and Grid Independence Study . . . . .	21
3.2	Results and Discussion . . . . .	22
3.3	Conclusions . . . . .	46

<b>4</b>	<b>Computational Study of Heat Transfer in a Conjugate Turbulent Wall Jet Flow at High Reynolds Number</b>	<b>47</b>
4.1	Introduction . . . . .	47
4.2	Results and Discussion . . . . .	49
4.3	Concluding Remarks . . . . .	57
<b>5</b>	<b>Computational Study of Heat Transfer in a Conjugate Turbulent Wall Jet Flow with Constant Heat Flux</b>	<b>58</b>
5.1	Introduction . . . . .	58
5.2	Results and Discussion . . . . .	59
5.3	Concluding Remarks . . . . .	68
<b>6</b>	<b>Conjugate Heat Transfer Study of Incompressible Turbulent Offset Jet Flows</b>	<b>69</b>
6.1	Introduction . . . . .	69
6.2	Results and Discussion . . . . .	70
6.3	Concluding Remarks . . . . .	86
<b>7</b>	<b>Study of Conjugate Heat Transfer from a Flat Plate by Turbulent Offset Jet Flow</b>	<b>87</b>
7.1	Introduction . . . . .	87
7.2	Results and Discussion . . . . .	88
7.3	Concluding Remarks . . . . .	103
<b>8</b>	<b>Numerical Simulation of the Turbulent Flow Interaction Between a Plane Wall Jet and a Parallel Offset Jet</b>	<b>104</b>
8.1	Introduction . . . . .	104
8.1.1	Boundary Conditions . . . . .	105
8.1.2	Code Validation and Grid Independence Study . . . . .	105
8.2	Results and Discussion . . . . .	107

8.3	Conclusions . . . . .	120
<b>9</b>	<b>Different Turbulent Flow Behaviours of a Combined Plane Wall Jet and a Parallel Offset Jet</b>	<b>121</b>
9.1	Introduction . . . . .	121
9.2	Results and Discussion . . . . .	122
9.3	Conclusions . . . . .	146
<b>10</b>	<b>Study of the Heat Transfer Characteristics in a Turbulent Com- bined Wall and Offset Jet Flows</b>	<b>147</b>
10.1	Introduction . . . . .	147
10.2	Results and Discussion . . . . .	148
10.3	Conclusions . . . . .	163
<b>11</b>	<b>Conclusions and Scope for Future Work</b>	<b>164</b>
11.1	Summary . . . . .	164
11.2	Scope for Future Study . . . . .	167
<b>A</b>	<b>Deriving the expression for heat flux in the fluid side</b>	<b>168</b>
<b>B</b>	<b>Deriving the expression for Nusselt Number Calculation</b>	<b>169</b>
<b>C</b>	<b>Definition of the constant heat flux at the solid wall</b>	<b>170</b>
<b>D</b>	<b>Validation of the code</b>	<b>171</b>
D.1	Channel Flow . . . . .	171
D.2	Square and Rectangular Cavities . . . . .	171

# List of Figures

1.1	Schematic diagram of an offset jet flow . . . . .	2
1.2	Schematic diagram of a dual-jet jet flow . . . . .	5
1.3	Schematic diagram of a conjugate offset jet flow . . . . .	9
3.1	Sample grid used for the present computation for $OR = 7h$ . . . . .	22
3.2	Validation of code for $OR=7$ with experimental results of Pelfrey and Liburdy [3] . . . . .	28
3.3	Grid independence study . . . . .	28
3.4	Maximum velocity variation along the $X$ -direction . . . . .	29
3.5	Variation of wall shear stress . . . . .	29
3.6	Variation of pressure along the wall . . . . .	29
3.7	Streamlines of offset jet at different offset ratios . . . . .	30
3.8	Vector distribution of offset jet at different offset ratios . . . . .	31
3.9	$\bar{U}$ -contour distribution of offset jet at different offset ratios . . . . .	32
3.10	$\bar{V}$ -contour distribution of offset jet at different offset ratios . . . . .	33
3.11	Pressure distribution of offset jet at different offset ratios . . . . .	34
3.12	Turbulent kinetic energy ( $k$ ) distribution at different offset ratios . . . . .	35
3.13	Dissipation( $\epsilon$ ) distribution of offset jet at different offset ratios . . . . .	36
3.14	Turbulent viscosity ( $\nu_t$ ) distribution of offset jet at different offset ratios . . . . .	37
3.15	Similarity solution for different offset ratio at four downstream lo- cations . . . . .	38

3.16	Similarity solution at different downstream locations for various off- set ratios. . . . .	39
3.17	Comparison of temperature ( $\bar{\theta}$ ) profiles with experimental results of Holland and Liburdy [4] at different locations for wall jet . . . . .	40
3.18	Comparison of temperature ( $\bar{\theta}$ ) profiles with experimental results of Holland and Liburdy [4] at different locations for $OR = 3$ . . . . .	41
3.19	Comparison of temperature ( $\bar{\theta}$ ) profiles with experimental results of Holland and Liburdy [4] at different locations for $OR = 7$ . . . . .	42
3.20	Comparison of temperature ( $\bar{\theta}$ ) profiles with experimental results of Holland and Liburdy [4] at different locations for $OR = 11$ . . . . .	43
3.21	Comparison of surface temperature ( $\bar{\theta}$ ) profiles with experimental results of Holland and Liburdy [4] for different offset ratios. . . . .	44
3.22	Temperature ( $\bar{\theta}$ ) distribution of offset jet at different offset ratios .	45
4.1	Schematic and computational domain of the wall jet flow . . . . .	48
4.2	Interface temperature distribution ( $\bar{\theta}_i$ ) distribution for $S=10$ and $K = 1000$ at various Prandtl numbers . . . . .	54
4.3	Interface temperature distribution ( $\bar{\theta}_i$ ) distribution for $Pr = 1$ and $S = 10$ at various thermal conductivity ratios ( $K$ ). . . . .	54
4.4	Interface temperature distribution ( $\bar{\theta}_i$ ) distribution for $Pr = 1$ and $K = 1000$ at solid thickness ratios ( $S$ ). . . . .	54
4.5	Local Nusselt number ( $Nu_x$ ) distribution for $S=10$ and $K = 1000$ at various Prandtl numbers . . . . .	55
4.6	Local Nusselt number ( $Nu_x$ ) distribution for $Pr=1$ and $S = 10$ at various thermal conductivity ratios ( $K$ ). . . . .	55
4.7	Local Nusselt number ( $Nu_x$ ) distribution for $Pr=1$ and $K = 1000$ at various solid thickness ratios ( $S$ ). . . . .	55

4.8	Heat flux ( $Q_x$ ) distribution for $S=10$ and $K = 1000$ at various Prandtl numbers . . . . .	56
4.9	Heat flux ( $Q_x$ ) distribution for $Pr=1$ and $S = 10$ at various various thermal conductivity ratios ( $K$ ). . . . .	56
4.10	Heat flux ( $Q_x$ ) distribution for $Pr=1$ and $K = 1000$ at various various solid thickness ratios ( $S$ ). . . . .	56
5.1	Schematic and computational domain of the wall jet flow . . . . .	59
5.2	Bottom surface temperature distribution . . . . .	64
5.3	Interface temperature distribution . . . . .	65
5.4	Local Nusselt number distribution . . . . .	66
5.5	Heat flux distribution . . . . .	67
6.1	Schematic diagram of the offset jet and a solid bock. . . . .	70
6.2	Interface temperature distribution at the solid-fluid interface at different offset ratios. . . . .	80
6.3	Interface temperature distribution at the solid-fluid interface at $OR = 7$ . . . . .	81
6.4	Local Nusselt number distribution at different offset ratios. . . . .	82
6.5	Local Nusselt number distribution and at $OR = 7$ . . . . .	83
6.6	Interface heat transfer ( $q_x$ ) distribution for different offset ratios. . . . .	84
6.7	Interface heat transfer ( $q_x$ ) distribution and at $OR = 7$ . . . . .	85
7.1	Bottom wall temperature distribution at different offset ratios for $S=10$ and $K = 1000$ . . . . .	95
7.2	Bottom wall temperature distribution at $OR=7$ . . . . .	96
7.3	Interface temperature distribution at the solid-fluid interface at different offset ratios for $S=10$ and $K = 1000$ . . . . .	97
7.4	Interface temperature distribution at the solid-fluid interface at $OR=7$ . . . . .	98

7.5	Nusselt number distribution at different offset ratios $S=10$ and $K = 1000$ . . . . .	99
7.6	Nusselt number distribution at $OR=7$ . . . . .	100
7.7	Interface heat transfer distribution at the solid-fluid interface for different offset ratios $S=10$ and $K = 1000$ . . . . .	101
7.8	Interface heat transfer distribution at the solid-fluid interface at $OR=7$ . . . . .	102
8.1	Grid independence study. . . . .	106
8.2	Grid independence study. . . . .	110
8.3	Validation study for similarity solution (8.3(a), 8.3(b), 8.3(c)), outer boundary layer growth (8.3(e)) and maximum velocity decay (8.3(d)) with Wang and Tan [5]. . . . .	111
8.4	Comparison of similarity solution at different downstream location for different wall jet and offset jet velocities. . . . .	112
8.5	Pressure distribution along the wall at different offset and wall jet velocities. . . . .	113
8.6	Shear stress distribution along the wall at different offset and wall jet velocities. . . . .	114
8.7	Maximum velocity decay in the downstream at different wall jet and offset jet velocities. . . . .	115
8.8	Spreading rate of the jet in the downstream direction at different wall jet and offset jet velocities. . . . .	116
8.9	$U$ and $V$ velocity contours of combined jet flow . . . . .	117
8.10	$k_n$ and $\epsilon_n$ contours of combined jet flow . . . . .	118
8.11	$\bar{P}$ contours of combined jet flow . . . . .	119
9.1	Variation of different properties for $U_w = 1.0$ , $U_o = 1.0$ at $X=2.5$ , $Y=0.125$ , $1.25$ and $1.75$ locations during the iteration. . . . .	127

9.2	Variation of different properties for $U_w = 1.0$ , $U_o = 1.0$ at $X=5.0$ , $Y=0.125$ , $1.25$ and $1.75$ locations during the iteration. . . . .	128
9.3	Variation of different properties for $U_w = 1.0$ , $U_o = 1.0$ at $X=10.0$ , $Y=0.125$ , $1.25$ and $1.75$ locations during the iteration. . . . .	129
9.4	Variation of different properties for $U_w = 1.0$ , $U_o = 1.0$ at $X=15.0$ , $Y=0.125$ , $1.25$ and $1.75$ locations during the iteration. . . . .	130
9.5	Variation of different properties for $U_w = 1.0$ , $U_o = 0.25$ at $X=2.5$ , $Y=0.125$ , $1.25$ and $1.75$ locations during the iteration. . . . .	131
9.6	Variation of different properties for $U_w = 1.0$ , $U_o = 0.5$ at $X=2.5$ , $Y=0.125$ , $1.25$ and $1.75$ locations during the iteration. . . . .	132
9.7	Variation of different properties for $U_w = 1.0$ , $U_o = 0.75$ at $X=2.5$ , $Y=0.125$ , $1.25$ and $1.75$ locations during the iteration. . . . .	133
9.8	Variation of different properties for $U_w = 0.25$ , $U_o = 1.0$ at $X=2.5$ , $Y=0.125$ , $1.25$ and $1.75$ locations during the iteration. . . . .	134
9.9	Variation of different properties for $U_w = 0.5$ , $U_o = 1.0$ at $X=2.5$ , $Y=0.125$ , $1.25$ and $1.75$ locations during the iteration. . . . .	135
9.10	Variation of different properties for $U_w = 0.75$ , $U_o = 1.0$ at $X=2.5$ , $Y=0.125$ , $1.25$ and $1.75$ locations during the iteration. . . . .	136
9.11	Variation of different properties for $U_w = 0.75$ , $U_o = 1.0$ at $X=5.0$ , $Y=0.125$ , $1.25$ and $1.75$ locations during the iteration. . . . .	137
9.12	Variation of different properties for $U_w = 0.75$ , $U_o = 1.0$ at $X=10.0$ , $Y=0.125$ , $1.25$ and $1.75$ locations during the iteration. . . . .	138
10.1	Schematic diagram of the combined jet flow . . . . .	148
10.2	Variation of Local Nusselt number ( $Nu_x$ ) along the wall for different wall jet and offset velocities keeping the $Re=20000$ under constant wall temperature. . . . .	153

10.3	Comparison of $Nu_x$ along the wall for different wall jet and offset jet velocities for constant wall temperature and constant heat flux cases. . . . .	154
10.4	Local Nusselt number ( $Nu_x$ ) distribution along the wall for different Reynolds numbers for different wall jet and offset jet velocities under constant temperature case. . . . .	155
10.5	Variation of temperature ( $\theta$ ) along the wall for different wall jet and offset velocities keeping $Re=20000$ under constant wall heat flux. . .	156
10.6	Temperature ( $\theta$ ) distribution along the wall for different Reynolds numbers for different wall jet and offset jet velocities under constant wall heat flux. . . . .	157
10.7	$\bar{\theta}$ contours of combined jet flow . . . . .	158
D.1	Schematic diagram of square and rectangular cavities . . . . .	172
D.2	Validation study with channel flow at $Re=65600$ . . . . .	173
D.3	Validation study of square cavity flow at $Re = 4.8 \times 10^5$ . . . . .	174
D.4	Validation study of rectangular cavity flow at $Re = 2.0 \times 10^5$ . . . . .	175

# List of Tables

3.1	Comparisons of the reattachment length for different offset ratios . . . . .	27
4.1	Average Nusselt number ( $\overline{Nu}$ ) at various Prandtl numbers . . . . .	52
4.2	Heat Transfer across the interface ( $Q_i$ ) at various Prandtl numbers . . . . .	53
5.1	Average Nusselt number ( $\overline{Nu}$ ) at various Prandtl numbers . . . . .	63
6.1	Average Nusselt number ( $\overline{Nu}$ ) at various Prandtl numbers for $OR = 3$ . . . . .	74
6.2	Average Nusselt number ( $\overline{Nu}$ ) at various Prandtl numbers for $OR = 7$ . . . . .	75
6.3	Average Nusselt number ( $\overline{Nu}$ ) at various Prandtl numbers for $OR =$ 11 . . . . .	76
6.4	Heat Transfer across the interface ( $Q_i$ ) at various Prandtl numbers for $OR = 3$ . . . . .	77
6.5	Heat Transfer across the interface ( $Q_i$ ) at various Prandtl numbers for $OR = 7$ . . . . .	78
6.6	Heat Transfer across the interface ( $Q_i$ ) at various Prandtl numbers for $OR = 11$ . . . . .	79
7.1	Average Nusselt number ( $\overline{Nu}$ ) at various Prandtl numbers for $OR = 3$ . . . . .	92
7.2	Average Nusselt number ( $\overline{Nu}$ ) at various Prandtl numbers for $OR = 7$ . . . . .	93
7.3	Average Nusselt number ( $\overline{Nu}$ ) at various Prandtl numbers for $OR =$ 11 . . . . .	94
9.1	Percentage variation for $U_w = 1.0$ and $U_o = 1.0$ . . . . .	139

9.2	Percentage variation for $U_w = 1.0$ and $U_o = 0.25$ . . . . .	140
9.3	Percentage variation for $U_w = 1.0$ and $U_o = 0.5$ . . . . .	141
9.4	Percentage variation for $U_w = 1.0$ and $U_o = 0.75$ . . . . .	142
9.5	Percentage variation for $U_w = 0.25$ and $U_o = 1.0$ . . . . .	143
9.6	Percentage variation for $U_w = 0.5$ and $U_o = 1.0$ . . . . .	144
9.7	Percentage variation for $U_w = 0.75$ and $U_o = 1.0$ . . . . .	145
10.1	Average Nusselt number ( $\overline{Nu}$ ) and total heat transfer ( $Q$ ) at different $Re$ , keeping the $U_w=1.0$ and varying $U_o$ . . . . .	159
10.2	Average Nusselt number ( $\overline{Nu}$ ) and total heat transfer ( $Q$ ) at different $Re$ , keeping the $U_o=1.0$ and varying $U_w$ . . . . .	159
10.3	Percentage of change in $\overline{Nu}$ and $Q$ when the $Re$ is increased at different wall jet and offset jet velocities. . . . .	160
10.4	Percentage of change in $Nu$ and $Q$ when $U_w = 0.25$ , $U_o = 1.0$ and interchanging the velocities. . . . .	161
10.5	Percentage of change in $Nu$ and $Q$ when $U_w = 0.5$ , $U_o = 1.0$ and interchanging the velocities. . . . .	161
10.6	Percentage of increase in $Nu$ and $Q$ when $U_w = 0.75$ , $U_o = 1.0$ and interchanging the velocities. . . . .	162

# Nomenclature

$h$	width of the jet
$H$	offset height
$t$	normal distance from the edge of the nozzle to the wall
$OR$	offset Ratio, $H/h$
$\bar{p}$	static pressure
$p_0$	ambient pressure
$\bar{P}$	non-dimensional static pressure
$Pr$	Prandtl number
$Pr_t$	turbulent Prandtl number
$Re$	Reynolds number, $U_0 h / \nu$
$\bar{T}$	dimensional temperature
$\bar{T}_w$	dimensional temperature at the interface
$T_{in}$	inlet temperature
$T_\infty$	ambient temperature
$T_h$	constant hot wall temperature
$U_0$	Average inlet jet velocity
$x, y$	dimensional co-ordinates
$X, Y$	non-dimensional co-ordinates
$\bar{u}, \bar{v}$	dimensional mean velocities in $x, y$ -directions respectively
$\bar{U}, \bar{V}$	non-dimensional velocities in $X, Y$ -directions respectively
$k$	turbulent kinetic energy
$C_{1\epsilon}, C_{2\epsilon}, C_\mu$	-turbulence model constants.
$K$	thermal conductivity ratio of solid to fluid ( $k_s/k_f$ ).

$s$	dimensional thickness of solid slab.
$S$	non-dimensional thickness of solid slab.
$q_b$	dimensional heat flux at the bottom wall of the solid block
$Q_b$	non-dimensional heat flux at the bottom wall of the solid block
$q_x$	heat flux at the interface
$c_p$	specific heat
$\Delta T$	Reference temperature difference
$I$	turbulent intensity
$l$	length scale
$u_\tau$	friction velocity
$Y^+$	dimensionless distance
$Q$	total heat transfer
$U_w$	average inlet wall jet velocity
$U_o$	average inlet offset jet velocity
$U_r$	reference velocity, higher one between wall jet and offset jet velocity

## Greek symbols

$\alpha, \alpha_t$	laminar and turbulent thermal diffusivities respectively.
$\epsilon$	dissipation
$\bar{\theta}$	non-dimensionalized temperature.
$\nu, \nu_t$	laminar and turbulent kinematic viscosity
$\sigma_k, \sigma_\epsilon$	turbulence model constants.
$\rho$	density of the fluid

## Subscripts

<i>b</i>	bottom.
<i>f</i>	fluid.
<i>i</i>	interface.
<i>t</i>	turbulent.
<i>s</i>	solid.
<i>max</i>	maximum
<i>o</i>	represents offset jet
<i>w</i>	represents wall jet
<i>ref</i>	reference



## Abbreviations

<i>SC</i>	streamline curvature method
FVM	finite volume method
SIMPLE	semi implicit method for pressure linked equations
RANS	Reynolds averaged Navier-stokes equations
QUICKER	Quadratic interpolation for Convective kinematics Revised
RNG	Renormalization Group
PIV	Particle Image velocimetry



# Chapter 1

## Introduction

### 1.1 Introduction and Literature review

When a fluid is ejected from a nozzle, it forms a jet. Depending upon the distance of the confining boundaries from the discharge, a jet can be analyzed as a free jet or a bounded one. If the boundaries are sufficiently away from the origin of the jet and the effect of it is negligibly small, the flow is termed as a free jet. A bounded jet flow occurs, when jet interacts with wall and it can be described based on axis and its position relative to wall. Bounded jets can be classified into three types: (a) wall jet and (b) offset jet and (c) impinging jet. A schematic of diagram of offset jet is shown in Fig. 1.1. When  $t$  becomes zero, it becomes a wall jet. When the axis of jet is normal to the wall, it is called an impinging jet. Wall jet and offset jet commonly represent the flows like heat exchangers, fluid injectors, environmental dischargers, combustion chambers, cooling systems and many others.

Glauert [1] defined a plane wall jet as a stream of fluid blown tangential along a plane wall. The wall jet consists of an inner region and an outer region. It is a combination of boundary layer flow over flat plate at inner region and plane free jet at outer region. The velocity profile has a point of inflexion. The surrounding

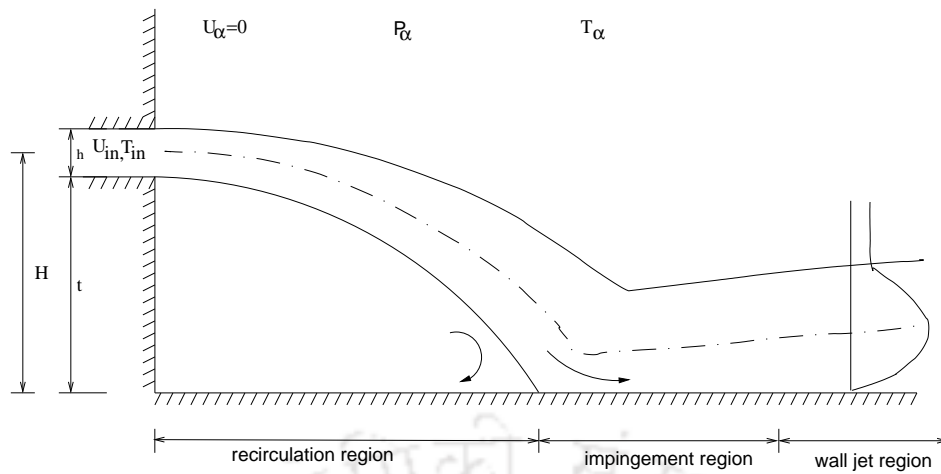


Figure 1.1: Schematic diagram of an offset jet flow

medium of wall jet may be quiescent or co-flow or counter-flow depending upon the applications.

Offset jet flow occurs when fluid is discharged from a slot in a vertical wall into the ambient near a horizontal solid boundary parallel to the inlet jet direction. Due to the entrainment of fluid between the jet and the bottom plate, there is a reduction of pressure in this region forcing the jet to deflect towards the boundary and eventually attach with it. This is called the Coanda effect [2]. The offset jet flow features are different in various regions. In the near-field within a very short distance from the point of discharge, the jet flow is dominated by momentum and has the properties of a free jet. Attachment occurs when the jet is deflected towards an adjacent solid wall and tends to flow along the boundary. In the region around the attachment point, i.e., the impingement region and part of the recirculation region, the jet can be partly characterized as an impingement jet. The offset jet becomes a wall jet in the far field. All regions of the offset jet are shown in Fig. 1.1. Other factors like free-stream velocity, ambient stratification, buoyancy (density difference), discharge orientation etc., further complicate the jet-boundary interaction and the behavior of an offset jet.

The understanding of the flow behavior of wall bounded jet is important in

engineering practices. If attachment is not desired for more mixing, a knowledge of calculation and design is required to prevent it. For a case where attachment is desirable, study of the involved variables is required so that a precise location of the attachment point and the containment of the flow can be established.

The details of the flow was studied by several authors. Glauert [1] has sought for the similarity solution in a plane wall jet as well as a radial wall jet for both the laminar and the turbulent cases are presented. The first detailed experimental study of the mean flow is reported by Bourque and Newman [6] followed by Sawyer [7] and [8]. They have examined the effect of offset height on the wall pressure distribution and reattachment locations. Seban and Back [9] have measured and compared the turbulent velocity profile and the adiabatic wall temperature with the results of Glauert [1]. The results agree generally well with each other. Rajaratnam and Subramanya [10] found that beyond the impingement region, the flow represents similar to a wall jet flow irrespective of the offset ratio. Gutmark and Wygnanski [11] have produced the hot-wire measurements in a plane incompressible jet. The flow was found to be self-preserving beyond  $x/d < 40$  and measurements were made up to  $x/d=120$ . Hoch and Jiji [12] have considered the case of an offset jet in the presence of a free-stream motion. The fluid flow solution has been provided by them. Utilizing this fluid flow solution, Hoch and Jiji [13] later on have provided the analytical solution for the temperature distribution for the same geometry.

Launder and Rodi [14] have given a review of the experimental literature on the turbulent wall jets. They have considered the cases of the two-dimensional wall jet on a plane surface, the two-dimensional wall jet on a curved surface, and the three-dimensional wall jet. Experiments with good accuracy and the ability to test the reliability of the new crop of calculation methods for turbulent flows are identified. Later on, Launder and Rodi [15] have reviewed the experimental data and theoretical models for expressing the computational fluid dynamics of turbu-

lent wall jets. The wall jet is defined as a boundary layer in which, due to some initially supplied momentum, the flow velocity over some region in the shear layer exceeds the free stream velocity. Attempts to formulate generalized expressions for the velocity profiles in a plane two-dimensional wall jet are reviewed, together with the turbulent energy balance in an equilibrium wall jet. The applications of Boussinesq viscosity models and Reynolds stress closure models to numerically express the turbulent wall jets are addressed. Dakos et al. [16] have made extensive single-point turbulence measurements in a heated wall jet on a convex wall and in an equivalent plane flow. They have reported that the turbulence structure and the transfer of heat and momentum are affected by the wall curvature.

In a study, Pelfrey and Liburdy [3] have provided the details of the mean flow and turbulent characteristics and showed how entrainment and local pressure and turbulent energy components are affected by the jet curvature in the reattachment region. For large Reynolds numbers generally larger than the  $10^4$ , the impingement distance becomes a function of the offset ratio only. Holland and Liburdy [4] presented the thermal characteristics of offset jets in a conditions similar to that of Pelfrey and Liburdy [3] for different offset ratios. In this case, the plate parallel to the jet was considered as adiabatic. They examined the surface temperature distribution, the maximum temperature decay and the temperature variations in three regions. Wygnanski *et al.* [17] measured the mean velocity in a two-dimensional turbulent wall jet for a variety of nozzle Reynolds numbers and found that bulk of the flow is self-similar and it depends on the momentum flux at the nozzle and on the viscosity and density of the fluid. Zhou and Wygnanski [18] have reported the mean velocity distributions in a plane, turbulent, and fully developed wall jet embedded in a uniform stream for a variety of initial velocity ratios and Reynolds numbers. Kim et al. [19] have conducted an experimental study for Reynolds number ranging from 6500 to 39000. They have reported that the time-averaged reattachment points are found to coincide with the maximum Nusselt number

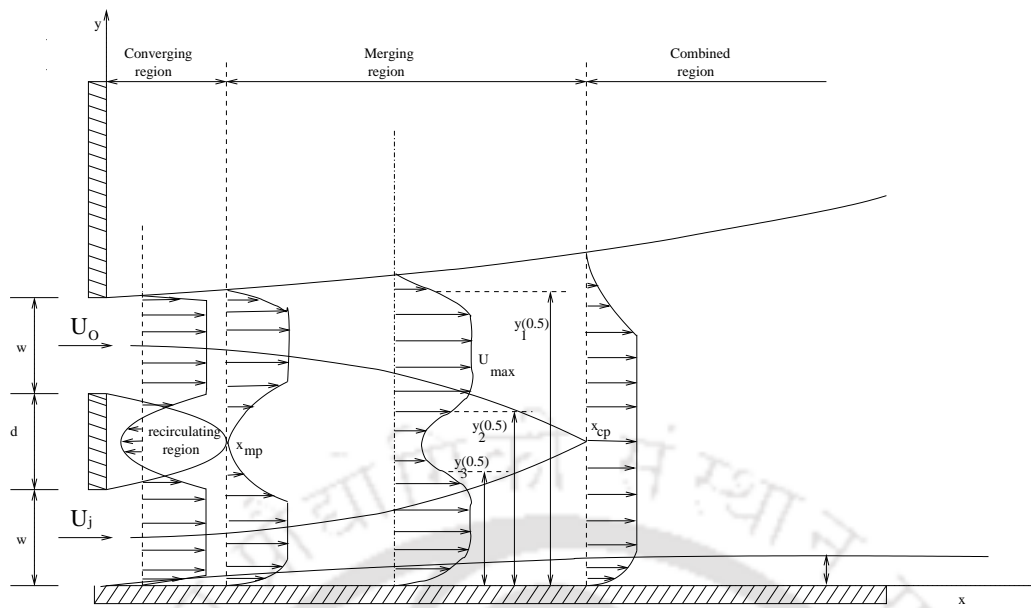


Figure 1.2: Schematic diagram of a dual-jet flow

locations.

Computations of the offset jet performed by Yoon *et al* [20] showed that in addition to the turbulence model, the numerical scheme also plays a profound effect in predicting the solution. It is observed that the numerical diffusion error due to the streamline to grid-skewness will be significant in the prediction of offset jet flows. Koo and Park [21] have used the QUICKER scheme to predict the turbulent offset jet flows. They have compared their numerical results with those from the skew-upwind and the hybrid schemes. They concluded that the QUICKER scheme is found to be superior to the other two schemes. Nasr and Lai [22] have done an experimental study for the OR (offset ratio) = 2.125 using Laser Doppler Anemometry (LDA). The LDA results had been used to examine the capability of three different turbulence models (i.e.  $k - \epsilon$ , RNG and Reynolds stress) in predicting the velocity field of this jet. It was found that although three turbulence models predict quantitatively, the standard  $k - \epsilon$  turbulence model predicts better the reattachment length with the experimental value.

A dual-jet flow is formed by a plane wall jet and a parallel offset jet. A schematic diagram of a dual-jet is shown in Fig. 1.2. The low pressure zone

in the downstream region between the jets causes to deflect each other and merge together at some downstream distance, where mean velocity is zero, and referred to as merging point ( $x_{mp}$ ). The region up to the merging point from the nozzle exit is called the converging region. Downstream of the merging point is combined point ( $x_{cp}$ ), where the mid-part of the  $U$  profile disappears. The region between the merging point and the combined point is called the merging region. The region beyond the combined point is called the combined region. All regions of the combined jet are shown in Fig. 1.2.

Both the turbulent plane wall jet and offset jet has been studied separately and reported in literature by many authors. However, the case of a combined jet flows consisting of two similar or different jets have rarely been studied. The work on two plane parallel jets has been reported by Ko and Lau [23], Lin and Sheu [24] and Nasr and Lai [25] on experimental. Numerical simulations on these type of combined jet flows have been reported by Wang et al. [26], Soong et al. [27] and Anderson and Spall [28]. A thorough literature survey reveals that research on the combination of jets have been concentrated on two parallel plane jets. Recently Wang and Tan [5] have experimentally studied the turbulent dual jet flow consisting of a plane wall jet and an offset jet. They have considered an offset ratio of  $d/w=1.0$  and have done the measurements using the Particle Image Velocimetry (PIV). Statistical characteristics of the flow are obtained through ensemble averaging of 360 instantaneous velocity fields. Results reveal that the near field of the flow is characterized by a periodic large-scale Karman-like vortex shedding similar to what would be expected in the wake of a bluff body. The jet half-widths at various shear layers have been plotted. Results reveal that close to the jet issuing plane, a vortex-shedding has been observed. Otherwise, they have presented an averaged velocity similarity profile and other jet widths distributions.

Yang and Shyu [29] have presented numerical predictions on the fluid flow and heat transfer characteristics of multiple impinging slot jets with an inclined

confinement surface. The parameters studied included the angle of inclined confinement surface and entrance Reynolds number, which is in the turbulent region. The numerical results showed that the maximum local Nusselt number and maximum pressure on the impinging surface move downstream while the inclination angle is increased. The maximum local Nusselt number decreases while the value of the local Nusselt number downstream increases with increasing inclination angle. The entrance  $Re$  has little effect on the size of the recirculation region, but the inclination angle has a significant effect on the recirculation zones. Shuja et al. [30] studied the jet impingement on a surface having a constant heat flux over a limited area. Air is considered as the impinging gas, and the process is simulated with a two-dimensional axisymmetric form of the governing conservation equations. Four turbulence models, including standard  $k - \epsilon$ , low Reynolds number  $k - \epsilon$ , and two Reynolds stress models, are introduced to account for the turbulence. They concluded that the agreement between the temperature profiles predicted from both the low Reynolds number  $k - \epsilon$  model and the Reynolds stress turbulence model are better than that obtained from the standard  $k - \epsilon$  model. Aldabbagh and Sezai [31] have investigated numerically the steady-state flow and heat transfer characteristics of impinging laminar square twin jets. The simulations have been carried out for various jet-to-jet spacings and nozzle exit-to-plate distances. The effect of these parameters on the flow structure has been studied. Yilbas et al. [32, 33] studied numerically the jet impingement onto a cavity and hole with a constant wall temperature. In the simulations, four hole wall temperatures and two jet velocities were considered. The Nusselt number ratio was computed and the mass flow ratio was determined. Heat transfer from a row of turbulent jets impinging on a stationary surface is investigated numerically by Salamah and Kaminski [34]. The jet-to-jet interaction, the geometric parameters of the jet array, and the effect of Reynolds number are investigated.

A conjugate heat transfer problem occurs when the fluid regime is coupled with

the conducting solid wall having a finite thickness. The temperature and the heat fluxes at the solid-fluid interface are considered to be equal. This is referred to as the fourth-kind boundary condition [35]. Conjugate heat transfer applies to a thermal system in which the multi-mode convection/conduction heat transfer is of particular importance to thermal design. In most instances, it arises where the external and the internal temperature fields are coupled. Conjugate heat transfer is involved in many applications like high speed jet engines, electronics cooling, film cooling of turbine blades, extrusion of materials etc.

Conjugate heat transfer is getting more attention by the researcher for the past two decades. Conjugate heat transfer on flat plate are devoted in Luikov [36] and Payvar [37] and many others. Ould-Amer *et al.* [38] have presented the laminar forced convection cooling of heat generating blocks mounted on a wall in a parallel plate channel. The effect on heat transfer of insertion of a porous matrix between the blocks is considered. In case of laminar flow, many publications are devoted to conjugate heat transfer on a flat plate, details of which may be found in Kanna and Das [39]. However, the conjugate heat transfer study involving a turbulent flow has received little attention. Kassab *et al.* [40] have reported the development and application of a coupled boundary element/finite volume method temperature-forward/flux-back algorithm developed to solve conjugate heat transfer arising in 3D film-cooled turbine blades. Iaccarino *et al.* [41] have reported the effect of thermal boundary conditions on numerical heat transfer predictions in rib-roughened passages. Results obtained using constant heat flux at the walls and conjugate heat transfer are compared to illustrate how the recirculation bubbles upstream and downstream of the rib have different effects on the local heat transfer. Hsieh and Lien [42] have observed the performance of various  $k-\epsilon$  models on turbulent forced convection in a channel with periodic ribs is assessed. Kim and Kim [43] have presented the numerical procedure to optimize the shape of two-dimensional channel with periodic ribs mounted on both of the walls to enhance turbulent heat

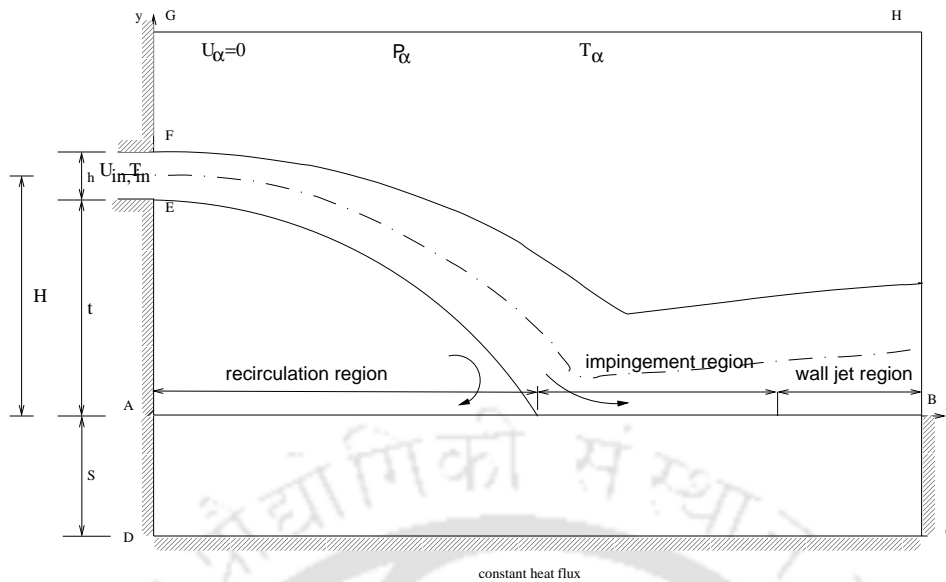


Figure 1.3: Schematic diagram of a conjugate offset jet flow

transfer. Recently, the conjugate heat transfer of a laminar offset jet is reported by Kanna and Das [44]. They found that the local Nusselt number increases to a peak value and further it is decreased in the downstream direction. In another study, the same authors [45] have carried out a steady-state heat transfer study for a two-dimensional, laminar, incompressible, plane wall jet over a backward-facing step. The heat transfer characteristics of the jet as functions of Reynolds number, Prandtl number, and step geometry (step length and step height) are reported in details. Results are presented in the form of isotherm, Nusselt number, and average Nusselt number. In some cases, the computed results are compared with the results when the step length is zero.

Although many studies have been conducted on the turbulent wall jet and offset jet, some of the characteristics are yet to be explored. The case of offset jet, which occurs at several practical applications has not been studied for self-similarity comparison with wall jet flow at various offset ratios and for temperature solution in detail. The conjugate heat transfer study of turbulent wall jet and offset jet is not analyzed. Figure. 1.3 shows the schematic diagram of a conjugate offset jet flow. When  $S$  becomes zero the geometry becomes offset jet flow. When  $t$  becomes zero,

it becomes conjugate wall jet flow. When both  $S$  and  $t$  becomes zero, it represents a wall jet flow. In the conjugate heat transfer approach, the conduction and the convection equations are solved simultaneously. At the interface of solid and fluid regions the temperature and heat flux are equal. The near-wall treatments of turbulence models are the key factors to yield an accurate wall heat transfer predictions. In the standard high Reynolds number  $k - \epsilon$  models, wall functions are commonly employed to bridge the turbulent and near-wall viscous regions.

In the present study, the flow features, non-conjugate and conjugate heat transfer of wall jet, offset jet at various offset ratios and combined jet at different wall jet and offset jet velocities are investigated. Self-similarity profile of wall jet and offset jet flow and its development in the downstream direction are reported. Pressure, shear stress along the wall and maximum velocity decay in the flow was observed. In the case of conjugate study, the parameters considered are Prandtl number ( $Pr$ ), slab thickness ( $S$ ) and thermal conductivity ratio ( $K$ ). A detailed analysis is provided for the local Nusselt number ( $Nu_x$ ), heat flux and interface temperature distribution. Average Nusselt number ( $Nu$ ) and total heat transfer ( $Q$ ) are tabulated and important observations are reported. Numerical study is carried out under both constant temperature and constant heat flux conditions at the bottom of the solid block.

## 1.2 Aim of the present work

The following situations are considered for carrying out the research.

- Fluid flow and heat transfer characteristics of wall jet and offset jet at different offset ratios.
- Conjugate heat transfer study of wall jet under constant temperature and constant heat flux at the bottom of solid block.

- Similarly, conjugate heat transfer study of offset jet for different offset ratio ( $OR$ ).
- Fluid flow characteristics of combined jet flow at different wall jet and offset jet velocities.
- Steady state analysis to describe the flow domain whether the flow is in steady or periodic.
- Thermal characteristics of combined jet flow at different wall jet and offset jet velocities.
- Conjugate heat transfer study of combined jet flow at different wall jet and offset jet velocities.

### 1.3 Contents of the thesis

The thesis is planned to include the following chapters. Chapter 1 describe the introduction and literature survey. Chapter 2 will discuss about the numerical procedure. Chapter 3 will present the computation of mean flow and thermal characteristics of incompressible turbulent offset jet flows. Chapter 4 will discuss the conjugate heat transfer study of constant temperature at the bottom of the solid block. Under the same conditions, constant heat flux at the bottom of the solid block is studied in Chapter 5. Conjugate heat transfer study of the offset jet flow under constant wall temperature and heat flux at the bottom of the solid block are discussed in chapters 6 and 7 respectively. Fluid flow characteristics of combined jet flow is discussed in chapter 8. Applicability of the steady state analysis of combined jet by describing the different flow features is discussed in chapter 9. Chapter 10 discuss the heat transfer characteristics of the combined jet under constant heat flux and temperature. Finally, thesis concludes with the conclusions and future scope which is described in chapter 11.

# Chapter 2

## Mathematical Formulation

### 2.1 Introduction

This chapter will describe the brief description about theory, governing equations and numerical procedure to solve the problems considered here. Most of the flows occurring in the nature are turbulent flows. Since there is no precise definition for turbulent flows, it is determined by its characteristics like, irregularity, high diffusivity, large Reynolds number, three dimensional vorticity fluctuations and dissipation. The physics of the turbulence is very well described in the [46], [47] and many others. As the turbulence consists of random velocity fluctuations, so that it is treated with statistical approach.

All most all the turbulence models use time averaged equations. The origin of this approach is pioneered by Reynolds and it is also called Reynolds averaging. Boussinesq introduced the concept of eddy viscosity. The widely used models are eddy viscosity models which uses the concept of eddy viscosity. Out of the eddy viscosity models two-equation models are complete. Most widely used two-equation model is  $k - \epsilon$  model. Low-Re modelling and High-Re modelling are the two variants of  $k - \epsilon$  models. High- $Re$  modelling is also called standard  $k - \epsilon$  model. Launder and Spalding [48] explained the two variants of  $k - \epsilon$  and described

about its implementation by applying to different flow geometries. The details of the modelling, its history and its merits and demerits of different models are well described in Wilcox [49]. The other books which are useful for modelling are Chen and Jaw [50] and Biswas [51] and many others.

## 2.2 Governing Equations

The governing equations are considered to be steady, two-dimensional and incompressible. Thermo-physical properties are assumed to be constant. In the fluid region, the flow is fully turbulent and the Reynolds averaged Navier-Stokes (RANS) equations are used for predicting the turbulent flow. Boussinesq approximation is used to link the Reynolds stresses to the velocity gradients. The  $k - \epsilon$  model is used for calculating the turbulent viscosity ( $\nu_t$ ). In the solid region, the two-dimensional heat transfer equation is solved. By assuming the above conditions, the governing equations in dimensional form can be written as,

Continuity equation:

$$\frac{\partial \bar{u}}{\partial x} + \frac{\partial \bar{v}}{\partial y} = 0 \quad (2.1)$$

$x$ -momentum equation:

$$\frac{\partial(\bar{u}^2)}{\partial x} + \frac{\partial(\bar{u}\bar{v})}{\partial y} = -\frac{1}{\rho} \frac{\partial \bar{p}}{\partial x} + \frac{\partial}{\partial x} \left[ \nu \frac{\partial \bar{u}}{\partial x} - \overline{u'u'} \right] + \frac{\partial}{\partial y} \left[ \nu \frac{\partial \bar{u}}{\partial y} - \overline{u'v'} \right] \quad (2.2)$$

$y$ -momentum equation:

$$\frac{\partial(\bar{u}\bar{v})}{\partial x} + \frac{\partial(\bar{v}^2)}{\partial y} = -\frac{1}{\rho} \frac{\partial \bar{p}}{\partial y} + \frac{\partial}{\partial x} \left[ \nu \frac{\partial \bar{v}}{\partial x} - \overline{v'u'} \right] + \frac{\partial}{\partial y} \left[ \nu \frac{\partial \bar{v}}{\partial y} - \overline{v'v'} \right] \quad (2.3)$$

Energy equation:

$$\frac{\partial(\bar{u}\bar{T})}{\partial x} + \frac{\partial(\bar{v}\bar{T})}{\partial y} = \frac{\partial}{\partial x} \left[ \alpha \frac{\partial \bar{T}}{\partial x} - \overline{u'T'} \right] + \frac{\partial}{\partial y} \left[ \alpha \frac{\partial \bar{T}}{\partial y} - \overline{v'T'} \right] \quad (2.4)$$

Boussinesq approximation is used for calculating Reynolds stresses.

$$-\overline{u_i' u_j'} = \nu_t \left( \frac{\partial \bar{u}_i}{\partial x_j} + \frac{\partial \bar{u}_j}{\partial x_i} \right) - \frac{2}{3} k \delta_{ij} \quad (2.5)$$

similarly for the energy equation

$$-\overline{u_i' T'} = \alpha_t \frac{\partial \overline{T}}{\partial x_i} \quad (2.6)$$

The resulting equations are

$x$ -momentum equation:

$$\frac{\partial(\overline{u^2})}{\partial x} + \frac{\partial(\overline{uv})}{\partial y} = -\frac{1}{\rho} \frac{\partial \overline{p}}{\partial x} + \frac{\partial}{\partial x} \left[ (\nu + \nu_t) \frac{\partial \overline{u}}{\partial x} - \frac{2}{3} k \right] + \frac{\partial}{\partial y} \left[ (\nu + \nu_t) \frac{\partial \overline{u}}{\partial y} \right] \quad (2.7)$$

$y$ -momentum equation:

$$\frac{\partial(\overline{uv})}{\partial x} + \frac{\partial(\overline{v^2})}{\partial y} = -\frac{1}{\rho} \frac{\partial \overline{p}}{\partial y} + \frac{\partial}{\partial x} \left[ (\nu + \nu_t) \frac{\partial \overline{v}}{\partial x} \right] + \frac{\partial}{\partial y} \left[ (\nu + \nu_t) \frac{\partial \overline{v}}{\partial y} - \frac{2}{3} k \right] \quad (2.8)$$

Energy equation:

$$\frac{\partial(\overline{uT})}{\partial x} + \frac{\partial(\overline{vT})}{\partial y} = \frac{\partial}{\partial x} \left[ (\alpha + \alpha_t) \frac{\partial \overline{T}}{\partial x} \right] + \frac{\partial}{\partial y} \left[ (\alpha + \alpha_t) \frac{\partial \overline{T}}{\partial y} \right] \quad (2.9)$$

Turbulent kinetic energy ( $k$ ) equation :

$$\frac{\partial(\overline{uk})}{\partial x} + \frac{\partial(\overline{vk})}{\partial y} = \frac{\partial}{\partial x} \left[ \left( \nu + \frac{\nu_t}{\sigma_k} \right) \frac{\partial k}{\partial x} \right] + \frac{\partial}{\partial y} \left[ \left( \nu + \frac{\nu_t}{\sigma_k} \right) \frac{\partial k}{\partial y} \right] + G - \epsilon \quad (2.10)$$

Rate of dissipation ( $\epsilon$ ) equation :

$$\begin{aligned} \frac{\partial(\overline{u\epsilon})}{\partial x} + \frac{\partial(\overline{v\epsilon})}{\partial y} &= \frac{\partial}{\partial x} \left[ \left( \nu + \frac{\nu_t}{\sigma_\epsilon} \right) \frac{\partial \epsilon}{\partial x} \right] + \frac{\partial}{\partial y} \left[ \left( \nu + \frac{\nu_t}{\sigma_\epsilon} \right) \frac{\partial \epsilon}{\partial y} \right] \\ &+ C_{1\epsilon} \frac{\epsilon}{k} G - C_{2\epsilon} \frac{\epsilon^2}{k} \end{aligned}$$

where production by shear ( $G$ ):

$$G = \nu_t \left[ 2 \left( \frac{\partial \overline{u}}{\partial x} \right)^2 + 2 \left( \frac{\partial \overline{v}}{\partial y} \right)^2 + \left( \frac{\partial \overline{u}}{\partial y} + \frac{\partial \overline{v}}{\partial x} \right)^2 \right] \quad (2.11)$$

Eddy viscosity ( $\nu_t$ ) is given as:

$$\nu_t = C_\mu \frac{k^2}{\epsilon} \quad (2.12)$$

In the solid region, the energy equation is:

$$\frac{\partial^2 T}{\partial x^2} + \frac{\partial^2 T}{\partial y^2} = 0; \quad (2.13)$$

## 2.3 Non-dimensionalization

The dimensionless variable are defined as:

$$\bar{U} = \frac{\bar{u}}{U_0}, \quad \bar{V} = \frac{\bar{v}}{U_0}, \quad X = \frac{\bar{x}}{h}, \quad Y = \frac{\bar{y}}{h}, \quad \bar{\theta} = \frac{\bar{T} - T_\infty}{T_{in} - T_\infty} \quad (2.14)$$

$$\bar{P} = \frac{\bar{p} - \bar{p}_0}{\rho U_0^2}, \quad k_n = \frac{k}{U_0^2}, \quad \epsilon_n = \frac{\epsilon}{U_0^3/h}, \quad \nu_{t,n} = \frac{\nu_t}{\nu}, \quad \alpha_{t,n} = \frac{\alpha_t}{\alpha}$$

The non-dimensionalized equations are:

Continuity Equation:

$$\frac{\partial \bar{U}}{\partial X} + \frac{\partial \bar{V}}{\partial Y} = 0 \quad (2.15)$$

$x$ -momentum equation:

$$\frac{\partial (\bar{U}^2)}{\partial X} + \frac{\partial (\bar{U}\bar{V})}{\partial Y} = -\frac{\partial}{\partial X} \left( \bar{P} + \frac{2}{3}k \right) + \frac{1}{Re} \frac{\partial}{\partial X} \left[ (1 + \nu_{t,n}) \frac{\partial \bar{U}}{\partial X} \right] + \frac{1}{Re} \frac{\partial}{\partial Y} \left[ (1 + \nu_{t,n}) \frac{\partial \bar{U}}{\partial Y} \right] \quad (2.16)$$

$y$ -momentum equation:

$$\frac{\partial (\bar{U}\bar{V})}{\partial X} + \frac{\partial (\bar{V}^2)}{\partial Y} = -\frac{\partial}{\partial Y} \left( \bar{P} + \frac{2}{3}k \right) + \frac{1}{Re} \frac{\partial}{\partial X} \left[ (1 + \nu_{t,n}) \frac{\partial \bar{V}}{\partial X} \right] + \frac{1}{Re} \frac{\partial}{\partial Y} \left[ (1 + \nu_{t,n}) \frac{\partial \bar{V}}{\partial Y} \right] \quad (2.17)$$

Temperature equation ( $\bar{\theta}$ ) is:

$$\frac{\partial (\bar{U}\bar{\theta})}{\partial X} + \frac{\partial (\bar{V}\bar{\theta})}{\partial Y} = \frac{1}{RePr} \cdot \frac{\partial}{\partial X} \left[ (1 + \alpha_{t,n}) \frac{\partial \bar{\theta}}{\partial X} \right] + \frac{1}{RePr} \cdot \frac{\partial}{\partial Y} \left[ (1 + \alpha_{t,n}) \frac{\partial \bar{\theta}}{\partial Y} \right] \quad (2.18)$$

Turbulent kinetic energy ( $k_n$ ) equation is:

$$\frac{\partial (\bar{U}k_n)}{\partial X} + \frac{\partial (\bar{V}k_n)}{\partial Y} = \frac{1}{Re} \cdot \frac{\partial}{\partial X} \left[ \left( 1 + \frac{\nu_{t,n}}{\sigma_k} \right) \frac{\partial k_n}{\partial X} \right] + \frac{1}{Re} \cdot \frac{\partial}{\partial Y} \left[ \left( 1 + \frac{\nu_{t,n}}{\sigma_k} \right) \frac{\partial k_n}{\partial Y} \right] + G_n - \epsilon_n \quad (2.19)$$

Rate of dissipation ( $\epsilon_n$ ) equation is:

$$\begin{aligned} \frac{\partial (\bar{U}\epsilon_n)}{\partial X} + \frac{\partial (\bar{V}\epsilon_n)}{\partial Y} &= \frac{1}{Re} \cdot \frac{\partial}{\partial X} \left[ \left( 1 + \frac{\nu_{t,n}}{\sigma_\epsilon} \right) \frac{\partial \epsilon_n}{\partial X} \right] + \frac{1}{Re} \cdot \frac{\partial}{\partial Y} \left[ \left( 1 + \frac{\nu_{t,n}}{\sigma_\epsilon} \right) \frac{\partial \epsilon_n}{\partial Y} \right] \\ &\quad + C_{1\epsilon} \frac{\epsilon_n}{k_n} G_n - C_{2\epsilon} \frac{\epsilon_n^2}{k_n} \end{aligned}$$

Production ( $G$ ):

$$G_n = \frac{\nu_{t,n}}{Re} \left[ 2 \left( \frac{\partial \bar{U}}{\partial X} \right)^2 + 2 \left( \frac{\partial \bar{V}}{\partial Y} \right)^2 + \left( \frac{\partial \bar{U}}{\partial Y} + \frac{\partial \bar{V}}{\partial X} \right)^2 \right] \quad (2.20)$$

Eddy diffusivity ( $\alpha_{t,n}$ ):

$$\alpha_{t,n} = \nu_{t,n}/Pr \quad (2.21)$$

In the solid region, the energy equation is:

$$\frac{\partial^2 \theta}{\partial X^2} + \frac{\partial^2 \theta}{\partial Y^2} = 0; \quad (2.22)$$

## 2.4 The Standard $k - \epsilon$ model

In the standard version of  $k - \epsilon$  model, as described by the Launder and Spalding [48] the turbulent viscosity is calculated as:

Eddy viscosity ( $\nu_{t,n}$ ):

$$\nu_{t,n} = C_\mu Re \frac{k_n^2}{\epsilon_n} \quad (2.23)$$

The values of the model constants used in the above equations are:

$$\sigma_k = 1.0, \sigma_\epsilon = 1.30, C_{1\epsilon} = 1.44, C_{2\epsilon} = 1.92, C_\mu = 0.09$$

## 2.5 Streamline curvature modification

Cheng and Farokhi [52] derived the streamline curvature modification to the standard  $k - \epsilon$  model from the algebraic Reynolds stress model proposed by Rodi [53].

In this modification,  $\nu_{t,n}$  is given as:

$$\nu_{t,n} = \frac{2\phi}{3} \left[ 1 - R_f - \phi \frac{G_n R_f^2 + 4R_f + 1}{\epsilon} \right] Re \frac{k_n^2}{\epsilon_n} \quad (2.24)$$

So the  $C_\mu$  can be defined as:

$$C_\mu = \frac{2\phi}{3} \left[ 1 - R_f - \phi \frac{G_n R_f^2 + 4R_f + 1}{\epsilon} \right] \quad (2.25)$$

Where  $R_f$  is called the flux Richardson number

$$R_f = \frac{\partial \bar{V} / \partial X}{\partial \bar{U} / \partial Y} \quad (2.26)$$

and  $\phi$  is defined as:

$$\phi = \frac{1 - C_b}{C_a - 1 + \frac{G_n}{\epsilon_n}} \quad (2.27)$$

where,  $C_a = 1.5$  and  $C_b = 0.76$ . The values of the remaining model constant are same as in standard  $k - \epsilon$  model. Cheng and Farokhi [52] used the curvature modification for predicting the backward facing step flow, where the flow is predominant in the x-direction and is characterised by weak curvature. Similarly, Pathak *et al* [54] assessed the same model for jet in cross flow. In the present study for the combined jet flow this modification is applied. The comparisons are made for the two variants with the experimental results and are discussed in chapter 8.

## 2.6 Numerical Procedure

The governing equations are discretized using the finite volume method (FVM). The attractive feature of the finite volume method (FVM) is that the solution would imply that the integral conservation of the quantities, such as mass, momentum and other quantities are satisfied over any group of control volumes and of course over the whole computational domain. In order to overcome the checker board configuration of the pressure, the momentum equations are integrated over the staggered control volume and the other equations are integrated over the main control volume. In order to improve the guessed pressure, pressure correction equation derived from the continuity equation is used. In order to overcome the instability that arises due to the central difference scheme, different upwinding schemes are proposed to discretize the convective part of the governing equation. In the present approach, power-law scheme is used for discretizing convection part of the governing equations. Since, divergence occurs due to the higher order schemes (Peric and Ferziger [55]), specially for the turbulent quantities and present experience also suggested to use the lower order schemes. For the turbulent flows most widely used scheme is power-law scheme. The diffusive terms in the governing

equations are discretized by the central difference scheme. SIMPLE algorithm as specified by Patankar [56] is used to solve the discretized equations. The complete details of numerical procedure is well described in Patankar [56], Versteeg and Malalasekera [57] and Norris [58]. To overcome the fine grid required near the wall, the wall function method proposed by Launder and Spalding [48] and Craft *et al.* [59] is used. The conduction equation in the solid is discretized by the finite difference method using the central difference scheme which is appropriate in the solid. In case of the conjugate heat transfer study, the energy equation in the solid and fluid are solved simultaneously. The heat transfer across the interface and temperature at the interface must be equal. The details are given in appendix A.

## 2.7 Validation Study

In order to validate the developed code, flow in a (a) two-dimensional channel, (2) square and (3) rectangular cavities are considered. The geometric details, boundary conditions, the definition of  $Re$  and its value for each flow is given in the Appendix D.

The channel flow results are compared with the experimental results of Telbany and Reynolds [60]. Figures D.2(a) and D.2(b) shows the comparison of  $\bar{U}/\bar{U}_c$  ( $\bar{U}_c$  represents the velocity at the center of the channel) at downstream locations of  $X=13.5$  and 22 respectively. The results are in good agreement with the experimental solution. Similarly, Fig. D.2(c) shows the Reynolds stress at the exit of the channel. It is also in good agreement with the experimental solution. Though the present model under-predicts the turbulent kinetic energy ( $k_n$ ) with the experimental, but it is slightly better compared to the numerical solution provided by Jaw [61].

The validation study of square cavity is shown in Fig. D.3. Mills [62] has provided the experimental results for the centerline velocities. Chen and Chang [63]

have numerically studied with standard  $k - \epsilon$  model. Figures D.3(a) and D.3(b) show the centerline  $\bar{U}$  and  $\bar{V}$  velocities along the  $Y$  and  $X$  directions respectively. The present solution is compared and are in good agreement with the experimental solution of Mills and numerical solution of Chen and Chang. Figures D.3(c), D.3(d) and D.3(e) show the comparison of the Reynolds stress ( $-\overline{u'v'}$ ), turbulent kinetic energy ( $k_n$ ) and dissipation ( $\epsilon_n$ ) respectively. The results are found in good agreement with the results of Chen and Chang [63]. Similarly, Fig. D.4 shows the validation study for rectangular cavity flow. The predicted solution is found in qualitatively good agreement with the Chen and Chang [63]. The discrepancy in the two results may occur due to the schemes used, algorithm and the method and location of the first grid point also plays an important role.

The comparisons with the channel flow, square cavity and rectangular cavity has proven the validity and applicability of the code for both inflow and outflow boundary conditions and for the solid wall boundary conditions also. Similarly, the comparisons for offset flow (Fig. 3.2) and for combined jet flow (Fig. 8.3) has given the rich experience on boundary conditions and applicability of code.

# Chapter 3

## Computation of Mean Flow and Thermal Characteristics of Incompressible Turbulent Offset Jet Flows

### 3.1 Introduction

In the present study, computational details of the various offset ratios (wall jet, OR = 3,7 and 11) are presented. Power-law scheme is used for discretizing the convective terms. In order to have the same numerical accuracy for the fluid flow solution as reported in Koo and Park [21], higher grid size is used and non-uniform grids are used along the walls and at the entrance of jet. The geometry is similar to that of Pelfrey and Liburdy [3]. The results are compared and are found to be in good agreement with it. For the temperature solution, the case of Holland and Liburdy [4] has been considered. The computed results have been compared and found to be in good agreement with the experimental results. Development of the self-similarity, wall pressure, shear stress on the wall and different flow and

heat transfer characteristics are presented. The numerical scheme and method of solution as explained in chapter 2.6 is used in the present computations.

### 3.1.1 Boundary Conditions

Figure. 1.1 shows a schematic diagram of an offset jet flow. In this case, the flow of jet is emanating into a quiescent ambient fluid. The cases computed here are OR = 0 (i.e. wall jet), 3, 7 and 11. The non-dimensionalized boundary conditions are provided as input to the solution. At the inlet of the jet  $\bar{U} = 1.0$ ,  $\bar{V} = 0.0$ ,  $\bar{\theta} = 1.0$  are the boundary conditions for the velocities and temperature. For the turbulent kinetic energy equation, the boundary condition at inlet is  $k_n = 1.5I^2$  where  $I$  is the turbulence intensity and is equal to 0.02. For the dissipation equation, the boundary condition is  $\epsilon_n = (k_n^{3/2} C_\mu^{3/4})/l$ , where  $l = 0.07h$  is considered. For the solid wall, no slip boundary condition is considered for velocity. For the bottom surface, an adiabatic condition is considered whereas for the vertical wall, an isothermal condition is considered for the energy equation. Neumann boundary conditions are provided for the top boundary (i.e. entrainment side) and at the exit boundary, a developed condition of  $\partial\phi/\partial n = 0$  is considered where  $\phi = \bar{U}, \bar{v}, \bar{\theta}, k_n, \epsilon_n$ . It has been ensured that the first grid point near the wall falls in the logarithmic region i.e.  $30 < Y^+ < 100$  where  $Y^+ = yu_\tau/\nu$ ,  $u_\tau$  being the friction velocity.

### 3.1.2 Code Validation and Grid Independence Study

To validate the code developed, results obtained from the present computation are compared with the experimental results given by Pelfrey and Liburdy [3] for OR = 7. Figure. 3.2 shows the comparisons at different downstream locations of  $X = 3$  (recirculation region), 6 (recirculation region), 9 (impingement region), 12 (impingement region) and 15 ( wall jet region). It is observed that very good agreement with the experimental results have been obtained. After ensuring the

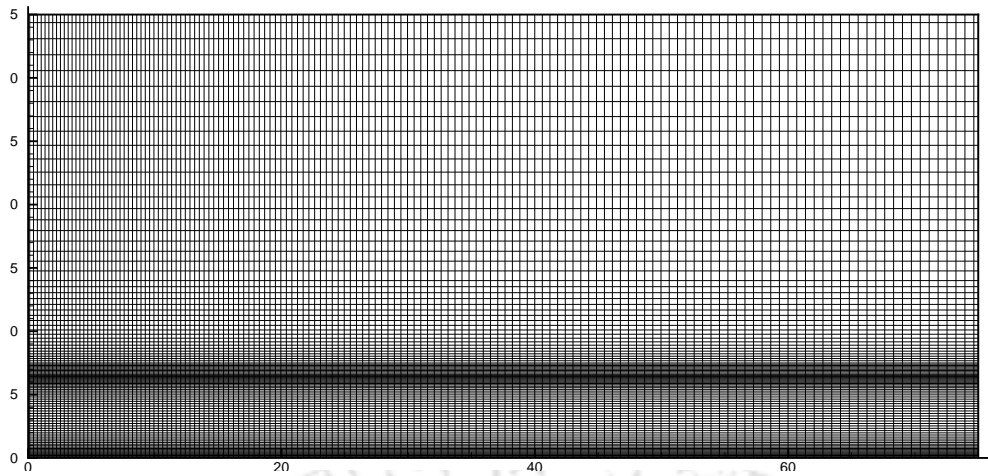


Figure 3.1: Sample grid used for the present computation for  $OR = 7h$

code validation, a grid independence study is carried out for all the cases and the effect of domain size is also considered and tested. After doing considerable numerical testing, it is found that the domain size of  $75 \times 35$  and grid size of  $151 \times 101$  are satisfactory for all the cases. Figure. 3.3 shows the grid independence study. Even though a grid size of  $121 \times 101$  produces a good solution, the grid size of  $151 \times 101$  is considered for all the cases to avoid the numerical diffusion due to streamline curvature to the grid pattern. The sample grid used for the present computation for  $OR = 7.0$  is shown in Fig.3.1

## 3.2 Results and Discussion

The computations are performed for  $OR = 0$  (i.e. wall jet), 3.0, 7.0 and 11. In all the computations,  $Re$  considered is 15000. The reattachment lengths obtained from the computations are compared with the experimental results and are shown in Table. 3.1. The reattachment point is defined as the point where wall shear stress changes its direction. For  $OR = 3$  and 7, the present  $k - \epsilon$  model under-predicts and for  $OR = 11$ , it slightly over-predicts than the experimental value. As the  $OR$  increases, the computed and the experimental results are close. This is due to the numerical diffusion and the applicability of the wall functions in the

impingement region.

Figure 3.4 shows the variation of maximum velocity ( $\bar{U}_{max}$ ) in the  $X$ -direction. In the case of wall jet,  $\bar{U}_{max}$  is almost constant up to a certain distance and then gradually reduces. For  $OR = 3, 7$  and  $11$ ,  $\bar{U}_{max}$  consists of mainly three regions, viz. a decreasing region, an increasing region and a very slowly decreasing region (i.e. this is the region where slope of the curve is almost constant). In the decreasing region,  $\bar{U}_{max}$  decreases slowly as  $OR$  increases. It is observed that the minimum value of  $\bar{U}_{max}$  occurs very near to the reattachment point in the downstream direction and it decreases as  $OR$  increases. In the increasing region also,  $\bar{U}_{max}$  increases slowly as  $OR$  increases. At any particular location in the slowly decreasing region,  $\bar{U}_{max}$  decreases as  $OR$  increases.

Figure 3.5 describes the variation of the wall shear stress ( $\tau_w$ ) along the  $X$ -direction. In case of wall jet,  $\tau_w$  decreases suddenly and increases up to a certain distance and then increases very slowly. In case of the offset jet flows,  $\tau_w$  increases slowly and also decreases slowly as  $OR$  increases. The maximum value of  $\tau_w$  decreases as  $OR$  increases. The positive region shows the recirculation region. In the very slowly increasing region, at any particular point  $\tau_w$  increases as  $OR$  increases.

Figure 3.6 represents the variation of pressure along the wall. For the wall jet, pressure remains almost constant along the wall. In case of the offset flows, pressure attains a minimum value as  $OR$  decreases because for low  $OR$  value, the jet impingement velocity is more. For the same reason, wall pressure attains a maximum value as  $OR$  increases. The variation is slow as  $OR$  increases. The minimum and the maximum value of pressures are very close to the center of the vortex in the upstream direction in the recirculation region and downstream to the impingement location. Farther downstream, pressure is almost constant and increases as  $OR$  increases at any particular location.

From the above discussions, it may be concluded that the wall jet region starts

from where the point of slope of the curve becomes almost constant and this point moves further downstream as OR increases. Impingement region starts from the location where  $\tau_w=0$ . The longitudinal distance from the inlet to the point where  $\tau_w=0$  represents the recirculation region.

Figures 3.7 and 3.8 represents the plot for streamline, velocity vector plots respectively. Figs. 3.9 and 3.10 shows the contours of  $\bar{U}$  and  $\bar{V}$  respectively. It is noticed that cluster of contours observed at the entrance of the jet says expected changes in the profile of the jet immediate to the interaction with the quiescent fluid. Outside the boundary layer  $\bar{U}$  is very small and negligible. Negative values of  $\bar{V}$  at the boundary layer in wall jet region implies that fluid enters into the boundary layer. The maximum value of  $\bar{V}$  observed in the offset flows is 0.4 for all OR, where streamlines are strongly deflected towards the plate before the impingement.

Figure 3.11 shows the pressure distribution in the domain. In offset jets, the clustered contours clearly shows that the variation of pressure in the recirculation and impingement regions is high. In the wall jet region and the wall jet case, pressure decreases up to  $\bar{U}_{max}$  and then increases to  $p_\infty$  along the cross-wise direction at any point. It is observed that the pressure at the wall is lower than  $P_\infty$ . The maximum and the minimum pressure are found at the impingement point and at the center of the vortex in the recirculation region respectively.

The distribution of the turbulent kinetic energy ( $k$ ) in the flow field for various offset ratios are shown in Fig. 3.12. In both the wall and the offset jet cases, maximum value of the turbulent kinetic energy is found in the entrance region of the jet where it strongly interacts with the quiescent ambient fluid. In case of offset jets,  $k$  is higher in the recirculation region than the impingement region and the wall jet region. In the wall jet region,  $k$  increases up to  $\bar{U}_{max}$  and beyond that, it decreases to almost zero. Figure 3.13 shows the dissipation of turbulent energy. In both wall and offset jet cases maximum value of dissipation occurs on either

side of the jet, but has minimum value in the recirculation region. The dissipation decreases along the stream-wise direction. In the cross-wise direction (similar to the case of  $k$ ),  $\epsilon$  increases up to  $\bar{U}_{max}$  and decreases to almost zero.

Figure 3.14 shows the contours of turbulent viscosity ( $\nu_t$ ). In case of wall jet,  $\nu_t$  increases in the stream-wise direction. In offset jet case,  $\nu_t$  is maximum at the center of the recirculation region, modestly decreases in the impingement region and then increases in the stream-wise direction as in the wall jet case. In the wall region,  $\nu_t$  increases up to  $\bar{U}_{max}$  in the cross-wise direction and then decreases. Outside the boundary layer,  $\nu_t$  is found to be of high value even though both  $k$  and  $\epsilon$  are very small and this represents a situation of high viscous zone where flow is almost quiescent.

Figure 3.15 shows the velocity similarity profile at four downstream locations for wall jet and three offset ratios. The  $Y$ -direction is normalized with  $Y_{0.5}$  which is the distance at which  $\bar{U} = U_{max}/2$ . For wall jet (Fig. 3.15(a), even at  $X = 30$ , similarity profile is observed whereas for OR=3 (Fig. 3.15(b)), a little deviation is observed from  $X=30$  to 40. For OR = 7 and 11, the same has been observed at  $X = 40$  and 50 respectively.

In a different figure (Fig. 3.16), it has been observed that the  $U$  velocity profile plotted in a normalized way approaches that of the wall jet case at different downstream locations. For small offset ratio (OR=3), the profile is close to that of wall jet at  $X=30$  (Fig. 3.16(a)). However, for higher offset ratio, the deviation is appreciable. In the downstream directions, the profiles for the offset ratios approach that of wall jet (Figs. 3.16(b) and 3.16(c)) and finally at  $X=60$  (Fig. 3.16(d)), they merge with each other.

The temperature profiles at different downstream locations for the wall jet and three other offset ratios are shown in Figs. 3.17-3.20. The coordinate axes have been properly scaled to represent the present nondimensional values in comparison with those of Holland and Liburdy [4]. For the wall jet case, the downstream loca-

tions considered are 10.4, 20.3 and 30.1 and are shown in Figs. 3.17(a), 3.17(b) and 3.17(c) respectively. It is observed that the temperature within the jet is gradually decreasing in the downstream direction. Figures 3.18(a), 3.18(b), 3.18(c) and 3.18(d) show the comparison of the temperature profiles at four downstream locations viz. 0.57, 2.5, 5.0 and 21.5 respectively for OR=3. It is observed that except for location 0.57, a good agreement has been obtained with the experimental results for the three downstream locations. A strong convection effect has been observed in the temperature profile at  $X=0.57$  which is not predominant in the experimental profile. For the offset ratio 7, the comparison of the temperature profile has been made at downstream locations of 3.35, 6.69, 15.75 and 38.2 (Figs. 3.19(a), 3.19(b), 3.19(c) and 3.19(d) respectively). The first two locations are within the recirculation region, the third one is after the reattachment location and the last one is close to the wall jet region. It is observed that within the recirculation region, the temperature remains constant up to a certain height before attaining the free-stream temperature of zero value. Away from the jet exit, temperature gradually decreases. In all the cases, the computed results are in good agreement with the experimental results. Figures 3.20(a), 3.20(b), 3.20(c) and 3.20(d) show the temperature distribution at four downstream locations for OR=11. It has been observed that near the surface, the computed results are over-predicting compared to the experimental results. This can be attributed partially due to wall function method and applicability of adiabatic boundary condition.

The computed surface temperature has been compared with the experimental data for the four cases considered here. It is observed that for the case of wall jet (Fig. 3.21(a)), the temperature starts falling down after a downstream location of approximately 20 whereas the experimental data shows a gradual decrease. For OR=3 (Fig. 3.21(b)), it is observed that within the recirculation region, there is a marginal increase of surface temperature and after that, it gradually decreases. A similar type of trend has also been obtained from the experimental results.

Figure 3.21(c) shows the comparison for OR=7. The numerical prediction is in good agreement though there is some discrepancy after a downstream distance of 20. For an offset ratio of 11 (Fig. 3.21(d)), the trend of the surface temperature distribution is similar to that of the experimental data. However, the computed results are overpredicting with the maximum deviation of 33% at  $X=40$ . This needs further investigation.

Figure. 3.22 shows the contours for wall jet and offset with ratios 3, 7 and 11. It is found that the temperature at wall decreases with increasing the OR and the variation in temperature in recirculation region is very small. The average temperature of recirculation region decreases with increasing OR. The temperature in the quiescent flow field (i.e. where the velocities are very small) is almost zero as shown in figure.

Table 3.1: Comparisons of the reattachment length for different offset ratios

OR	Present computation	Holland and Liburdy [4]	% error
3	5.95	7.02	-15.24
7	11.975	12.42	-3.58
11	17.29	17.02	+2.35

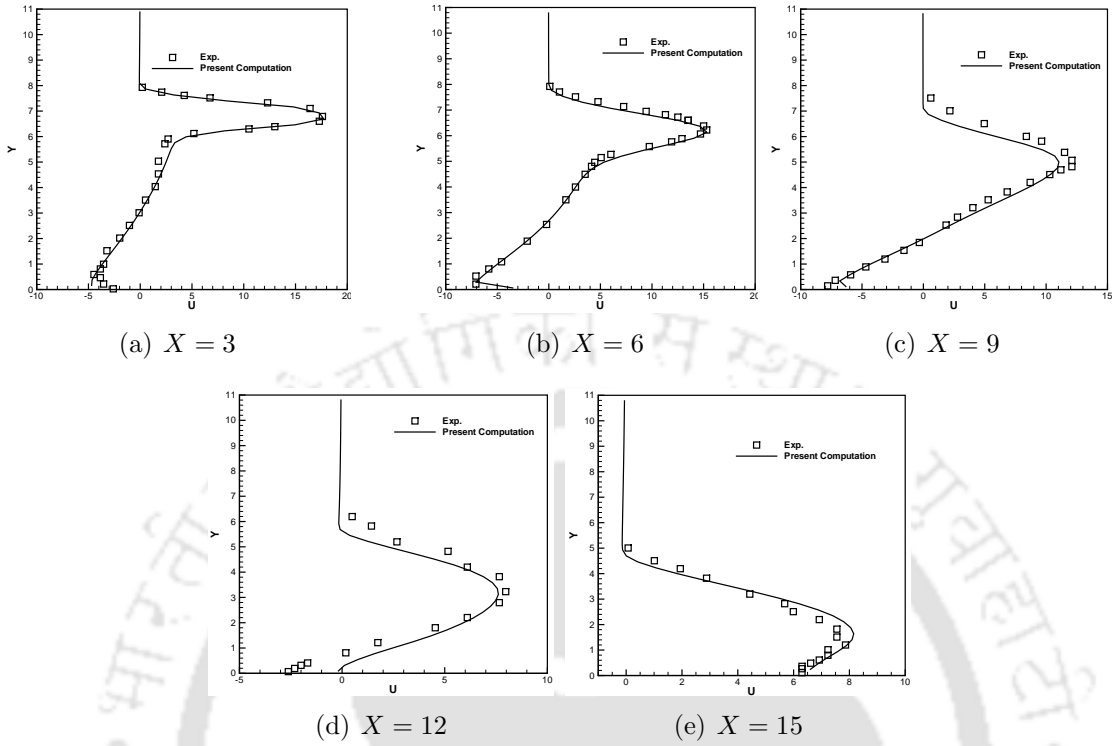


Figure 3.2: Validation of code for OR=7 with experimental results of Pelfrey and Liburdy [3]

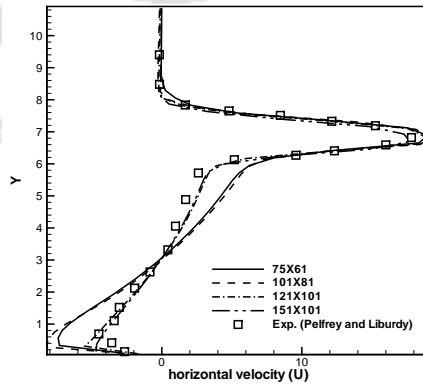


Figure 3.3: Grid independence study

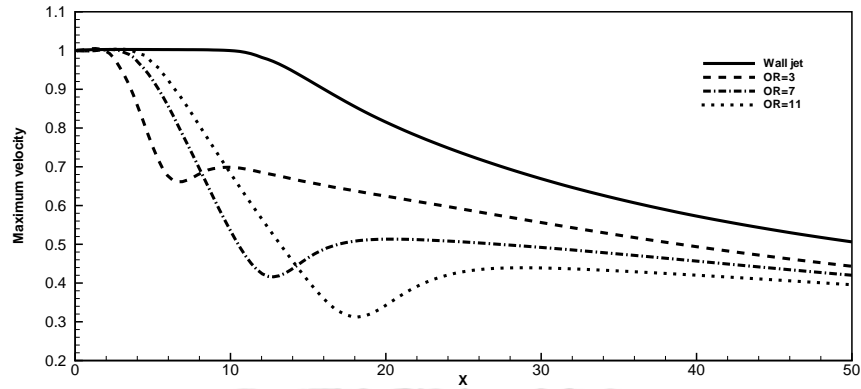


Figure 3.4: Maximum velocity variation along the X-direction

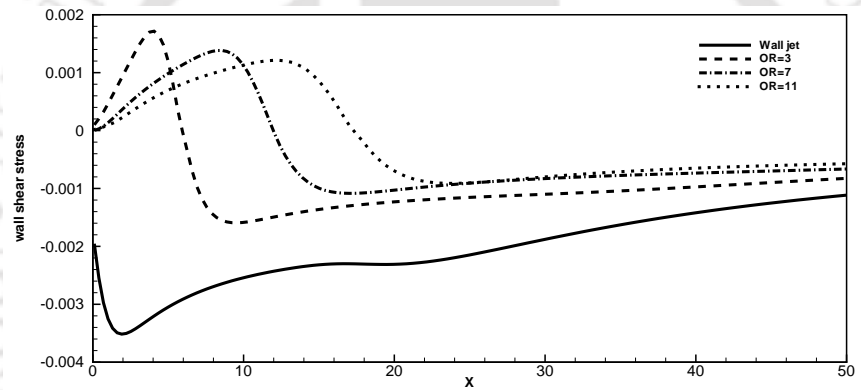


Figure 3.5: Variation of wall shear stress

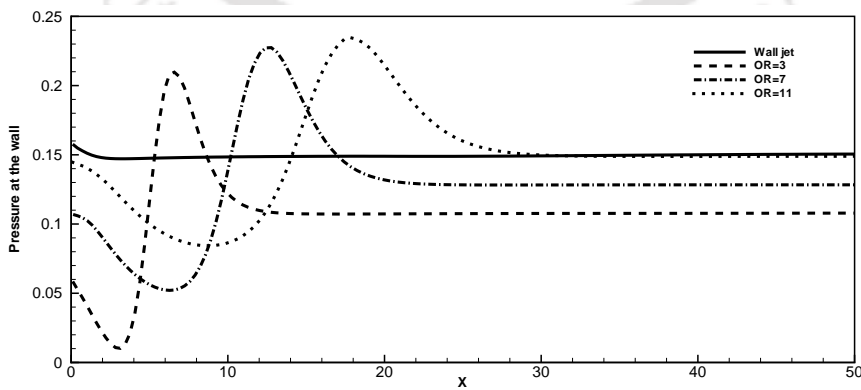
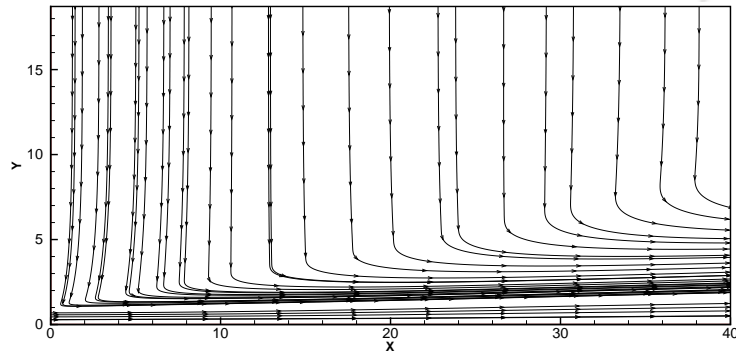
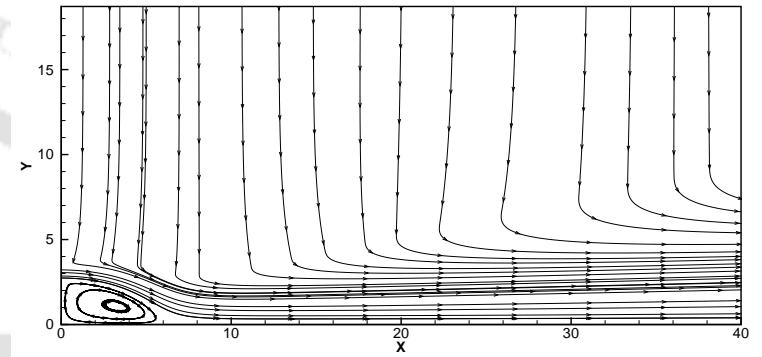


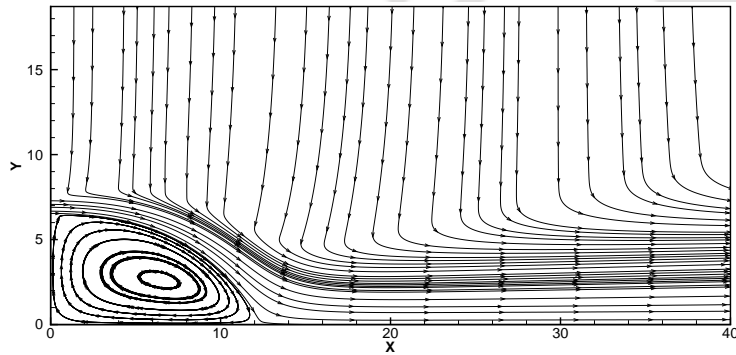
Figure 3.6: Variation of pressure along the wall



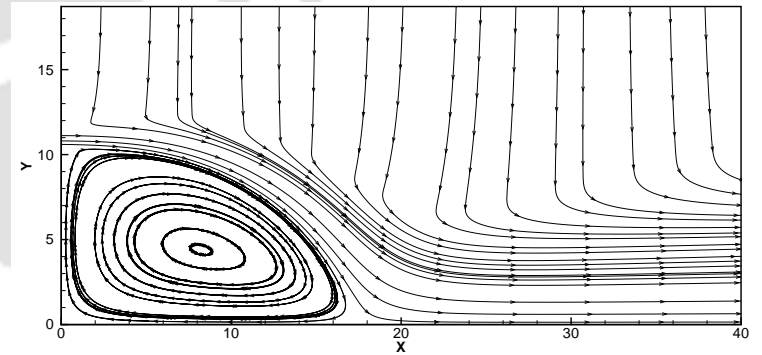
(a) Wall jet



(b) OR=3



(c) OR=7



(d) OR=11

Figure 3.7: Streamlines of offset jet at different offset ratios

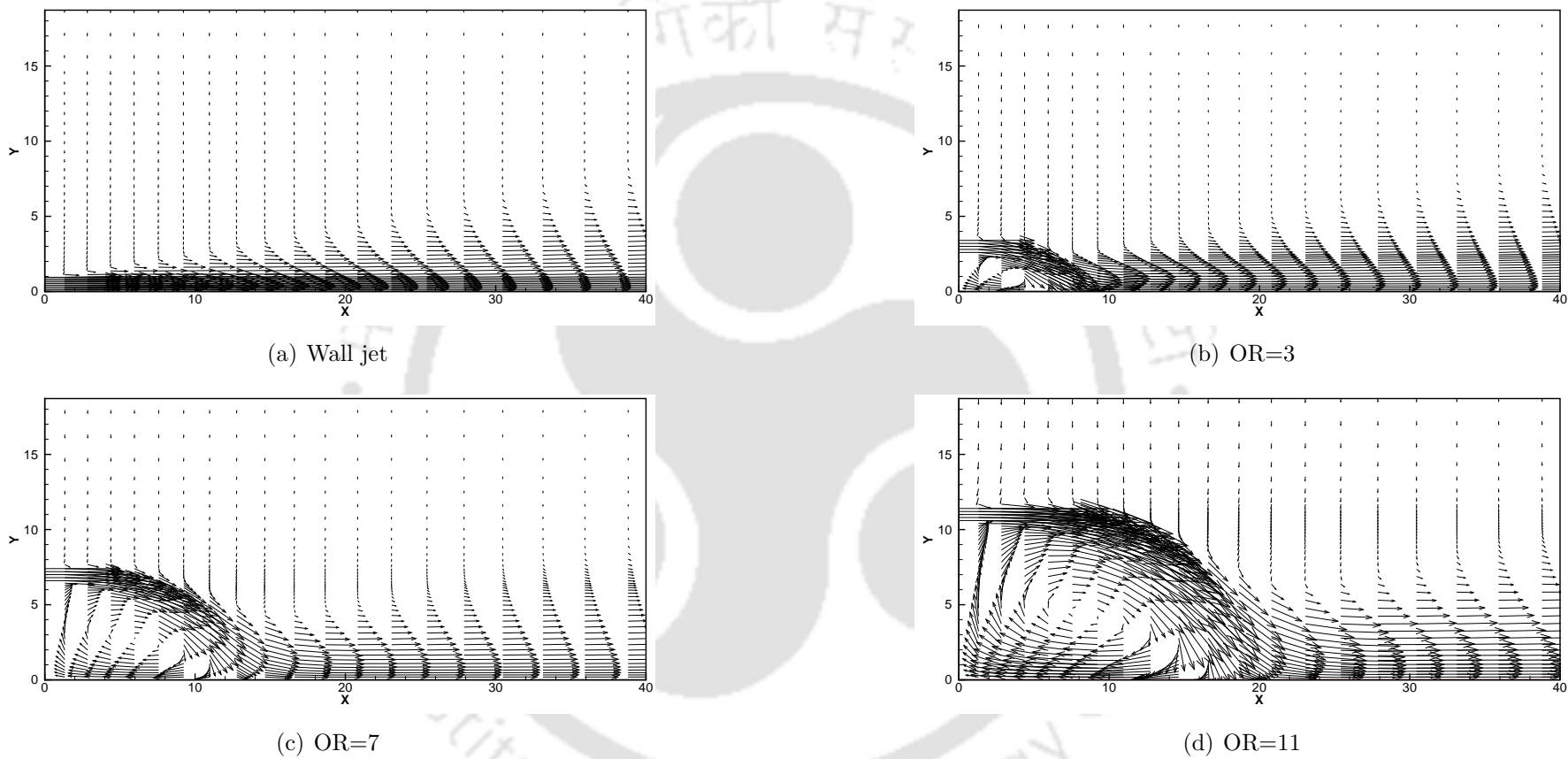
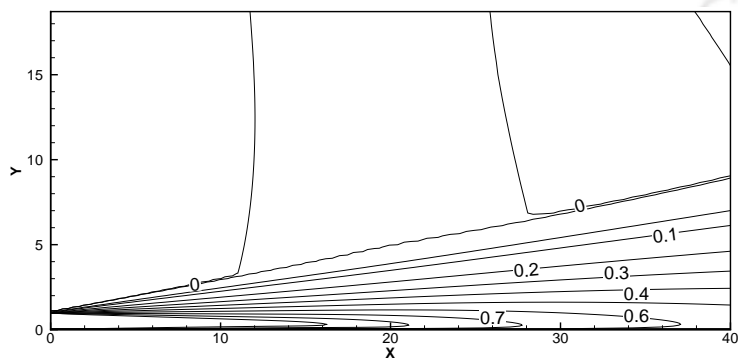
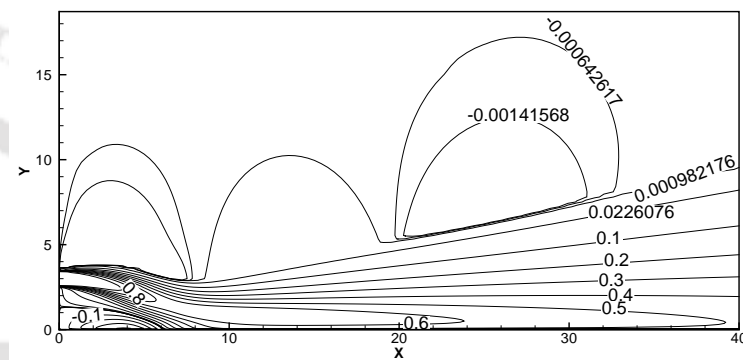


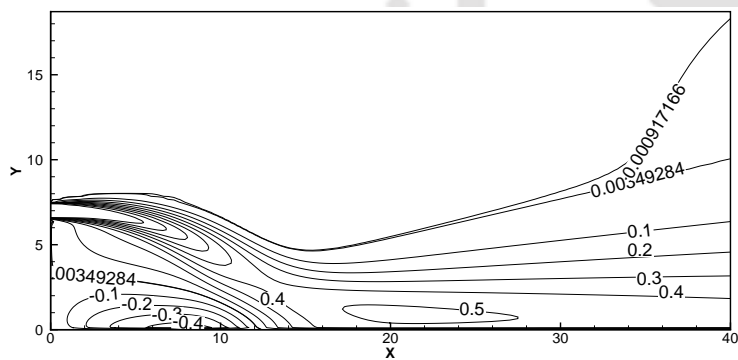
Figure 3.8: Vector distribution of offset jet at different offset ratios



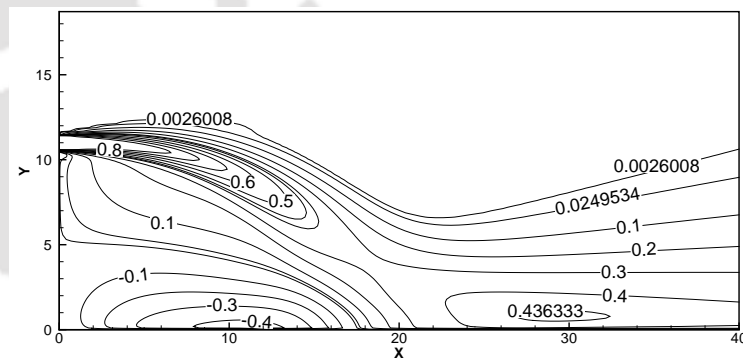
(a) Wall jet



(b) OR=3

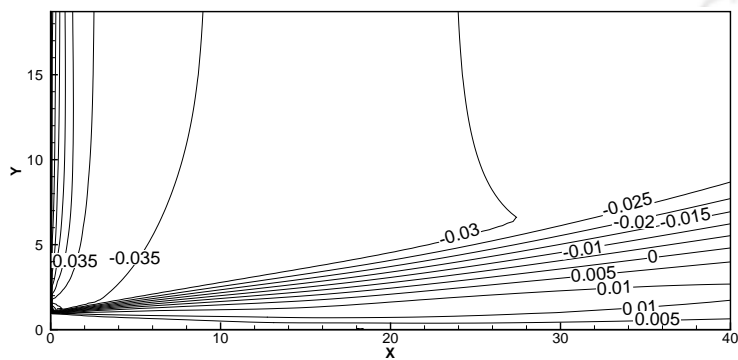


(c) OR=7

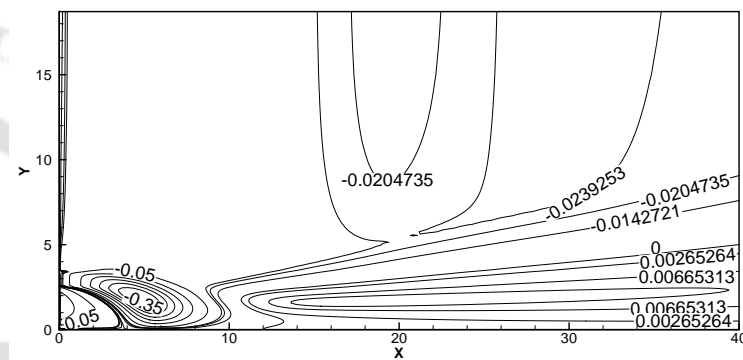


(d) OR=11

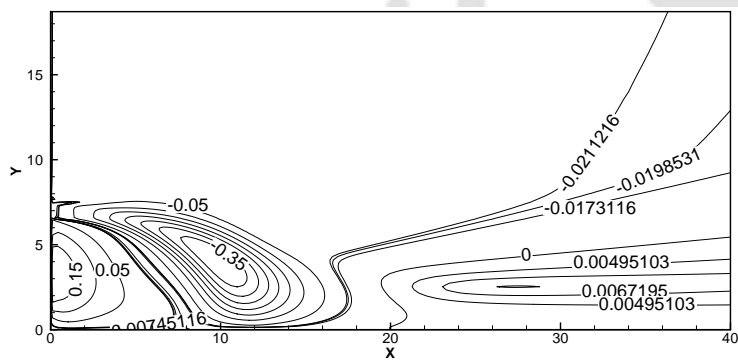
Figure 3.9:  $\bar{U}$ -contour distribution of offset jet at different offset ratios



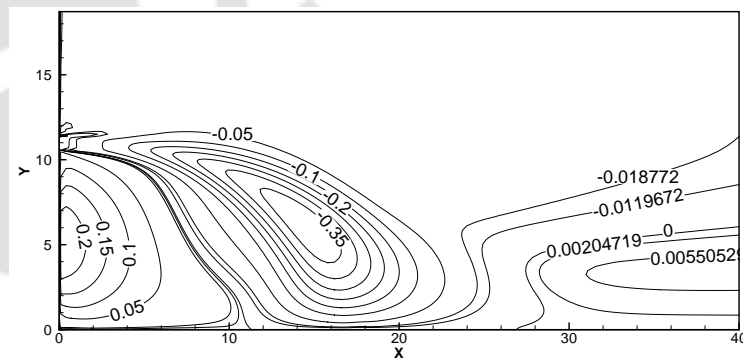
(a) Wall jet



(b) OR=3



(c) OR=7



(d) OR=11

Figure 3.10:  $\bar{V}$ -contour distribution of offset jet at different offset ratios

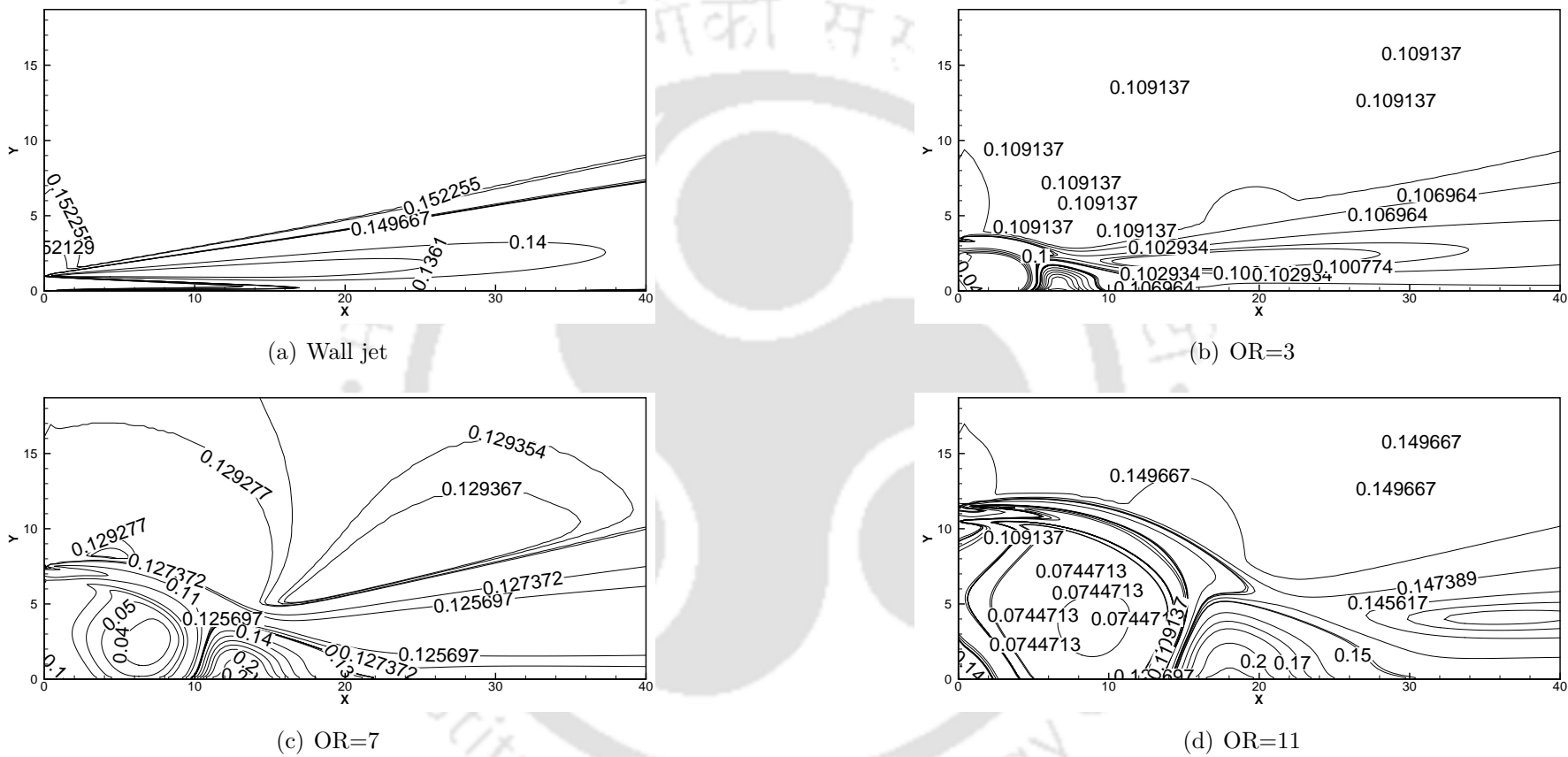


Figure 3.11: Pressure distribution of offset jet at different offset ratios



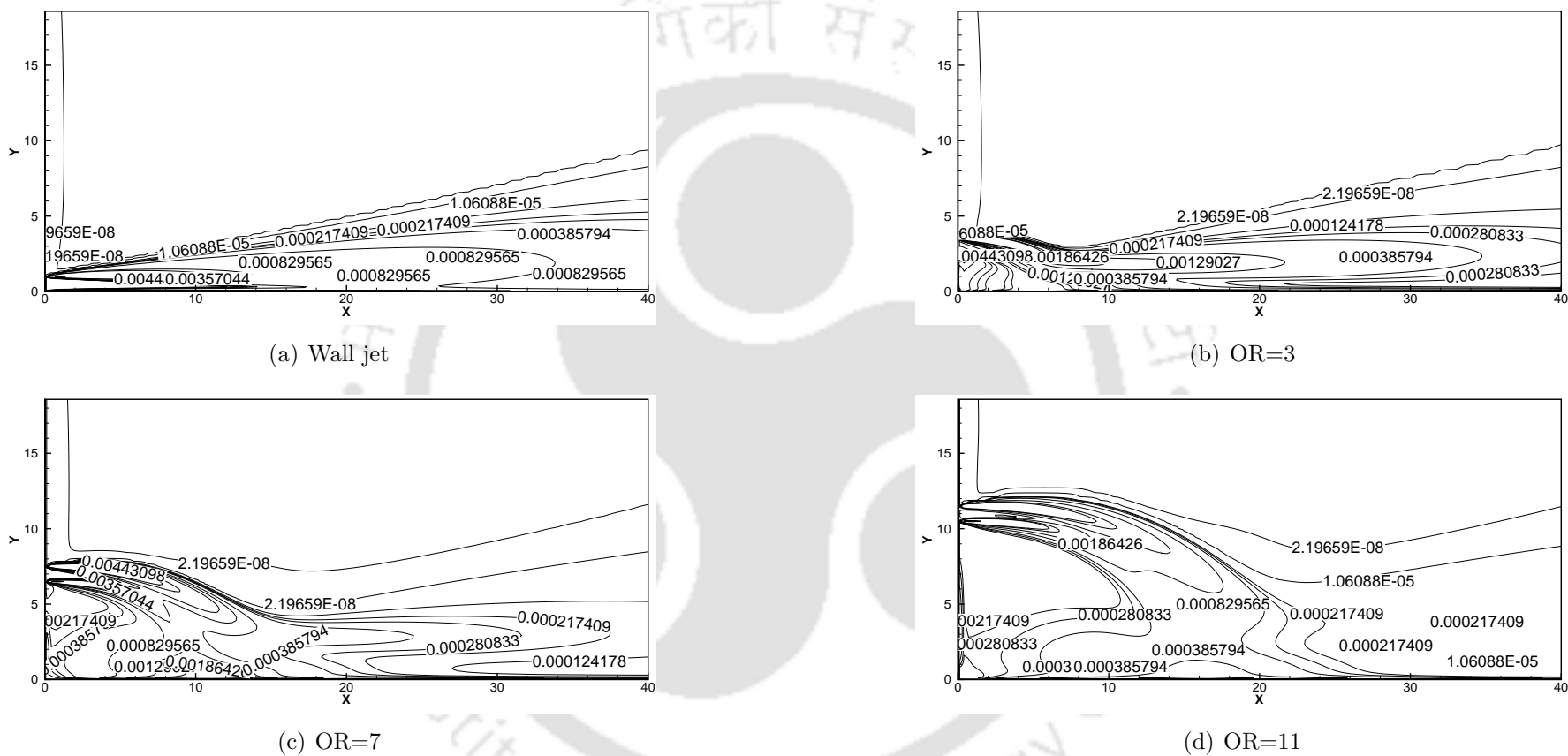


Figure 3.13: Dissipation( $\epsilon$ ) distribution of offset jet at different offset ratios

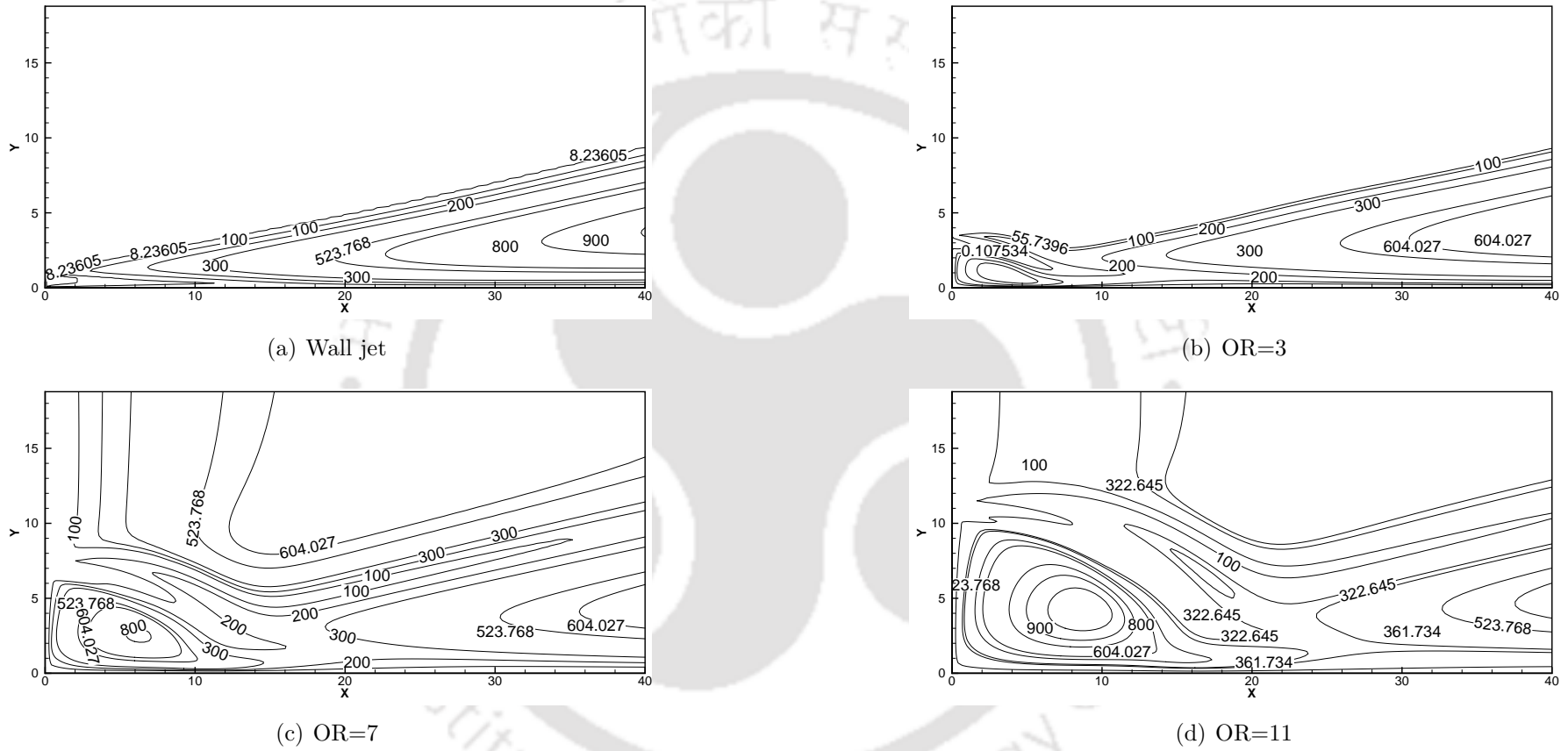


Figure 3.14: Turbulent viscosity ( $\nu_t$ ) distribution of offset jet at different offset ratios

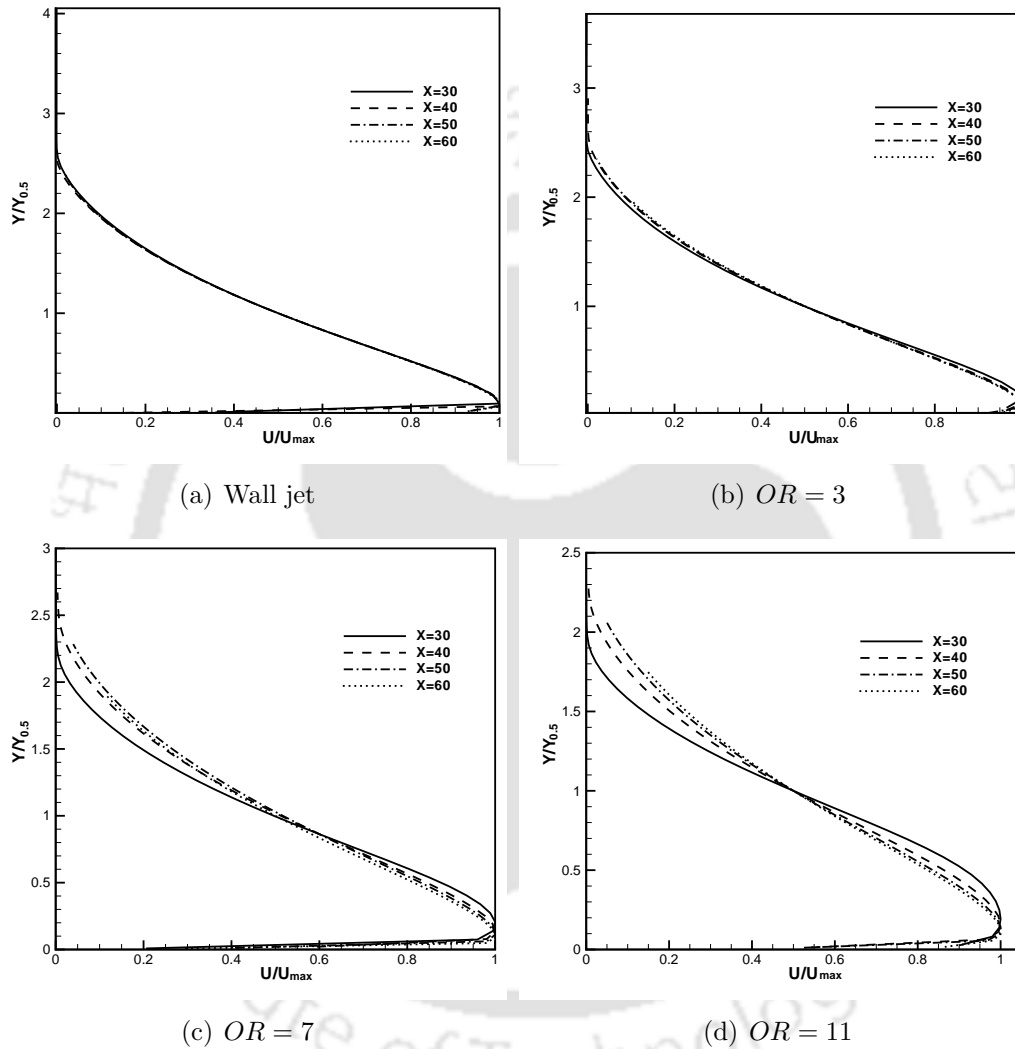


Figure 3.15: Similarity solution for different offset ratio at four downstream locations

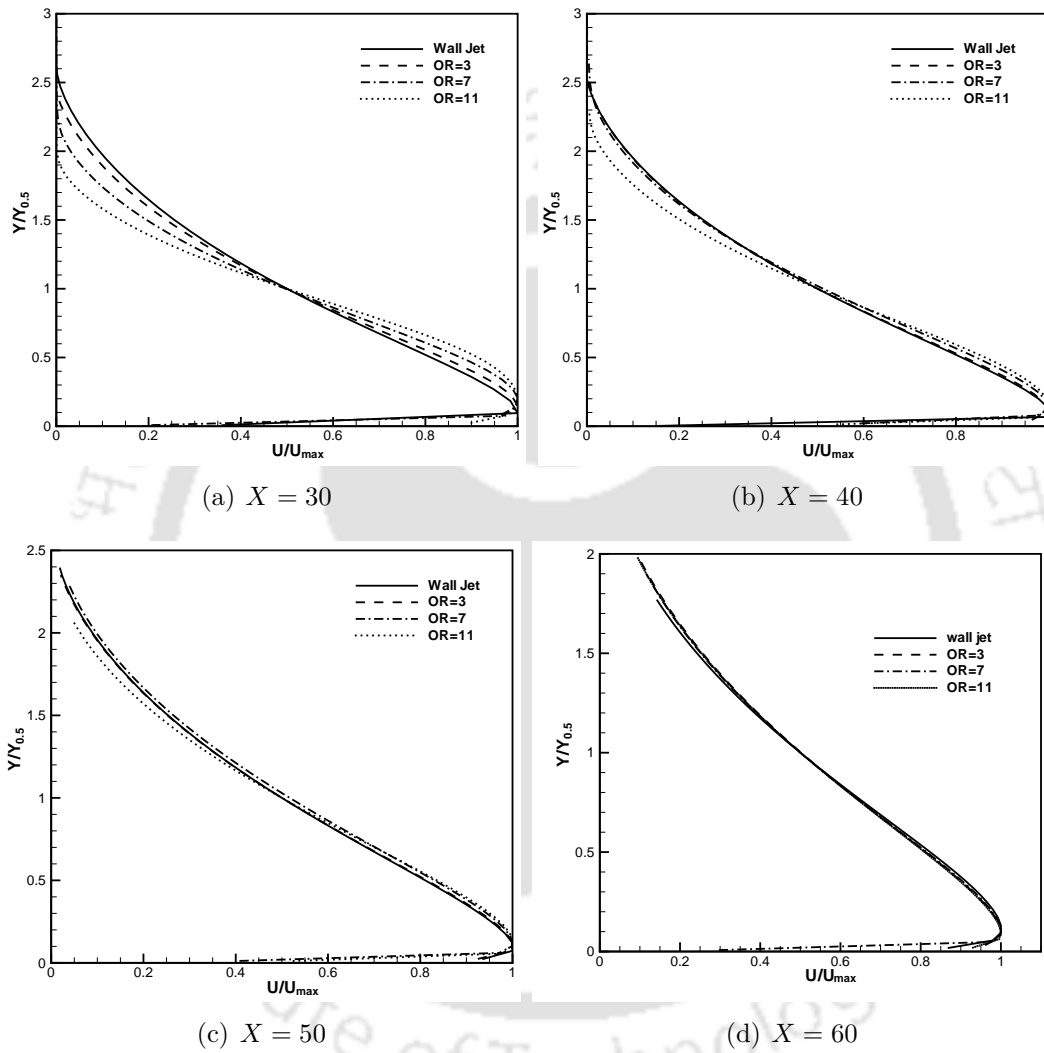


Figure 3.16: Similarity solution at different downstream locations for various offset ratios.

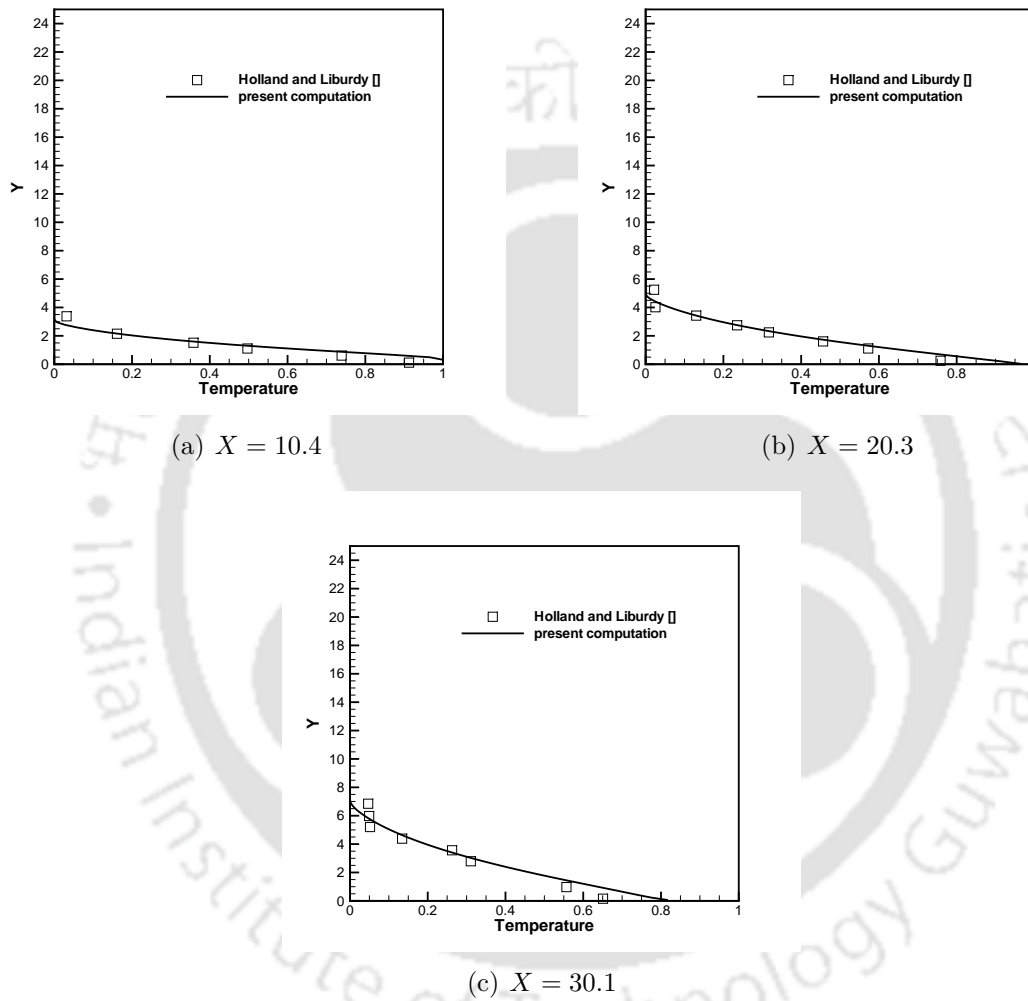


Figure 3.17: Comparison of temperature ( $\bar{\theta}$ ) profiles with experimental results of Holland and Liburdy [4] at different locations for wall jet

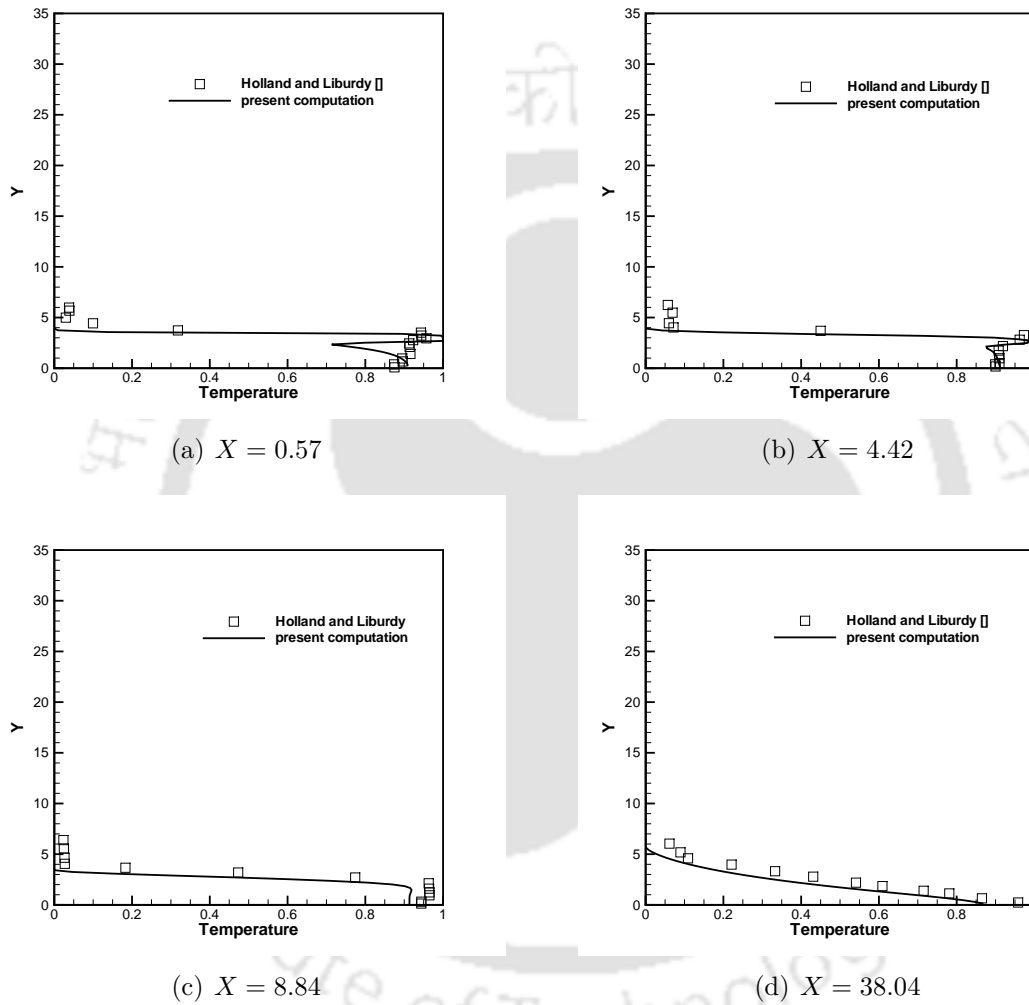


Figure 3.18: Comparison of temperature ( $\bar{\theta}$ ) profiles with experimental results of Holland and Liburdy [4] at different locations for  $OR = 3$

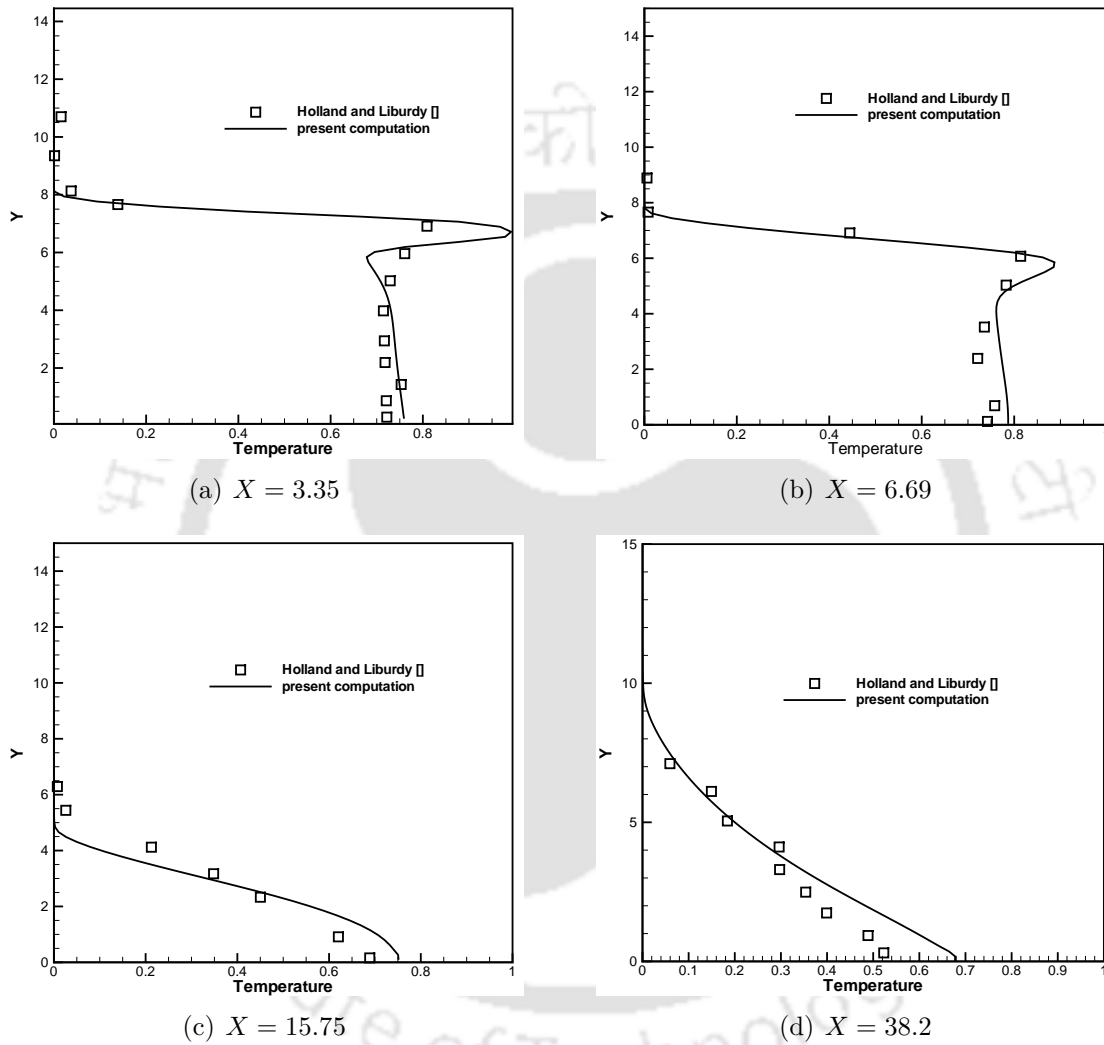


Figure 3.19: Comparison of temperature ( $\bar{\theta}$ ) profiles with experimental results of Holland and Liburdy [4] at different locations for  $OR = 7$

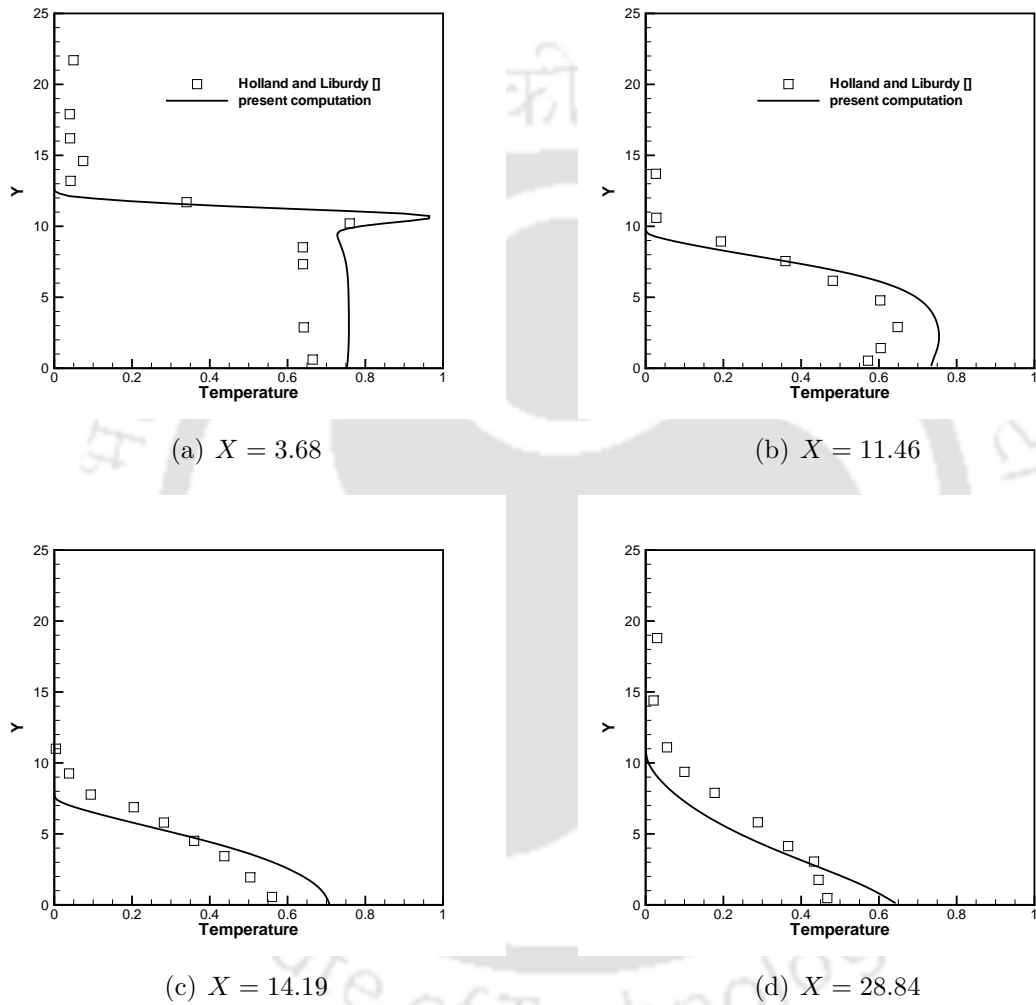


Figure 3.20: Comparison of temperature ( $\bar{\theta}$ ) profiles with experimental results of Holland and Liburdy [4] at different locations for  $OR = 11$

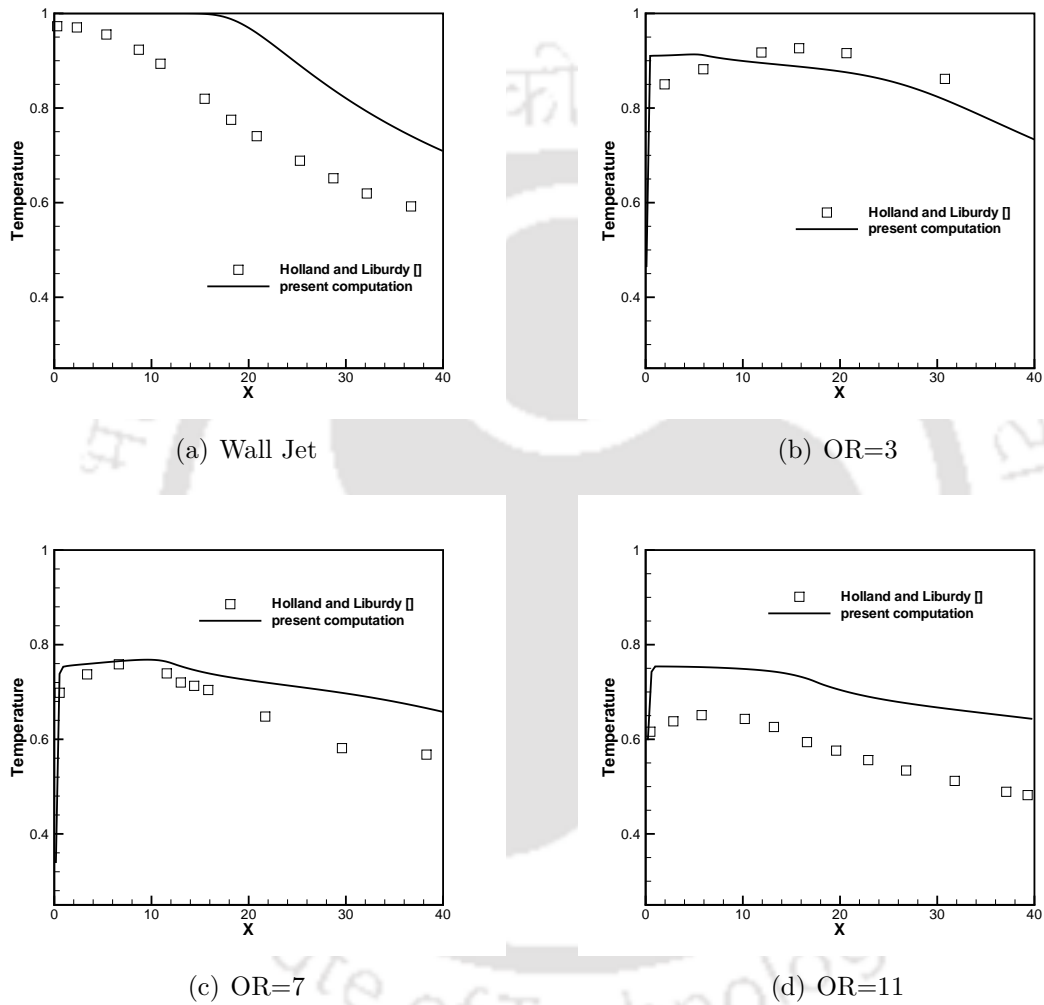


Figure 3.21: Comparison of surface temperature ( $\bar{\theta}$ ) profiles with experimental results of Holland and Liburdy [4] for different offset ratios.



### 3.3 Conclusions

The flow and heat transfer study of heated offset jet has been carried out numerically using two-equation  $k-\epsilon$  turbulence model. A standard wall function has been used. The impinging surface is considered as adiabatic so that the downstream temperature distribution illustrate the entrainment characteristics. The following conclusions may be drawn:

- Minimum value of  $\bar{U}_{max}$  occurs very near to the reattachment point in the downstream direction and it decreases as  $OR$  increases.
- The maximum value of wall shear stress decreases as  $OR$  increases. The positive region of  $\tau_w$  shows the recirculation region.
- The pressure distribution along the wall remains nearly constant for wall jet case.
- For wall jet, the similarity profile for the velocity has been obtained at  $X = 30$ . For  $OR = 3, 7$  and  $11$ , the distances at which the similarity profile has been observed are approximately  $40, 50$  and  $60$ . It has been observed that at a distance of approximately  $60$ , the velocity profile for wall jet and other three  $OR$  cases overlap with each other implying that a wall jet situation arises in far downstream for all the cases.
- The computed temperature profile at different downstream locations for the cases considered are in very good agreement with the experimental results. The temperature profile in the recirculation region is within the acceptable accuracy implying that the present turbulence model is suitable for predicting offset jet flows.
- The computed temperature of the adiabatic surface is on the higher side for wall jet and  $OR = 11$ . This is because of the presence of the zero heat flux adiabatic boundary condition.

# Chapter 4

## Computational Study of Heat

## Transfer in a Conjugate

## Turbulent Wall Jet Flow at High

## Reynolds Number

### 4.1 Introduction

In the present case, the conjugate heat transfer involving a turbulent plane wall jet under constant bottom wall temperature is considered. The parameters considered are the conductivity ratio, the solid slab thickness and the Prandtl number. The Reynolds number considered is 15000 because the flow becomes fully turbulent and then it becomes independent of the Reynolds number as has been experimentally observed by Pelfrey and Liburdy [4]. The purpose of the study is to observe and describe the effect of Prandtl number ( $Pr$ ), thermal conductivity ratio ( $K$ ) and the thickness of solid slab ( $S$ ) on the interface surface temperature, heat transfer between the solid and the fluid, local Nusselt number distribution, average Nusselt number and the temperature distribution in the solid and the fluid. The range of

parameters considered are: for  $Pr$  it is 0.01 to 100, for  $K$  it is 1 to 1000 and for  $S$  it is 1 to 10. The schematic diagram of the conjugate wall jet is shown in Fig. 4.1.

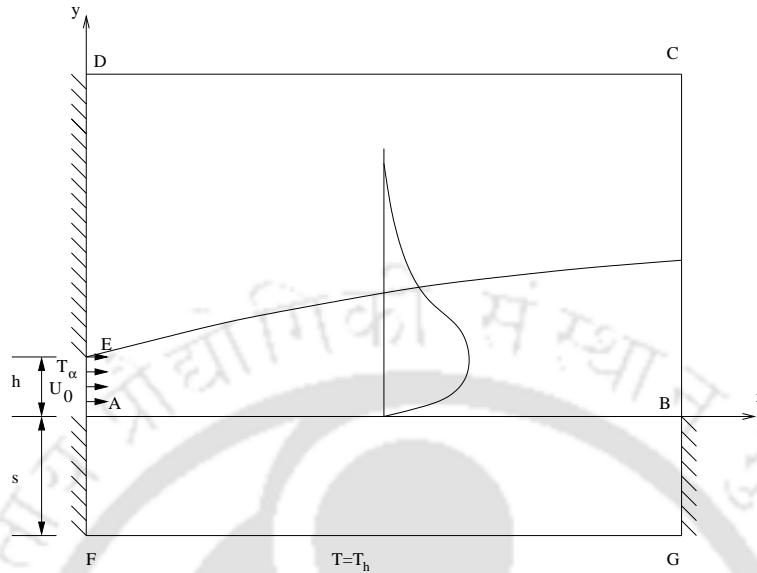


Figure 4.1: Schematic and computational domain of the wall jet flow

The numerical scheme and method of solution as explained in section 2.6 is used in the present computations. Similarly, the hydro-dynamic boundary conditions are explained in section 3.1.1. For the temperature, at the inlet(AE),  $\theta=0$  and the entrainment and exit boundaries (i.e CD and BC respectively), Neumann boundary conditions are provided i.e.  $\partial\theta/\partial n = 0$ . At the solid-fluid interface(AB), the equality of temperature and flux i.e.  $(\theta_s)_w = (\theta_f)_w$  and  $(Q_w)_s = (Q_w)_f$  are applied and the details are mentioned in the appendix (Appendix A). The left and right side (AF and BG respectively as shown in Fig. 4.1) of the solid block are considered as adiabatic. The code validation and grid independence details are given in section 3.1.2. Since the flow is incompressible, the Already available fluid flow solution is used to solve the energy equation in both the solid and the fluid regions. Grid independence is done in the solid for  $S=1$  by varying the Prandtl number and thermal conductivity ratio ( $K$ ). For other sizes, the grid size is correspondingly increased, which is reasonably valid in the solid block.

## 4.2 Results and Discussion

In the present work,  $Re = 15000$  is chosen for all computations. The flow becomes fully turbulent and there is no discernible Reynolds number effect on the mean flow characteristics [4]. Since the uniform velocity and some turbulent intensity is given at the inlet of the jet, it takes some length for the flow to become fully turbulent and develop the self similar region, which is observed in the fluid solution. It is observed that approximately at  $X \simeq 30$  the flow become fully turbulent and self similarity is achieved. The effects of  $Pr$ ,  $K$  and  $S$  on the interface surface temperature ( $\theta_i$ ), heat transfer between the solid and the fluid ( $Q_i$ ), local Nusselt number distribution ( $Nu_x$ ), average Nusselt number ( $\overline{Nu}$ ) and the temperature distribution in the solid and the fluid have been discussed. In the present study,  $Pr$  is varied between 0.01 to 100,  $K$  is varied between 1 to 1000 and  $S$  is varied between 1 to 10. The derivation of heat flux is given in Appendix A. The definitions of  $Nu_x$  and  $\overline{Nu}$  are shown in Appendix B.

### Interface Temperature

Figure 4.2 shows the interface temperature ( $\theta_i$ ) distribution at various Prandtl numbers keeping the solid thickness ( $S = 10$ ) and the thermal conductivity ratio ( $K = 1000$ ) constant. It is observed that  $\theta_i$  is high at low  $Pr$ . This is because at low  $Pr$ , the thermal boundary layer is large. A large surface temperature is required to dissipate the heat to the jet fluid. Conversely, the interface temperature decreases significantly as  $Pr$  increases because the thermal boundary layer gets correspondingly smaller and a lower surface temperature is sufficient to dissipate the heat. The surface temperature increases along the wall at high Prandtl numbers because initially the heat transfer is large which decreases gradually along the length. The interface temperature distribution at various thermal conductivity ratios keeping the Prandtl number equal to 1.0 and solid thickness equal to 10

are given in Fig. 4.3. When  $K$  is small, the resistance to heat transfer is large, the drop in temperature is large and thus the interface temperature is small. As  $K$  increases to 1000, the interface temperature is relatively large because of the same reason. The variation of  $\theta_i$  distribution at various solid thickness ( $S$ ) keeping the Prandtl number ( $Pr = 1.0$ ) and thermal conductivity ratio ( $K = 1000$ ) is plotted in Fig. 4.4. For a small slab thickness  $S = 1$ , the thermal resistance is less leading to a higher interface temperature. As  $S$  is increased to 10, it is observed that the interface temperature has dropped down because of the same reason.

### Local Nusselt Number

The local Nusselt number variation is shown in Figure 4.5 for various Prandtl numbers keeping the solid thickness ( $S = 10$ ) and thermal conductivity ratio ( $K = 1000$ ) constant. In general,  $Nu_x$  increases to a large value near the jet entry and then gradually decreases in the direction of flow. This is a characteristics of the jet boundary layer formation. As shown in Fig. 4.5, it demonstrates clearly that  $Nu_x$  increases with  $Pr$  because of the thinning of the thermal boundary layer. Figure 4.6 shows the  $Nu_x$  distribution at various thermal conductivity ratios keeping  $Pr = 1.0$  and  $S = 10$ . It is observed that for the range of  $K$ , the  $Nu_x$  distribution superimposes with each other. The  $Nu_x$  distribution at various solid thickness ( $S$ ) keeping  $Pr = 1.0$  and thermal conductivity ratio  $K = 1000$  is shown in Fig. 4.7. Similar to the previous case, the  $Nu_x$  distributions for the range of  $S$  superimposes with each other. From these three figures, it is concluded that  $Nu_x$  is dependent on the fluid property  $Pr$  and remains unaltered for the variation of  $K$  and  $S$ . In the region between  $X = 25$  to 30 the  $Nu_x$  increases. This can be attributed to the flow attains self-similarity.

### Local Heat Flux

Figure 4.8 shows the local heat flux  $Q_w$  distribution at various Prandtl numbers keeping  $S = 10$  and  $K = 1000$ . On contrary to the  $Nu_x$ , heat flux ( $Q_w$ ) shown

in Fig. 4.8 decreases as the  $Pr$  increases. Heat flux is almost constant along the wall and increases as the  $Pr$  decreases. The rate of decrement also increases as  $Pr$  decreases. Figure 4.9 shows the  $Q_w$  distribution at various thermal conductivity ratios keeping  $Pr = 1.0$  and  $S = 10$ . Heat flux increases as  $K$  increases and it decreases along the wall at higher thermal conductivity ratio. Figure 4.10 shows the  $Q_w$  distributions at various solid thickness ( $S$ ) keeping  $Pr = 1.0$  and  $K = 1000$ . As expected the heat flux ( $Q_w$ ) increases as the solid thickness decreases.

### Average Nusselt Number

Extensive computations are done in their respective ranges and results of the average Nusselt number ( $\overline{Nu}$ ) are presented in Table 4.1. It shows clearly that  $\overline{Nu}$  is a function of Prandtl number only. The effect of solid thickness ( $S$ ) and thermal conductivity ratio ( $K$ ) are negligibly small. It is observed that  $\overline{Nu}$  increases with the increase of  $Pr$ .

### Average Heat Transfer

The average heat transfer integrated over the interface for various  $S$ ,  $K$  and  $Pr$  are shown in Table 4.2. The heat transfer for the conjugate case is compared with the non-conjugate case ( $S=0$ ). It is observed that as the solid thickness increases, heat transfer decreases. However, as  $K$  is increasing,  $Q_i$  increases. For  $K=1000$ ,  $Q_i$  approaches almost equal to the non-conjugate case.

Table 4.1: Average Nusselt number ( $\overline{Nu}$ ) at various Prandtl numbers

$S$ (thickness of solid slab)	thermal conductivity ratio $K(k_s/k_f)$	$Nu (Pr = 0.01)$	$Nu (Pr = 0.1)$	$Nu (Pr = 1)$	$Nu (Pr = 10)$	$Nu (Pr = 100)$
0(non-conjugate)	-	1.27179	8.30537	31.096	72.7912	152.969
1	1	1.33476	8.83939	31.6452	73.0195	153.062
1	100	1.27354	8.36272	31.2762	72.9244	153.043
1	1000	1.27197	8.31165	31.1207	72.8155	152.989
5	1	1.35813	8.8736	31.6568	73.0216	153.062
5	100	1.27916	8.48842	31.5269	73.0311	153.075
5	1000	1.27258	8.33092	31.203	72.8876	153.033
10	1	1.36203	8.8775	31.6584	73.0219	153.062
10	100	1.28428	8.55228	31.6108	73.0585	153.082
10	1000	1.27321	8.34651	31.2697	72.9384	153.056

Table 4.2: Heat Transfer across the interface ( $Q_i$ ) at various Prandtl numbers

$S$ (thickness of solid slab)	thermal conductivity ratio $K(k_s/k_f)$	$Q_i (Pr = 0.01)$	$Q_i (Pr = 0.1)$	$Q_i (Pr = 1)$	$Q_i (Pr = 10)$	$Q_i (Pr = 100)$
0(non-conjugate)	-	0.635897	0.415269	0.15548	0.0363956	0.00764847
1	1	0.282885	0.0448034	0.00484193	0.000492944	4.97E-05
1	100	0.628321	0.384863	0.118324	0.0208609	0.00299052
1	1000	0.635132	0.41203	0.150738	0.0338425	0.00659982
5	1	0.0868023	0.00977382	0.000993511	9.97E-05	9.99E-06
5	100	0.599475	0.296107	0.060686	0.00779314	0.00088023
5	1000	0.63207	0.399399	0.1344	0.0264942	0.00428858
10	1	0.0464729	0.00494282	0.000498372	4.99E-05	5.00E-06
10	100	0.56658	0.229028	0.0377512	0.004378	0.00046808
10	1000	0.628251	0.384457	0.118385	0.0208823	0.00299318

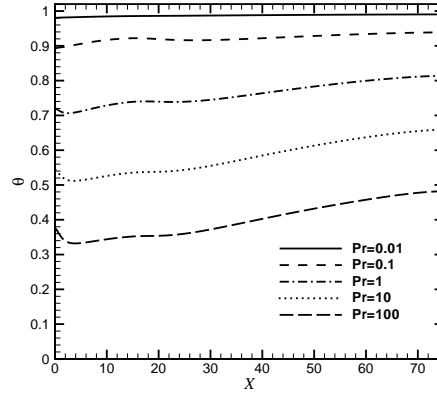


Figure 4.2: Interface temperature distribution ( $\bar{\theta}_i$ ) distribution for  $S=10$  and  $K = 1000$  at various Prandtl numbers

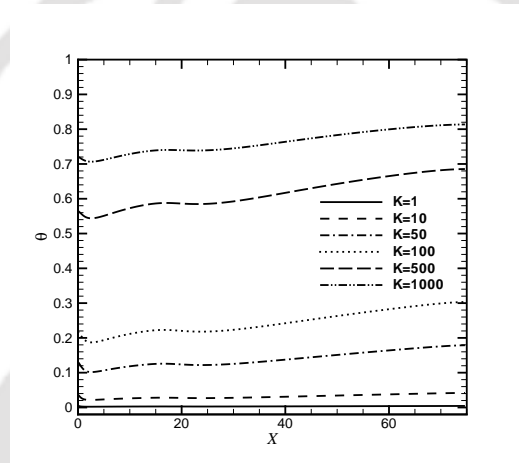


Figure 4.3: Interface temperature distribution ( $\bar{\theta}_i$ ) distribution for  $Pr = 1$  and  $S = 10$  at various thermal conductivity ratios ( $K$ ).

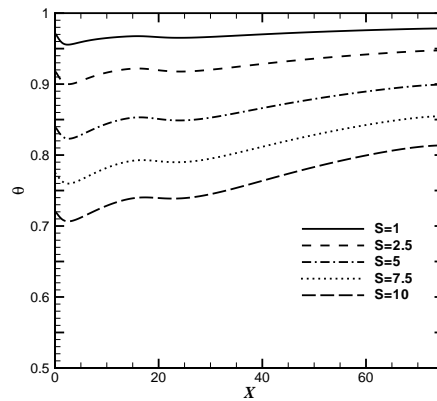


Figure 4.4: Interface temperature distribution ( $\bar{\theta}_i$ ) distribution for  $Pr = 1$  and  $K = 1000$  at solid thickness ratios ( $S$ ).

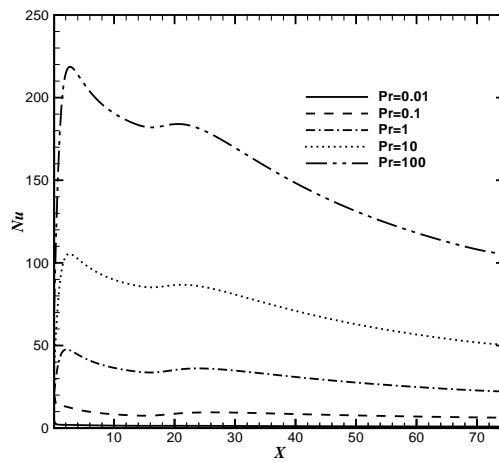


Figure 4.5: Local Nusselt number ( $Nu_x$ ) distribution for  $S=10$  and  $K = 1000$  at various Prandtl numbers

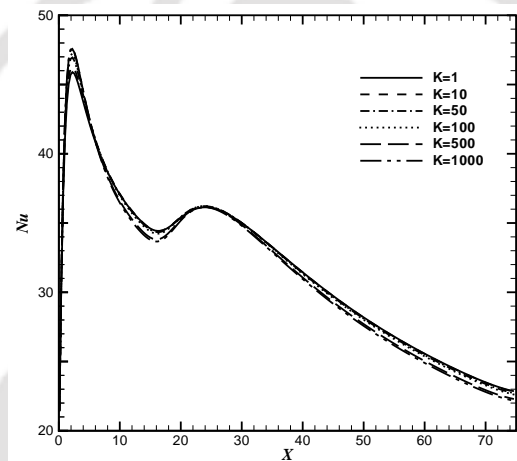


Figure 4.6: Local Nusselt number ( $Nu_x$ ) distribution for  $Pr=1$  and  $S = 10$  at various thermal conductivity ratios ( $K$ ).

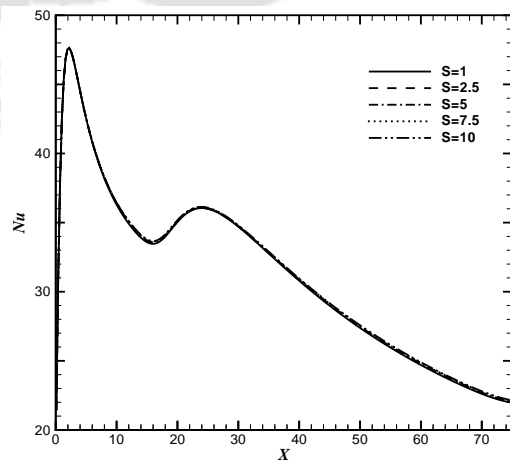


Figure 4.7: Local Nusselt number ( $Nu_x$ ) distribution for  $Pr=1$  and  $K = 1000$  at various solid thickness ratios ( $S$ ).

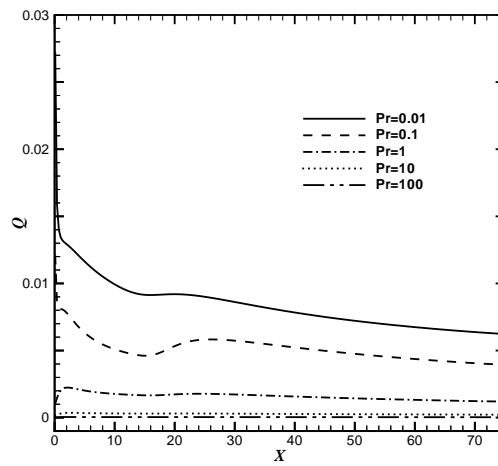


Figure 4.8: Heat flux ( $Q_x$ ) distribution for  $S=10$  and  $K = 1000$  at various Prandtl numbers

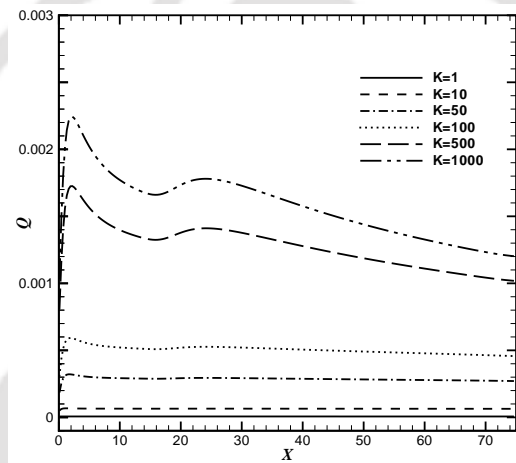


Figure 4.9: Heat flux ( $Q_x$ ) distribution for  $Pr=1$  and  $S = 10$  at various various thermal conductivity ratios ( $K$ ).

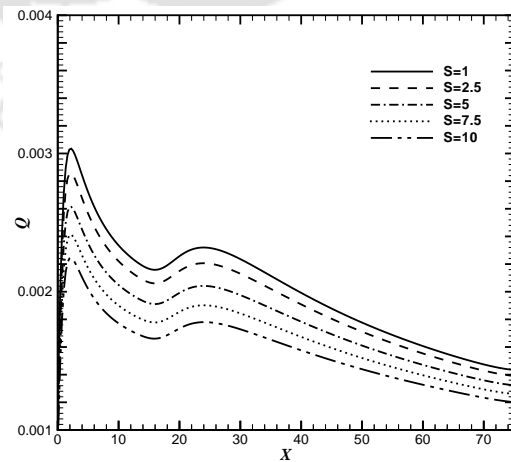


Figure 4.10: Heat flux ( $Q_x$ ) distribution for  $Pr=1$  and  $K = 1000$  at various various solid thickness ratios ( $S$ ).

## 4.3 Concluding Remarks

In the present case, the conjugate heat transfer involving a turbulent plane wall jet is considered. The parameters considered are the conductivity ratio, the solid slab thickness and the Prandtl number. The Reynolds number considered is 15000 because the flow becomes fully turbulent and then it becomes independent of the Reynolds number. It is observed that the interface temperature is high at low  $Pr$ . Conversely, the interface temperature decreases significantly as  $Pr$  increases. When  $K$  is small, the interface temperature is small. As  $K$  increases to 1000, the interface temperature is relatively large. For a small slab thickness  $S = 1$ , the thermal resistance is less leading to a higher interface temperature. As  $S$  is increased to 10, it is observed that the interface temperature has dropped down. It is demonstrated clearly that  $Nu_x$  increases with  $Pr$  because of the thinning of the thermal boundary layer. It is observed that for the range of  $K$  and  $S$ , the  $Nu_x$  distribution superimposes with each other. Heat flux increases as  $K$  increases and it decreases along the wall at higher thermal conductivity ratio. The heat flux increases as the solid thickness decreases. It shows clearly that average  $Nu$  is a function of Prandtl number is independent of  $K$  and  $S$ . As  $K$  is increasing, the average heat transfer increases. For  $K=1000$ , the average heat transfer approaches almost equal to the non-conjugate case.

# Chapter 5

## Computational Study of Heat Transfer in a Conjugate Turbulent Wall Jet Flow with Constant Heat Flux

### 5.1 Introduction

In the present case, the conjugate heat transfer involving a turbulent plane wall jet is considered. The bottom of the solid slab is heated by a constant heat flux. The parameters considered are the conductivity ratio (solid/fluid), the solid slab thickness and the Prandtl number. The Reynolds number considered is 15000 because the flow becomes fully turbulent and then it becomes independent of the Reynolds number [4]. Important heat transfer characteristics such as Local nusselt number ( $Nu_x$ ), heat flux ( $Q_x$ ) and temperature ( $\bar{\theta}$ ) at the interface are described. Average nusselt number at the interface is presented in tabular form and observations are reported. The schematic diagram of the conjugate wall jet is shown in Fig. 5.1. The numerical scheme and method of solution as explained

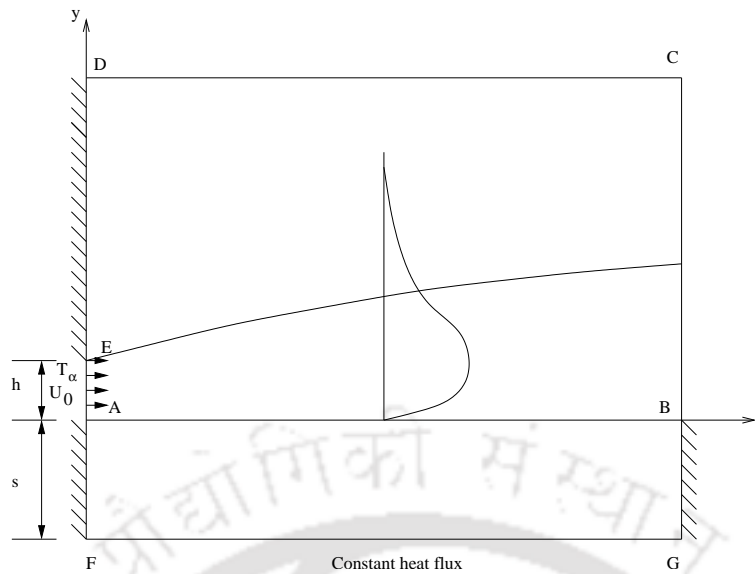


Figure 5.1: Schematic and computational domain of the wall jet flow

in section 2.6 is used in the present computations. Similarly, the hydro-dynamic boundary conditions are explained in section 3.1.1. For the temperature, the boundary conditions are same as given in section 4.1, except constant heat flux at bottom of the slab(EG) and shown in Fig. 5.1.

## 5.2 Results and Discussion

In the present work,  $Re = 15000$  is chosen for all computations. The flow becomes fully turbulent and there is no discernible Reynolds number effect on the mean flow characteristics [4]. Since the uniform velocity and some turbulent intensity is given at the inlet of the jet, it takes some length for the flow to become fully turbulent and develop the self similar region, which is observed in the fluid solution. It is observed that approximately at  $X \simeq 30$ , the flow become fully turbulent and a self-similarity is achieved. At the bottom, a constant heat flux boundary condition is applied. The purpose of the study is to observe and describe the effect of Prandtl number ( $Pr$ ), thermal conductivity ratio ( $K$ ) and the thickness of solid slab ( $S$ ) on the bottom wall temperature, interface surface temperature ( $\theta_i$ ), heat

transfer between the solid and the fluid ( $Q_i$ ), local Nusselt number distribution ( $Nu_x$ ), average Nusselt number ( $\overline{Nu}$ ) and the temperature distribution in the solid and the fluid. For this,  $Pr$  is varied between 0.01 to 100,  $K$  is varied between 1 to 1000 and  $S$  is varied between 1 to 10. The derivation of heat flux is given in Appendix A. The definition of constant heat flux at the solid wall is given in Appendix C. The definitions of  $Nu_x$  and  $\overline{Nu}$  are shown in Appendix B.

### Bottom Wall Temperature

As discussed in Appendix C, the constant heat flux boundary condition is applied by  $-\frac{\partial \theta}{\partial Y} = \frac{Pr}{K}$  (Eq. C.2). Here  $Q_b$  is taken as  $1/Re$ . For a fixed  $K$ , as  $Pr$  is increasing, the bottom wall temperature is also increasing (Fig. 5.2(a)). Unlike a constant wall temperature case, the bottom wall temperature is changing with the change in  $Pr$  and  $K$ . Similarly, as  $K$  is increasing, the bottom wall temperature is decreasing (Fig. 5.2(b)). As  $S$  increases, the resistance to heat transfer increases. So the bottom wall temperature increases (Fig. 5.2(c)). In the downstream direction  $Nu_x$  decreases and thus the bottom wall temperature increases.

### Interface Temperature

Figure 5.3(a) shows the interface temperature ( $\theta_i$ ) distribution at various Prandtl numbers keeping the solid thickness ( $S = 10$ ) and the thermal conductivity ratio ( $K = 1000$ ) constant. Since the bottom wall temperature is high for high  $Pr$  case, the interface temperature is also high. The  $Nu_x$  is high near the inlet and thus there is decrease of the interface temperature for  $Pr=100$ . Similarly, as  $Pr$  decreases, the interface temperature also decreases. Figure 5.3(b) shows the  $\theta_i$  distribution at various thermal conductivity ratios keeping the Prandtl number equal to 1.0 and solid thickness equal to 10. The interface temperature for the first half is low for low  $K$  and the situation reverses for the last half. Figure 5.3(c) shows the  $\theta_i$  distribution at various solid thicknesses ( $S$ ) keeping the Prandtl number

( $Pr = 1.0$ ) and thermal conductivity ratio ( $K = 1000$ ). Similar trend is observed in this case also.

### Local Nusselt Number

Figure 5.4(a) shows the  $Nu_x$  distribution at various Prandtl numbers keeping the solid thickness ( $S = 10$ ) and thermal conductivity ratio ( $K = 1000$ ) constant. In general,  $Nu_x$  increases to a large value near the jet entry and then gradually decreases in the direction of flow. This is a characteristics of the jet boundary layer formation. As shown in the figure, it demonstrates clearly that  $Nu_x$  increases with  $Pr$  because of the thinning of the thermal boundary layer. Figure 5.4(b) shows the  $Nu_x$  distribution at various thermal conductivity ratios keeping  $Pr = 1.0$  and  $S = 10$ . It is observed that for the range of  $K$ , the  $Nu_x$  distribution superimposes with each other. Figure 5.4(c) shows the  $Nu_x$  distribution at various solid thickness ( $S$ ) keeping  $Pr = 1.0$  and thermal conductivity ratio  $K = 1000$ . Similar to the previous case, the  $Nu_x$  distributions for the range of  $S$  superimposes with each other. From these three figures, it is concluded that  $Nu_x$  depends on the fluid property  $Pr$  and remains unaltered for the variation of  $K$  and  $S$ . The increase in  $Nu_x$  in the region between  $X = 25$  to  $30$  can be attributed to the flow attains self-similarity.

### Local Heat Flux

Figure 5.5(a) shows the local heat flux  $Q_x$  distribution occurring through the interface at various Prandtl numbers keeping  $S = 10$  and  $K = 1000$ . There are minor variation of heat flux as  $Pr$  is being changed. Though a constant heat flux is applied at the bottom of the wall, it is observed that the heat flux along the wall varies at the interface. The local heat flux is high at the inlet and decreases along the wall. The variation of local heat flux is high for low Prandtl numbers. Figure 5.5(b) shows the  $Q_w$  distribution at various thermal conductivity ratios keeping

$Pr = 1.0$  and  $S = 10$ . At low thermal conductivity ratios the local heat flux along the wall is constant and increases as  $K$  increases. The heat flux applied at the bottom is constant. The same heat flux has to pass through the interface. As the heat flux is high in the initial part, the same thus decreases in the later part to satisfy the continuity of heat flux. Figure 5.5(c) shows the  $Q_w$  distributions at various solid thickness ( $S$ ) keeping  $Pr = 1.0$  and  $K = 1000$ . It is found that there is an effect of slab thickness on the local heat flux along the wall. At inlet of the jet, the local heat flux increases as the slab thickness increases. The decrement of heat flux along the later part can be justified by the reason given above.

### Average Nusselt Number

Extensive computations are done in the respective ranges of the parameters. The results of the average Nusselt number ( $\overline{Nu}$ ) are presented in Table 5.1. It shows clearly that  $\overline{Nu}$  is a function of Prandtl number only. The effect of the solid thickness ( $S$ ) and the thermal conductivity ratio ( $K$ ) are negligibly small. It is observed that  $\overline{Nu}$  increases with the increase of  $Pr$ .

### Average Heat Transfer

The average heat transfer integrated over the interface for various  $S$ ,  $K$  and  $Pr$  are obtained. It has been ensured that the average heat transfer from the interface matches with that occurring from the bottom surface for all the cases. This computation satisfies the overall energy balance.

Table 5.1: Average Nusselt number ( $\overline{Nu}$ ) at various Prandtl numbers

$S$ (thickness of solid slab)	thermal conductivity ratio $K(k_s/k_f)$	$Nu (Pr = 0.01)$	$Nu (Pr = 0.1)$	$Nu (Pr = 1)$	$Nu (Pr = 10)$	$Nu (Pr = 100)$
0(non-conjugate)	-	1.36885	8.88723	31.6527	73.019	153.062
1	1	1.36751	8.88378	31.6592	73.0218	153.062
1	100	1.34832	8.79847	31.7535	73.085	153.085
1	1000	1.30349	8.64074	31.729	73.1181	153.106
5	1	1.36634	8.88148	31.66	73.0223	153.063
5	100	1.322	8.71103	31.7363	73.0925	153.089
5	1000	1.28271	8.47891	31.6082	73.0989	153.106
10	1	1.36575	8.88066	31.6598	73.0223	153.063
10	100	1.30699	8.67783	31.7199	73.0901	153.089
10	1000	1.27948	8.42292	31.5114	73.0744	153.101

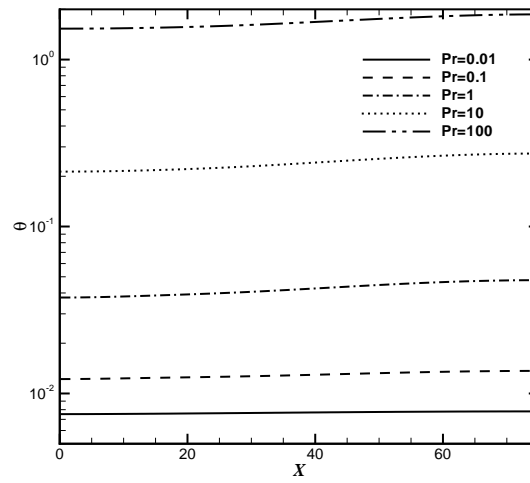
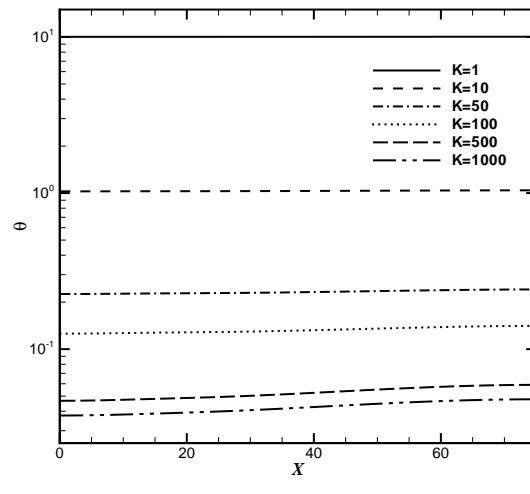
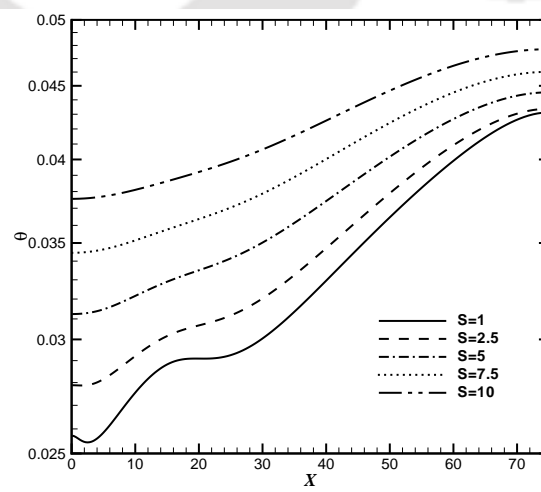
(a)  $S=10$  and  $K = 1000$ (b)  $Pr = 1$  and  $S = 10$ (c)  $Pr = 1$  and  $K = 1000$ 

Figure 5.2: Bottom surface temperature distribution

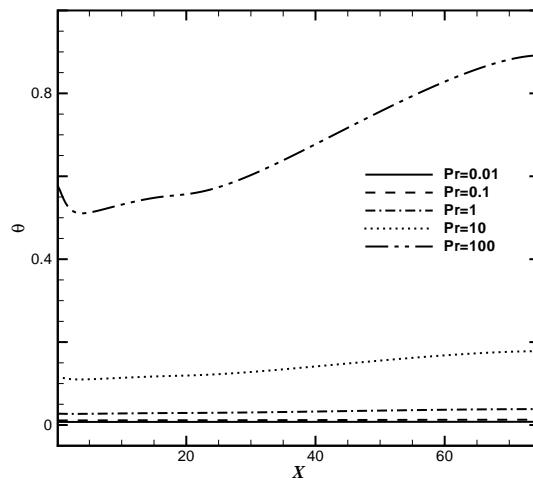
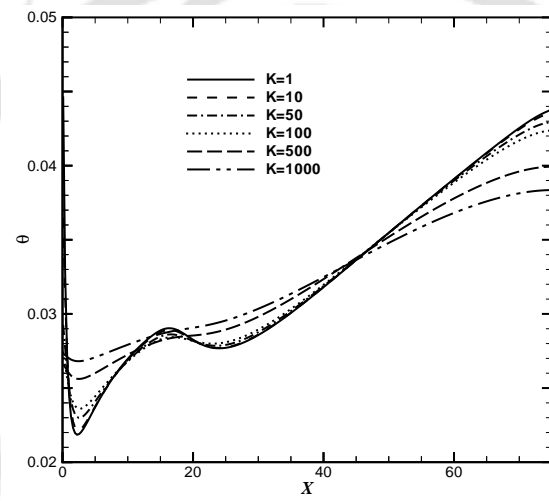
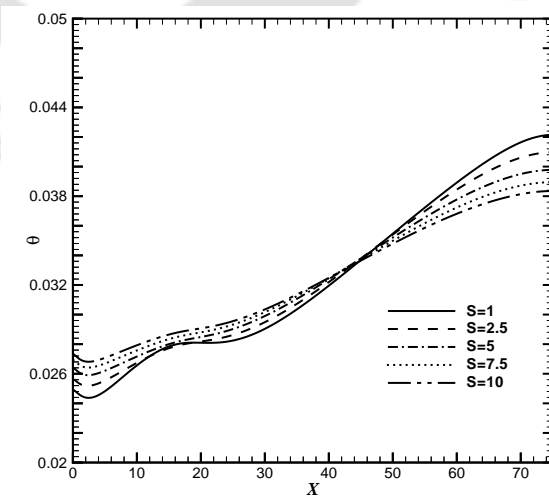
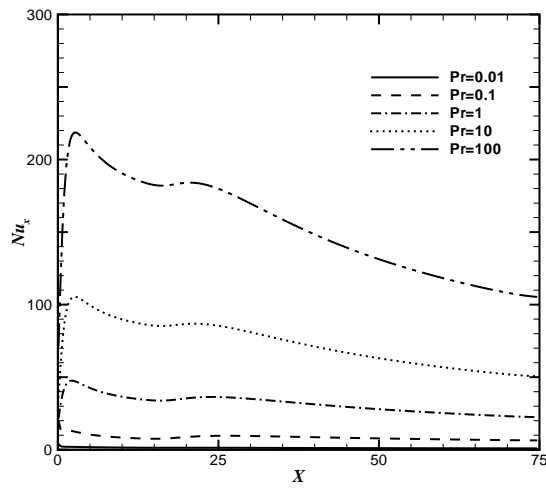
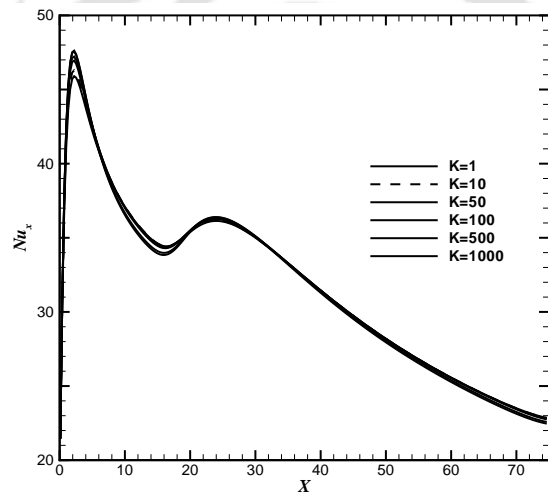
(a)  $S=10$  and  $K = 1000$ (b)  $Pr = 1$  and  $S = 10$ (c)  $Pr = 1$  and  $K = 1000$ 

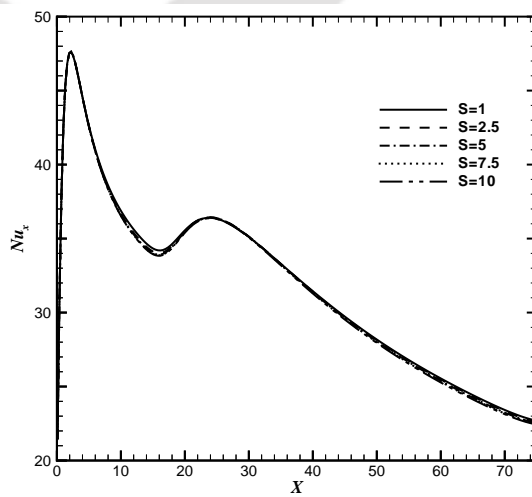
Figure 5.3: Interface temperature distribution



(a)  $S=10$  and  $K = 1000$



(b)  $Pr=1$  and  $S = 10$



(c)  $Pr=1$  and  $K = 1000$

Figure 5.4: Local Nusselt number distribution

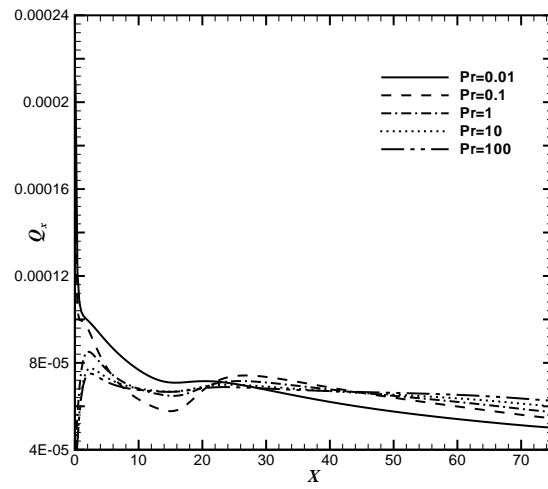
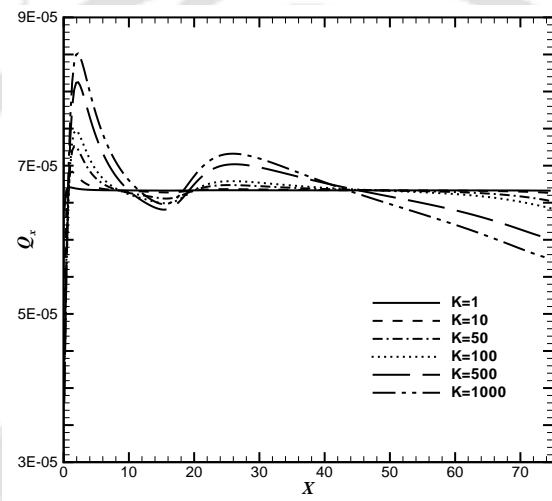
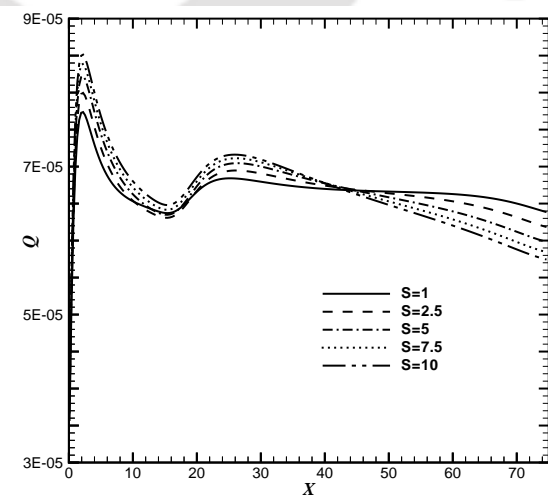
(a)  $S=10$  and  $K = 1000$ (b)  $Pr=1$  and  $S = 10$ (c)  $Pr=1$  and  $K = 1000$ 

Figure 5.5: Heat flux distribution

## 5.3 Concluding Remarks

In the present case, the conjugate heat transfer involving a turbulent plane wall jet is considered. The bottom surface is maintained at a constant heat flux boundary condition. The parameters considered are the conductivity ratio, the solid slab thickness and the Prandtl number. The Reynolds number considered is 15000 because the flow becomes fully turbulent and is independent of the Reynolds number. The non-dimensionalization of the heat flux boundary condition for a conjugate heat transfer case has been done. The non-dimensional bottom surface temperature is high for high  $Pr$  fluid and vice versa. As  $K$  increases, it decreases whereas it increases with the increase in  $S$ . Similar trend is observed for the distribution of the interface temperature. The Nusselt number computed based on the interface temperature increases with  $Pr$  because of the thinning of the thermal boundary layer. It is observed that for the range of  $K$  and  $S$ ,  $Nu_x$  distribution superimposes with each other. The local heat flux increases near the inlet because  $Nu_x$  is large and decreases at the later part to satisfy the equality of heat flux coming from the bottom wall and the heat flux dissipated by the wall jet. The average heat flux at the interface has been computed and found to be equal with average heat flux at the bottom which ensures the overall heat balance.

# Chapter 6

## Conjugate Heat Transfer Study of Incompressible Turbulent Offset Jet Flows

### 6.1 Introduction

Wall jet and offset jet are commonly used for cooling applications. A schematic diagram of an offset jet used for cooling a heated solid block is shown in Fig. 6.1. When the height  $t = 0$ , the offset jet becomes a wall jet. The jet is mainly divided into three regions, viz. the recirculation region, the impingement region and the wall jet region (as shown in Fig. 6.1).

In the present case, a conjugate heat transfer from a solid block heated with a constant wall temperature is considered. It is being cooled by a turbulent plane offset jet. In the laminar flow regime, many publications are devoted to conjugate heat transfer on flat plate details of which may be found in Kanna and Das [39]. However, the conjugate heat transfer study involving a turbulent flow has received little attention. Some of the conjugate heat transfer work published in literature (involving turbulent flow) are by Iaccarino et al. [41], Yilbas [32], Kassab et al. [40],

Hsieh and Lien [42]. The numerical scheme and method of solution as explained

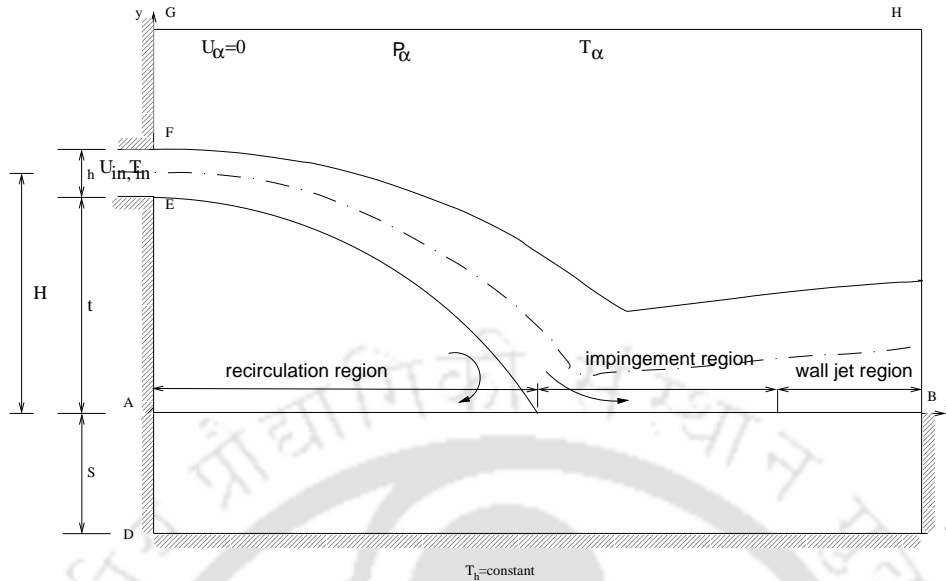


Figure 6.1: Schematic diagram of the offset jet and a solid block.

in section 2.6 is used in the present computations. Similarly, the hydro-dynamic boundary conditions are explained in section 3.1.1 (except, the inlet is offset from the wall). For the temperature, the boundary conditions are same as given in section 4.1, except constant temperature at bottom of the slab(CD) and shown in Fig. 6.1.

## 6.2 Results and Discussion

In the present work,  $Re = 15000$  is chosen for all computations. Three offset ratios 3, 7 and 11 are considered. At each offset ratio, Prandtl number is varied from 0.01 to 100, solid thickness is varied from 1 to 10 and thermal conductivity ratio is varied from 1 to 1000. In order to study the heat transfer characteristics, results are presented in both graphical and tabulated forms.

### Interface Temperature

Figures 6.2(a), 6.2(b) and 6.2(c) show the effect of offset ratio on the interface

temperature ( $\bar{\theta}_i$ ) for Prandtl numbers 0.01, 1 and 100 respectively, keeping the solid thickness ( $S = 10$ ) and the thermal conductivity ratio ( $K = 1000$ ) constant. It is found that the minimum temperature is found at the reattachment point and it increases with the offset ratio. Interface temperature reduces rapidly up to the reattachment point and increases in the same way in the development region. In the similarity region,  $\bar{\theta}_i$  increases very slowly. It is observed that the average temperature in the recirculation region increases with the offset ratio for all Prandtl numbers. For  $Pr = 0.01$ , in the developed and similarity regions for  $OR = 11$ , average temperature falls below  $OR = 7$ . But, for  $Pr = 1$  and 100, average temperature in all the three regions increases with the offset ratio. Figure 6.3(a) shows the effect of Prandtl number on the interface temperature, keeping the  $S = 10$  and  $K = 1000$  at  $OR = 7$ . It is found that the interface temperature reduces as the Prandtl number increases. Figures 6.3(b) and 6.3(c) show the effect of thermal conductivity ratio ( $K$ ) and slab thickness ( $S$ ). As expected interface temperature reduces with the decrease in thermal conductivity ratio and increase in the slab thickness.

### Local Nusselt Number

Figures 6.4(a), 6.4(b) and 6.4(c) show the effect of the offset ratio on the local Nusselt number ( $Nu_x$ ) distribution for Prandtl numbers 0.01, 1 and 100 respectively, keeping the solid thickness ( $S = 10$ ) and thermal conductivity ratio ( $K = 1000$ ) constant. The reattachment points are 5.95, 12 and 17.29 for  $OR = 3, 7$  and 11 respectively. The local Nusselt number is maximum at the reattachment point and reduces with the offset ratio.  $Nu_x$  increases rapidly up to the reattachment point and decreases in the same way after the impingement region. It then decreases slowly in the similarity region. Figure 6.5(a) shows the effect Prandtl number on  $Nu_x$  at  $S = 10$  and  $K = 1000$  for offset ratio 7. It clearly shows that the local Nusselt number decreases with the decrease in Prandtl number. It is found that,

at the same offset ratio peak Nusselt number occurs always at the reattachment point. Figs. 6.5(b) and 6.5(c) elucidates that there is no effect of thermal conductivity ratio and slab thickness on the local Nusselt number for a conjugate heat transfer situation.

### Local Heat Flux

Figures 6.6(a), 6.6(b) and 6.6(c) show the variation of local heat transfer ( $q_x$ ) across the interface for Prandtl number ( $Pr$ ) 0.01, 1 and 100 respectively at constant solid thickness ( $S=10$ ) and thermal conductivity ratio ( $K=1000$ ) for different offset ratios ( $OR$ ). It is observed that the local heat transfer is maximum ( $q_{max}$ ) at the reattachment point and reduces with the offset ratio. Heat transfer rapidly increases up to the reattachment point and then decreases in the same way in the impingement region. It then decreases gradually in the wall jet region. Figure 6.7(a) shows the variation of  $q_x$  at various  $Pr$  at constant  $S = 10$ ,  $K = 1000$  and  $OR = 7$ .  $q_x$  increases with the decrease in the Prandtl number. Though  $q_x$  decreases with increase in the  $Pr$ , heat transfer is maximum at the reattachment point. Figure 6.7(b) shows the effect of thermal conductivity ratio ( $K$ ) on the heat transfer at constant  $S = 10$ ,  $Pr = 1$  and  $OR = 7$ . As expected, the heat transfer reduces drastically with the decrease in  $K$ . It is found that at low  $K$ , heat transfer is constant and the effect of recirculating region, impingement region are negligible. Figure 6.7(c) shows the effect of solid thickness ( $S$ ) at constant  $Pr = 1$ ,  $K = 1000$  and  $OR = 7$ . It is found that there is a considerable effect of the slab thickness on the heat transfer and the heat transfer reduces as  $S$  increases.

### Average Nusselt Number

Extensive computations are done in their respective ranges and results of the average Nusselt number ( $\overline{Nu}$ ) are presented in Tables 6.1, 6.2 and 6.3 for offset ratios 3, 7 and 11 respectively. It shows clearly that  $\overline{Nu}$  is a function of Prandtl

number only. The effect of solid thickness ( $S$ ) and thermal conductivity ratio ( $K$ ) are negligibly small. It is observed that  $\overline{Nu}$  increases with the increase of  $Pr$ . It is found that, for high Prandtl number fluids, average Nusselt number reduces with the increase in offset ratio. At  $Pr = 0.01$ ,  $\overline{Nu}$  of  $OR = 11$  is higher than that of  $OR = 7$ .

### Average Heat Transfer

The average heat transfer ( $Q_i$ ) integrated over the surface for various  $S$ ,  $K$  and  $Pr$  are shown in Tables 6.4, 6.5 and 6.6 for offset ratio 3, 7 and 11 respectively. The heat transfer for the conjugate case is compared with the non-conjugate case ( $S=0$ ). It is observed that as the solid thickness increases, heat transfer decreases. However, as  $K$  is increasing,  $Q_i$  increases. For  $K=1000$ ,  $Q_i$  approaches almost equal to the non-conjugate case. It is observed that at high Prandtl number, the non-dimensionalized average heat transfer reduces with the offset ratio. At  $Pr = 0.01$ ,  $Q_i$  of  $OR = 11$  is higher than the  $OR = 7$ .

Table 6.1: Average Nusselt number ( $\overline{Nu}$ ) at various Prandtl numbers for  $OR = 3$ 

$S$ (thickness of solid slab)	thermal conductivity ratio $K(k_s/k_f)$	$Nu (Pr = 0.01)$	$Nu (Pr = 0.1)$	$Nu (Pr = 1)$	$Nu (Pr = 10)$	$Nu (Pr = 100)$
0(non-conjugate)	-	1.20773	7.10002	27.4381	63.4983	133.003
1	1	1.26125	7.53327	28.1117	63.8422	133.152
1	100	1.20915	7.14658	27.6411	63.667	133.102
1	1000	1.20787	7.10515	27.4661	63.529	133.028
5	1	1.28284	7.56459	28.1249	63.8451	133.153
5	100	1.21388	7.25205	27.8785	63.7765	133.137
5	1000	1.20839	7.12142	27.5423	63.5978	133.071
10	1	1.28659	7.5685	28.1264	63.8455	133.153
10	100	1.21837	7.31407	27.9545	63.8006	133.143
10	1000	1.20893	7.13671	27.6013	63.6398	133.091

Table 6.2: Average Nusselt number ( $\overline{Nu}$ ) at various Prandtl numbers for  $OR = 7$ 

$S$ (thickness of solid slab)	thermal conductivity ratio $K(k_s/k_f)$	$Nu (Pr = 0.01)$	$Nu (Pr = 0.1)$	$Nu (Pr = 1)$	$Nu (Pr = 10)$	$Nu (Pr = 100)$
0(non-conjugate)	-	1.03974	6.32644	24.5308	56.619	118.506
1	1	1.07596	6.65482	25.0298	56.869	118.614
1	100	1.04063	6.35873	24.6713	56.7367	118.577
1	1000	1.03983	6.32996	24.5495	56.6392	118.523
5	1	1.09243	6.68167	25.0405	56.8713	118.615
5	100	1.04364	6.4383	24.8561	56.8232	118.604
5	1000	1.04015	6.34185	24.6048	56.6895	118.555
10	1	1.09546	6.68516	25.0418	56.8716	118.615
10	100	1.04651	6.48665	24.9184	56.8432	118.609
10	1000	1.04049	6.35284	24.6472	56.7205	118.57

Table 6.3: Average Nusselt number ( $\overline{Nu}$ ) at various Prandtl numbers for  $OR = 11$ 

$S$ (thickness of solid slab)	thermal conductivity ratio $K(k_s/k_f)$	$Nu (Pr = 0.01)$	$Nu (Pr = 0.1)$	$Nu (Pr = 1)$	$Nu (Pr = 10)$	$Nu (Pr = 100)$
0(non-conjugate)	-	1.11616	6.32302	23.8996	54.6758	114.202
1	1	1.15479	6.68075	24.4173	54.928	114.31
1	100	1.11719	6.35867	24.0395	54.7891	114.27
1	1000	1.11627	6.32691	23.918	54.6947	114.217
5	1	1.17064	6.70955	24.429	54.9306	114.311
5	100	1.12077	6.44792	24.2327	54.8783	114.299
5	1000	1.11666	6.34041	23.9746	54.7441	114.249
10	1	1.17341	6.71329	24.4305	54.9309	114.311
10	100	1.12405	6.5016	24.2992	54.8995	114.304
10	1000	1.11705	6.35269	24.0184	54.7754	114.264

Table 6.4: Heat Transfer across the interface ( $Q_i$ ) at various Prandtl numbers for  $OR = 3$ 

$S$ (thickness of solid slab)	thermal conductivity ratio $K(k_s/k_f)$	$Q_i (Pr = 0.01)$	$Q_i (Pr = 0.1)$	$Q_i (Pr = 1)$	$Q_i (Pr = 10)$	$Q_i (Pr = 100)$
0(non-conjugate)	-	0.603864	0.355001	0.13719	0.03174	0.00665
1	1	0.275973	0.043828	0.00481	0.00049	4.96E-05
1	100	0.596952	0.331407	0.10669	0.0191	0.002806
1	1000	0.603166	0.352491	0.13332	0.0297	0.005820
5	1	0.086138	0.009726	0.00099	9.97E-05	9.98E-06
5	100	0.570637	0.261842	0.05723	0.00752	0.000863
5	1000	0.600376	0.342777	0.12001	0.02381	0.003931
10	1	0.046282	0.004930	0.00049	4.99E-05	5.00E-06
10	100	0.540632	0.207507	0.03635	0.00429	0.000463
10	1000	0.59691	0.331391	0.10687	0.01915	0.002812

Table 6.5: Heat Transfer across the interface ( $Q_i$ ) at various Prandtl numbers for  $OR = 7$ 

$S$ (thickness of solid slab)	thermal conductivity ratio $K(k_s/k_f)$	$Q_i (Pr = 0.01)$	$Q_i (Pr = 0.1)$	$Q_i (Pr = 1)$	$Q_i (Pr = 10)$	$Q_i (Pr = 100)$
0(non-conjugate)	-	0.51987	0.316322	0.12265	0.02831	0.005925
1	1	0.256775	0.043144	0.00479	0.00049	4.96E-05
1	100	0.514697	0.297312	0.09762	0.0177	0.002664
1	1000	0.519348	0.31431	0.11954	0.0266	0.005257
5	1	0.084177	0.009691	0.00099	9.96E-05	9.98E-06
5	100	0.494899	0.239924	0.05444	0.00730	0.000848
5	1000	0.517264	0.306531	0.10870	0.02181	0.003663
10	1	0.045711	0.004922	0.00049	4.99E-05	5.00E-06
10	100	0.472091	0.19345	0.03520	0.00421	0.000459
10	1000	0.514676	0.297375	0.09781	0.01784	0.002672

Table 6.6: Heat Transfer across the interface ( $Q_i$ ) at various Prandtl numbers for  $OR = 11$ 

$S$ (thickness of solid slab)	thermal conductivity ratio $K(k_s/k_f)$	$Q_i$ ( $Pr = 0.01$ )	$Q_i$ ( $Pr = 0.1$ )	$Q_i$ ( $Pr = 1$ )	$Q_i$ ( $Pr = 10$ )	$Q_i$ ( $Pr = 100$ )
0(non-conjugate)	-	0.55808	0.316151	0.11949	0.02733	0.005710
1	1	0.266138	0.043158	0.00479	0.00049	4.95E-05
1	100	0.552174	0.297238	0.09561	0.01739	0.002619
1	1000	0.557486	0.314151	0.11655	0.02582	0.005089
5	1	0.085170	0.009692	0.00099	9.96E-05	9.98E-06
5	100	0.529653	0.239985	0.05378	0.00723	0.000843
5	1000	0.555109	0.306407	0.10621	0.02123	0.003578
10	1	0.046002	0.004922	0.00049	4.99E-05	5.00E-06
10	100	0.503774	0.193531	0.03491	0.00419	0.000457
10	1000	0.552154	0.297281	0.09576	0.01744	0.002625

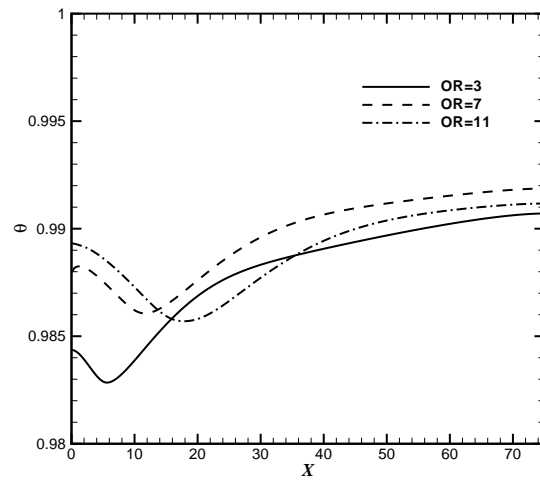
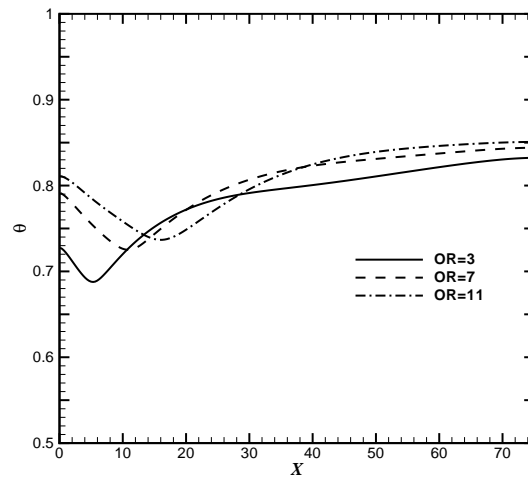
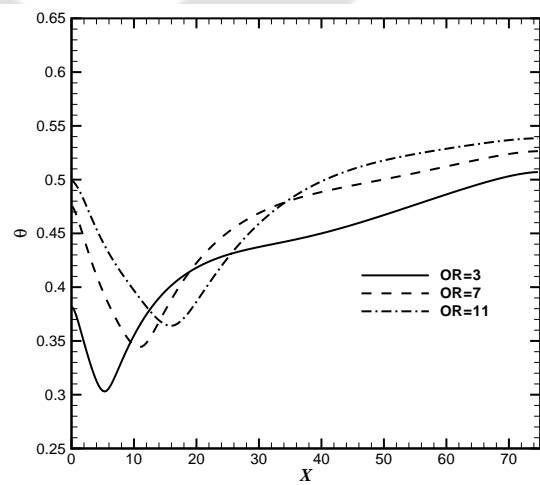
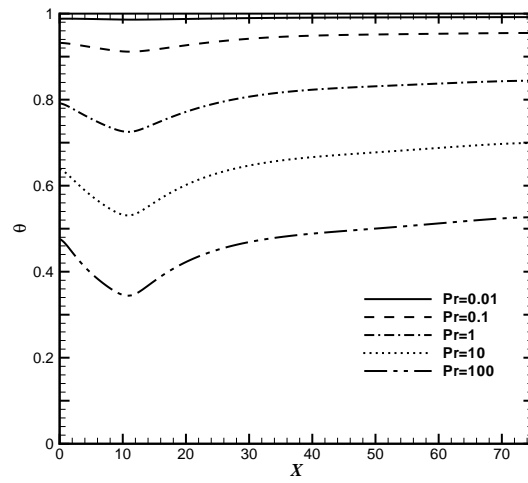
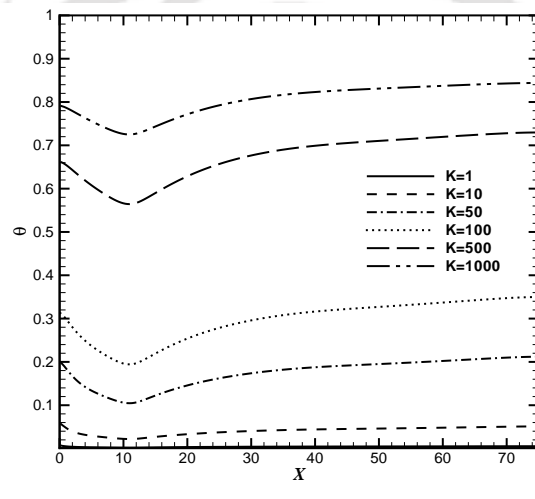
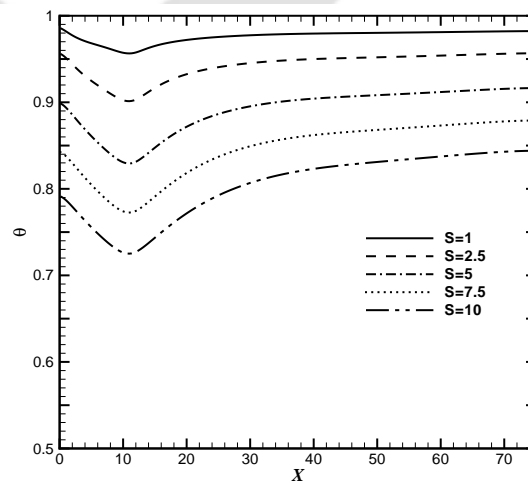
(a)  $Pr = 0.01$ ,  $S = 10$  and  $K = 1000$ .(b)  $Pr = 1$ ,  $S = 10$  and  $K = 1000$ .(c)  $Pr = 100$ ,  $S = 10$  and  $K = 1000$ .

Figure 6.2: Interface temperature distribution at the solid-fluid interface at different offset ratios.

(a)  $S=10$  and  $K = 1000$ .(b)  $Pr = 1$  and  $S = 10$ .(c)  $Pr = 1$  and  $K = 1000$ .Figure 6.3: Interface temperature distribution at the solid-fluid interface at  $OR = 7$ .

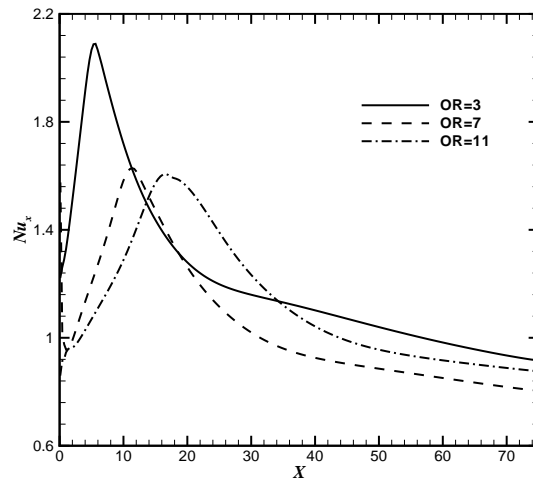
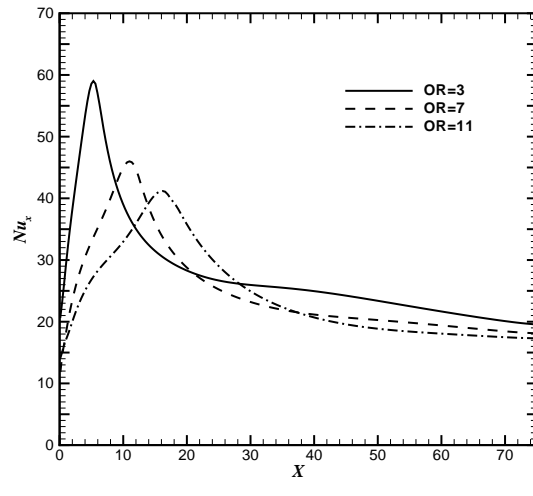
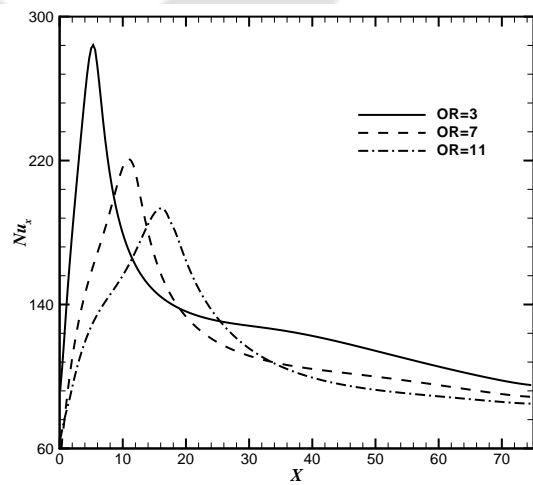
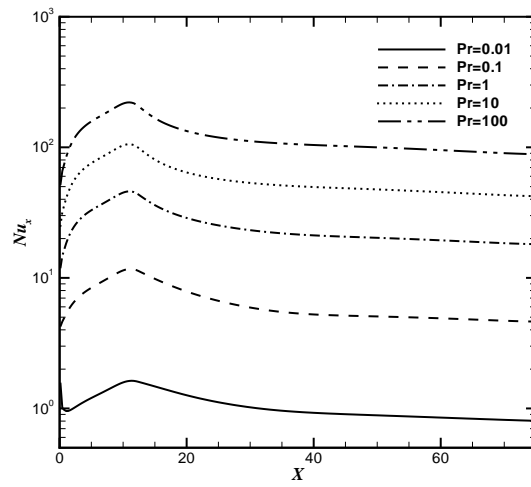
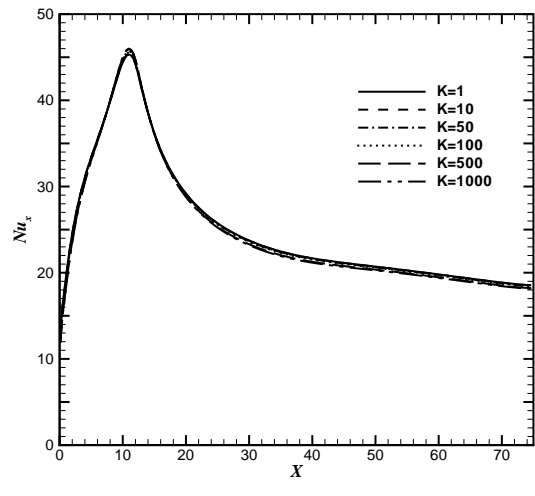
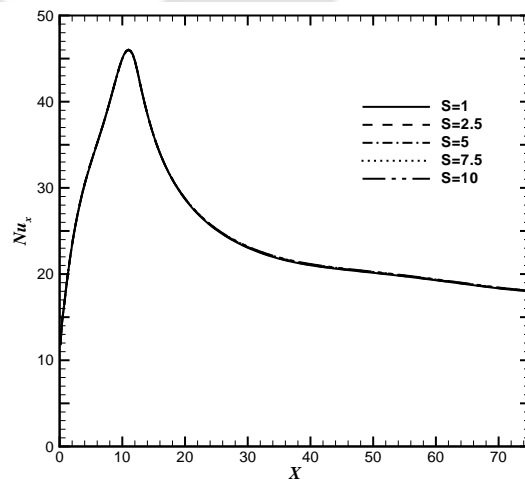
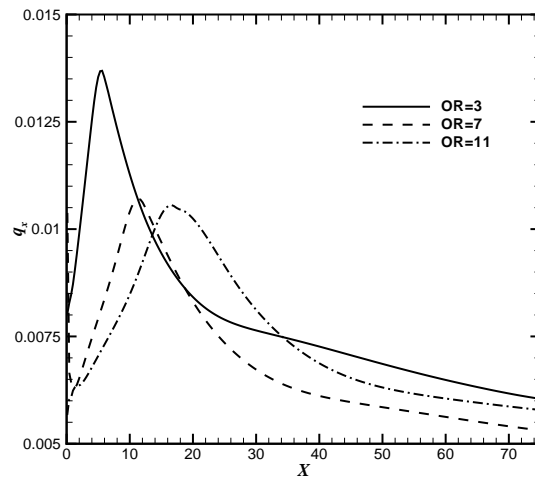
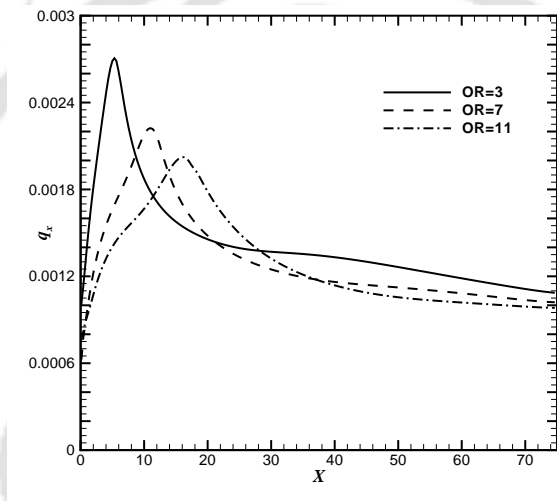
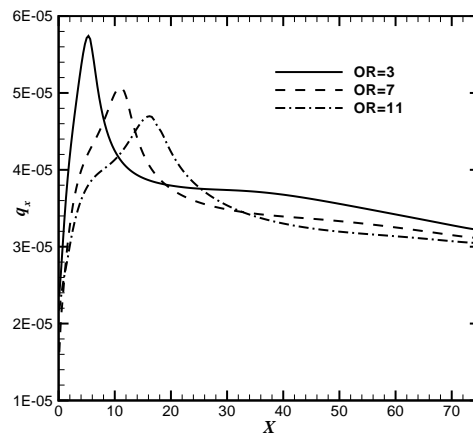
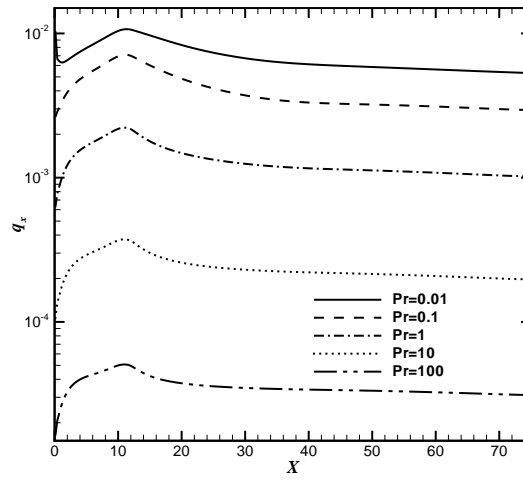
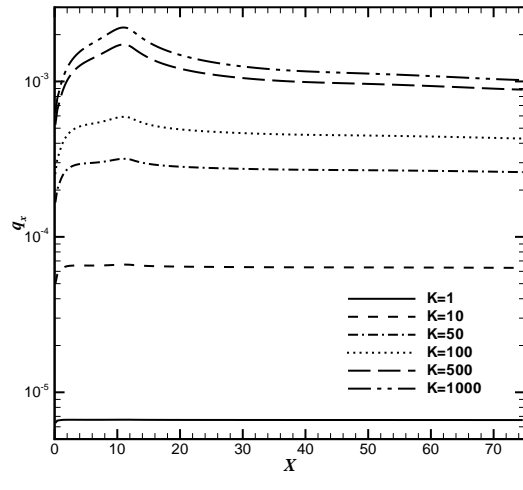
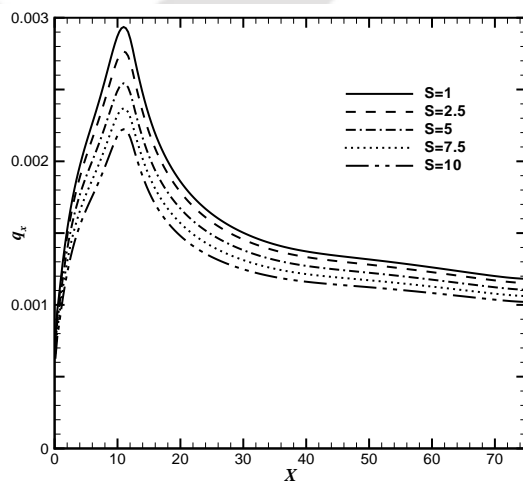
(a)  $Pr = 0.01$ ,  $S = 10$  and  $K = 1000$ (b)  $Pr = 1$ ,  $S = 10$  and  $K = 1000$ .(c)  $Pr = 100$ ,  $S = 10$  and  $K = 1000$ .

Figure 6.4: Local Nusselt number distribution at different offset ratios.

(a)  $S=10$  and  $K = 1000$ .(b)  $Pr = 1$  and  $S = 10$ .(c)  $Pr = 1$  and  $K = 1000$ .Figure 6.5: Local Nusselt number distribution and at  $OR = 7$ .

(a)  $Pr = 0.01$ ,  $S=10$  and  $K = 1000$ .(b)  $Pr = 1$ ,  $S=10$  and  $K = 1000$ .(c)  $Pr = 100$ ,  $S=10$  and  $K = 1000$ .Figure 6.6: Interface heat transfer ( $q_x$ ) distribution for different offset ratios.

(a)  $S=10$  and  $K=1000$ .(b)  $Pr=1$  and  $S=10$ .(c)  $Pr=1$  and  $K=1000$ .Figure 6.7: Interface heat transfer ( $q_x$ ) distribution and at  $OR=7$ .

## 6.3 Concluding Remarks

In the present case, the conjugate heat transfer study involving a turbulent plane offset jet is considered. The bottom of the solid block is maintained at a constant isothermal temperature. The parameters considered are the offset ratio, the conductivity ratio, the solid slab thickness and the Prandtl number. The Reynolds number considered is 15000 because the flow becomes fully turbulent and then it becomes independent of the Reynolds number. It is observed that the minimum interface temperature is found at the reattachment point. The interface temperature reduces rapidly up to the reattachment point and thereafter it increases. With the increase in  $OR$ , the interface temperature increases. The interface temperature decreases with increase in  $Pr$ . It increases with  $K$  and decreases with  $S$ . The local  $Nu_x$  decreases with the increase in  $OR$ . It increases with the increase in  $Pr$ . However,  $Nu_x$  remains nearly unaffected by the variation of  $K$  and  $S$ . The non-dimensional local heat flux ( $q_x$ ) decreases with the increase in  $OR$ . It decreases with the increase in  $Pr$ . It increases with the increase in  $K$  and decrease with the increase in  $S$ . The average Nusselt number data as tabulated shows clearly that  $Nu$  is a function of Prandtl number and  $OR$  only. As  $K$  is increasing, the average heat transfer increases. For  $K=1000$ , the average heat transfer approaches almost equal to the non-conjugate case.

# Chapter 7

## Study of Conjugate Heat Transfer from a Flat Plate by Turbulent Offset Jet Flow

### 7.1 Introduction

The cooling of a hot body is frequently conducted by injecting a jet of cold fluid. In some cases, this cold fluid is issued in a parallel direction a little distance away from the the wall. This situation is called an offset jet. In the present case, the conjugate heat transfer involving a turbulent plane offset jet is considered. The bottom of the solid slab is heated by a constant heat flux. The parameters considered are the offset ratio, the conductivity ratio (solid/fluid), the solid slab thickness and the Prandtl number. The Reynolds number considered is 15000 for all the cases in the study. The numerical scheme and method of solution as explained in section 2.6 is used in the present computations. Similarly, the hydro-dynamic boundary conditions are explained in section 3.1.1 (except, the inlet is offset from the wall). For the temperature, the boundary conditions are same as given in section 4.1, except constant heat flux at bottom of the slab(CD) as shown in Fig. 6.1.

## 7.2 Results and Discussion

In the present work,  $Re = 15000$  is chosen for all computations. Three offset ratios 3, 7 and 11 are considered. At each offset ratio, Prandtl number is varied from 0.01 to 100, solid thickness is varied from 1 to 10 and thermal conductivity ratio is varied from 1 to 1000. In order to study the heat transfer characteristics, results are presented in both the graphical and tabulated forms and the effect of each parameter has been discussed.

### Temperature at the Bottom of the Solid Block

Figures 7.1(a), 7.1(b) and 7.1(c) show the effect of offset ratio on the bottom wall temperature ( $\theta_b$ ) for Prandtl numbers 0.01, 1 and 100 respectively, keeping the solid thickness ( $S = 10$ ) and thermal conductivity ratio ( $K = 1000$ ) constant. It is observed that, for low  $Pr$ , the effect of recirculating region is negligible. As  $Pr$  is increased, the effect of recirculating and impingement regions are found on the bottom wall temperature also (for  $Pr=1$  and 100). The bottom wall temperature increases in the downstream direction because the heat flux is constant and the heat transfer coefficient decreases in the downstream direction. For  $Pr=0.01$ ,  $\theta_b$  of  $OR=11$  is in between 3 and 7. Figure 7.2(a) shows that as the Prandtl number is increased,  $\theta_b$  also increases. This nature is obtained because of the non-dimensionalised heat flux boundary condition given by Eq. C.2 (Appendix). Figures 7.2(b) and 7.2(c) show the effect of thermal conductivity ratio and solid thickness respectively. It is observed that  $\theta_b$  increases, as  $K$  decreases and  $S$  increases. In both the cases, the resistance to heat transfer increases which results in higher bottom wall temperature.

### Interface Temperature

Figures 7.3(a), 7.3(b) and 7.3(c) show the effect of offset ratio on the interface

temperature ( $\theta_i$ ) for Prandtl numbers 0.01, 1 and 100 respectively, keeping the solid thickness ( $S = 10$ ) and thermal conductivity ratio ( $K = 1000$ ) constant. For  $Pr=0.01$ , the interface temperatures in the recirculation and in the impingement regions are almost constant and increases slowly in the similarity region. The interface temperature for the case  $OR = 11$  is in between the cases of  $OR = 3$  and 7. For  $Pr=1$  and 100, the interface temperature reduces rapidly up to the reattachment point and increases in the development region. The Nusselt number is maximum at the reattachment point and thus the interface temperature is minimum at that point. In the similarity region,  $\theta_i$  increases very slowly. The average temperature in each region increases with the offset ratio. Figure 7.4(a) shows the effect of Prandtl number on the interface temperature. It is found that  $\theta_i$  increases with  $Pr$  (for the same reason as given for bottom wall temperature). For  $Pr = 0.01$ , effect of recirculation region is negligible (the temperature remaining constant) and considerable effect is observed as  $Pr$  increases. Figures 7.4(b) and 7.4(c) show the effect of the thermal conductivity ratio ( $K$ ) and the thickness of the solid block respectively. It is found that as  $K$  increases, variation of interface temperature reduces along the wall. As expected, as the solid thickness decreases,  $\theta_i$  increases.

### Local Nusselt Number

Figures 7.5(a), 7.5(b) and 7.5(c) show the effect of offset ratio on the local Nusselt number ( $Nu_x$ ) for Prandtl numbers 0.01, 1 and 100 respectively, keeping the solid thickness ( $S = 10$ ) and thermal conductivity ratio ( $K = 1000$ ) constant. It is observed that the local Nusselt number is maximum at the reattachment points which reduces with the increase in offset ratio.  $Nu_x$  increases and decreases rapidly in the recirculation and impingement regions respectively whereas it decreases slowly in the wall jet (similarity) region. Figure 7.6(a) shows the effect Prandtl number on  $Nu_x$  at constant  $S = 10$  and  $K = 1000$  for offset ratio 7.

It shows that the local Nusselt number increases with the Prandtl number. It is also found that, at the same offset ratio, peak Nusselt number occurs always at the reattachment point. Figures 7.6(b) and 7.6(c) elucidates that there is no effect of thermal conductivity ratio and slab thickness on the local Nusselt number.

### Local Heat Flux

Figures 7.7(a), 7.7(b) and 7.7(c) show the variation of local heat transfer ( $q_x$ ) across the interface for Prandtl number 0.01, 1 and 100 respectively at a constant solid thickness ( $S=10$ ) and thermal conductivity ratio ( $K=1000$ ) for different offset ratios. It is observed that local heat transfer is maximum at the reattachment point and the maximum local heat flux reduces with the offset ratio. The local heat transfer rapidly increases up to reattachment point and then decreases in the same way in the impingement region. It then decreases monotonically in the wall jet region. However the total heat transfer remains the same to satisfy the applied boundary condition. Figure 7.8(a) shows the variation of  $q_x$  at various  $Pr$  at constant  $S = 10$ ,  $K = 1000$  and  $OR = 7$ .  $q_x$  increases with the decrease in the Prandtl number because of the type of non-dimensionalisation used in the present study. Though the  $q_x$  decreases with increase in  $Pr$ , the heat transfer is maximum at the reattachment point. Figure 7.8(b) shows effect of the thermal conductivity ratio ( $K$ ) on the heat transfer at constant  $S = 10$ ,  $Pr = 1$  and  $OR = 7$ . As expected the heat transfer increases near the impingement region with the increase in  $K$ . It is found that at low  $K$ , heat transfer is constant and the effects of recirculating region, impingement region are negligible. Figure 7.8(c) shows the effect of solid thickness ( $S$ ) at constant  $Pr = 1$ ,  $K = 1000$  and  $OR = 7$ . It is found that there is considerable effect of slab thickness on the heat transfer and the maximum heat flux increases as  $S$  increases.

### Average Nusselt Number

Extensive computations are done in their respective ranges and results of the average Nusselt number ( $\overline{Nu}$ ) are presented in Tables 7.1, 7.2 and 7.3 for offset ratios 3, 7 and 11 respectively. It shows clearly that  $\overline{Nu}$  is a function of Prandtl number only. The effect of solid thickness ( $S$ ) and the thermal conductivity ratio ( $K$ ) are small. From the data, it is found that  $\overline{Nu}$  decreases with  $K$  and  $S$  which is of the order of 4-6%. It is observed that  $\overline{Nu}$  increases with the increase of  $Pr$ . It is found that, for high Prandtl number fluids, average Nusselt number reduces with the increase in offset ratio. At  $Pr = 0.01$ ,  $\overline{Nu}$  of  $OR = 11$  is higher than the  $OR = 7$ .



Table 7.1: Average Nusselt number ( $\overline{Nu}$ ) at various Prandtl numbers for  $OR = 3$ 

$S$	$K(k_s/k_f)$	$\overline{Nu} (Pr = 0.01)$	$\overline{Nu} (Pr = 0.1)$	$\overline{Nu} (Pr = 1)$	$\overline{Nu} (Pr = 10)$	$\overline{Nu} (Pr = 100)$
0(non-conjugate)	-	1.29223	7.57428	28.1286	63.8459	133.153
1	1	1.29169	7.5737	28.1284	63.8459	133.153
1	100	1.27742	7.53429	28.1047	63.8404	133.152
1	1000	1.245	7.44469	28.0236	63.8102	133.143
5	1	1.29075	7.57249	28.128	63.8458	133.153
5	100	1.25661	7.48692	28.0716	63.8309	133.15
5	1000	1.21957	7.30432	27.9086	63.7732	133.132
10	1	1.2903	7.57204	28.1278	63.8458	133.153
10	100	1.24479	7.45744	28.0567	63.8274	133.149
10	1000	1.21441	7.2421	27.8345	63.7493	133.126

Table 7.2: Average Nusselt number ( $\overline{Nu}$ ) at various Prandtl numbers for  $OR = 7$ 

$S$	$K(k_s/k_f)$	$\overline{Nu} (Pr = 0.01)$	$\overline{Nu} (Pr = 0.1)$	$\overline{Nu} (Pr = 1)$	$\overline{Nu} (Pr = 10)$	$\overline{Nu} (Pr = 100)$
0(non-conjugate)	-	1.09997	6.68923	25.0427	56.8717	118.615
1	1	1.09948	6.68927	25.0432	56.8719	118.615
1	100	1.08933	6.67198	25.0412	56.8736	118.616
1	1000	1.06498	6.68927	24.9879	56.8596	118.613
5	1	1.09887	6.68873	25.0431	56.8719	118.615
5	100	1.07347	6.63151	25.0183	56.8689	118.615
5	1000	1.04738	6.48315	24.8882	56.8264	118.604
10	1	1.09852	6.68834	25.043	56.8719	118.615
10	100	1.06478	6.60673	25.005	56.8657	118.614
10	1000	1.04401	6.43393	24.8287	56.8068	118.599

Table 7.3: Average Nusselt number ( $\overline{Nu}$ ) at various Prandtl numbers for  $OR = 11$ 

$S$	$K(k_s/k_f)$	$\overline{Nu} (Pr = 0.01)$	$\overline{Nu} (Pr = 0.1)$	$\overline{Nu} (Pr = 1)$	$\overline{Nu} (Pr = 10)$	$\overline{Nu} (Pr = 100)$
0(non-conjugate)	-	1.17704	6.71755	24.4319	54.9311	114.311
1	1	1.17699	6.71766	24.4321	54.9312	114.311
1	100	1.16794	6.70346	24.4289	54.9316	114.311
1	1000	1.14272	6.62028	24.3776	54.919	114.309
5	1	1.17648	6.71712	24.4319	54.9312	114.311
5	100	1.1515	6.65833	24.4061	54.9268	114.31
5	1000	1.12436	6.48996	24.263	54.8825	114.299
10	1	1.17613	6.71669	24.4318	54.9311	114.311
10	100	1.14272	6.62928	24.3905	54.9232	114.31
10	1000	1.12079	6.43733	24.199	54.8608	114.293

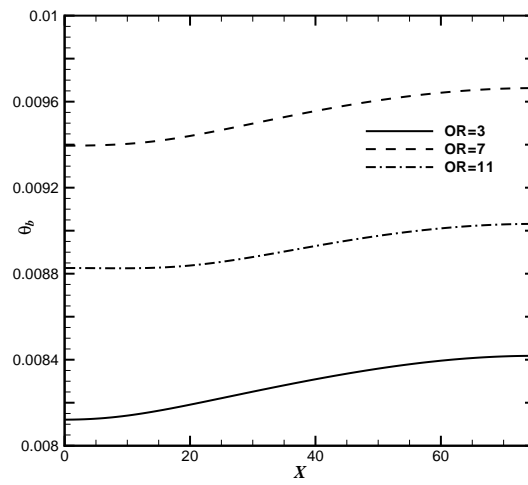
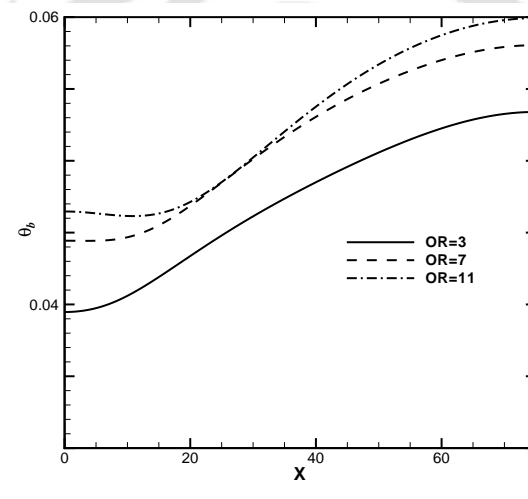
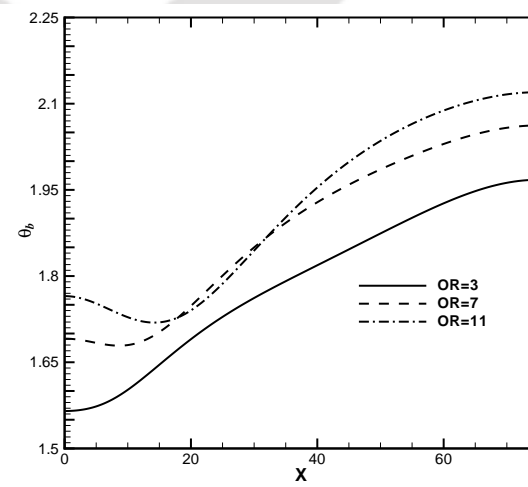
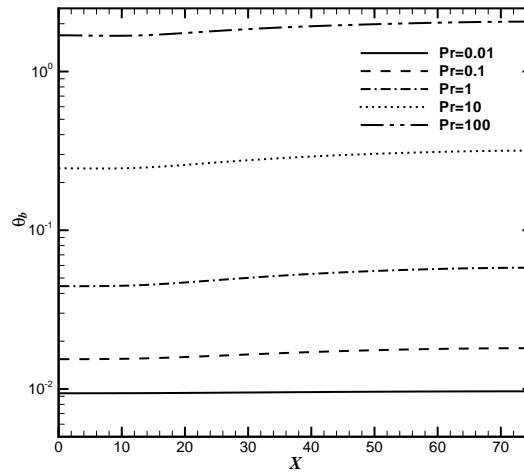
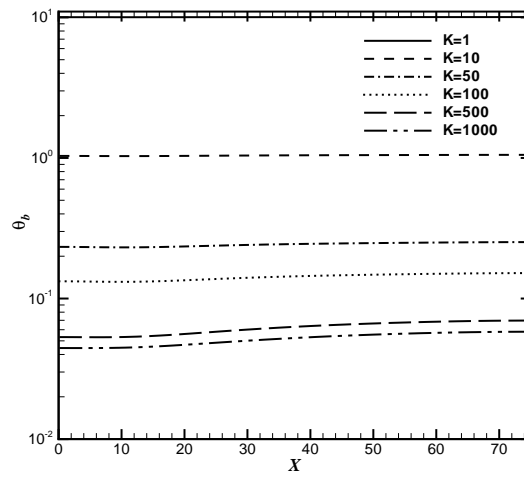
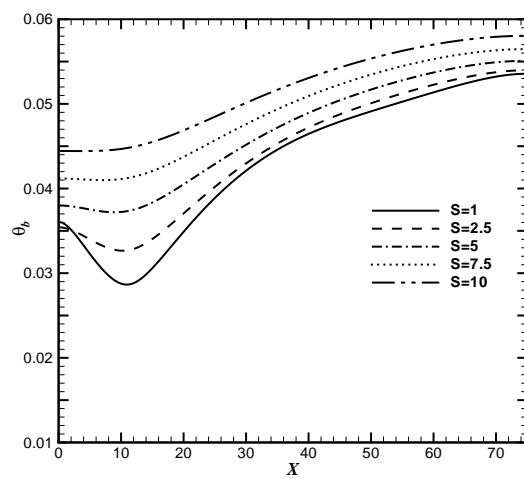
(a)  $Pr = 0.01$ .(b)  $Pr = 1$ .(c)  $Pr = 100$ .

Figure 7.1: Bottom wall temperature distribution at different offset ratios for  $S=10$  and  $K = 1000$ .

(a)  $S=10$  and  $K = 1000$ .(b)  $Pr = 1$  and  $S = 10$ .(c)  $Pr = 1$  and  $K = 1000$ .Figure 7.2: Bottom wall temperature distribution at  $OR=7$ .

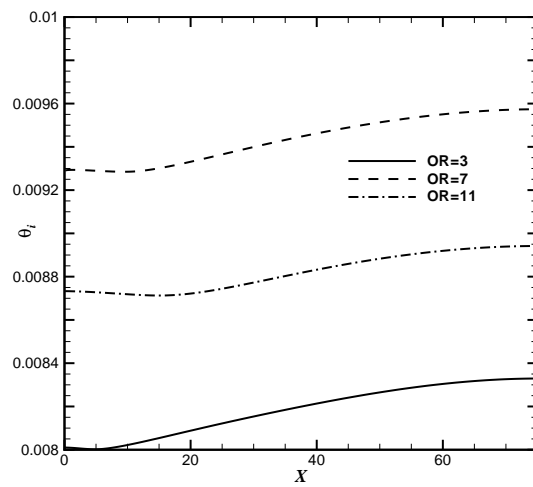
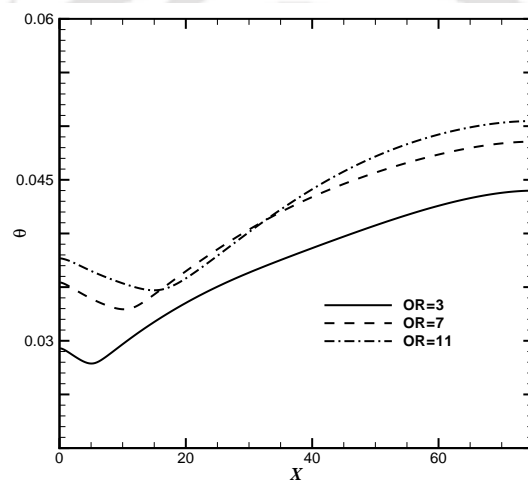
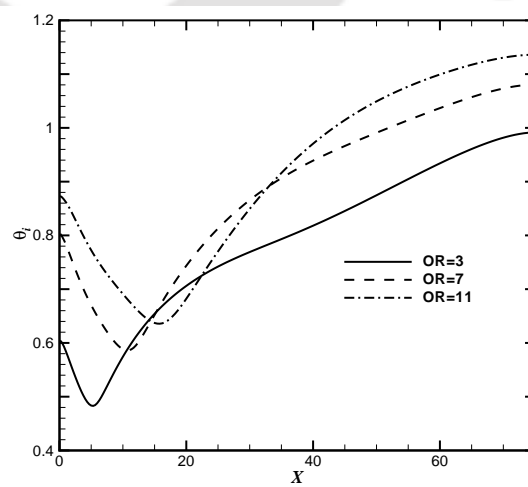
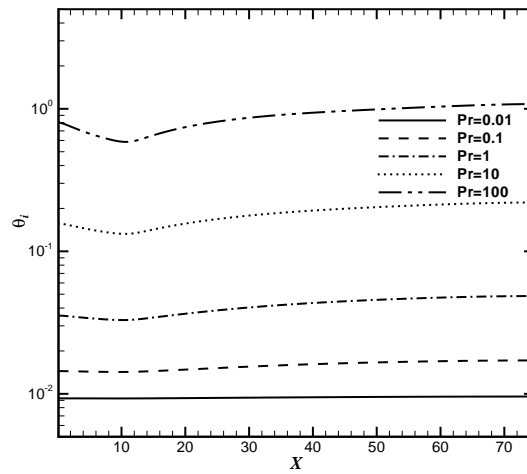
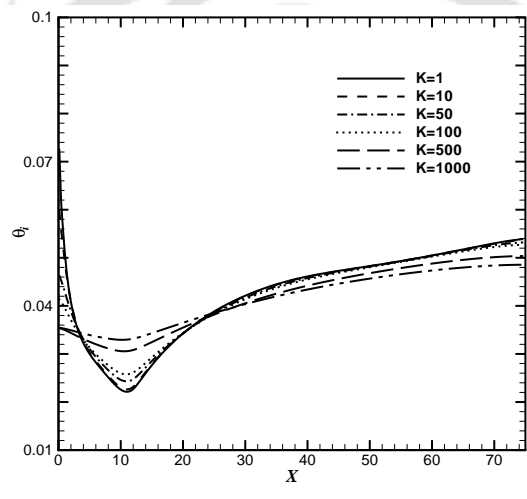
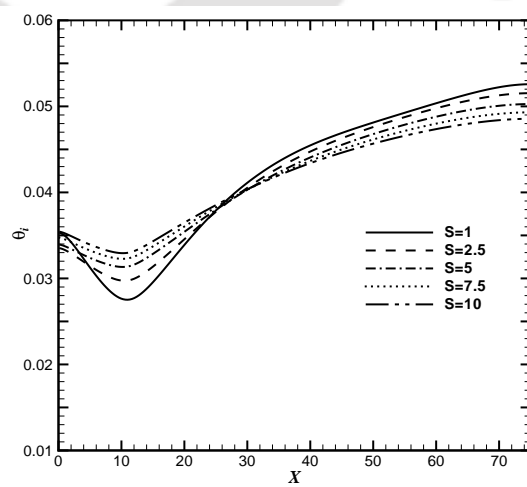
(a)  $Pr = 0.01$ .(b)  $Pr = 1$ .(c)  $Pr = 100$ .

Figure 7.3: Interface temperature distribution at the solid-fluid interface at different offset ratios for  $S=10$  and  $K = 1000$ .

(a)  $S=10$  and  $K = 1000$ .(b)  $Pr = 1$  and  $S = 10$ .(c)  $Pr = 1$  and  $K = 1000$ .Figure 7.4: Interface temperature distribution at the solid-fluid interface at  $OR=7$ .

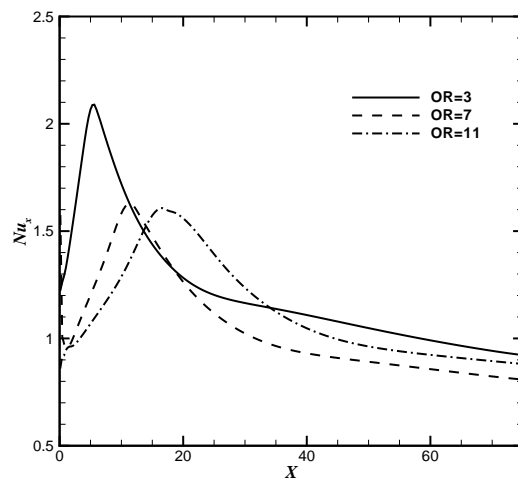
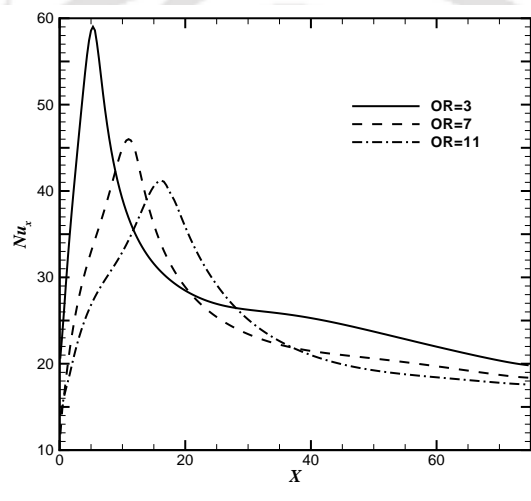
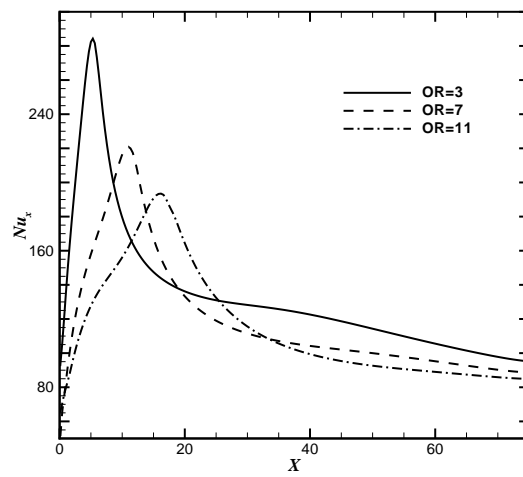
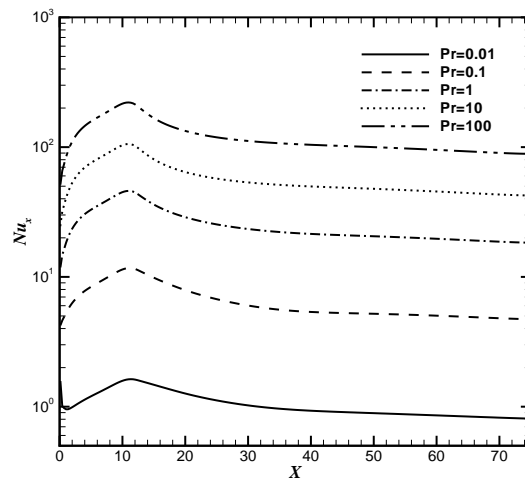
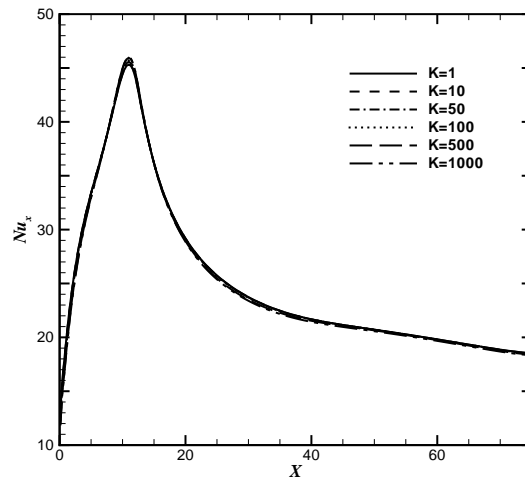
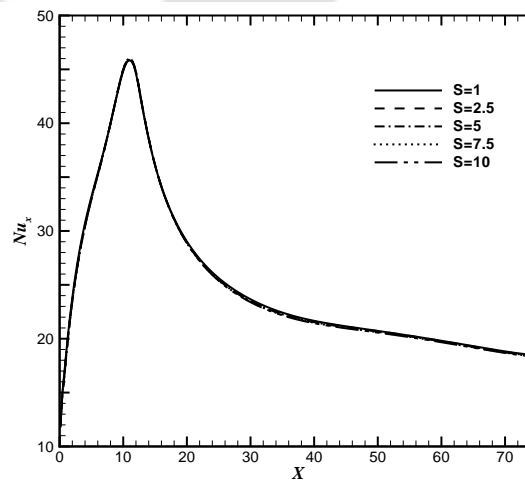
(a)  $Pr = 0.01$ .(b)  $Pr = 1$ .(c)  $Pr = 100$ .

Figure 7.5: Nusselt number distribution at different offset ratios  $S=10$  and  $K = 1000$ .

(a)  $S=10$  and  $K = 1000$ .(b)  $Pr = 1$  and  $S = 10$ .(c)  $Pr = 1$  and  $K = 1000$ .Figure 7.6: Nusselt number distribution at  $OR=7$ .

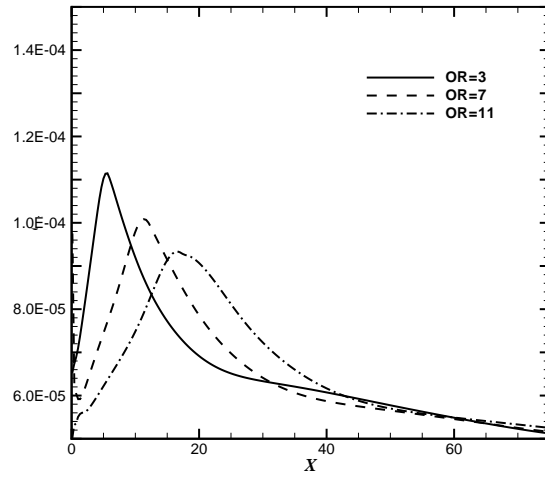
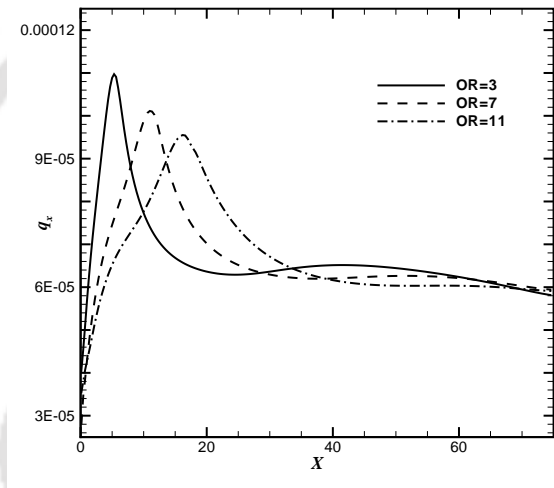
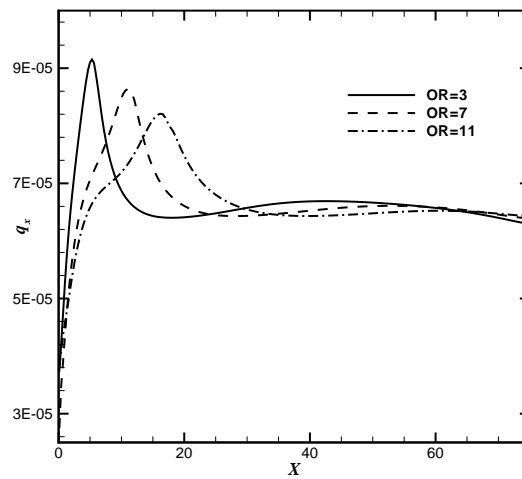
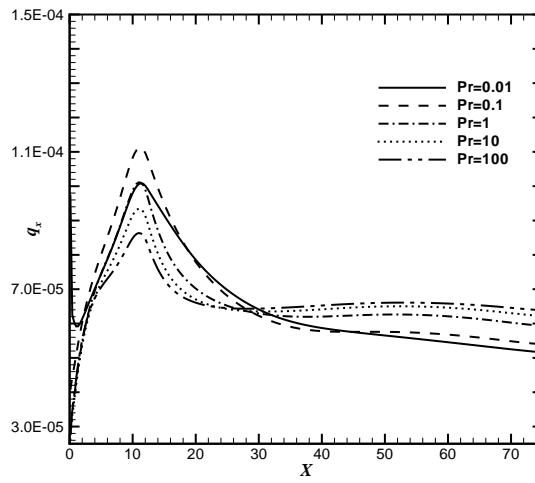
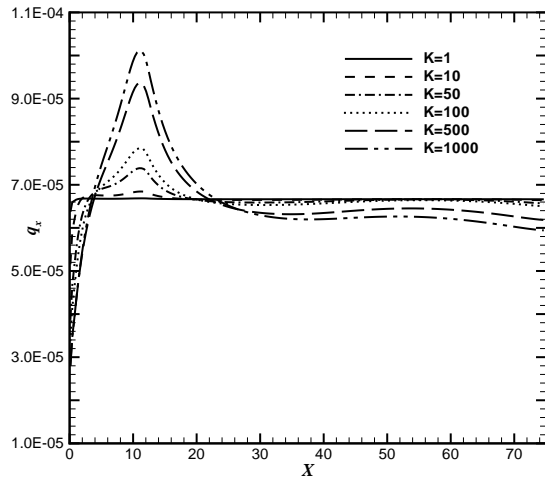
(a)  $Pr = 0.01$ .(b)  $Pr = 1$ .(c)  $Pr = 100$ .

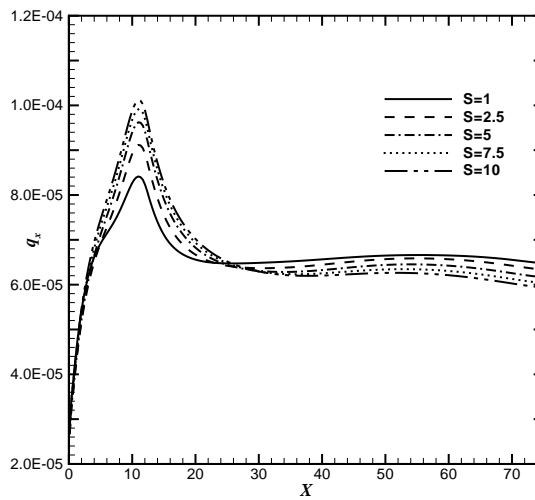
Figure 7.7: Interface heat transfer distribution at the solid-fluid interface for different offset ratios  $S=10$  and  $K = 1000$ .



(a)  $S=10$  and  $K=1000$  at various Prandtl numbers and at  $OR=7h$ .



(b)  $Pr=1$  and  $S=10$  at  $OR=7h$ .



(c)  $Pr=1$  and  $K=1000$  at  $OR=7$ .

Figure 7.8: Interface heat transfer distribution at the solid-fluid interface at  $OR=7$ .

## 7.3 Concluding Remarks

In the present case, the conjugate heat transfer study of a solid block by a turbulent plane offset jet is considered. The bottom of the solid block is maintained at a constant heat flux boundary condition. The parameters considered are the offset ratio, the conductivity ratio, the solid slab thickness and the Prandtl number. The Reynolds number considered is 15000 because the flow becomes fully turbulent and becomes independent of the Reynolds number. It is observed that the bottom wall temperature increases in the downstream direction. For  $Pr=0.01$ ,  $\theta_b$  increases as  $OR$  increases from 3 to 7 and then decreases for  $OR=11$ . However, for  $Pr=1$  and 100,  $\theta_b$  increases as  $OR$  increases. With the increase in  $Pr$  and  $S$ ,  $\theta_b$  increases. It decreases as  $K$  is increased. The minimum interface temperature is found at the reattachment point. The interface temperature reduces rapidly up to the reattachment point and thereafter it increases. For  $Pr=1$  and 100, with the increase in  $OR$ , the interface temperature increases. However, for  $Pr=0.01$ , it increases as  $OR$  is increased up to 7 and then decreases for  $OR=11$ . The interface temperature increases with the increase in  $Pr$ . The local  $Nu_x$  decreases with the increase in  $OR$ . It increases with the increase in  $Pr$ . However,  $Nu_x$  remains nearly unaffected by the variation of  $K$  and  $S$ . The non-dimensional local maximum heat flux ( $q_x$ ) decreases with the increase in  $OR$ . It decreases with the increase in  $Pr$ . The average Nusselt number data as tabulated shows clearly that  $Nu$  is a function of Prandtl number and  $OR$  only. As  $K$  is increasing, the average Nusselt number decreases.

# Chapter 8

## Numerical Simulation of the Turbulent Flow Interaction Between a Plane Wall Jet and a Parallel Offset Jet

### 8.1 Introduction

In the present study, a detailed numerical simulation of the dual-jet consisting of a plane wall jet and an offset jet has been conducted for a range of wall jet and offset jet velocities. The spacing between the wall jet and the offset jet has been kept constant at 1. The turbulence modeling has been conducted by the standard high  $Re$   $k - \epsilon$  model. The modified streamline-curvature method as reported in Cheng and Farokhi [52] has been applied. The Reynolds number considered is 20000. The characterization of the dual jet has been done by plotting the similarity profile, the variation of the jet half-width, the maximum velocity decay, wall shear stress and wall pressure distribution for the range of velocities considered. The numerical scheme and method of solution as explained in chapter 2.6 is used in the present

computations.

### 8.1.1 Boundary Conditions

The flow of a combined wall jet and offset jet emanating into the quiescent fluid is considered (Fig. 1.2). Since the governing equations are non-dimensionalized, the boundary conditions are also non-dimensionalized and given as the input to the solution. The Reynolds number equal to 20000 is considered for all the computations. The inlets of combined jet,  $U_w$  and  $U_o$  represents the non-dimensional wall jet and offset jet velocities respectively. In the present study, keeping  $U_w=1.0$ ,  $U_o$  is varied for 0.25, 0.5, 0.75 and 1.0. Similarly, keeping  $U_o=1.0$ ,  $U_w$  is varied for 0.25, 0.5, 0.75 and 1.0, which totally represents seven possible combinations. For the turbulent kinetic energy equation, the boundary condition at inlets is  $k_n = 1.5I^2$  where  $I$  is the turbulence intensity and is equal to 0.02. For the dissipation equation, the boundary condition is  $\epsilon_n = (k_n^{3/2} C_\mu^{3/4})/l$ , where  $l = 0.07h$  is considered. For the solid wall, no slip boundary condition is considered for velocity. Neumann boundary conditions are provided for the top boundary (i.e. entrainment side) and at the exit boundary, a developed condition of  $\partial\phi/\partial n = 0$  is considered where  $\phi = \bar{U}, \bar{V}, k_n, \epsilon_n$ . It has been ensured that the first grid point near the wall falls in the logarithmic region i.e.  $30 < Y^+ < 100$  where  $Y^+ = yu_\tau/\nu$ ,  $u_\tau$  being the friction velocity.

### 8.1.2 Code Validation and Grid Independence Study

To validate the code developed, the steady state computations are performed for  $U_w = U_o = 1.0$  and  $Re=10000$  is considered. A domain independence study has been done by considering  $X=75$  and 100 (Fig.8.2). It is observed that the domain size of  $X=75$  is sufficient. However,  $X=100$  has been used. Similarly it has been done in the  $Y$ -direction (not shown here) and the size is 50. The grid independence

study has been done by taking the grid number of  $201 \times 101$ ,  $201 \times 121$ ,  $221 \times 101$  and  $221 \times 121$ . Figure 8.2 shows the  $\bar{U}$  velocity profile at  $X=30$  and they overlap with each other. However, even large grid number of  $201 \times 141$  is used. Fig. 8.1 shows the sample grid used for the present computations. Figs. 8.3(a), 8.3(b) and

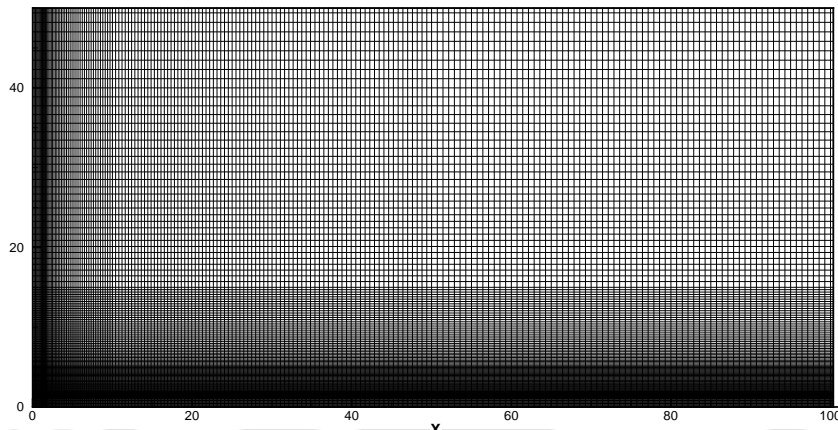


Figure 8.1: Grid independence study.

8.3(c) shows the similarity solution at  $X = 15, 25$  and  $30$  downstream locations respectively. The  $\bar{U}$  velocity is normalized by  $U_{max}$  whereas  $Y$  is normalized by  $Y_{0.5}$  which is the distance in the normal direction at which  $U = U_{max}/2$ . The results are compared with experimental results of Wang and Tan [5] and are in good agreement with the similarity solution of experimental study. In order to assess the difference between the standard  $k - \epsilon$  model and to its streamline curvature (SC) modification, the results of both are compared to the experimental solution. It clearly shows that the streamline curvature modification gives the better results. Fig. 8.3(d) shows the maximum velocity decay in the downstream direction. The results are compared for SC modified  $k - \epsilon$  with the experimental study. In the present computation, the computed results are in agreement with the experimental results up to  $X=15$ . In the downstream location  $X=25$ , the model over predicts compared to the experimental solution. Figure 8.3(e) shows the outer boundary layer growth and is given by that location in the outer layer of the offset jet where  $U = U_{max}/2$ . The results are in good agreement with experimental solution.

In most of the cases, the convergence has been taken to the limit of  $10^{-4}$ . However, it has been observed that when the wall jet and the offset jet velocities are close to 1, there is somewhat a loss of convergence and the residual fall was limited to  $10^{-3}$ . The iterations were carried out to 0.1 - 0.2 million time. A close inspection into the velocity field captured for a range of 10000 iterations revealed that close to the jet issue location, there are some oscillations. However, after a distance of few jet widths, the velocities are exactly constant for the range of iterations. Wang and Tan [5] have presented the ensemble averaging of 360 instantaneous velocity fields. As shown above, the numerically obtained results for various plots are in good agreement with them and it shows that the results presented here are indeed steady-state results.

## 8.2 Results and Discussion

The present study can be briefly classified into two cases. Those are: (1) keeping the wall jet velocity ( $U_w = 1.0$ ) constant, the offset jet velocity ( $U_o$ ) is varied for 0.25, 0.5 and 0.75. (2) keeping offset jet velocity ( $U_o = 1.0$ ) constant, the wall jet velocity is varied for 0.25, 0.5, 0.75 and 1.0. Under these conditions, the study is carried out to seek the similarity solutions and their approximate locations, distribution of wall pressure and shear stress on the wall, maximum velocity decay and spreading rate (half-width of the outer layer for the offset jet) of the combined jet.

Figures 8.4(a), 8.4(b) and 8.4(c) show the similarity profile at different downstream location for  $U_o=0.25$ , 0.5 and 0.75 respectively keeping  $U_w=1.0$ . It is observed that the flow attains the self-similarity in further downstream as  $U_o$  increases. For  $U_o=0.25$ , it is observed at  $X \cong 10$  and for  $U_o=0.75$ , it is  $X \cong 20$ . Similarly, Figs. 8.4(d), 8.4(e) and 8.4(f) show the similarity profile at different downstream locations for  $U_w=0.25$ , 0.5 and 0.75 respectively keeping  $U_o=1.0$ . Un-

like the above case, the flow attains the self-similarity approximately at  $X \cong 30$ , though the wall jet velocity is changed. Similarly, Fig. 8.4(g) describes the self-similarity profile for  $U_w = 1.0$  and  $U_o = 1.0$ . It is observed that the combined flow attains the self-similarity at  $X \cong 30$  which is in good agreement with the experimental results of Wang and Tan [5].

Figure 8.5(a) shows the dimensionless pressure distribution on the wall, for different  $U_o$  keeping  $U_w$  constant. It clearly shows that as  $U_o$  is increased, pressure on the wall also increases and it is almost constant along the wall. Similarly, Fig. 8.5(b) shows the pressure distribution on the wall for different  $U_w$  keeping  $U_o$  constant. It is observed that the pressure on the wall increases as  $U_w$  increases and is almost constant along the wall. For  $U_w=0.25$ , the pressure is 0.5 whereas for  $U_o=1$ , it is 0.92 which means an increase of 80%. Figures 8.5(c), 8.5(d) and 8.5(e) show the pressure distribution along the wall by interchanging the jet velocities. It means that the net mass flow rate is constant with only the exchange of the jet velocities. In Figs. 8.5(c) and 8.5(d), it is demonstrated that the pressure on the wall is more when  $U_w$  is more compared to  $U_o$  and the difference between them is reduced. But Fig. 8.5(e) shows that pressure on the wall is more when the wall jet has less velocity than the offset jet.

Figure 8.6 shows the non-dimensional shear stress ( $\tau_{w,n} = \tau_w / \rho U_r^2$ ) distribution along the wall for different combination of wall jet and offset jet velocities. Figure 8.6(a) shows the shear stress on the wall, keeping  $U_w=1.0$  and varying the  $U_o$ . It is observed that in the immediate downstream of the combined jet,  $\tau_{w,n}$  is more when the  $U_o$  is small and minimum when  $U_o$  is high. This is due to the fact that offset jet has the tendency to reduce the wall stress due to the Coanda effect. In the far downstream  $\tau_{w,n}$  is less, when the  $U_o$  is small. Figure 8.6(b) shows the shear stress on the wall, keeping the  $U_o=1.0$  and varying the  $U_w$ . It is observed that in

the immediate downstream for  $U_w=0.25$  and  $0.5$   $\tau_w$  is small, while for  $U_w=0.75$  and  $1.0$   $\tau_{w,n}$  is more because of the reason given earlier. In the far downstream of the jet  $\tau_{w,n}$  is less when  $U_w$  is small. Figures 8.6(c), 8.6(d) and 8.6(e) show the comparison of  $\tau_{w,n}$  when the jet velocities are exchanged. It is observed that in the immediate downstream,  $\tau_{w,n}$  is very small when the  $U_w < U_o$ . But in the far downstream shear stress on the wall is approximately same in both the cases.

Figure 8.7 shows the maximum velocity ( $U_{max}$ ) decay in the downstream direction for different wall jet and offset jet velocities. Figure 8.7(a) shows the decay of  $U_{max}$ , keeping the  $U_w=1.0$  and varying the  $U_o$ . It is observed that maximum velocity decay is more in the downstream direction, when the  $U_o$  increases beyond  $0.5$ . Figure 8.7(b) shows a similar characteristics in the case of keeping  $U_o=1.0$  and varying the  $U_w$ . It is observed that the decay is less as  $U_w$  is increased. The influence of reduced  $U_w$  is to reduce the  $U_{max}$  at downstream locations. Figures 8.7(c), 8.7(d) and 8.7(e) show the comparison of maximum velocity decay, when the jet velocities are interchanged. It is observed that  $U_{max}$  is small when  $U_w$  is small and the decay rate follows a similar trend.

Figure 8.8 shows the spreading rate of the combined jet in the downstream direction up to  $X = 30$ . This is the distance in the  $Y$  direction where  $U = U_{max}/2$  at the outer layer of the offset jet. Figure 8.8(a) shows the spreading rate, keeping the  $U_w=1.0$  and varying the  $U_o$ . It is observed that as the  $U_o$  is increasing, the jet half-width thickness increases, but the rate of spreading is observed to be nearly constant. Similarly, Figure 8.8(b) shows the spreading rate, keeping the  $U_o=1.0$  and varying the  $U_w$ . It is seen that for  $U_w=0.5$  and  $0.75$ , the boundary layer thickness and the spreading rate are approximately same. For  $U_w=0.25$ , it is small and the spreading rate is approximately same to the case of  $U_w=0.5$  and  $0.75$ . Figures 8.8(c), 8.8(d) and 8.8(e) compare the spreading rate of combined jet when the jet

velocities are exchanged. It is observed that, though the thickness of the boundary layer is small when the  $U_w=1.0$ , rate of spreading is approximately constant.

In order to give fluid flow behavior in the domain is given for  $U_w=1.0$  and  $U_o=0.5$  and interchanging them. Fig. 8.9 shows the  $U$  and  $V$  velocity contours. It shows that  $U$  velocity is predominant in both the cases. Fig. 8.10 shows the  $k_n$  and  $\epsilon_n$  contours. It is observed that the behavior of flow is almost similar in both the cases. Fig. 8.11 shows non-dimensional pressure contour in both cases.

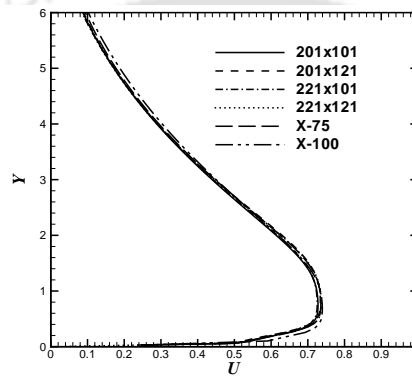


Figure 8.2: Grid independence study.

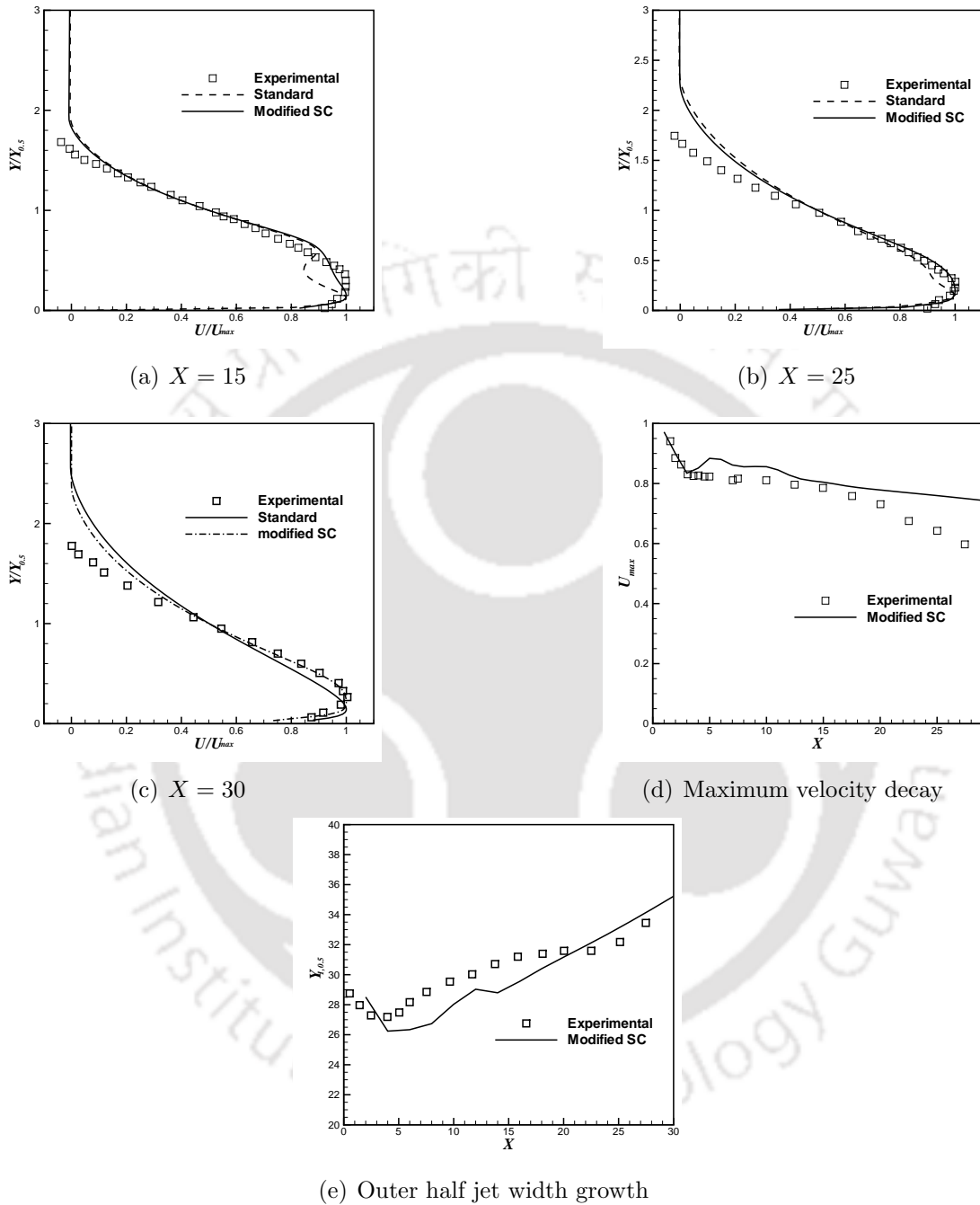
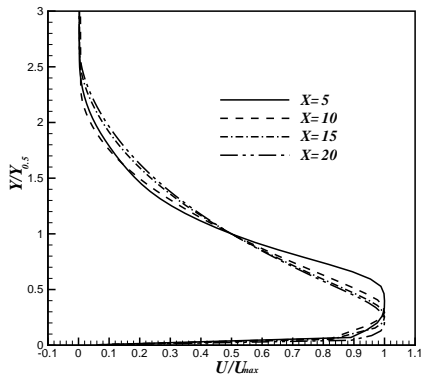
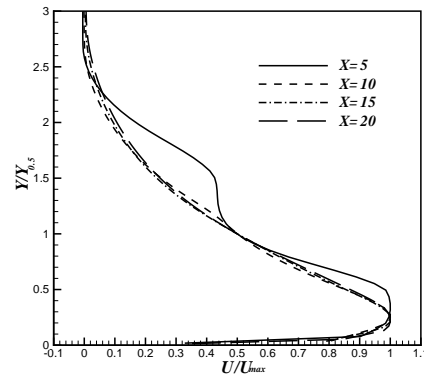


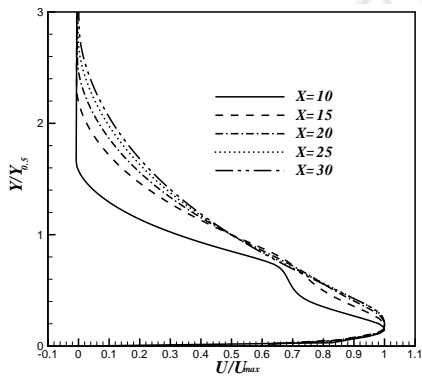
Figure 8.3: Validation study for similarity solution (8.3(a), 8.3(b), 8.3(c)), outer boundary layer growth (8.3(e)) and maximum velocity decay (8.3(d)) with Wang and Tan [5].



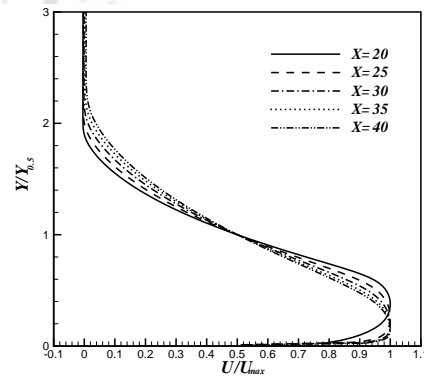
(a)  $U_w = 1.0$   $U_o = 0.25$



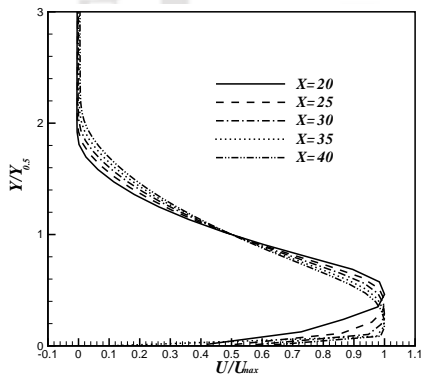
(b)  $U_w = 1.0$   $U_o = 0.5$



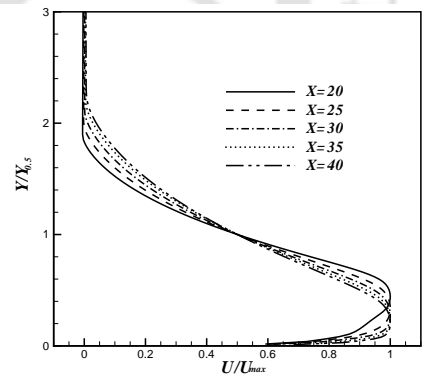
(c)  $U_w = 1.0$   $U_o = 0.75$



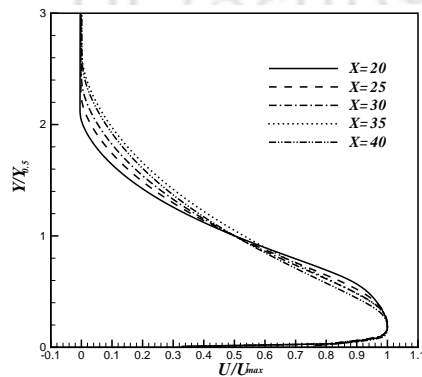
(d)  $U_w = 0.25$   $U_o = 1.0$



(e)  $U_w = 0.5$   $U_o = 1.0$



(f)  $U_w = 0.75$   $U_o = 1.0$



(g)  $U_w = 1.0$   $U_o = 1.0$

TH-608\_04610302

Figure 8.4: Comparison of similarity solution at different downstream location for different wall jet and offset jet velocities.

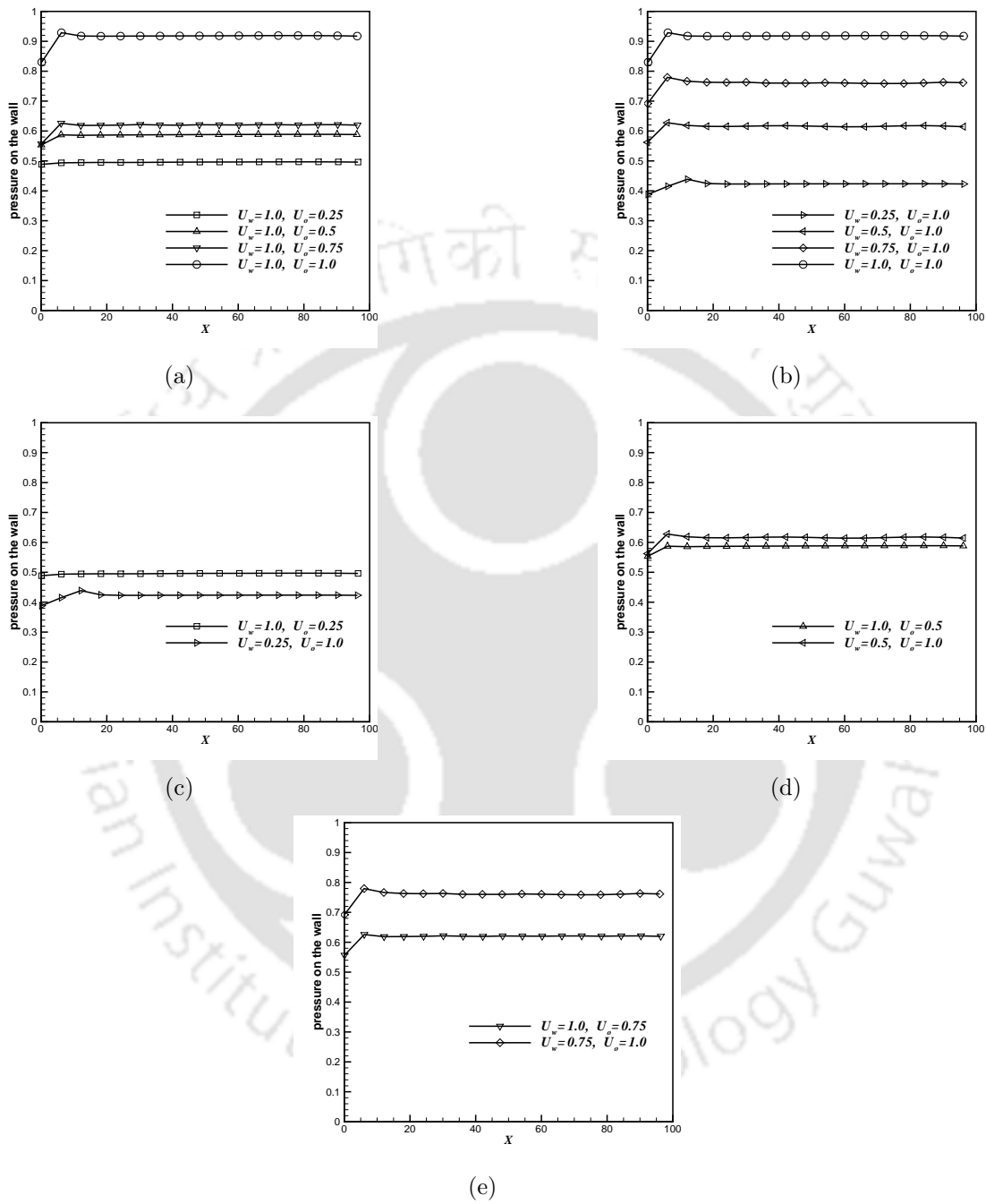


Figure 8.5: Pressure distribution along the wall at different offset and wall jet velocities.

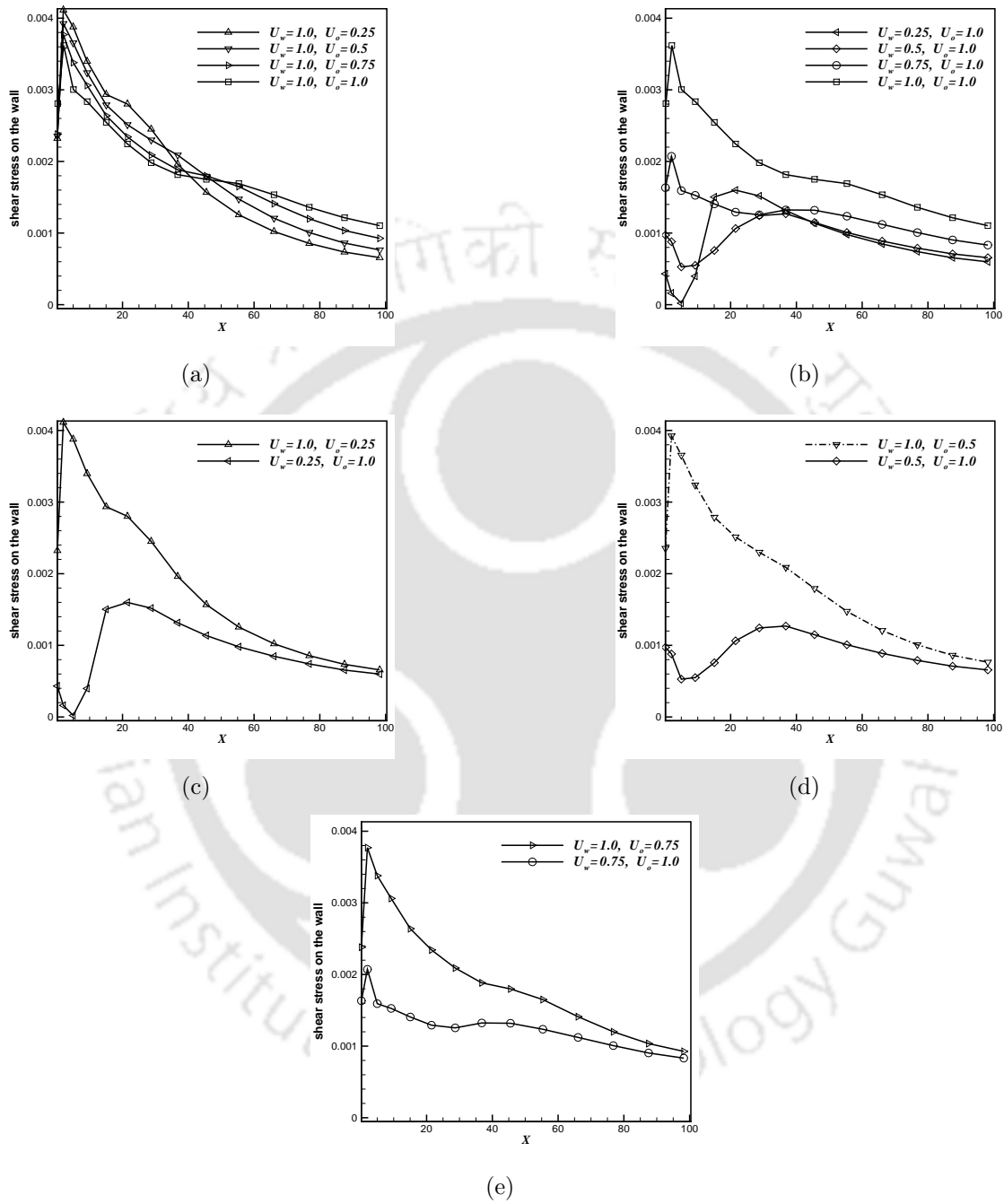


Figure 8.6: Shear stress distribution along the wall at different offset and wall jet velocities.

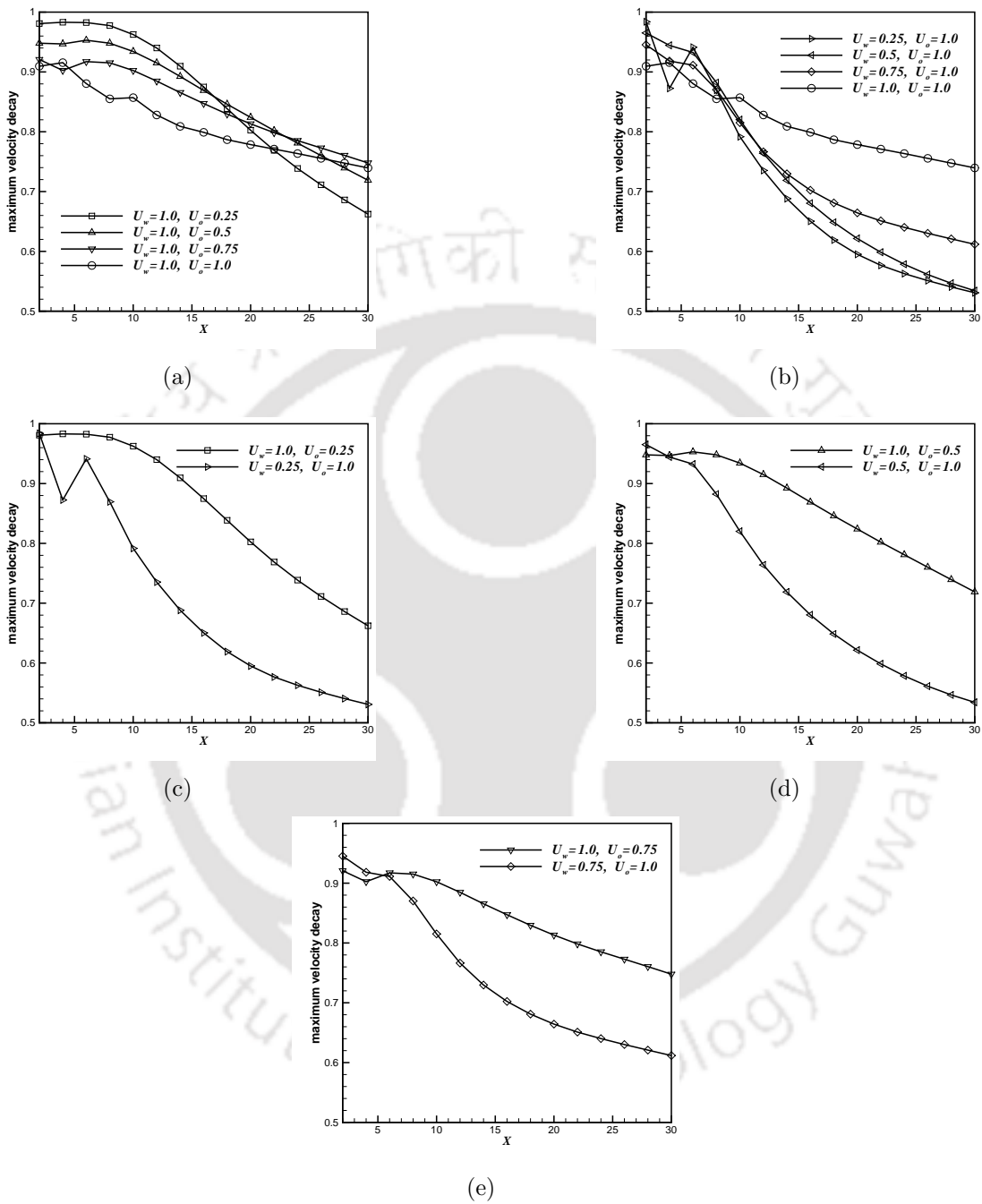


Figure 8.7: Maximum velocity decay in the downstream at different wall jet and offset jet velocities.

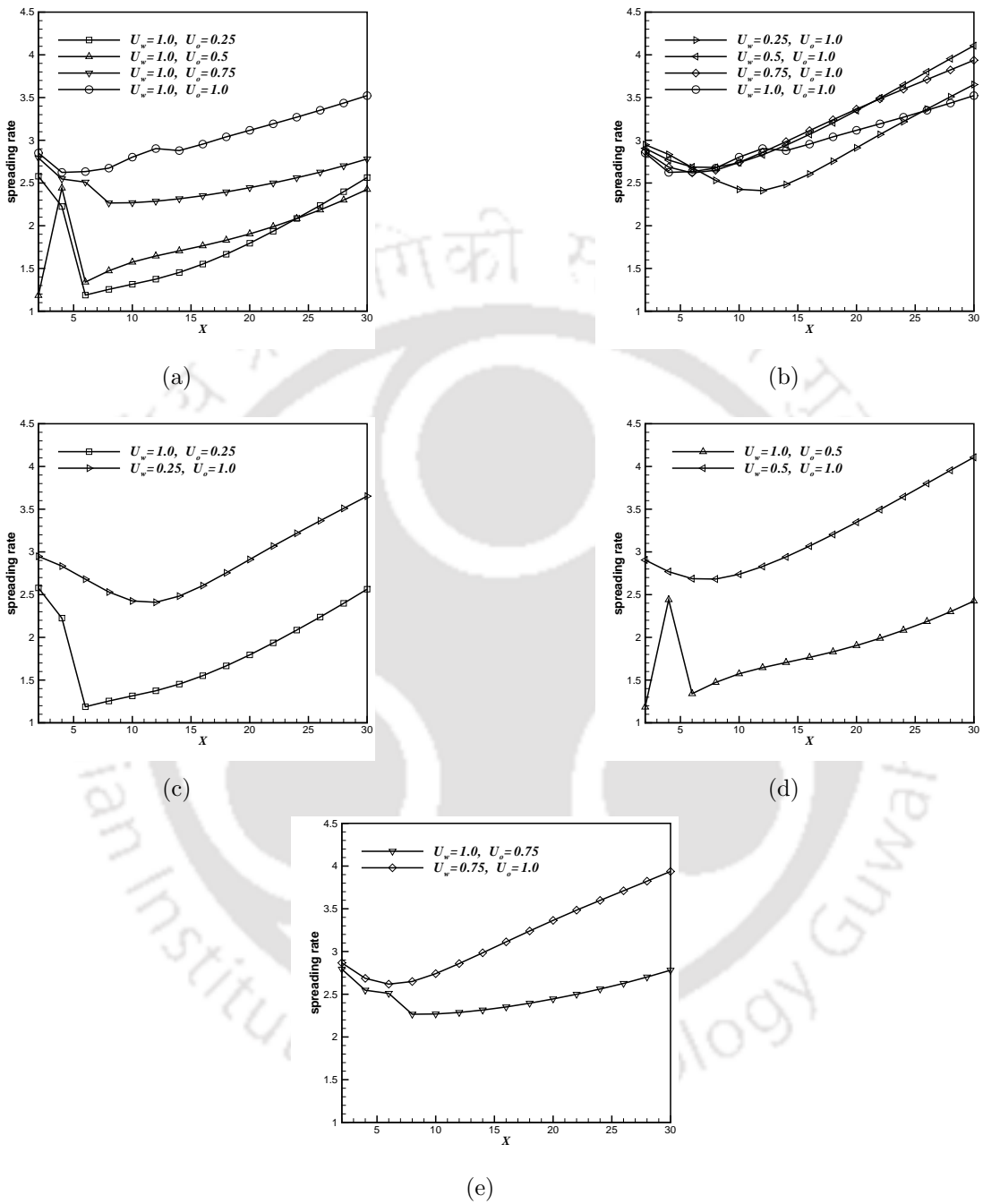
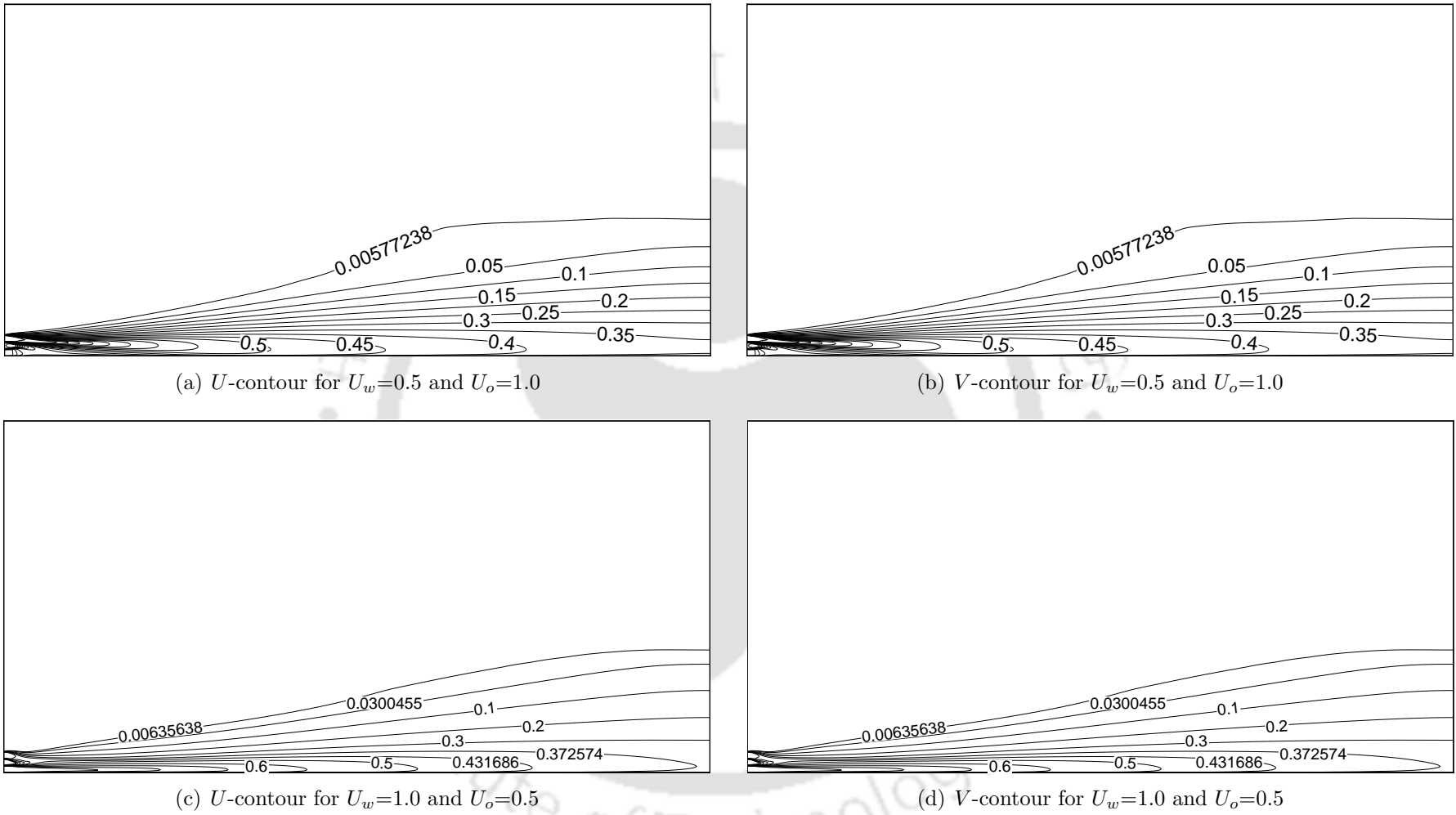
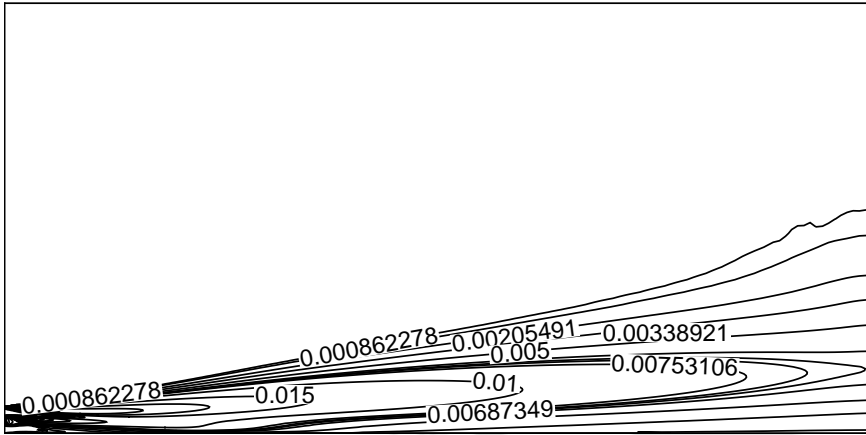
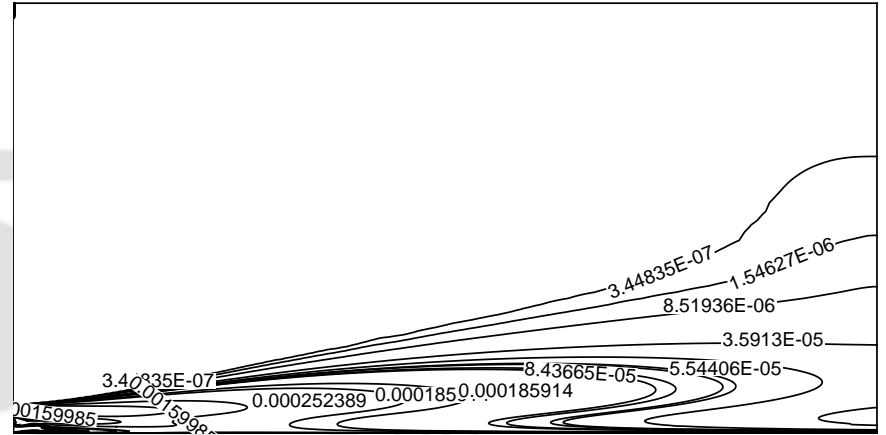


Figure 8.8: Spreading rate of the jet in the downstream direction at different wall jet and offset jet velocities.

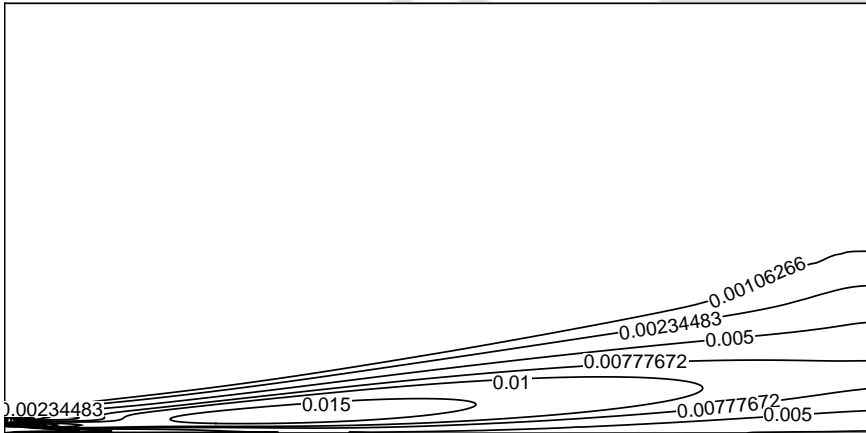
Figure 8.9:  $U$  and  $V$  velocity contours of combined jet flow



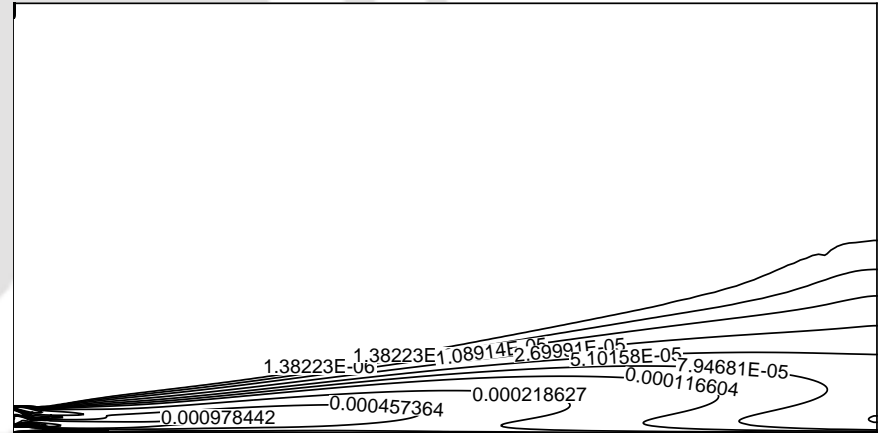
(a)  $k_n$ -contour for  $U_w=0.5$  and  $U_o=1.0$



(b)  $\epsilon_n$ -contour for  $U_w=0.5$  and  $U_o=1.0$

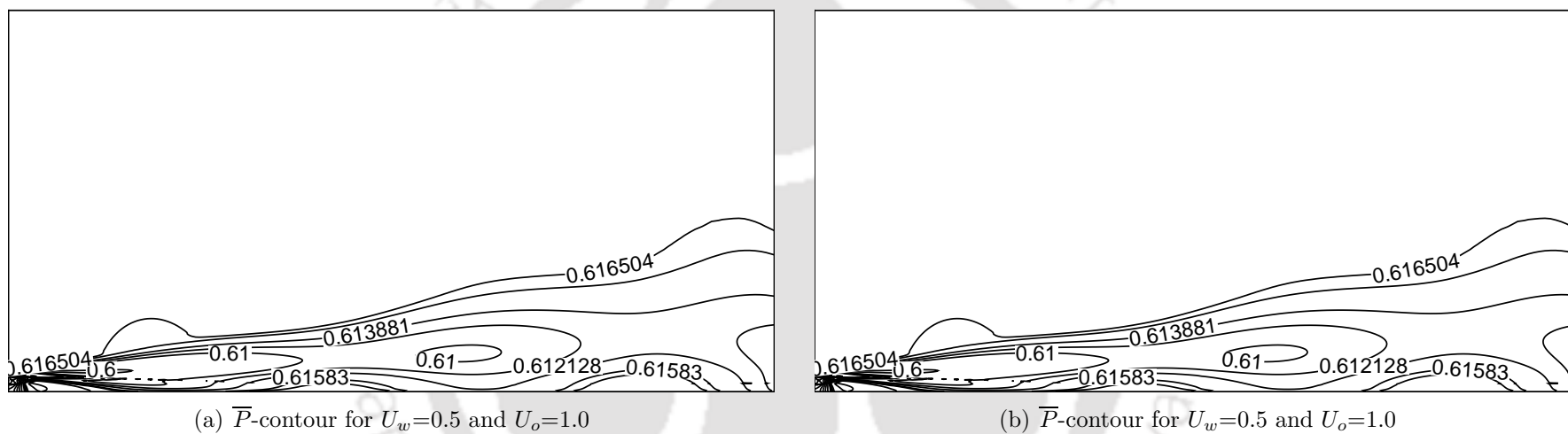


(c)  $k_n$ -contour for  $U_w=1.0$  and  $U_o=0.5$



(d)  $\epsilon_n$ -contour for  $U_w=1.0$  and  $U_o=0.5$

Figure 8.10:  $k_n$  and  $\epsilon_n$  contours of combined jet flow

Figure 8.11:  $\bar{P}$  contours of combined jet flow

## 8.3 Conclusions

The mean flow characteristics of a combined jet flow consisting of a wall jet and an offset jet is solved numerically using two-equation  $k - \epsilon$  turbulence model along with the modified streamline curvature method. A standard wall function has been used. Different flow features are studied mainly under two conditions. Those are: (1) keeping  $U_w=1.0$ ,  $U_o$  is varied for 0.25, 0.5 and 0.75. (2) keeping  $U_o=1.0$ ,  $U_w$  is varied for 0.25, 0.5, 0.75 and 1.0. The following conclusions may be drawn.

- The flow attains the self-similarity in the further downstream when  $U_o$  is increased, keeping  $U_w=1.0$ . But location of self-similarity is almost constant when  $U_w$  is increased, keeping  $U_o=1.0$ .
- Pressure on the wall is almost constant along the wall and it increases when one of the jet velocity is increased keeping the other constant. In case the jet velocities are interchanged, the wall pressure is more when the wall jet velocity is 0.5 or higher.
- For constant  $U_o$ , near to the converging region, the shear stress is less on the wall when  $U_w < U_o$  and it increases as  $U_w$  is increased. In the far downstream, shear stress is almost equal for the cases when the jet velocities are interchanged. For constant  $U_w$ , the shear stress increases with decreasing  $U_o$  in the converging region. In the downstream, the trend is reversed.
- At any location in the downstream,  $U_{max}$  increases with increasing the wall jet velocity for constant offset jet velocity. The maximum velocity is always less when  $U_w$  is less than  $U_o$ .
- The thickness of the outer boundary layer is more when  $U_w$  is less than that  $U_o$ . however, the rate of its growth is almost equal when jet velocities are interchanged.

# Chapter 9

## Different Turbulent Flow Behaviours of a Combined Plane Wall Jet and a Parallel Offset Jet

### 9.1 Introduction

The purpose of the present study is to identify the downstream locations up to which the flow behavior shows oscillations as reported by Wang and Tan [5]. Beyond this location in the downstream, the flow behavior is steady. In the present study, a detailed numerical simulation of the dual-jet consisting of a plane wall jet and an offset jet has been conducted for a range of wall jet and offset jet velocities. Wang and Tan [5] have considered only one combination of the wall jet and offset jet velocity. The spacing between the wall jet and the offset jet has been kept constant at 1. The turbulence modeling has been conducted by the standard high  $Re$   $k - \epsilon$  model. The modified streamline-curvature method of Cheng and Farokhi [52] has been applied. The Reynolds number considered is 20000. The characterization of the dual jet has been done by plotting the velocities, pressure, Reynolds stress and phase diagram for the range of 10000 iterations. These data

have been stored after allowing the computations to be carried out for 100000 iterations even after the fall of residual to a small value and becomes constant. The numerical scheme and method of solution as explained in chapter 2.6 is used in the present computations. The boundary conditions, code validation and grid independent studies are described in chapter 8.

## 9.2 Results and Discussion

In the present study,  $Re=20000$  is taken for all the computations. The present study can be briefly classified into two cases. Those are (1) keeping the wall jet velocity ( $U_w = 1.0$ ) constant, offset jet velocity ( $U_o$ ) is varied for 0.25, 0.5 and 0.75. (2) keeping offset jet velocity ( $U_o = 1.0$ ) constant, wall jet velocity is varied for 0.25, 0.5, 0.75 and 1.0. In their work, Wang and Tan [5] have reported the vortex shedding at the entrance of the jet. The present study is aimed at the effect of periodic flow due to the vortex shedding at the jet entrance in the downstream direction. Analyses are carried out for the changes in the flow variables/properties at different locations to discriminate the periodic and steady flow regions or whether the flow is steady. Since the maximum variations occur in the region between the wall jet and the offset jet, the observation is concentrated on the same region. For this  $Y=1.25, 1.5$  and  $1.75$  are chosen along with  $Y=0.125$  which is very close to wall (which represents the effects on the wall). At these  $Y$  locations, the distances in  $X$ -direction are chosen at 2.5, 5.0, 10.0, 15.0 and so on up to 40. Since the domain size of  $100 \times 50$  is taken,  $X=2.5$  shows comparatively very close to the wall. At these locations, the variables  $\bar{U}$ ,  $\bar{V}$ ,  $\bar{P}$  and  $-\overline{u'v'}$  are stored for a range of 10000 iterations. After the residual have fallen down to a very small value and become constant, the computations were carried out to 100000 iterations and the storing of the data was initiated.

Figure 9.1 shows the variation of different flow variables/properties during the iteration at  $X=2.5$ . Figure 9.1(a) demonstrates the mean velocity in the direction of axis of the jet ( $\bar{U}$ ). It clearly shows that the flow is oscillating. It is observed that amplitude of variation is less at  $Y=0.125$  (which is close to wall) and maximum at  $Y=1.75$  (which is near to offset jet). The  $\bar{U}$  is found maximum at the  $Y=0.125$  because the point is inline with wall jet and close to the wall. Similarly the Coanda effect causes the offset flow to deflect downwards. The point  $Y=1.75$  also falls in the offset jet, so the velocity is found high. The region in between the  $Y=0.125$  and  $1.75$ ,  $\bar{U}$  is less and approximately same amplitude of variation. Figure 9.1(b) shows the mean velocity in the direction normal to the axis of the jet ( $\bar{V}$ ). It is seen that the variation in  $\bar{V}$  at  $Y=0.125$  is negligibly small compared to  $Y=1.25, 1.5$  and  $1.75$ . It is understood that at  $Y=1.25$ ,  $\bar{V}$  periodically changes to upward and downward whereas the flow is always downward at  $Y=1.5$  and  $1.75$ . The pressure ( $\bar{P}$ ) variation has been shown in Fig. 9.1(c). It is noticed that the amplitude of variation in  $\bar{P}$  is approximately constant at all  $Y$  locations. The pressure is found comparatively maximum at  $Y=0.125$  and  $1.75$  than  $1.25$  and  $1.5$ . The variation in the Reynolds stress ( $-\overline{u'v'}$ ) during the iteration is shown in Fig. 9.1(d). It shows that  $-\overline{u'v'}$  is constant at the wall whereas  $-\overline{u'v'}$  is negative at  $Y=1.25$  and positive at  $1.5$  and  $1.75$ . Figure 9.1(e) shows the phase diagram plotted as  $\bar{U}$  vs  $\bar{V}$ . Similar type of phase diagrams are plotted to describe the periodic variation occurred during Hopf bifurcation in a lid-driven cavity problem by Goodrich et al. [64]. The effect is very small at  $Y=0.125$ . It is observed that as  $Y$  increases  $\Delta\bar{U}$  increases and  $\Delta\bar{V}$  decreases. Similarly, the variation of the different variables during the iteration at  $X=5.0$  is shown in Fig. 9.2. It is observed in all the variables that the amplitude is reduced compared to the location  $X=2.5$ . The amplitude of  $\bar{U}$  and  $\bar{V}$  increases as  $Y$  increased as shown in Fig. 9.2(a) and 9.2(b) respectively. The pressure on the wall is found to be maximum in Fig. 9.2(c) and the amplitude of variation is nearly constant. Figure 9.2(d) shows the Reynolds

stress on the wall. It is observed that at  $Y=1.25$ , the  $-\overline{u'v'}$  shows the sharp variations compared to other  $Y$  location. The reduction in the amplitude in  $\overline{U}$  and  $\overline{V}$  are also reflected in the phase diagram of Fig. 9.2(e). In further downstream, the reduction in the amplitude to very small values compared to  $X=2.5$  and  $5$  is observed in Fig. 9.3. Similar to  $X=5$ ,  $\overline{U}$  is maximum at  $X=1.75$  and reduces as  $Y$  decreases. Though the fluctuations still exists in  $\overline{V}$ , it is found to be constant across  $Y$  as shown in Fig. 9.3(b). Figure 9.3(c) shows the pressure across the wall at  $X=10$  is almost constant. The variation of Reynolds stress is also small as shown in Fig. 9.3(d). The phase diagram shown in Fig. 9.3(e) depicts that at  $Y=0.125$ , it is almost reduced to a point. The periodic nature of the flow is completely attenuated and flow become completely steady as observed in Fig. 9.4. The phase diagram shown in Fig. 9.4(e) reduced to invisibly small points clearly states that the flow is completely steady across  $Y$  at  $X=15$ . The results are also given in Table 9.1. It is observed that the percentage variation of  $|\overline{V}|$  and  $\overline{P}$  is very small at  $X=10.0$ . however, the variation in  $-\overline{u'v'}$  is appreciable. At  $X=15.0$ , the change in all the variables is small. From this stand point, we can conclude that the flow in the downstream from  $X \approx 15$  is steady.

Figure 9.5 shows the variation of different properties at different  $Y$ -locations and  $X=2.5$  for  $U_w=1.0$  and  $U_o=0.25$ . It is clearly demonstrated that for all variables at all locations the flow is in completely steady-state. Though the very small variations in the pressure is observed, the effect of it on the other variables is found negligible. It is almost invisible to trace the points on the phase diagram shown in Fig. 9.5(e) which reflects the steady flow behavior. Since the wall jet velocity is high compared to the offset jet velocity, it is found that  $\overline{U}$  at  $Y=0.125$  is high compared to other locations. The negative velocities of  $\overline{V}$  at  $Y=1.25$ ,  $1.5$  and  $1.75$  as shown in Fig. 9.5(b) represents the entrainment into the boundary. Fig. 9.5(d) shows the negative  $-\overline{u'v'}$  at  $Y=1.25$  causes for the momentum gain in the flow.

The results are also given Table 9.2. It is concluded that the flow is steady at  $X=2.5$ .

Figure 9.6 shows the variation of different properties at different  $Y$ -locations at  $X=2.5$  for  $U_w=1.0$  and  $U_o=0.5$ . As it shows, the flow is steady and similar conclusions can be drawn as explained in case of  $U_w=1.0$  and  $U_o=0.25$ . The results are also given Table 9.3.

Similarly, Fig. 9.7 shows the variation of different properties at different  $Y$ -locations at  $X=2.5$  for  $U_w=1.0$  and  $U_o=0.75$ . Though a noticeable variations in the pressure is observed, surprisingly it is found that remaining variables are still in steady-state. The behavior of the flow variables are in similar trend with the  $U_o=0.25$  and  $0.5$ . The results are also given Table 9.4.

The variation of different properties, when the wall jet and offset jet velocities are interchanged are shown in Figs. 9.8 -9.12. Figure 9.8 shows the variation of different properties at different  $Y$ -locations at  $X=2.5$  for  $U_w=0.25$  and  $U_o=1.0$ . It can be stated clearly that the flow is in completely steady-state. It is noticed that the pressure increases along the  $Y$ -direction as shown in Fig. 9.8(c). Since the  $U_o=1.0$ , the Reynolds stress at  $Y=1.75$  is more compared to other locations. It is almost invisible to locate the phase diagrams which also suggest that the flow is completely steady as shown in Fig. 9.5(e). The results are also given Table 9.5.

Figure 9.9 shows the variation different properties at different  $Y$ -locations at  $X=2.5$  for  $U_w=0.5$  and  $U_o=1.0$ . When compared to Fig. 9.6, strong oscillations in pressure are noticed as shown in Fig. 9.9(c). But the effect of it on other variables are negligible. Fig. 9.9(e) also justifies that the flow is in steady-steady state. The percentage variation for different variables are also given Table 9.6.

When the  $U_w$  is increased to 0.75 keeping the  $U_o=1.0$ , the variations at  $X=2.5$  downstream location is shown in Fig. 9.10. In the  $\bar{U}$  velocity, periodic nature of flow with small amplitude is observed at  $Y=1.75$ , but at other locations flow in  $\bar{U}$  is steady. Except at the wall, oscillations are observed at all locations in  $\bar{V}$  is shown in Fig. 9.10(b) and similar is the case with the Reynolds stress (Fig. 9.10(d)). In case of pressure, fluctuations are observed at all  $Y$ -locations. Phase diagram shown in Fig. 9.10(e) also shows that except at the wall, small fluctuations as observed in  $\bar{U}$  and  $\bar{V}$ . Figure 9.11 shows that at a location  $X=5$ .  $-\overline{u'v'}$  is observed to be steady at all  $Y$ -locations. But the similar trend is observed for other variables with reduced amplitude. It is observed that all the variables are steady, except the pressure as shown in Fig. 9.12. Though the oscillations in pressure is observed that does not have any significant effect on other variables, at further downstream the flow is steady. Table 9.7 shows the percentage variation for this particular case.

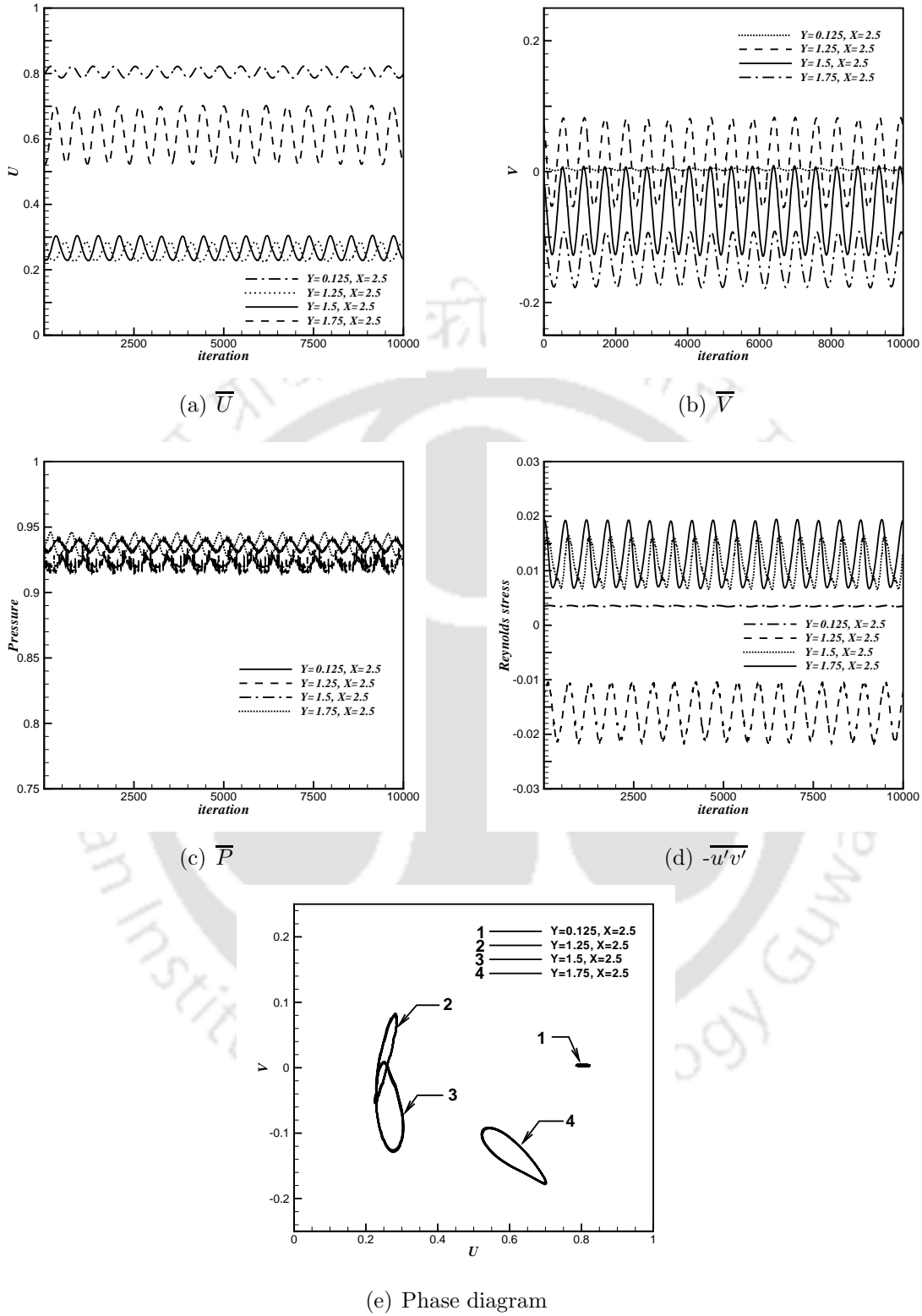
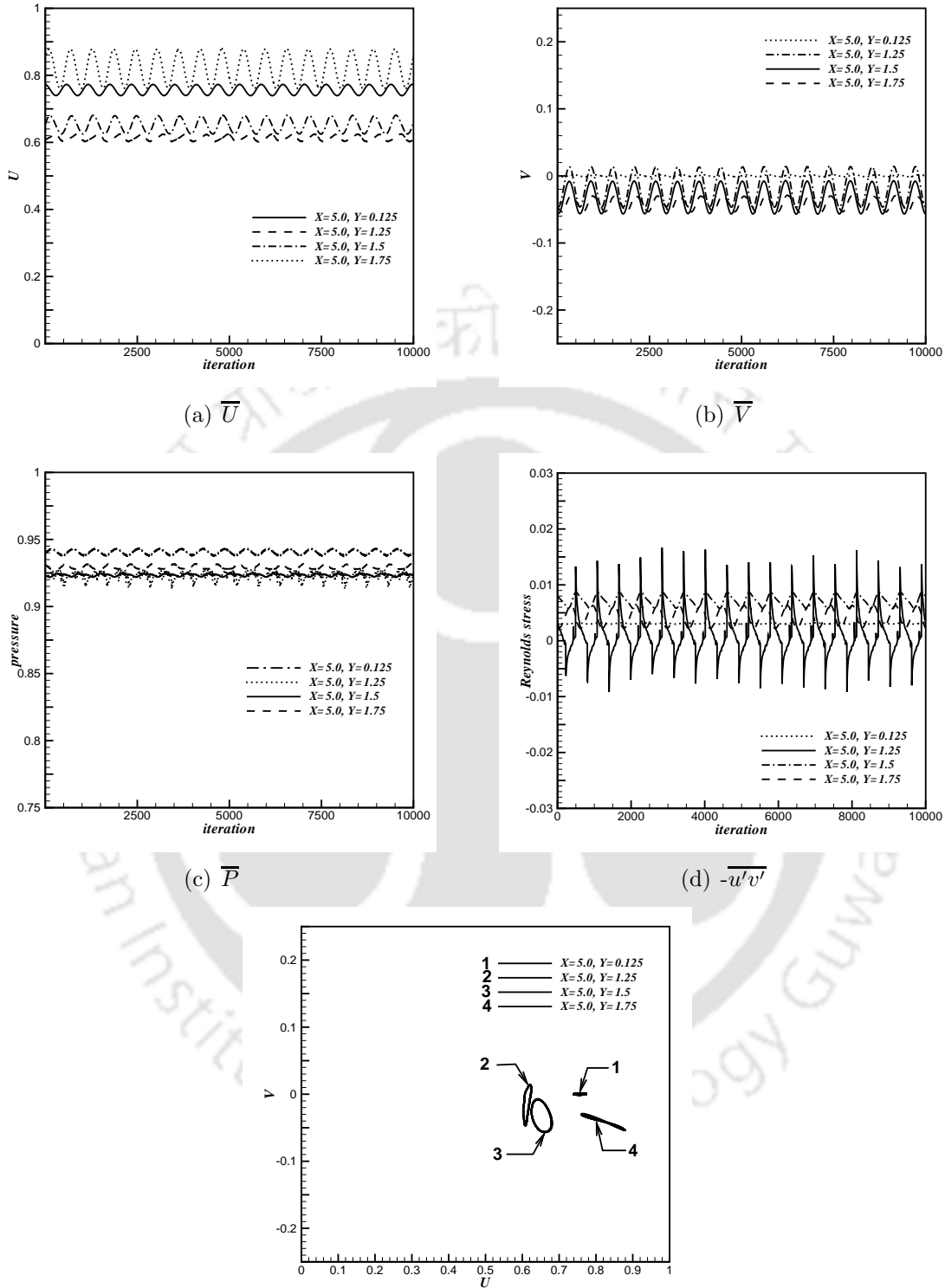


Figure 9.1: Variation of different properties for  $U_w = 1.0$ ,  $U_o = 1.0$  at  $X=2.5$ ,  $Y=0.125$ ,  $1.25$  and  $1.75$  locations during the iteration.



(a)  $\bar{U}$

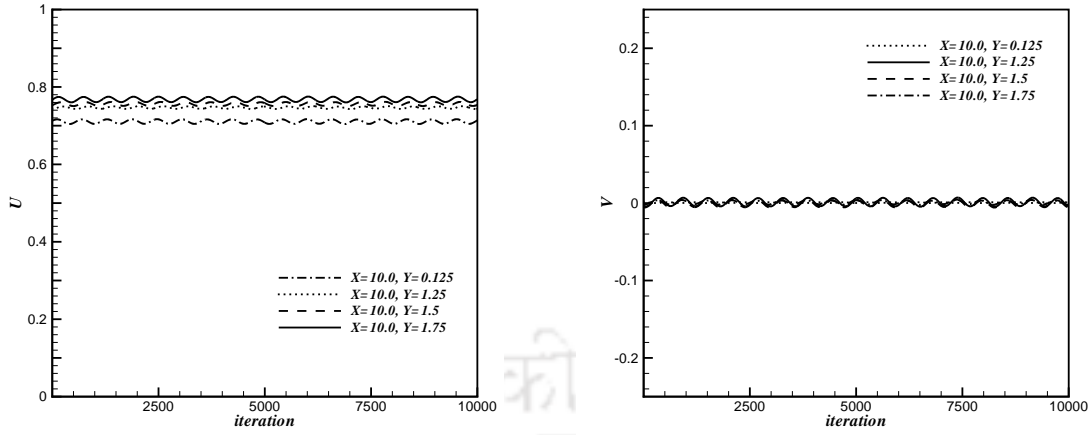
(b)  $\bar{V}$

(c)  $\bar{P}$

(d)  $-\overline{u'v'}$

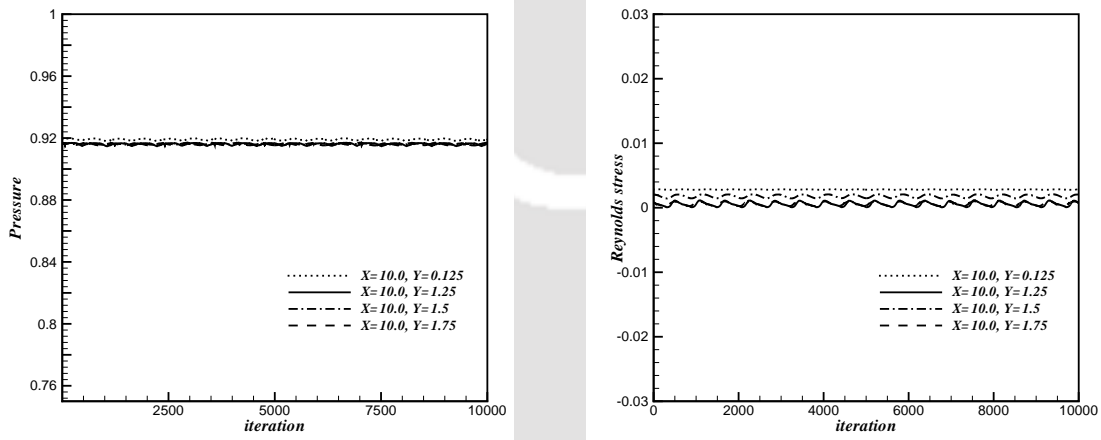
(e) Phase diagram

Figure 9.2: Variation of different properties for  $U_w = 1.0$ ,  $U_o = 1.0$  at  $X=5.0$ ,  $Y=0.125, 1.25$  and  $1.75$  locations during the iteration.



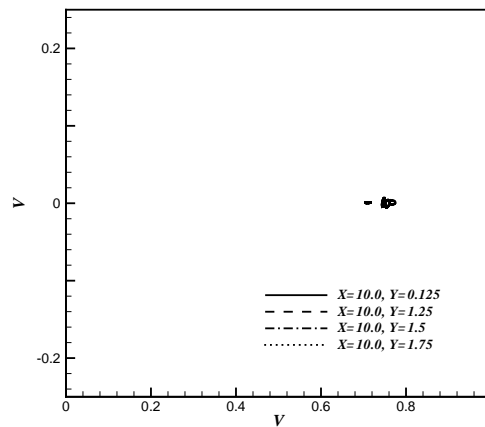
(a)  $\bar{U}$

(b)  $\bar{V}$



(c)  $\bar{P}$

(d)  $-\overline{u'v'}$



(e) Phase diagram

Figure 9.3: Variation of different properties for  $U_w = 1.0$ ,  $U_o = 1.0$  at  $X=10.0$ ,  $Y=0.125$ ,  $1.25$  and  $1.75$  locations during the iteration.

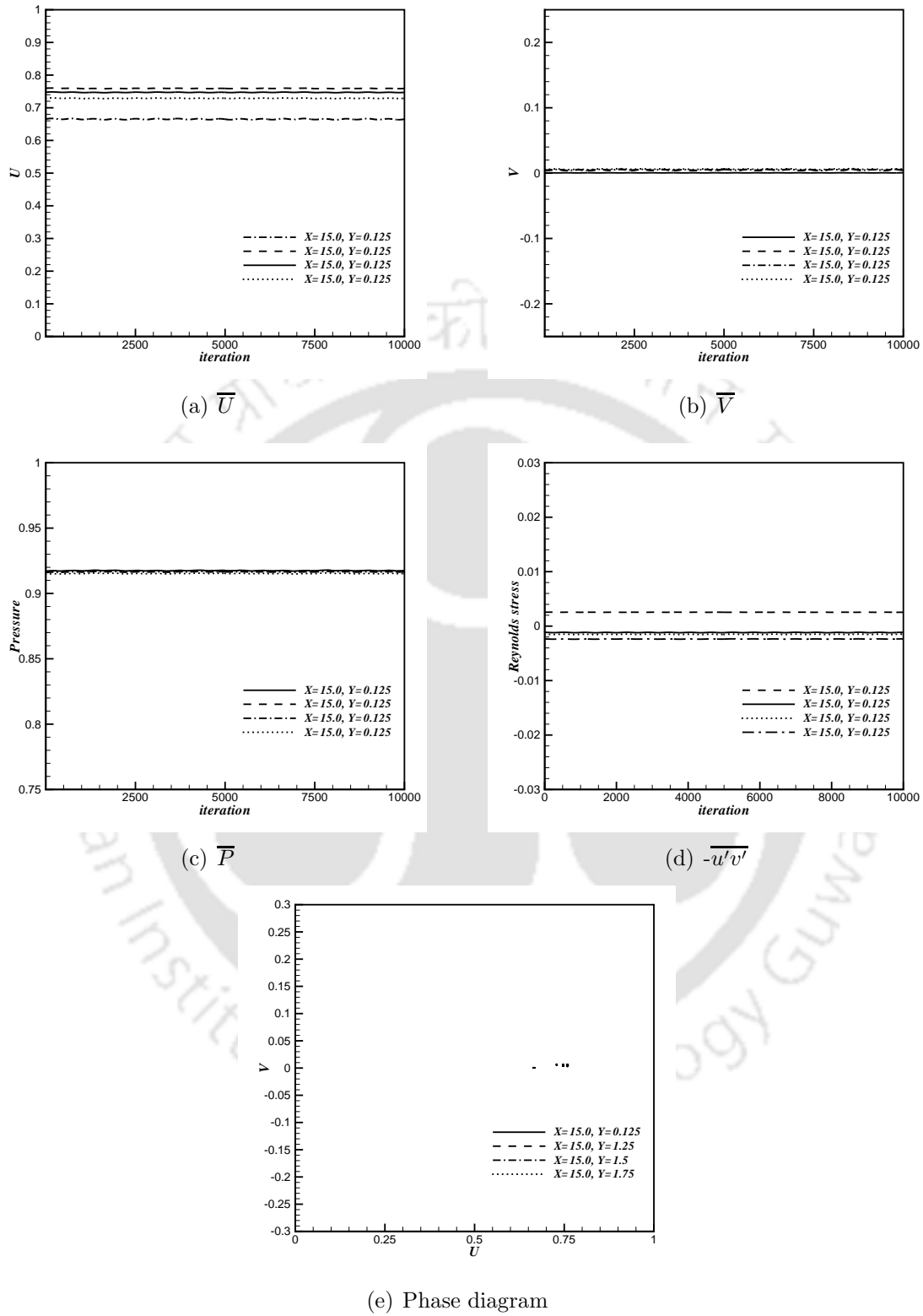


Figure 9.4: Variation of different properties for  $U_w = 1.0$ ,  $U_o = 1.0$  at  $X=15.0$ ,  $Y=0.125, 1.25$  and  $1.75$  locations during the iteration.

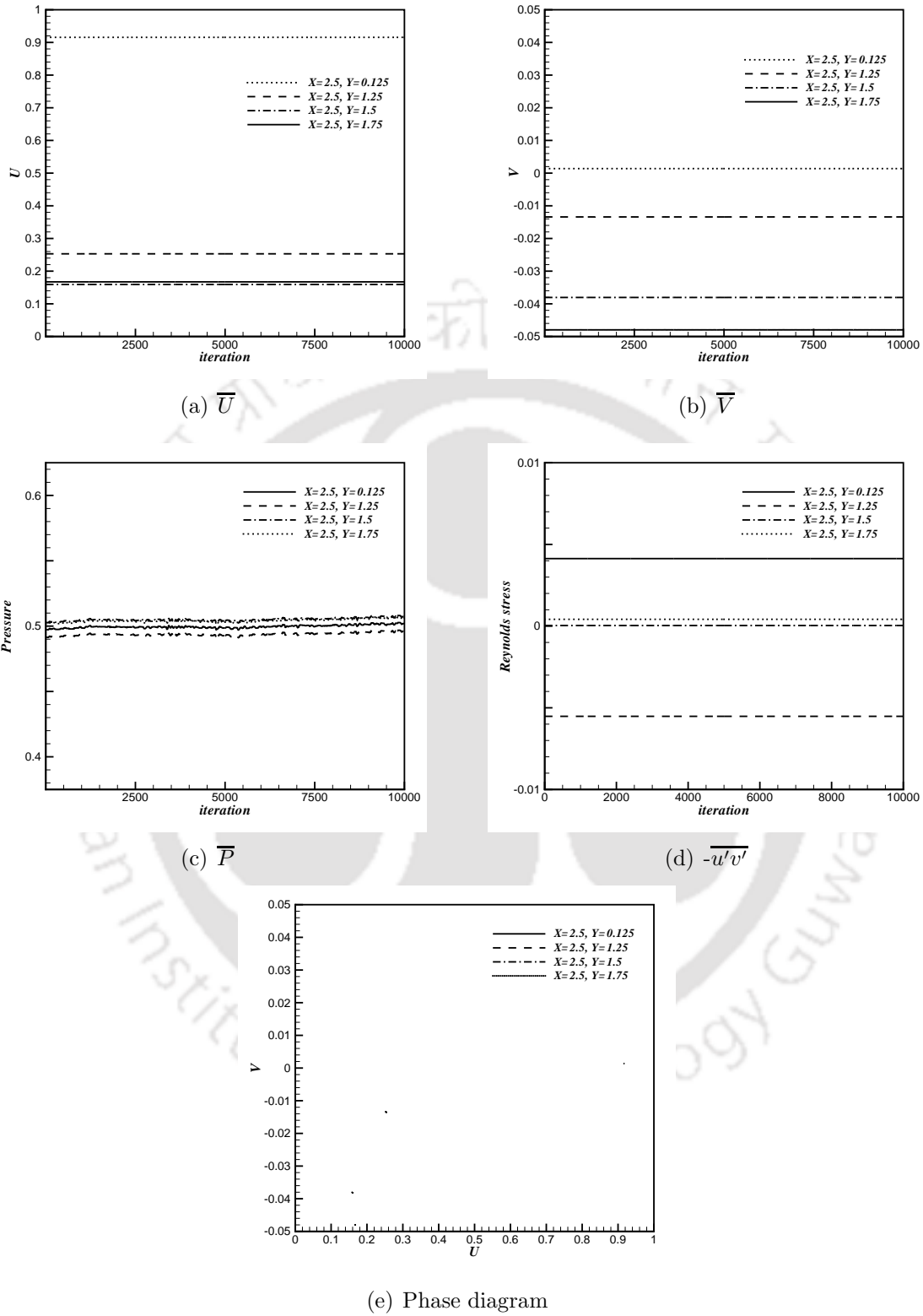


Figure 9.5: Variation of different properties for  $U_w = 1.0$ ,  $U_o = 0.25$  at  $X=2.5$ ,  $Y=0.125$ ,  $1.25$  and  $1.75$  locations during the iteration.

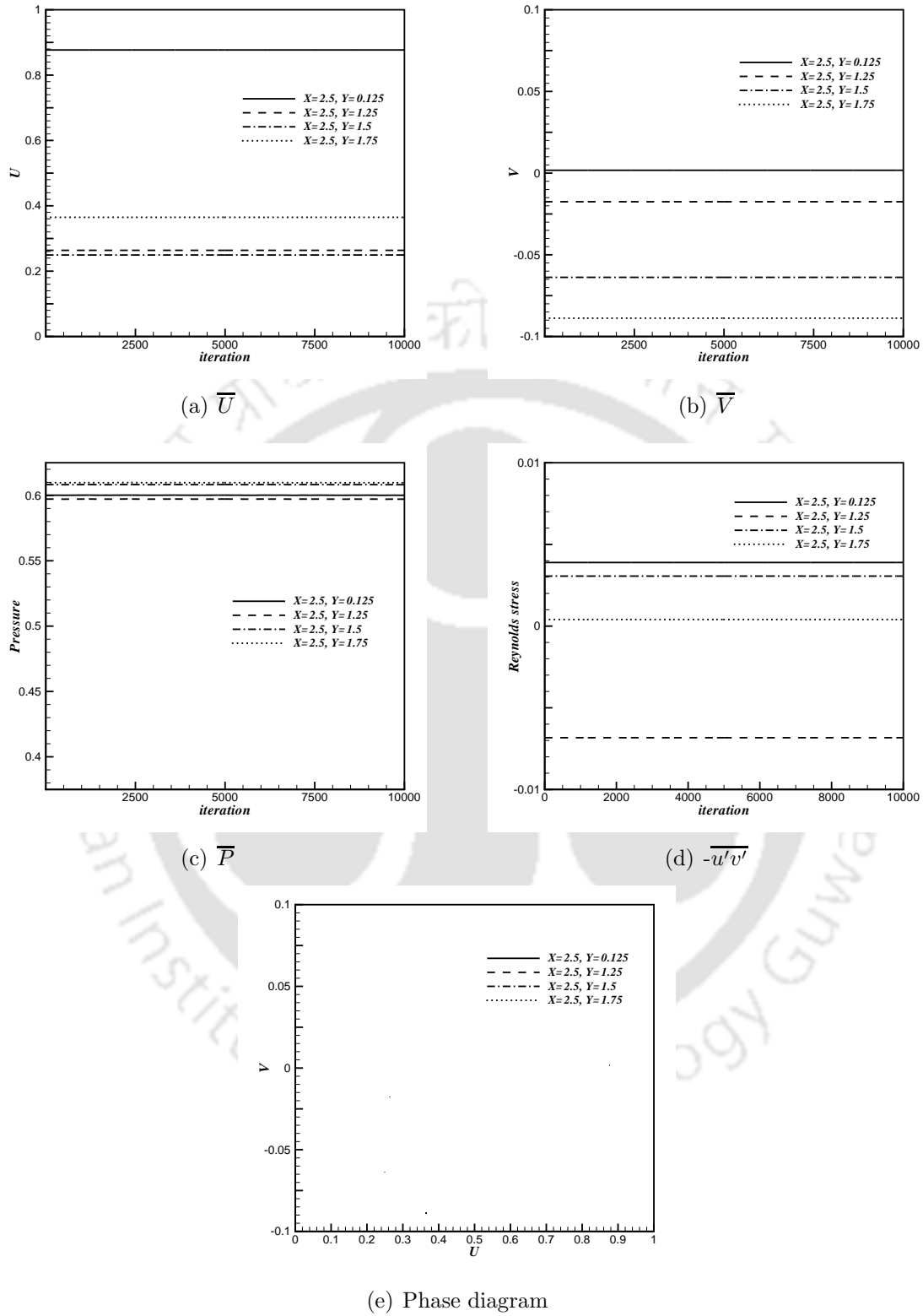


Figure 9.6: Variation of different properties for  $U_w = 1.0$ ,  $U_o = 0.5$  at  $X=2.5$ ,  $Y=0.125$ ,  $1.25$  and  $1.75$  locations during the iteration.

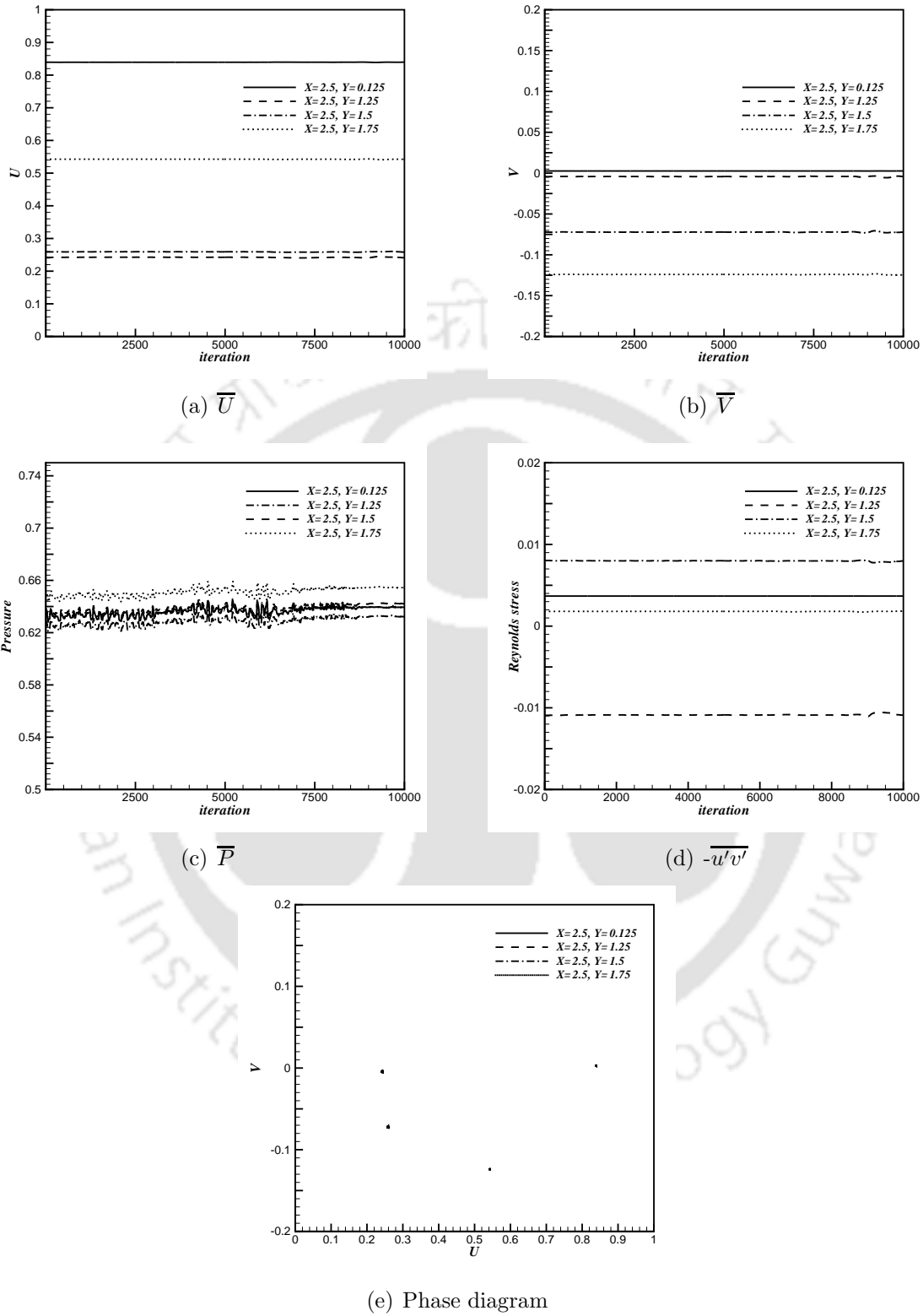


Figure 9.7: Variation of different properties for  $U_w = 1.0$ ,  $U_o = 0.75$  at  $X=2.5$ ,  $Y=0.125, 1.25$  and  $1.75$  locations during the iteration.

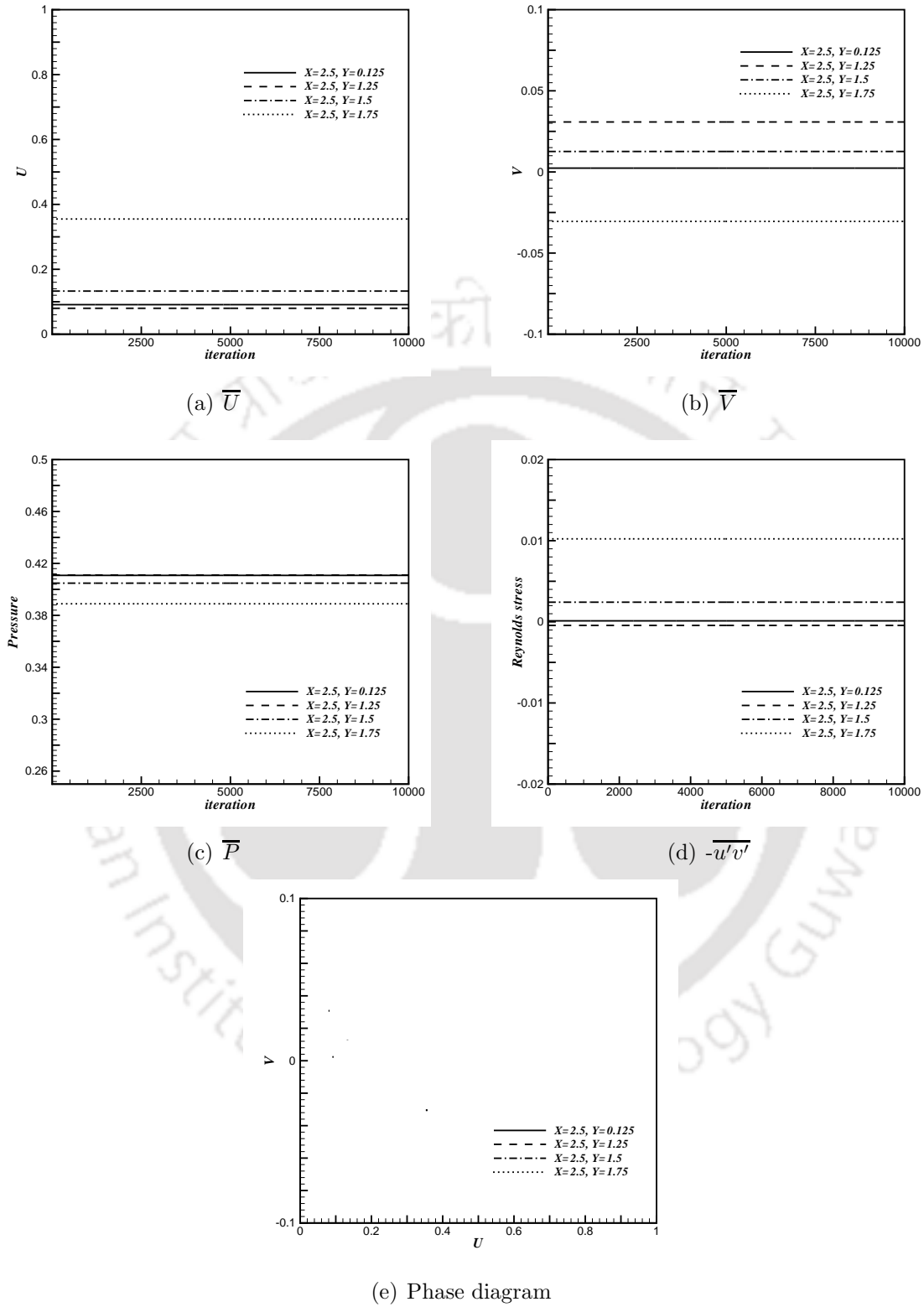


Figure 9.8: Variation of different properties for  $U_w = 0.25$ ,  $U_o = 1.0$  at  $X=2.5$ ,  $Y=0.125, 1.25$  and  $1.75$  locations during the iteration.

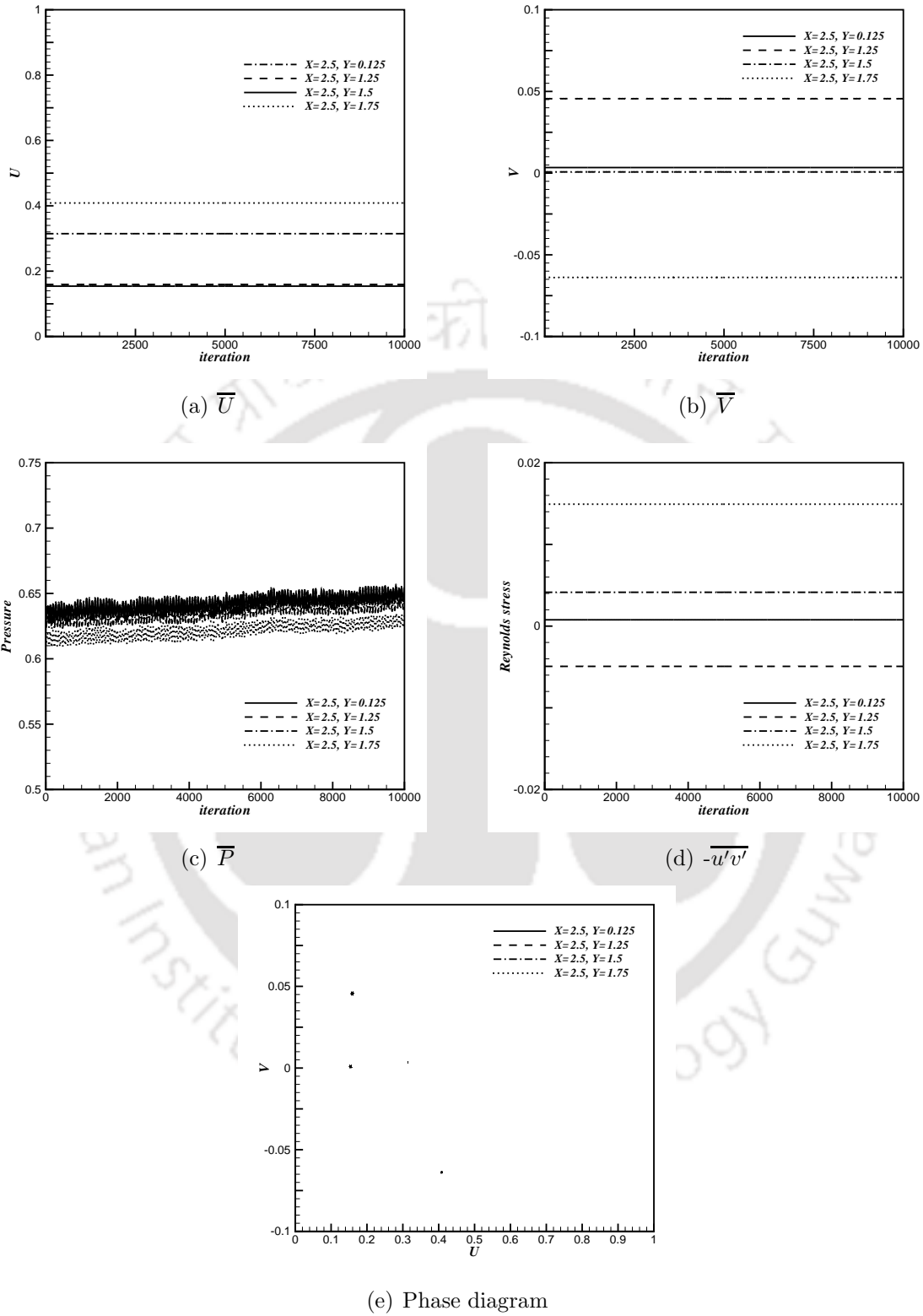


Figure 9.9: Variation of different properties for  $U_w = 0.5$ ,  $U_o = 1.0$  at  $X=2.5$ ,  $Y=0.125$ ,  $1.25$  and  $1.75$  locations during the iteration.

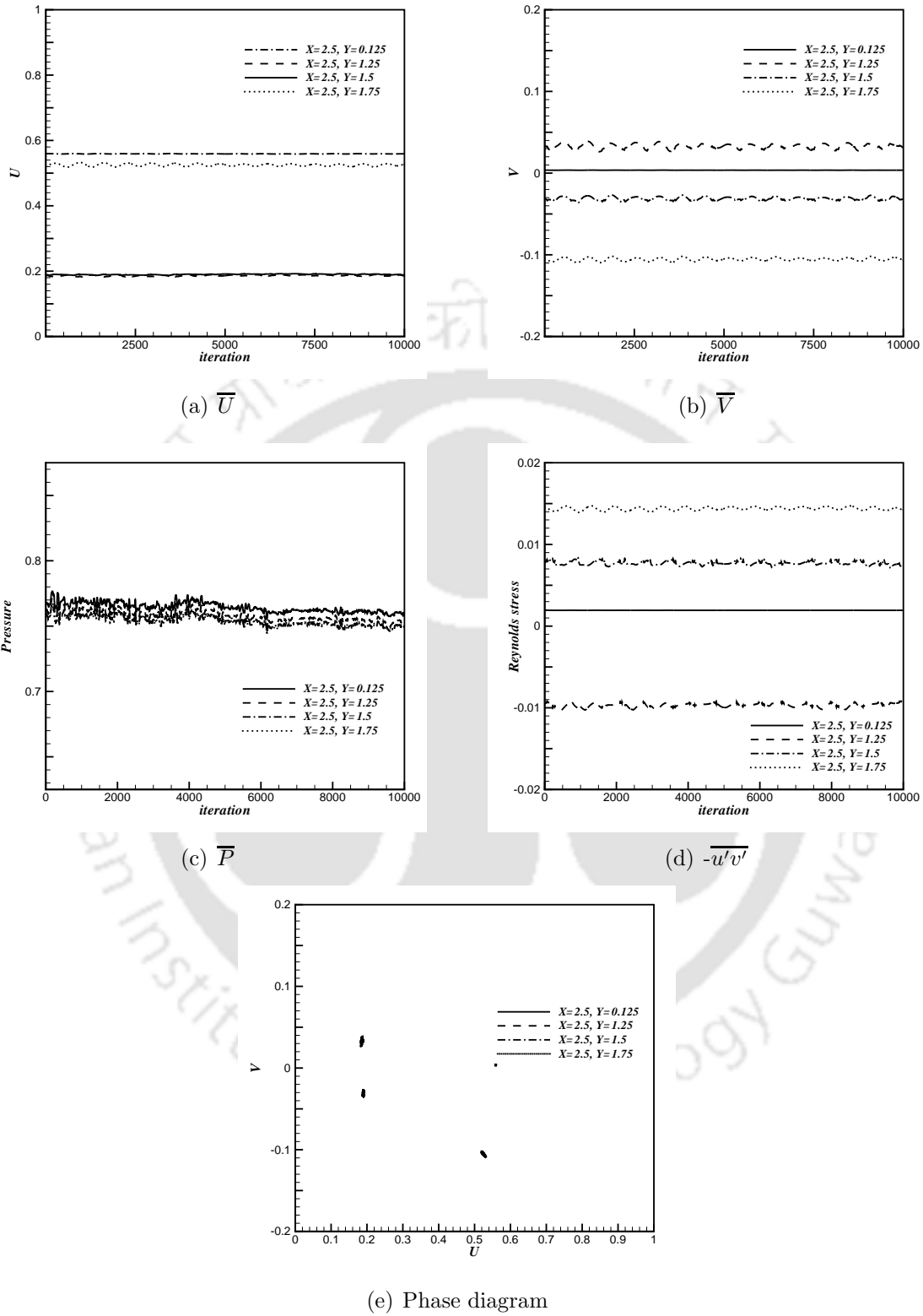


Figure 9.10: Variation of different properties for  $U_w = 0.75$ ,  $U_o = 1.0$  at  $X=2.5$ ,  $Y=0.125, 1.25$  and  $1.75$  locations during the iteration.

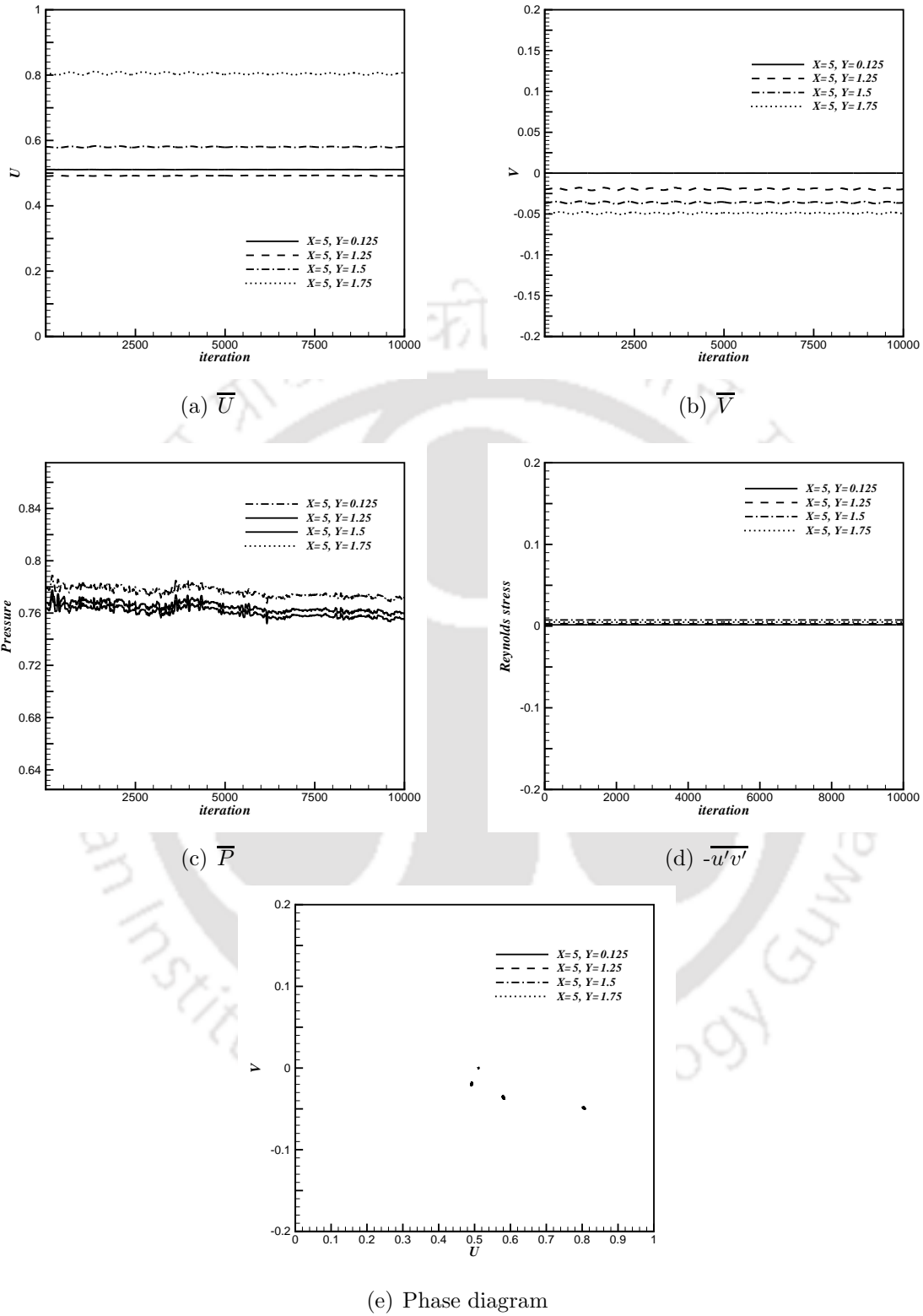


Figure 9.11: Variation of different properties for  $U_w = 0.75$ ,  $U_o = 1.0$  at  $X=5.0$ ,  $Y=0.125, 1.25$  and  $1.75$  locations during the iteration.

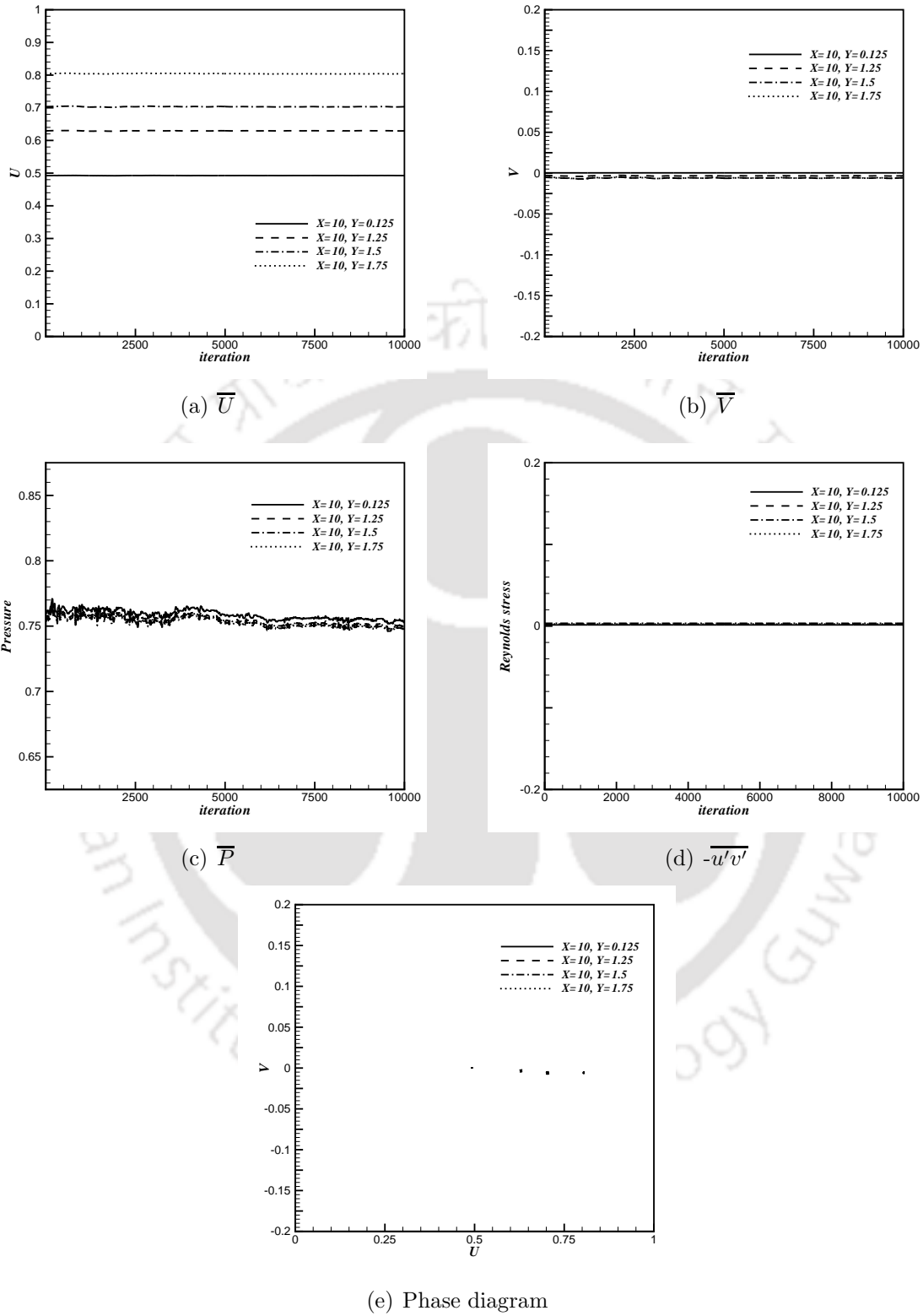


Figure 9.12: Variation of different properties for  $U_w = 0.75$ ,  $U_o = 1.0$  at  $X=10.0$ ,  $Y=0.125, 1.25$  and  $1.75$  locations during the iteration.

Table 9.1: Percentage variation for  $U_w = 1.0$  and  $U_o = 1.0$ 

		$\overline{ V }_{max}$	$\overline{ V }_{min}$	$\frac{(\overline{ V }_{max} - \overline{ V }_{min})}{\overline{ V }_{avg}}$	$\overline{P}_{max}$	$\overline{P}_{min}$	$\frac{\overline{P}_{max} - \overline{P}_{min}}{\overline{P}_{avg}}$	$-\overline{u'v'}_{max}$	$-\overline{u'v'}_{min}$	$\frac{-\overline{u'v'}_{max} + \overline{u'v'}_{min}}{\overline{u'v'}_{avg}}$
X=2.5	Y=0.125	0.8225	0.7863	4.5076	0.9437	0.9299	1.4675	0.00362255	0.0034062	6.1564
	Y=1.25	0.2964	0.2289	25.706	0.9355	0.9133	2.4075	-0.010336	-0.021891	-71.712
	Y=1.5	0.321	0.2302	32.922	0.9339	0.9161	1.9315	0.0165278	0.0063483	88.997
	Y=1.75	0.724	0.531	30.75	0.9466	0.9275	2.0304	0.0194335	0.0067121	97.313
X=5.0	Y=0.125	0.7732	0.7394	4.4801	0.9434	0.9372	0.6541	0.00320999	0.0029829	7.3339
	Y=1.25	0.6252	0.6023	3.7372	0.9281	0.913	1.6388	0.0166536	-0.009194	693.02
	Y=1.5	0.6831	0.625	8.8861	0.9251	0.9217	0.3678	0.00862896	0.0057547	39.965
	Y=1.75	0.8811	0.7606	14.69	0.9319	0.9278	0.4429	0.00634926	0.00219	97.414
X=10.0	Y=0.125	0.717	0.7041	1.8157	0.9199	0.9182	0.1886	0.00286085	0.0027772	2.9677
	Y=1.25	0.7506	0.7426	1.0818	0.917	0.9147	0.2546	0.00117507	6.73E-05	178.32
	Y=1.5	0.7616	0.7502	1.5078	0.9168	0.9156	0.1315	0.00208981	0.0014422	36.668
	Y=1.75	0.7752	0.7601	1.9641	0.9172	0.9148	0.2614	0.00100556	0.000251	120.09
X=15.0	Y=0.125	0.6673	0.6633	0.6095	0.9178	0.9171	0.0869	0.00256044	0.0025337	1.0514
	Y=1.25	0.7605	0.7584	0.2703	0.9176	0.9168	0.0891	-0.0011277	-0.00122	-7.8666
	Y=1.5	0.7485	0.7462	0.3098	0.9169	0.9161	0.0909	-0.0014645	-0.001553	-5.8698
	Y=1.75	0.6673	0.6633	0.6095	0.9178	0.9171	0.0869	0.00256044	0.0025337	1.0514
X=20.0	Y=0.125	0.6283	0.6263	0.3167	0.9179	0.9172	0.0824	0.00231635	0.0023048	0.4977
	Y=1.25	0.753	0.7518	0.1611	0.918	0.9172	0.0877	-0.0014488	-0.001463	-0.9999
	Y=1.5	0.7331	0.732	0.1558	0.9169	0.916	0.0898	-0.0020384	-0.00206	-1.0293
	Y=1.75	0.7035	0.7026	0.1259	0.9152	0.9143	0.0931	-0.0029582	-0.00299	-1.0729

Table 9.2: Percentage variation for  $U_w = 1.0$  and  $U_o = 0.25$ 

		$ \bar{V} _{max}$	$ \bar{V} _{min}$	$\frac{( \bar{V} _{max}- \bar{V} _{min})}{ \bar{V} _{avg}}$	$\bar{P}_{max}$	$\bar{P}_{min}$	$\frac{\bar{P}_{max}-\bar{P}_{min}}{\bar{P}_{avg}}$	$-\bar{u}'v'_{max}$	$-\bar{u}'v'_{min}$	$\frac{-\bar{u}'v'_{max}+\bar{u}'v'_{min}}{\bar{u}'v'_{avg}}$
X=2.5	Y=0.125	0.9156	0.9156	0.0024	0.5027	0.497	1.1343	0.00413382	0.0041337	0.0027
	Y=1.25	0.2534	0.2534	0.0087	0.4968	0.4912	1.146	-0.0055206	-0.005521	-0.0033
	Y=1.5	0.1638	0.1637	0.0116	0.5081	0.5024	1.1192	3.59E-05	3.59E-05	0.0977
	Y=1.75	0.174	0.174	0.0092	0.5071	0.5015	1.1194	0.00041748	0.0004174	0.0285
X=5.0	Y=0.125	0.864	0.8639	0.0049	0.4984	0.4928	1.1358	0.00389407	0.0038939	0.0046
	Y=1.25	0.4144	0.4144	0.0097	0.4903	0.4847	1.1528	-0.006236	-0.006236	-0.0027
	Y=1.5	0.2676	0.2676	0.0146	0.4975	0.4919	1.1347	-0.0027529	-0.002753	-0.0073
	Y=1.75	0.1751	0.1751	0.0217	0.5021	0.4965	1.1224	-0.000755	-0.000755	-0.0162

Table 9.3: Percentage variation for  $U_w = 1.0$  and  $U_o = 0.5$ 

		$\overline{ V }_{max}$	$\overline{ V }_{min}$	$\frac{(\overline{ V }_{max} - \overline{ V }_{min})}{\overline{ V }_{avg}}$	$\overline{P}_{max}$	$\overline{P}_{min}$	$\frac{\overline{P}_{max} - \overline{P}_{min}}{\overline{P}_{avg}}$	$-\overline{u'v'}_{max}$	$-\overline{u'v'}_{min}$	$\frac{-\overline{u'v'}_{max} + \overline{u'v'}_{min}}{\overline{u'v'}_{avg}}$
X=2.5	Y=0.125	0.8769	0.8769	0.0008	0.6002	0.6001	0.0253	0.00389473	0.0038947	0.001
	Y=1.25	0.2643	0.2643	0.0042	0.5973	0.5971	0.0253	-0.0068302	-0.006831	-0.0136
	Y=1.5	0.2574	0.2574	0.0054	0.6083	0.6082	0.025	0.00306188	0.0030609	0.0336
	Y=1.75	0.3754	0.3754	0.0051	0.6098	0.6097	0.0246	0.00040561	0.0004047	0.2211
X=5.0	Y=0.125	0.8348	0.8348	0.0008	0.5913	0.5912	0.025	0.00366566	0.0036656	0.0011
	Y=1.25	0.4781	0.4781	0.0015	0.5855	0.5854	0.0253	-0.0041409	-0.004141	-0.006
	Y=1.5	0.4221	0.4221	0.0014	0.5904	0.5902	0.0249	-0.0009355	-0.000936	-0.0294
	Y=1.75	0.413	0.413	0.0015	0.592	0.5918	0.0247	3.93E-06	3.89E-06	1.032

Table 9.4: Percentage variation for  $U_w = 1.0$  and  $U_o = 0.75$ 

		$\overline{ V }_{max}$	$\overline{ V }_{min}$	$\frac{(\overline{ V }_{max} - \overline{ V }_{min})}{\overline{ V }_{avg}}$	$\overline{P}_{max}$	$\overline{P}_{min}$	$\frac{\overline{P}_{max} - \overline{P}_{min}}{\overline{P}_{avg}}$	$-\overline{u'v'}_{max}$	$-\overline{u'v'}_{min}$	$\frac{-\overline{u'v'}_{max} + \overline{u'v'}_{min}}{\overline{u'v'}_{avg}}$
X=2.5	Y=0.125	0.8398	0.8388	0.1146	0.6444	0.6286	2.4848	0.00368413	0.0036779	0.1703
	Y=1.25	0.2448	0.2405	1.761	0.6371	0.6212	2.5289	-0.0105632	-0.011074	-4.7224
	Y=1.5	0.2704	0.2677	1.004	0.6468	0.631	2.4793	0.00806345	0.0077653	3.7668
	Y=1.75	0.5575	0.5551	0.444	0.6593	0.6436	2.4039	0.00183612	0.0017236	6.3247
X=5.0	Y=0.125	0.7982	0.7972	0.1252	0.6396	0.6248	2.3511	0.00339146	0.0033846	0.2016
	Y=1.25	0.5488	0.5473	0.274	0.6298	0.615	2.3871	-0.0024214	-0.002509	-3.5507
	Y=1.5	0.5489	0.5478	0.2053	0.6312	0.6163	2.3794	0.00303077	0.0029571	2.4617
	Y=1.75	0.6486	0.6458	0.4288	0.6374	0.6226	2.3486	0.00084002	0.0007621	9.7317
X=10.0	Y=0.125	0.7361	0.735	0.1592	0.6249	0.6116	2.1465	0.00299741	0.0029903	0.2368
	Y=1.25	0.6471	0.6456	0.2329	0.6244	0.6112	2.1374	-0.0018359	-0.001861	-1.3541
	Y=1.5	0.6245	0.6228	0.2612	0.6252	0.6121	2.1236	-0.0011626	-0.001193	-2.5945
	Y=1.75	0.6078	0.6063	0.2614	0.6254	0.6124	2.1062	-0.0012743	-0.001316	-3.2038
X=15.0	Y=0.125	0.6808	0.6793	0.2246	0.6252	0.6123	2.0906	0.00265503	0.0026458	0.3479
	Y=1.25	0.6681	0.6666	0.2305	0.6253	0.6125	2.0751	-0.0018539	-0.001869	-0.8112
	Y=1.5	0.6292	0.6276	0.2513	0.6252	0.6125	2.0555	-0.0017802	-0.001802	-1.2382
	Y=1.75	0.5895	0.5881	0.2244	0.6243	0.6117	2.0294	-0.0022176	-0.00226	-1.8917
X=20.0	Y=0.125	0.6424	0.6408	0.2544	0.6249	0.6129	1.9408	0.00241123	0.002402	0.3852
	Y=1.25	0.6746	0.6734	0.1712	0.6244	0.6124	1.9366	-0.0020996	-0.002119	-0.907
	Y=1.5	0.6248	0.6236	0.1884	0.6236	0.6117	1.9305	-0.0024227	-0.002453	-1.2262
	Y=1.75	0.5725	0.5715	0.1729	0.6223	0.6105	1.9224	-0.0030285	-0.003066	-1.2339

Table 9.5: Percentage variation for  $U_w = 0.25$  and  $U_o = 1.0$ 

		$ \bar{V} _{max}$	$ \bar{V} _{min}$	$\frac{( V _{max}- V _{min})}{ V _{avg}}$	$\bar{P}_{max}$	$\bar{P}_{min}$	$\frac{\bar{P}_{max}-\bar{P}_{min}}{\bar{P}_{avg}}$	$-\bar{u}'v'_{max}$	$-\bar{u}'v'_{min}$	$\frac{-\bar{u}'v'_{max}+\bar{u}'v'_{min}}{\bar{u}'v'_{avg}}$
X=2.5	Y=0.125	0.091	0.091	0.0014	0.4108	0.4108	0.0066	0.00012071	0.0001207	0.0017
	Y=1.25	0.0856	0.0856	0.0029	0.4111	0.411	0.0061	-0.0004395	-0.00044	-0.0118
	Y=1.5	0.1335	0.1335	0.0015	0.4048	0.4048	0.0057	0.00242231	0.0024222	0.0037
	Y=1.75	0.3563	0.3563	0.0014	0.3889	0.3889	0.0057	0.0102284	0.0102283	0.001
X=5.0	Y=0.125	0.0255	0.0255	0.0098	0.415	0.4149	0.007	2.25E-05	2.25E-05	0.0089
	Y=1.25	0.2877	0.2877	0.001	0.4024	0.4023	0.0065	0.00499931	0.0049992	0.0028
	Y=1.5	0.4736	0.4736	0.0008	0.397	0.3969	0.0063	0.00799362	0.0079934	0.0022
	Y=1.75	0.7169	0.7169	0.001	0.3998	0.3998	0.0058	0.00792069	0.0079205	0.0021

Table 9.6: Percentage variation for  $U_w = 0.5$  and  $U_o = 1.0$ 

		$\overline{ V }_{max}$	$\overline{ V }_{min}$	$\frac{(\overline{ V }_{max} - \overline{ V }_{min})}{\overline{ V }_{avg}}$	$\overline{P}_{max}$	$\overline{P}_{min}$	$\frac{\overline{P}_{max} - \overline{P}_{min}}{\overline{P}_{avg}}$	$-\overline{u'v'}_{max}$	$-\overline{u'v'}_{min}$	$\frac{-\overline{u'v'}_{max} + \overline{u'v'}_{min}}{\overline{u'v'}_{avg}}$
X=2.5	Y=0.125	0.3148	0.3146	0.0521	0.6551	0.6286	4.1147	0.00077378	0.0007734	0.0507
	Y=1.25	0.1659	0.1657	0.1249	0.6568	0.6305	4.0914	-0.0049262	-0.004931	-0.1033
	Y=1.5	0.1542	0.154	0.111	0.6489	0.6227	4.1193	0.00414801	0.0041381	0.2387
	Y=1.75	0.4136	0.4134	0.0409	0.6347	0.6088	4.1781	0.0149295	0.0149272	0.0154
X=5.0	Y=0.125	0.2658	0.2656	0.1027	0.6644	0.642	3.4233	0.00053027	0.0005297	0.1021
	Y=1.25	0.3716	0.3713	0.0735	0.6558	0.6335	3.4594	0.00367333	0.0036721	0.0348
	Y=1.5	0.5082	0.5079	0.0549	0.6482	0.626	3.4862	0.00753041	0.007529	0.0187
	Y=1.75	0.7312	0.7309	0.0404	0.6484	0.6263	3.4639	0.00752674	0.007525	0.023

Table 9.7: Percentage variation for  $U_w = 0.75$  and  $U_o = 1.0$ 

		$\overline{ V }_{max}$	$\overline{ V }_{min}$	$\frac{(\overline{ V }_{max} - \overline{ V }_{min})}{\overline{ V }_{avg}}$	$\overline{P}_{max}$	$\overline{P}_{min}$	$\frac{\overline{P}_{max} - \overline{P}_{min}}{\overline{P}_{avg}}$	$-\overline{u'v'}_{max}$	$-\overline{u'v'}_{min}$	$\frac{-\overline{u'v'}_{max} + \overline{u'v'}_{min}}{\overline{u'v'}_{avg}}$
X=2.5	Y=0.125	0.56	0.5584	0.2804	0.7766	0.755	2.8184	0.0019417	0.0019332	0.4361
	Y=1.25	0.1931	0.1844	4.584	0.7709	0.7481	3.0094	-0.0091698	-0.010272	-11.343
	Y=1.5	0.1955	0.1896	3.0654	0.7674	0.7441	3.0761	0.00836066	0.0070733	16.682
	Y=1.75	0.5442	0.5284	2.943	0.7666	0.7441	2.9761	0.0147323	0.0139161	5.698
X=5.0	Y=0.125	0.5112	0.5104	0.1429	0.7887	0.7675	2.7229	0.00159681	0.001593	0.2383
	Y=1.25	0.4936	0.4912	0.5041	0.7775	0.7564	2.7449	0.00304249	0.0027652	9.5509
	Y=1.5	0.5843	0.579	0.9186	0.7729	0.7519	2.7542	0.00758269	0.0074477	1.7962
	Y=1.75	0.8128	0.8017	1.3789	0.7768	0.7558	2.7412	0.0050856	0.00471	7.6681
X=10.0	Y=0.125	0.4929	0.492	0.1848	0.7709	0.7519	2.4918	0.00150889	0.0015049	0.2661
	Y=1.25	0.6304	0.6282	0.3591	0.7668	0.748	2.4916	0.00241237	0.0023437	2.8872
	Y=1.5	0.7051	0.7014	0.5267	0.7649	0.7461	2.4812	0.00349202	0.0034328	1.711
	Y=1.75	0.806	0.8034	0.3265	0.7659	0.7473	2.4541	0.00261626	0.002568	1.8633
X=15.0	Y=0.125	0.469	0.4675	0.3293	0.7664	0.7495	2.2233	0.00141273	0.0014051	0.5394
	Y=1.25	0.6672	0.6644	0.4193	0.7642	0.7474	2.2184	0.00197053	0.0019258	2.2986
	Y=1.5	0.7081	0.7063	0.2558	0.763	0.7463	2.2139	0.00206811	0.0020446	1.1448
	Y=1.75	0.7161	0.7146	0.2207	0.7622	0.7456	2.204	-0.00017	-0.000208	-20.249
X=20.0	Y=0.125	0.4489	0.447	0.4335	0.7659	0.7486	2.2848	0.00131858	0.0013096	0.6834
	Y=1.25	0.6615	0.66	0.2272	0.7639	0.7468	2.2658	0.00107586	0.0010502	2.411
	Y=1.5	0.6649	0.6636	0.1974	0.763	0.7461	2.2431	-2.05E-05	-5.07E-05	-84.762
	Y=1.75	0.6603	0.6591	0.1849	0.7619	0.7453	2.2111	-0.0014404	-0.001471	-2.1361

## 9.3 Conclusions

Steady-state computations are performed with  $Re=20000$  for the seven combinations of  $U_w$  and  $U_o$ . Study is carried out for case (a) keeping the  $U_w=1.0$  by varying  $U_o=0.25, 0.5$  and  $0.75$  and case (b) exchanging the wall jet velocity to offset jet velocity. Under these conditions, different variables are observed at different locations in the domain to distinguish whether the flow is steady or periodic and the behavior is analyzed. The following conclusions may be drawn.

- When both  $U_w = U_o=1.0$ , the steady state solutions are obtained at  $X \cong 15$ . Strong periodic nature of the flow is observed to be damped in the downstream direction and finally the steady-state is obtained.
- If  $U_w=1.0$ ,  $U_o= 0.25$  and  $0.5$ , the flow demonstrates the steady-state nature.
- Though the oscillations in pressure are observed at  $U_w=1.0$  and  $U_o=0.75$ , the effect of it on the other variables are negligible and the flow is in steady-state.
- Flow is in steady-state when the  $U_w=0.25$  and  $U_o=1.0$ .
- Except the oscillations in pressure, the flow is steady for the remaining variable when  $U_w=0.5$  and  $U_o=1.0$ . Phase diagrams also suggest the same.
- For  $U_w=0.75$  and  $U_o=1.0$ , fluctuations in all the variables are observed at  $X=2.5$ . Reynolds stress attains a steady-state at  $X=5.0$ . At  $X=10$ , except the pressure all the variables are in steady-state.

# Chapter 10

## Study of the Heat Transfer Characteristics in a Turbulent Combined Wall and Offset Jet Flows

### 10.1 Introduction

The objective of the present study is a detailed numerical simulation of the heat transfer characteristics of a dual-jet flow for a range of wall jet and offset jet velocities. The offset height has been kept constant at 1. The turbulence modelling has been conducted by the standard high  $Re$   $k - \epsilon$  model with streamline curvature modification. The study is conducted for constant temperature and constant heat flux at the wall. The Reynolds number is varied between 10000 and 40000.  $Pr=0.71$  is taken for all computations. The detailed analysis of the local Nusselt number ( $Nu_x$ ) distribution, local heat flux ( $q_x$ ), surface temperature ( $\theta_w$ ), average Nusselt number ( $\overline{Nu}$ ), total heat transfer ( $Q$ ) are studied both in qualitatively and quantitatively. The schematic diagram of the geometry and its boundary con-

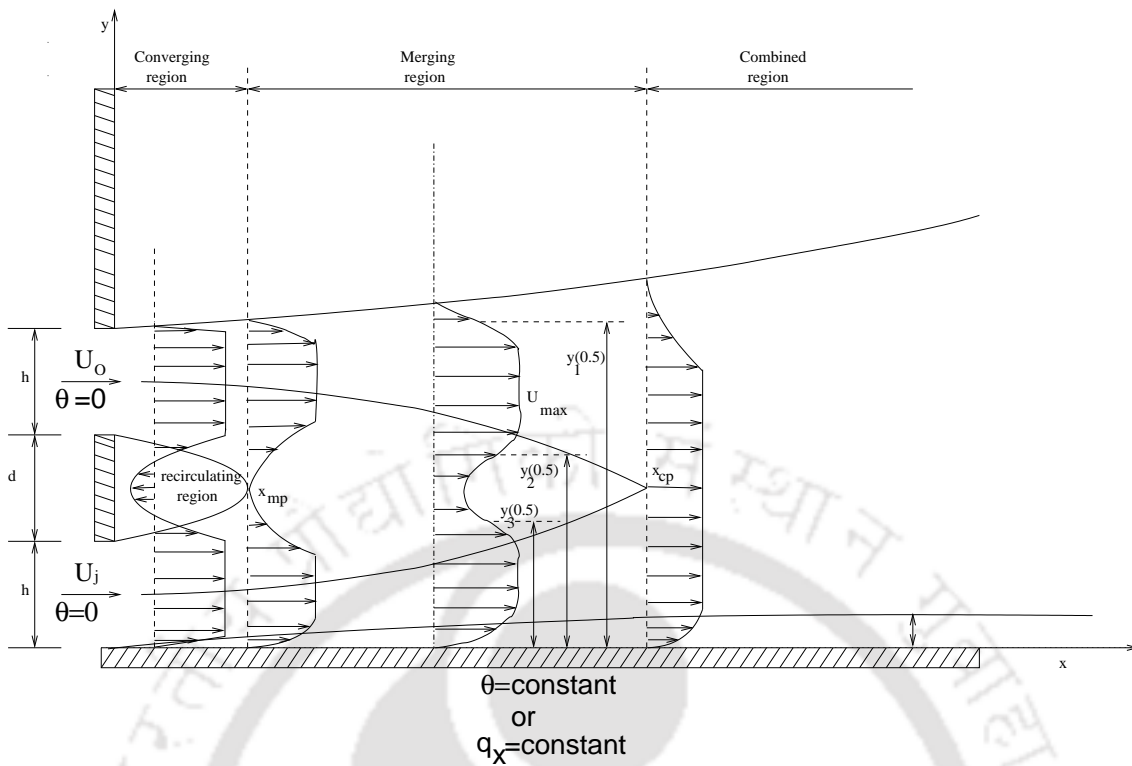


Figure 10.1: Schematic diagram of the combined jet flow

ditions are shown in Fig. 10.1. The numerical scheme and method of solution as explained in chapter 2.6 is used in the present computations. The boundary conditions for the hydro-dynamic solution, code validation and grid independence study are described in chapter 8. For temperature, the conditions are same as explained in chapters of wall jet and offset jet heat transfer analysis.

## 10.2 Results and Discussion

The present study can be briefly classified into two cases. Those are (1) keeping the wall jet velocity ( $U_w = 1.0$ ) constant, offset jet velocity ( $U_o$ ) is varied for 0.25, 0.5 and 0.75. (2) keeping offset jet velocity ( $U_o = 1.0$ ) constant, wall jet velocity is varied for 0.25, 0.5, 0.75 and 1.0. Reynolds number is varied from  $1 \times 10^4$  to  $4 \times 10^4$  for a constant Prandtl number ( $Pr=0.71$ ). The increase in the Reynolds number can be inferred as increasing the jet velocities while maintaining the same

velocity ratio. Two cases of the solid wall boundary conditions are considered: viz. constant wall temperature and constant wall heat flux. Under these conditions, the heat transfer study is carried out for local Nusselt number ( $Nu_x$ ) distribution, local heat flux ( $q_x$ ) and surface temperature distribution ( $\theta_w$ ) along the wall.

### Local Nusselt number

The  $Nu_x$  distribution along the wall for different wall and offset jet velocities, keeping the  $Re = 2 \times 10^4$  is shown in Fig. 10.2. Figure 10.2(a) demonstrates the case for  $U_w=1.0$  and varying the  $U_o$ . For  $U_o = 1.0$ , the fluctuations in the  $Nu_x$  near the inlet can be viewed as vortex shedding as observed in Wang and Tan [5] along the wall up to  $X \cong 15$ . Beyond this region the flow is observed to be steady. Near the inlet local Nusselt number ( $Nu_x$ ) is almost same for all  $U_o$  except for  $U_o=1.0$  up to  $X \cong 20$ . Hence, it can be inferred that  $U_o$  has very little influence on the local Nusselt number up to  $X \cong 20$ . It can be observed from Fig. 10.2(a) that, for  $U_o=0.25$ , the  $Nu_x$  is maximum at the inlet and decreases up some point say,  $P_1(X \cong 20)$  in the downstream. Further downstream, there is an increase in  $Nu_x$  up to point say,  $P_2(X \cong 30)$  and beyond which it decreases continuously. Similar trends are observed for other values  $U_o$  (Fig. 10.2(a)). However, as the value of  $U_o$  increases, the corresponding points  $P_1$  and  $P_2$  shifts towards downstream and the distance between them also widens. The increase in  $Nu_x$  between points  $P_1$  and  $P_2$  (for all values of  $U_o$ ) can be due to the influence of mixing of two streams and development of self-similarity. In far downstream ( $X \geq 60$ )  $Nu_x$  is larger as the offset jet velocity increases.

The variation of  $Nu_x$  with  $U_w$  at constant  $U_o$  (1.0) is shown in Fig. 10.2(b). At the inlet  $Nu_x$  increases with  $U_w$ , which suggests that the wall jet velocity has considerable influence as compared to offset jet velocity. For values of  $U_w > 0.5$ , the maximum  $Nu_x$  occurs near the inlet and for values of  $U_w < 0.5$ , the maxi-

imum  $Nu_x$  occurs at some point in the downstream. It is found that for  $U_w=0.25$ ,  $Nu_x$  decreases to very low compared to other  $U_w$  and then rapidly increases to maximum value. Similar trend can be observed for  $U_w=0.5$ , but increases slowly compared to  $U_w=0.25$ . For values of  $U_w=0.75$  and 1.0 at constant  $U_o$  the trends are similar to the constant  $U_w$  as seen in Fig. 10.2(a). In the far downstream ( $X \geq 60$ ),  $Nu_x$  increases as the wall jet velocity increases. Figures 10.2(c), 10.2(d) and 10.2(e) show the  $Nu_x$  distribution along the wall for different  $U_w$  and  $U_o$  by interchanging them. It is observed that almost in the entire flow domain,  $Nu_x$  is more when the  $U_w > U_o$ . Near the inlet, the difference in  $Nu_x$  is found more, but this difference in  $Nu_x$  decreases as the distance from the inlet increases finally becomes equal which states that it depends on the total mass flow rate.

The comparison of  $Nu_x$  distribution at the wall for different  $U_w$  and  $U_o$  under constant heat flux and constant temperature conditions applied at the wall is shown in Fig. 10.3. As it demonstrates, though the  $Nu_x$  is slightly more under constant heat flux condition, the behavior is almost the same.

Figure 10.4 shows the variation of  $Nu_x$  with Reynolds number along the wall when the wall temperature is constant. It clearly demonstrates that at all locations in the flow domain, as  $Re$  is increased  $Nu_x$  is increased, but no change in the behavior is observed. As Fig. 10.3 suggests, a similar phenomenon is found in case of constant wall heat flux case also.

### Wall temperature distribution

The variation in wall temperature ( $\theta_w$ ), which occurs in the case of constant heat flux condition is shown in Fig. 10.5. Figure 10.5(a) shows the variation of  $\theta_w$  with  $U_o$  at constant  $U_w = 1.0$ . The wall temperature ( $\theta_w$ ) is same and increases for all values of  $U_o$  except  $U_o=1.0$  up to a distance of  $X \cong 20$ . Further downstream (the

region in which the local Nusselt number increases as shown in Fig. 10.2(a) between the points  $P_1$  and  $P_2$ ), the wall temperature decreases due to increase in heat transfer up to point  $P_2$  beyond which temperature increases. In the far downstream ( $X \geq 60$ ) at any location  $\theta_w$  is more when  $U_o$  is less. The  $\theta_w$  distribution with  $U_w$  at constant  $U_o = 1.0$  is shown in Fig. 10.5(b). A sharp rise in wall temperature in the case of  $U_w=0.25$  near inlet can be observed which is obvious due to steep reduction in Local Nusselt number as seen in Fig. 10.2(b). In the far downstream region at any location,  $\theta_w$  decreases as the  $U_w$  increases. Figures 10.5(c), 10.5(d) and 10.5(e) show the variation of  $\theta_w$  when the  $U_w$  and  $U_o$  are interchanged. As it demonstrates, the surface temperature is found more when the  $U_w < U_o$ . It can be concluded from above observations that the Local Nusselt number and wall temperature are complementary to each other. It is observed that as  $Re$  is increased  $\theta_w$  increases, but no change in its behavior is found Fig. 10.6. The difference in  $\theta_w$  between any two consecutive  $Re$  reduces as  $Re$  increases. In order to give  $\bar{\theta}$  behavior in the domain is given for  $U_w=1.0$  and  $U_o=0.5$  and interchanging them. Fig. 10.7 shows the  $\bar{\theta}$  distribution in the domain. It is observed that non-dimensional distribution is almost similar in all the cases.

### Average Nusselt number and total heat transfer

In order to quantify the results, the average Nusselt number ( $\overline{Nu}$ ) and total heat transfer ( $Q$ ) are tabulated in Tables 10.1 to 10.6 for constant temperature ( $\theta_w=C$ ) and constant flux ( $q_x=C$ ) conditions. Table 10.1 shows the variation of  $\overline{Nu}$  and  $Q$  with  $U_o$  at constant  $U_w=1.0$ . The value within the parenthesis shows the percentage change of  $\overline{Nu}$  and  $Q$  with  $U_o=1.0$  is as reference value. It is noticed that  $\overline{Nu}$  decreases with increase in  $U_o$  at all values of  $Re$ . Though the  $\overline{Nu}$  increases as  $Re$  increases, the percentage change with the reference value ( $U_o=1.0$ ) is fairly constant. At any  $Re$ ,  $\overline{Nu}$  is more for the constant heat flux condition compared to the constant wall temperature condition, however the trends are observed to be same. It is found that the total heat transfer ( $Q$ ) decreases with  $U_o$  and  $Re$ . It is

observed that there is a decrease in heat flux though  $Nu_x$  increases with  $Re$ , which is due to increase in reference heat flux ( $\rho c_p U_o \Delta T$ ). Table 10.2 shows the variation of  $\overline{Nu}$  and  $Q$  with  $U_w$  at constant  $U_o=1.0$ . The value within the parenthesis shows the percentage change with the reference value of  $U_w=1.0$ . It is observed that  $\overline{Nu}$  is maximum at  $U_w=1.0$  and minimum at  $U_w=0.5$ . A decrease of 15 percent in  $\overline{Nu}$  is observed for  $U_w=0.5$ . For any Reynolds number,  $\overline{Nu}$  is more in case of constant heat flux compared to the constant wall temperature condition. It is noticed that the total heat transfer decreases with  $Re$ . The variation of  $\overline{Nu}$  and  $Q$  at all wall jet and offset jet velocities with  $Re$  is shown in Table 10.3. In this case  $Re = 10^4$  is taken as the reference to evaluate the percentage change which is given in the parenthesis. It is observed that for any  $U_w$  and  $U_o$ ,  $\overline{Nu}$  increases almost linearly with  $Re$ . An increase in  $\overline{Nu}$  by nearly 230% is observed as  $Re$  is increased to  $4 \times 10^4$ . However, the non-dimensional  $Q$  is observed to decrease by 17 percent. Tables 10.4, 10.5 and 10.6 show the  $\overline{Nu}$  and  $Q$  when the  $U_w$  and  $U_o$  are interchanged. In order to calculate the percentage change, the value of  $U_w=1.0$  condition is considered as reference value. It is observed that both  $\overline{Nu}$  and  $Q$  are more for  $U_w=1.0$  compared to the case in which  $U_o=1.0$ . The maximum percentage change is found to the case of  $U_w = 1.0, U_o = 0.5$ .

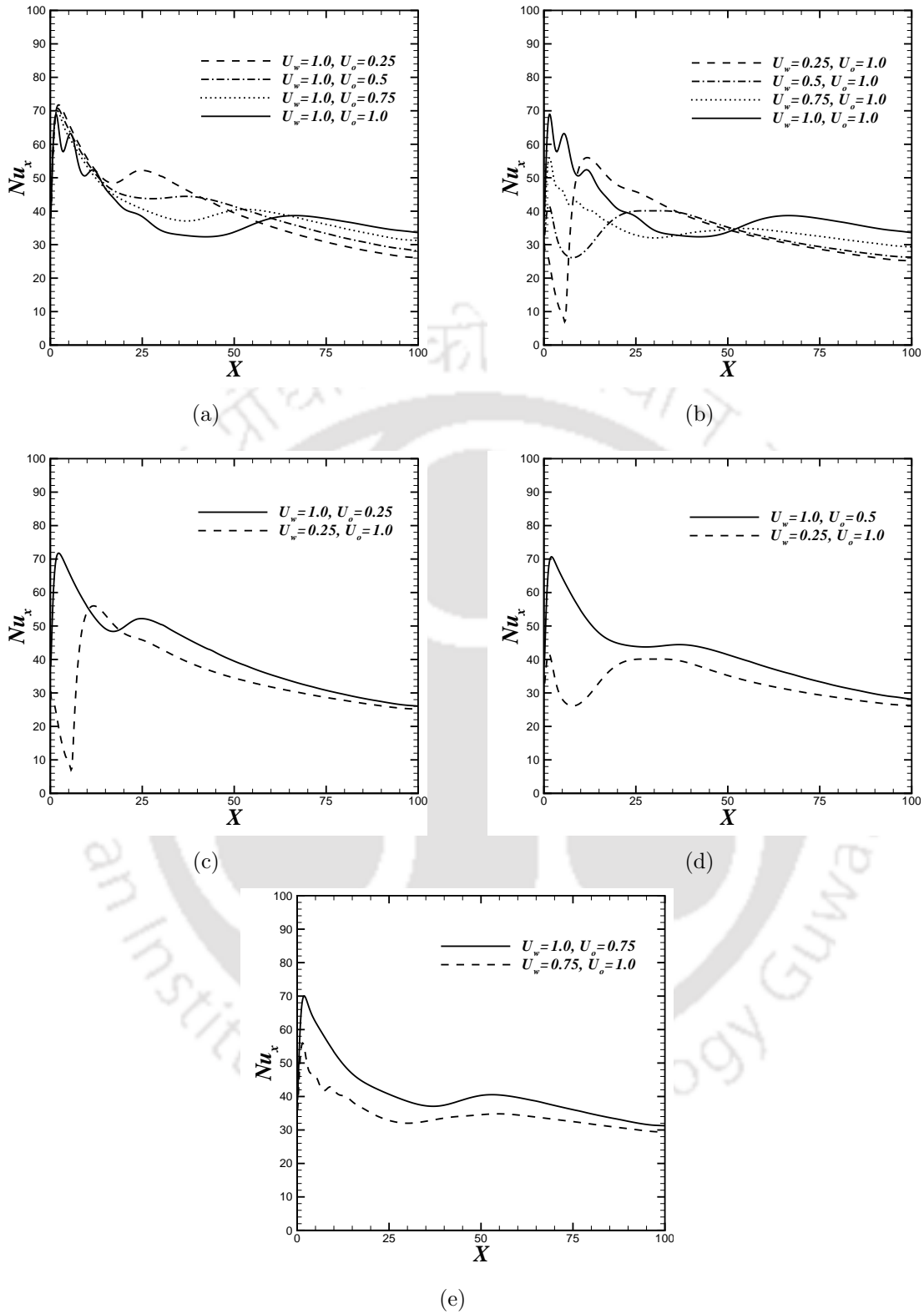
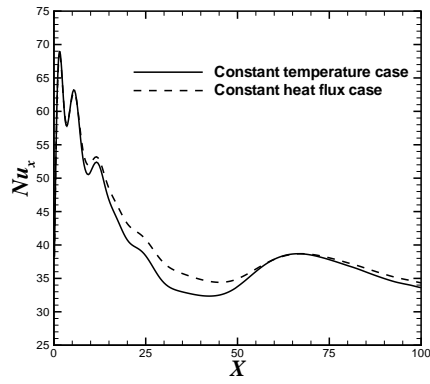
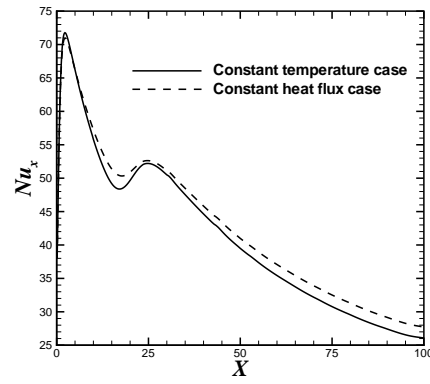


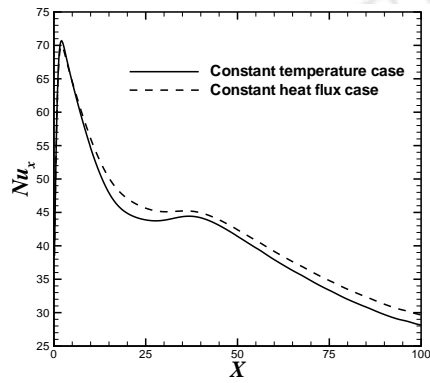
Figure 10.2: Variation of Local Nusselt number ( $Nu_x$ ) along the wall for different wall jet and offset velocities keeping the  $Re=20000$  under constant wall temperature.



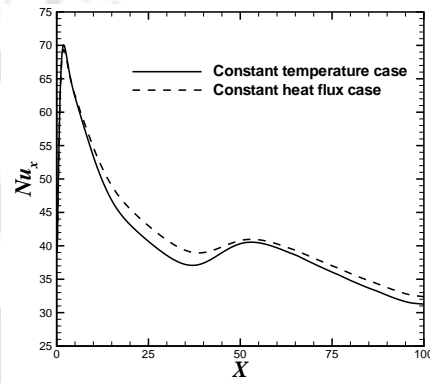
(a)  $U_w=1.0, U_o=1.0$



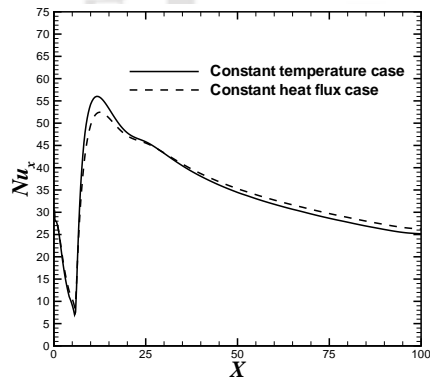
(b)  $U_w=1.0, U_o=0.25$



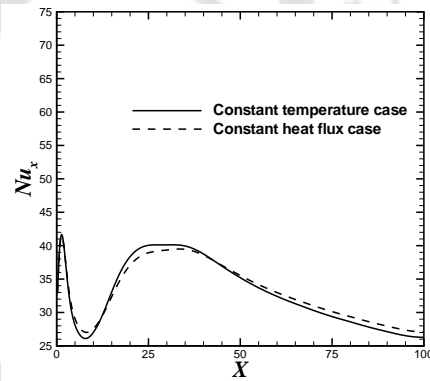
(c)  $U_w=1.0, U_o=0.5$



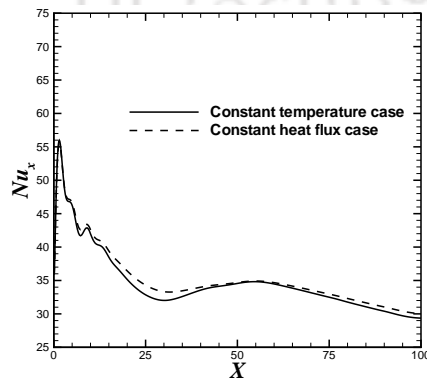
(d)  $U_w=1.0, U_o=0.75$



(e)  $U_w=0.25, U_o=1.0$



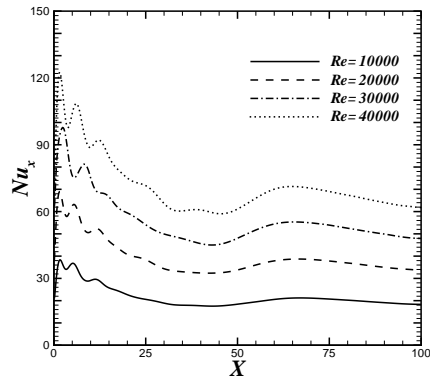
(f)  $U_w=0.5, U_o=1.0$



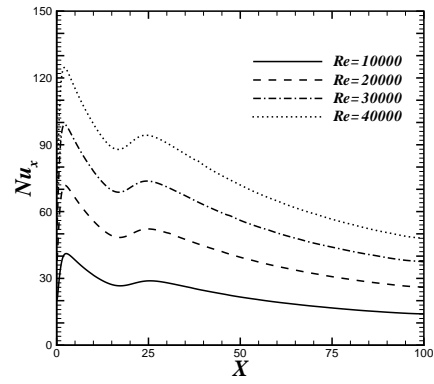
(g)  $U_w=0.75, U_o=1.0$

TH-608\_04610302

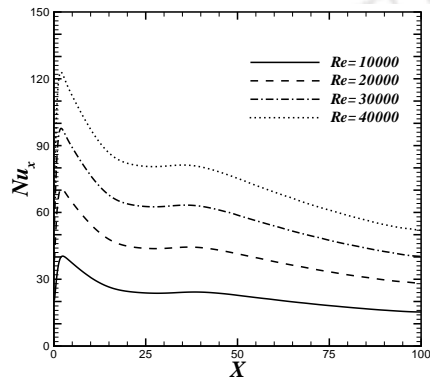
Figure 10.3: Comparison of  $Nu_x$  along the wall for different wall jet and offset jet velocities for constant wall temperature and constant heat flux cases.



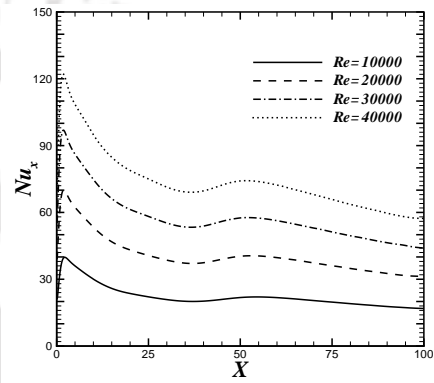
(a)  $U_w=1.0, U_o=1.0$



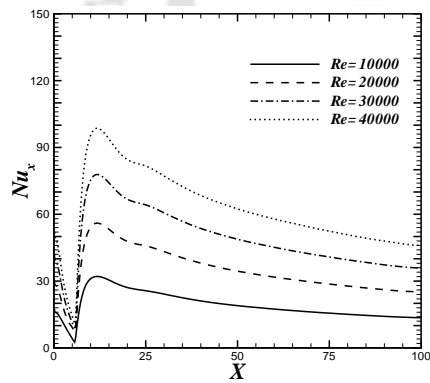
(b)  $U_w=1.0, U_o=0.25$



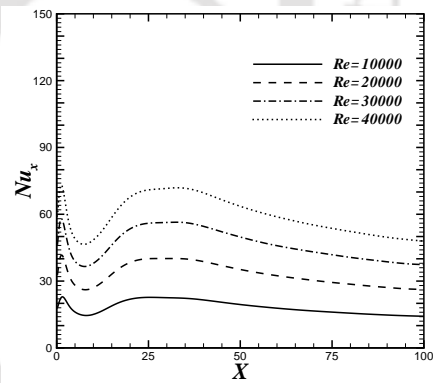
(c)  $U_w=1.0, U_o=0.5$



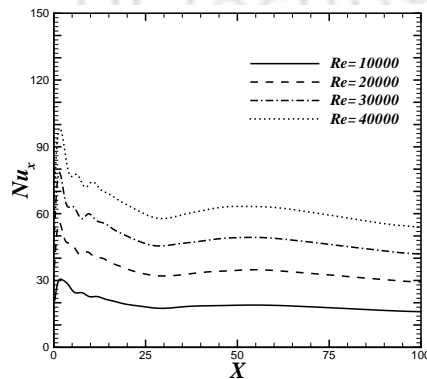
(d)  $U_w=1.0, U_o=0.75$



(e)  $U_w=0.25, U_o=1.0$



(f)  $U_w=0.5, U_o=1.0$



(g)  $U_w=0.75, U_o=1.0$

TH-608\_04610302

Figure 10.4: Local Nusselt number ( $Nu_x$ ) distribution along the wall for different Reynolds numbers for different wall jet and offset jet velocities under constant temperature case.

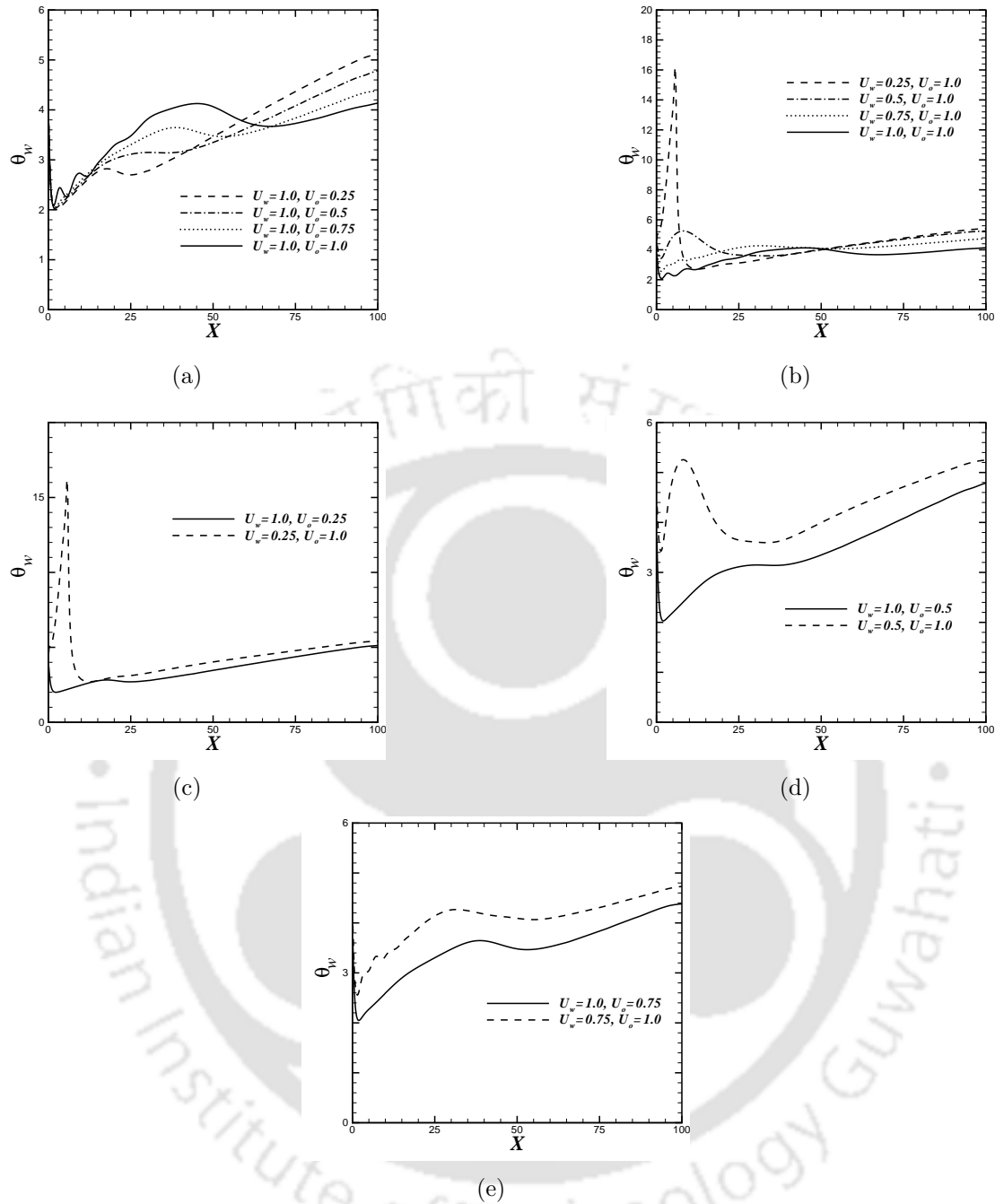
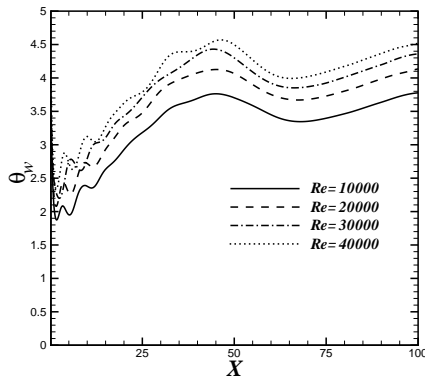
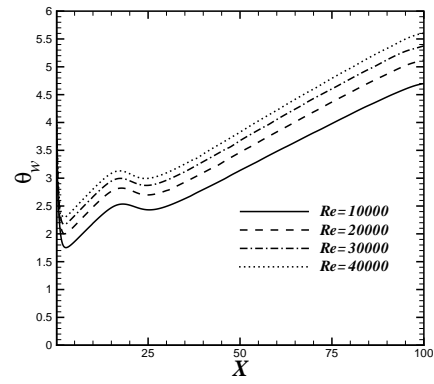


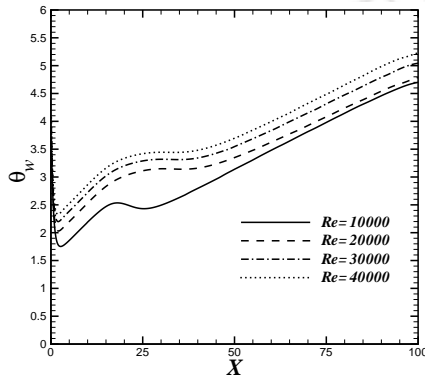
Figure 10.5: Variation of temperature ( $\theta$ ) along the wall for different wall jet and offset velocities keeping  $Re=20000$  under constant wall heat flux.



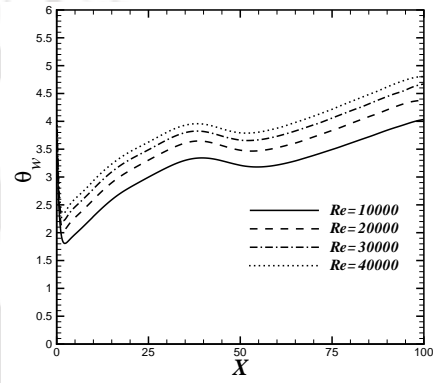
(a)  $U_w=1.0, U_o=1.0$



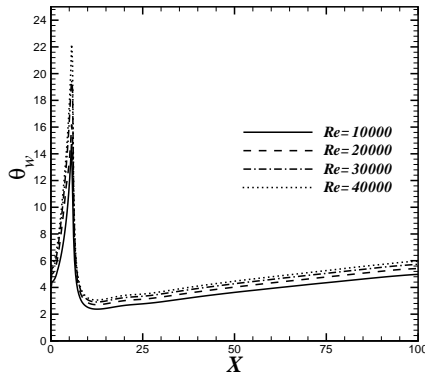
(b)  $U_w=1.0, U_o=0.25$



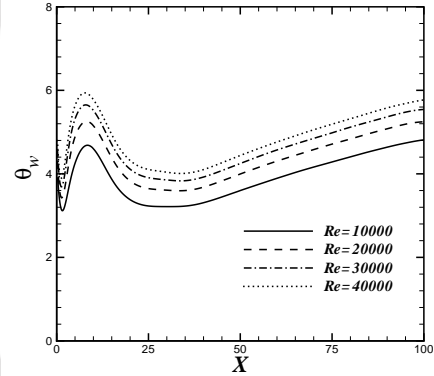
(c)  $U_w=1.0, U_o=0.5$



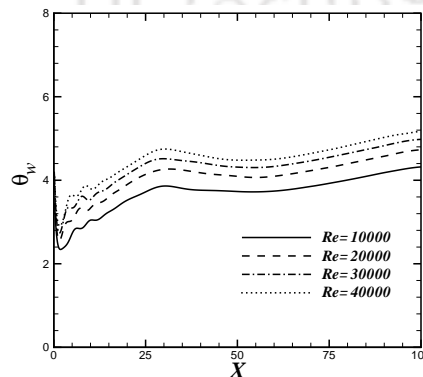
(d)  $U_w=1.0, U_o=0.75$



(e)  $U_w=0.25, U_o=1.0$



(f)  $U_w=0.5, U_o=1.0$



(g)  $U_w=0.75, U_o=1.0$

TH-608\_04610302

Figure 10.6: Temperature ( $\theta$ ) distribution along the wall for different Reynolds numbers for different wall jet and offset jet velocities under constant wall heat flux.

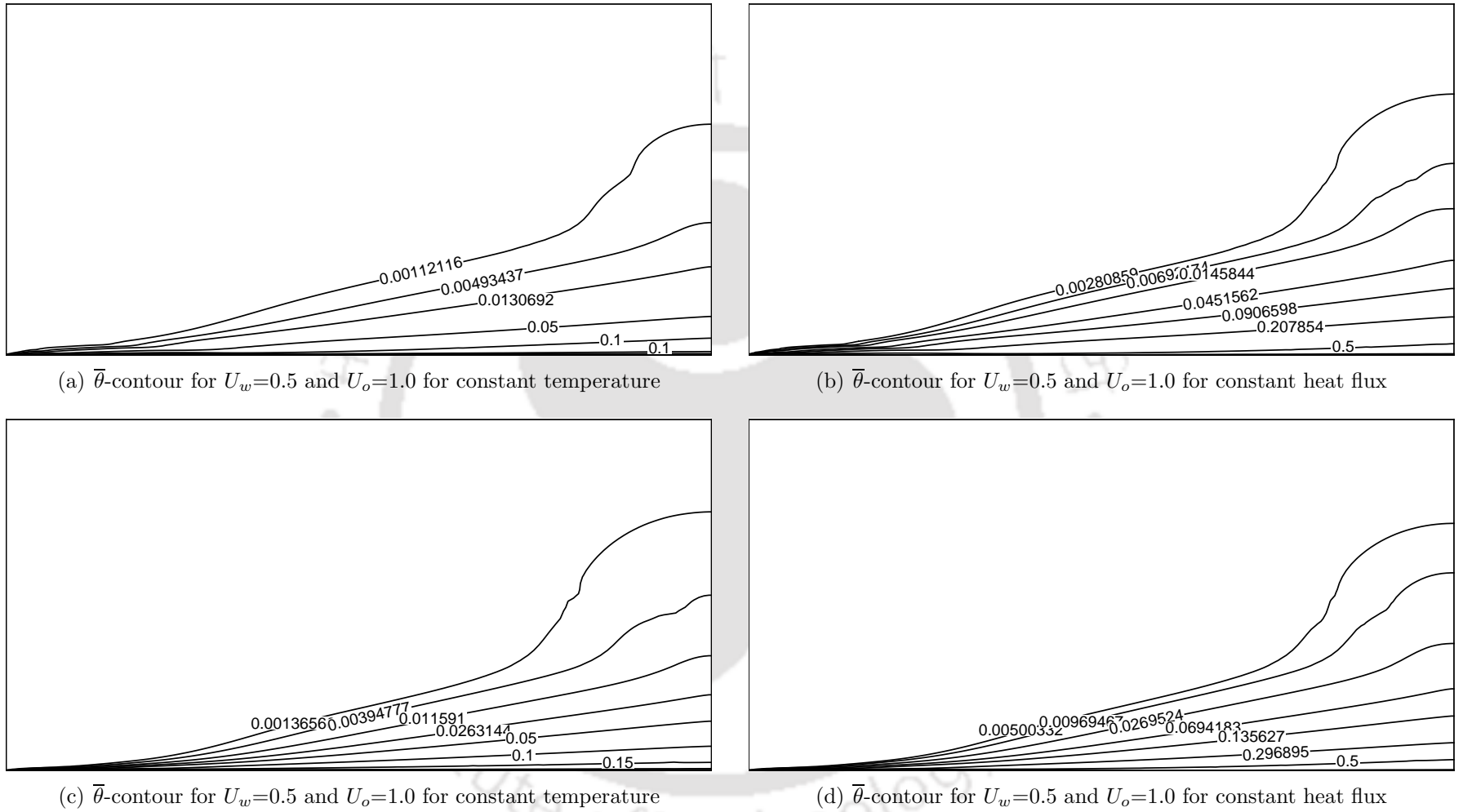


Figure 10.7:  $\bar{\theta}$  contours of combined jet flow

Table 10.1: Average Nusselt number ( $\overline{Nu}$ ) and total heat transfer ( $Q$ ) at different  $Re$ , keeping the  $U_w=1.0$  and varying  $U_o$ .

	B.C	$Re$	$U_o = 0.25$	$U_o = 0.5$	$U_o = 0.75$	$U_o = 1.0$
$\overline{Nu}$	$\theta_w = C$	$10^4$	30.3388(5.367)	30.1936(4.863)	29.7268(3.241)	28.7934
		$2 \times 10^4$	55.0086(5.128)	54.9122(4.944)	54.2049(3.592)	52.3252
		$3 \times 10^4$	77.8658(4.606)	77.8354(4.564)	76.9002(3.308)	74.4378
		$4 \times 10^4$	99.5772(4.564)	99.6774(4.984)	98.6782(3.62)	95.2309
	$q_w = C$	$10^4$	31.5061(5.876)	31.5061(5.876)	30.7894(3.468)	29.7574
		$2 \times 10^4$	56.7962(5.573)	56.617(5.24)	55.8176(3.754)	53.7978
		$3 \times 10^4$	80.145(4.967)	80.0039(4.782)	78.9511(3.403)	76.3527
		$4 \times 10^4$	102.288(4.985)	102.247(4.943)	101.092(3.758)	97.4308
$Q$	$\theta_w = C$	$10^4$	0.320481(5.367)	0.318947(4.863)	0.314015(3.241)	0.304156
		$2 \times 10^4$	0.290539(5.128)	0.290029(4.943)	0.286294(3.592)	0.276366
		$3 \times 10^4$	0.274175(4.605)	0.274068(4.562)	0.270775(3.307)	0.262105
		$4 \times 10^4$	0.262968(4.563)	0.263232(4.669)	0.260594(3.62)	0.25149

Table 10.2: Average Nusselt number ( $\overline{Nu}$ ) and total heat transfer ( $Q$ ) at different  $Re$ , keeping the  $U_o=1.0$  and varying  $U_w$ .

	B.C	$Re$	$U_w = 0.25$	$U_w = 0.5$	$U_w = 0.75$	$U_w = 1.0$
$\overline{Nu}$	$\theta_w = C$	$10^4$	25.6966(-10.755)	24.4261(-15.167)	25.5035(-11.426)	28.7934
		$2 \times 10^4$	46.2771(-11.558)	44.0201(-15.872)	46.2877(-11.538)	52.3252
		$3 \times 10^4$	65.1709(-12.45)	62.0621(-16.626)	65.6028(-11.869)	74.4378
		$4 \times 10^4$	83.1486(-12.687)	79.215(-16.818)	83.8711(-11.928)	95.2309
	$q_w = C$	$10^4$	26.0511(-12.455)	24.6294(-17.232)	26.0526(-12.45)	29.7574
		$2 \times 10^4$	46.644(-13.297)	44.2912(-17.671)	47.0871(-12.474)	53.7978
		$3 \times 10^4$	65.5673(-14.126)	62.3684(-18.315)	66.5912(-12.785)	76.3527
		$4 \times 10^4$	83.5845(-14.211)	79.5426(-18.36)	85.0345(-12.723)	97.4308
$Q$		$10^4$	0.2714(-10.755)	0.2580(-15.167)	0.2694(-11.426)	0.3041
		$2 \times 10^4$	0.2444(-11.558)	0.2325(-15.872)	0.2444(-11.538)	0.2763
		$3 \times 10^4$	0.2294(-12.449)	0.2185(-16.625)	0.2309(-11.868)	0.2621
		$4 \times 10^4$	0.2195(-12.687)	0.2091(-16.817)	0.2214(-11.928)	0.2515

Table 10.3: Percentage of change in  $\overline{Nu}$  and  $Q$  when the  $Re$  is increased at different wall jet and offset jet velocities.

		$Re$	$U_w = 1, U_o = 0.25$	$U_w = 1, U_o = 0.5$	$U_w = 1, U_o = 0.75$	$U_w = 0.25, U_o = 1.0$	$U_w = 0.5, U_o = 1.0$	$U_w = 0.75, U_o = 1.0$	$U_w = 1.0, U_o = 1.0$
$\overline{Nu}$	$\theta_w = C$	$10^4$	30.3388	30.1936	29.7268	25.6966	24.4261	25.5035	28.7934
		$2 \times 10^4$	55.0086(81.3)	54.9122(81.8)	54.2049(82.3)	46.2771(80.1)	44.0201(80.2)	46.2877(81.5)	52.3252(81.7)
		$3 \times 10^4$	77.8658(156.7)	77.8354(157.7)	76.9002(158.6)	65.1709(153.6)	62.0621(154.1)	65.6028(157.2)	74.4378(158.5)
		$4 \times 10^4$	99.5772(228.2)	99.6774(230.1)	98.6782(231.9)	83.1486(223.6)	79.215(224.3)	83.8711(228.8)	95.2309(230.7)
	$q_w = C$	$10^4$	31.5061	31.5061	30.7894	26.0511	24.6294	26.0526	29.7574
		$2 \times 10^4$	56.7962(83.4)	56.617(79.7)	55.8176(81.2)	46.644(79)	44.2912(79.8)	47.0871(80.7)	53.7978(80.7)
		$3 \times 10^4$	80.145(159.4)	80.0039(153.9)	78.9511(156.4)	65.5673(151.7)	62.3684(153.2)	66.5912(155.6)	76.3527(156.6)
		$4 \times 10^4$	102.288(224.6)	102.247(224.5)	101.092(228.3)	83.5845(220.8)	79.5426(222.9)	85.0345(226.4)	97.4308(227.4)
$Q$	$\theta_w = C$	$10^4$	0.320	0.318	0.314	0.271	0.258	0.269	0.304
		$2 \times 10^4$	0.290(-9.34)	0.290(-9.06)	0.286(-8.82)	0.244(-9.95)	0.2325(-9.89)	0.2444(-9.25)	0.2763(-9.13)
		$3 \times 10^4$	0.274(-14.48)	0.274(-14.07)	0.270(-13.77)	0.229(-15.46)	0.218(-15.30)	0.230(-14.25)	0.262(-13.82)
		$4 \times 10^4$	0.262(-17.94)	0.263(-17.46)	0.260(-17.01)	0.219(-19.10)	0.209(-18.92)	0.221(-17.78)	0.251(-17.31)

Table 10.4: Percentage of change in  $Nu$  and  $Q$  when  $U_w = 0.25$ ,  $U_o = 1.0$  and interchanging the velocities.

	B.C	$Re$	$U_w = 0.25, U_o = 1.0$	$U_w = 1.0, U_o = 0.25$	% increase
$\overline{Nu}$	$\theta_w = C$	$10^4$	25.6966	30.3388	18.052
		$2 \times 10^4$	46.2771	55.0086	18.867
		$3 \times 10^4$	65.1709	77.8658	19.479
		$4 \times 10^4$	83.1486	99.5772	19.758
	$q_w = C$	$10^4$	26.0511	31.5061	20.939
		$2 \times 10^4$	46.644	56.7962	21.765
		$3 \times 10^4$	65.5673	80.145	22.233
		$4 \times 10^4$	83.5845	102.288	22.376
$Q$	$\theta_w = C$	$10^4$	0.271443	0.320481	18.065
		$2 \times 10^4$	0.244421	0.290539	18.868
		$3 \times 10^4$	0.229475	0.274175	19.479
		$4 \times 10^4$	0.219583	0.262968	19.579

Table 10.5: Percentage of change in  $Nu$  and  $Q$  when  $U_w = 0.5$ ,  $U_o = 1.0$  and interchanging the velocities.

	B.C	$Re$	$U_w = 0.5, U_o = 1.0$	$U_w = 1.0, U_o = 0.5$	% increase
$\overline{Nu}$	$\theta_w = C$	$10^4$	24.4261	30.1936	23.612
		$2 \times 10^4$	44.0201	54.9122	24.743
		$3 \times 10^4$	62.0621	77.8354	25.415
		$4 \times 10^4$	79.215	99.6774	25.831
	$q_w = C$	$10^4$	24.6294	31.5061	27.921
		$2 \times 10^4$	44.2912	56.617	27.829
		$3 \times 10^4$	62.3684	80.0039	28.276
		$4 \times 10^4$	79.5426	102.247	28.543
$Q$	$\theta_w = C$	$10^4$	0.258023	0.318947	23.611
		$2 \times 10^4$	0.2325	0.290029	24.743
		$3 \times 10^4$	0.218529	0.274068	25.414
		$4 \times 10^4$	0.209195	0.263232	25.831

Table 10.6: Percentage of increase in  $Nu$  and  $Q$  when  $U_w = 0.75$ ,  $U_o = 1.0$  and interchanging the velocities.

	B.C	$Re$	$U_w = 0.75, U_o = 1.0$	$U_w = 1.0, U_o = 0.75$	% increase
$\overline{Nu}$	$\theta_w = C$	$10^4$	25.5035	29.7268	16.559
		$2 \times 10^4$	46.2877	54.2049	17.104
		$3 \times 10^4$	65.6028	76.9002	17.221
		$4 \times 10^4$	83.8711	98.6782	17.655
	$q_w = C$	$10^4$	26.0526	30.7894	18.187
		$2 \times 10^4$	47.0871	55.8176	18.541
		$3 \times 10^4$	66.5912	78.9511	18.561
		$4 \times 10^4$	85.0345	101.092	18.883
$Q$	$\theta_w = C$	$10^4$	0.269403	0.314015	16.559
		$2 \times 10^4$	0.244477	0.286294	17.105
		$3 \times 10^4$	0.230996	0.270775	17.221
		$4 \times 10^4$	0.221491	0.260594	17.654

## 10.3 Conclusions

The heat transfer study of combined wall jet and offset jet flow is considered. Different wall jet and offset velocities are considered. Analysis is carried out in the graphical form for local Nusselt number ( $Nu_x$ ), local heat flux ( $q_x$ ), wall temperature ( $\theta_w$ ) and in tabular form for average heat transfer ( $\overline{Nu}$ ) and total heat transfer ( $Q$ ) for constant temperature and constant heat flux conditions.  $Pr=0.71$  is taken for all computations. The important conclusions may be drawn are as follows:

- In the far downstream region, the  $Nu_x$  increases with mass flow rate, i.e, by increasing either the wall jet or offset velocity keeping the other constant.
- At the same mass flow rate, when the  $U_w$  and  $U_o$  are interchanged, the  $Nu_x$  is more when the  $U_w=1.0$ . In the far downstream location, the  $Nu_x$  is same irrespective of the jet velocities.
- As  $Re$  is increased,  $Nu_x$  is increased for all  $U_o$  and  $U_w$ , but no change in the behavior is observed.
- Comparison of two boundary condition (i.e., constant temperature and constant heat flux conditions)  $Nu_x$  is more in case of constant heat flux condition.
- When the jet velocities are interchanged,  $\theta_w$  is more when  $U_w < U_o$ . As  $Re$  increased at any location in the flow domain,  $\theta_w$  also increased.
- Average Nusselt number is found maximum in the case of  $U_o=0.25$  and  $U_w=1.0$  which is 5% higher than the reference. The percentage of change in  $\overline{Nu}$  decreases with  $Re$ .
- Approximately linear increase in percent of change with  $Re$  suggests that the  $\overline{Nu}$  increases linearly.

# Chapter 11

## Conclusions and Scope for Future Work

Wall bounded jet flows have profound industrial importance in many applications. Conjugate heat transfer study is the subject of interest for the past few decades. The present study is aimed to gain some of the insights of the topics considered.

### 11.1 Summary

Chapter 3 presented the mean flow and thermal characteristics of wall jet and offset jet at different offset ratios. It observed that minimum value of  $\bar{U}_{max}$  occurs very near to the reattachment point in the downstream direction and it decreases as  $OR$  increases. The pressure distribution along the wall remains nearly constant for wall jet case. It has been observed that at a distance of approximately 60, the velocity profile for wall jet and other three  $OR$  cases overlap with each other implying that a wall jet situation arises in far downstream for all the cases. The maximum value of wall shear stress decreases as  $OR$  increases. The positive region of  $\tau_w$  shows the recirculation region. The temperature at different locations under adiabatic wall condition are compared with the experimental results of Holland

and liburdy [4] and are found in good agreement.

Conjugate heat transfer study of wall jet is described in chapter 4 and chapter 5 for constant temperature and constant heat flux conditions at the bottom of the solid block, respectively. Keeping the  $Re=15000$  constant, parametric study is carried out for slab thickness ( $S$ ), Prandtl number ( $Pr$ ) and thermal conductivity ratio ( $K$ ). It is observed that under both the conditions,  $Nu_x$  is independent of  $K$  and  $S$ . Average Nusselt number is found increasing with the  $Pr$ . Interface temperature is found decreasing, when  $K$  and  $S$  are increasing in both the conditions. Total heat transfer is found reducing with Prandtl number in case of constant temperature condition. Interface temperature is high for high  $Pr$  and heat flux is constant along  $X$  for  $K=1$  at the interface for constant heat flux condition at the bottom of the solid block.

Similarly, conjugate heat transfer study of offset jet is described in chapter 6 and chapter 7 for constant temperature and constant heat flux conditions at the bottom of the solid block respectively. It is observed that the minimum interface temperature is found at the reattachment point and reduces rapidly up to the reattachment point and thereafter it increases under both conditions. Under both the conditions,  $Nu_x$  is independent of  $K$  and  $S$  as observed in the wall jet study. The non-dimensional local heat flux ( $q_x$ ) decreases with the increase in  $OR$  in case of constant temperature condition. Interface temperature decreases as the  $Pr$  increases in case of constant temperature condition, but increases in case of constant flux condition. The local  $Nu_x$  decreases with the increase in  $OR$  and Prandtl number under both the conditions. For  $K=1000$ , the average heat transfer approaches almost equal to the non-conjugate case for the constant temperature at the bottom of the solid block.

Chapter 8 describes the flow features of the combined jet. Important flow features are observed mainly under two conditions. Those are: (1) keeping  $U_w=1.0$ ,  $U_o$  is varied for 0.25, 0.5 and 0.75. (2) keeping  $U_o=1.0$ ,  $U_w$  is varied for 0.25, 0.5,

0.75 and 1.0. The flow attains the self-similarity in the further downstream when  $U_o$  is increased, keeping  $U_w=1.0$ . But location of self-similarity is almost constant when  $U_w$  is increased, keeping  $U_o=1.0$ . Pressure on the wall is almost constant along the wall and it increases when one of the jet velocity is increased keeping the other constant. In the far downstream, shear stress is almost equal for the cases when the jet velocities are interchanged. The half-width thickness of the outer boundary layer is more when  $U_w$  is less than that of  $U_o$ . However, the rate of its growth is almost equal when jet velocities are interchanged.

Chapter 9 presents the study to identify the downstream locations up to which the flow behavior shows oscillations as reported by Wang and Tan [5]. The study is carried out for different flow variables at different locations in the downstream. When both  $U_w = U_o=1.0$ , the steady state solutions are obtained at  $X \cong 15$ . Strong periodic nature of the flow is observed to be damped in the downstream direction and finally the steady-state is obtained. If  $U_w=1.0$ , for  $U_o=0.25$  and  $0.5$ , and except some oscillations in pressure for  $0.75$ , the flow demonstrates the steady-state nature. Flow is in steady-state when the  $U_w=0.25$  and  $U_o=1.0$ . Except the oscillations in pressure, the flow is steady for the remaining variable when  $U_w=0.5$  and  $U_o=1.0$ . Phase diagrams also suggest the same. Similarly, except for pressure for  $U_w=0.75$  and  $U_o=1.0$ , the flow attains a steady-state at  $X = 10$ .

Heat transfer characteristics of combined jet flow is described in chapter 10. It is observed that in the far downstream region, the  $Nu_x$  increases with mass flow rate, i.e, by increasing either the wall jet or offset velocity keeping the other constant. At the same mass flow rate, when the  $U_w$  and  $U_o$  are interchanged, the  $Nu_x$  is more when the  $U_w=1.0$ . In the far downstream location, the  $Nu_x$  is same irrespective of the jet velocities. Comparison of two boundary conditions (i.e., constant temperature and constant heat flux conditions) demonstrated that at the same conditions  $Nu_x$  is more in case of constant heat flux condition. As  $Re$  is increased at any location in the flow domain,  $\theta_w$  also increased. Approximately

linear increase of percentage of change with  $Re$  suggests that the  $\overline{Nu}$  increases linearly. Average Nusselt number is found maximum in the case of  $U_o=0.25$  and  $U_w=1.0$  which is 5% higher than when the jet velocities are interchanged.

## 11.2 Scope for Future Study

In the present study the wall jet, offset jet and combined jet are investigated. Similar study can be carried out for an impingement jet. In case of wall jet flow, the free stream motion can be considered for similar study. An empirical relation for  $OR$  and reattachment length gives more insight in the study. Heat transfer study can be carried out for the free stream motion for the numerical study as carried out by Hoch and Jiji [13]. In case of combined jet, spacing between the jets is taken one ( $d/w=1$ ). The flow features can be observed by varying the spacing between the jets. Similarly, considering the two offset jets spacing between them and height of offset jet from the wall can be considered as parameters of study. Transient study of a combined jet flow in case of periodic vortex shedding gives the good understanding of vortex frequency and its behavior. Buoyancy effects are neglected in the entire study. The work can be extended to understand the effect of buoyancy in the geometry and problems considered here. Similarly mixed convection can be done to understand the importance of buoyancy compared to forced convection.

# Appendix A

## Deriving the expression for heat flux in the fluid side

At the interface between the solid and fluid, the following conditions are applied.

- $\bar{\theta}_s = \bar{\theta}_f$  at the interface.
- heat transfer across the interface must be equal.

wall heat flux in the fluid side is given by:

$$Q_f = \frac{(\bar{\theta}_w - \bar{\theta}_{p,f}) c_\mu^{\frac{3}{4}} k_n^{\frac{1}{2}}}{Pr_t \left( \frac{1}{\kappa} \log(EY^+) + P_f \right)} \quad (A.1)$$

Where  $P_f$  pee-function, which is given by:

$$P_f = 9.24 \left[ \left( \frac{Pr}{Pr_t} \right)^{\frac{3}{4}} - 1 \right] \times \left[ 1 + 0.28 \exp \left( -0.007 \frac{Pr}{Pr_t} \right) \right] \quad (A.2)$$

Heat transfer in the solid side is given by:

$$Q_s = -\frac{1}{Re.Pr} \left( \frac{k_s}{k_f} \right) \frac{\partial \theta}{\partial Y} = \frac{1}{Re.Pr} \left( \frac{k_s}{k_f} \right) \frac{\theta_{p,s} - \bar{\theta}_w}{\Delta Y} \quad (A.3)$$

Interface temperature is calculated by equating Eqns. A.1 and A.3. where  $\bar{\theta}_{p,f}, \theta_{p,s}$  are neighbor temperatures in the fluid and solid regions.

Total heat transfer ( $Q$ ) is given by:

$$Q = \int Q_x dx = \int Q_f dx \quad (A.4)$$

## Appendix B

### Deriving the expression for Nusselt Number Calculation

$$Nu_x = \frac{h_c h}{k} = h_c (\bar{T}_w - T_{in}) \times \frac{\nu}{\alpha} \cdot \frac{1}{\rho C_p} \cdot \frac{1}{U_0 (\bar{T}_w - T_{in})} \cdot \frac{U_0 h}{\nu} \quad (B.1)$$

$$Nu_x = \frac{q_w Pr Re}{\rho C_p U_0 (\bar{T}_w - T_{in})} \quad (B.2)$$

We can write the above equation as:

$$Nu_x = \frac{q_w Pr Re}{\rho C_p U_0 (\bar{T}_w - T_{in})} \cdot \frac{(\bar{T}_h - T_{in})}{(\bar{T}_h - T_{in})} \quad (B.3)$$

The non-dimensional heat flux is defined as:

$$q_{w,n} = \frac{q_w}{\rho C_p U_0 (\bar{T}_w - T_{in})} \quad (B.4)$$

Finally:

$$Nu_x = \frac{Q_{w,n} Pr Re}{\bar{\theta}_w} \quad (B.5)$$

since  $\bar{\theta}_\infty = 0$ .

Which is used for calculating the Local Nusselt number distribution. The average Nusselt number is calculated as:

$$\bar{Nu} = \frac{1}{L} \int_0^L Nu_x dx \quad (B.6)$$

# Appendix C

## Definition of the constant heat flux at the solid wall

Heat flux at the bottom of the wall is given by:

$$q_b = -k_s \frac{\partial T}{\partial y} \quad (\text{C.1})$$

Since the heat flux across the wall is non-dimensionalized by the  $Q_{ref} = \rho c_p U_0 \Delta \bar{T}$ . Here  $\Delta \bar{T}$  is some assumed temperature difference. So the same reference heat flux is used to non-dimensionalized Eq. C.1. Finally Eq. C.1 becomes,

$$Q_b = -\frac{k_s}{k_f} \frac{\partial \theta}{\partial Y} \frac{1}{Re.Pr} \quad (\text{C.2})$$

In the present calculations Reynolds number is constant in all cases. In order to give the same heat flux at the bottom wall in all cases  $Q_b$  is taken as  $1/Re$  (heat flux applied  $Q_b = 1/Re$ ).

# Appendix D

## Validation of the code

### D.1 Channel Flow

In this case  $Re$  is defined on the basis of channel half-width. The length of the channel 35 is taken. The non-dimensionalized boundary conditions are provided as input to the solution. At the inlet of the channel,  $U = 1.0$  and  $V = 0$  are the boundary conditions for the velocities. For the turbulent kinetic energy equation, the boundary condition at inlet of channel is  $k_n = 1.5I^2$  where  $I$  is the turbulence intensity and is equal to 0.02 [51]. For the dissipation equation, the boundary condition at inlet is  $\epsilon_n = k_n c_\mu^{3/4} / l$ , where  $l = 0.07h$  [51]. At the solid walls of the channel, no-slip boundary condition is used for velocities. At the exit of the channel, Neumann boundary conditions are provided i.e.  $\partial\phi/\partial n = 0$  where  $\phi = \bar{U}$ ,  $\bar{V}$ ,  $k_n$  and  $\epsilon_n$ . The results are presented in Fig. D.2 and are in good agreement with the experimental solution.

### D.2 Square and Rectangular Cavities

The domain size  $1 \times 1$  and  $1 \times 3$  is considered for square cavity and rectangular cavity respectively and the schematic diagram is shown in Fig. D.1. In both the

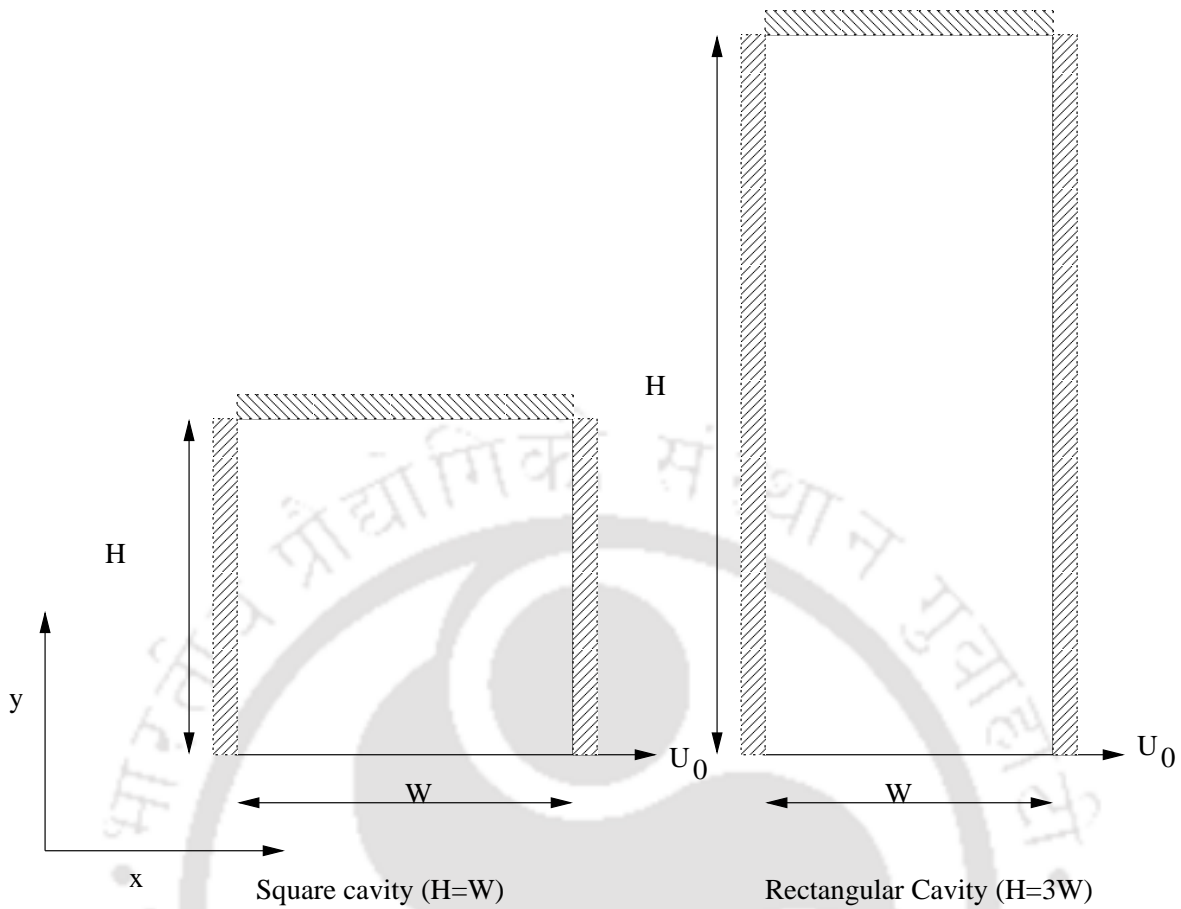
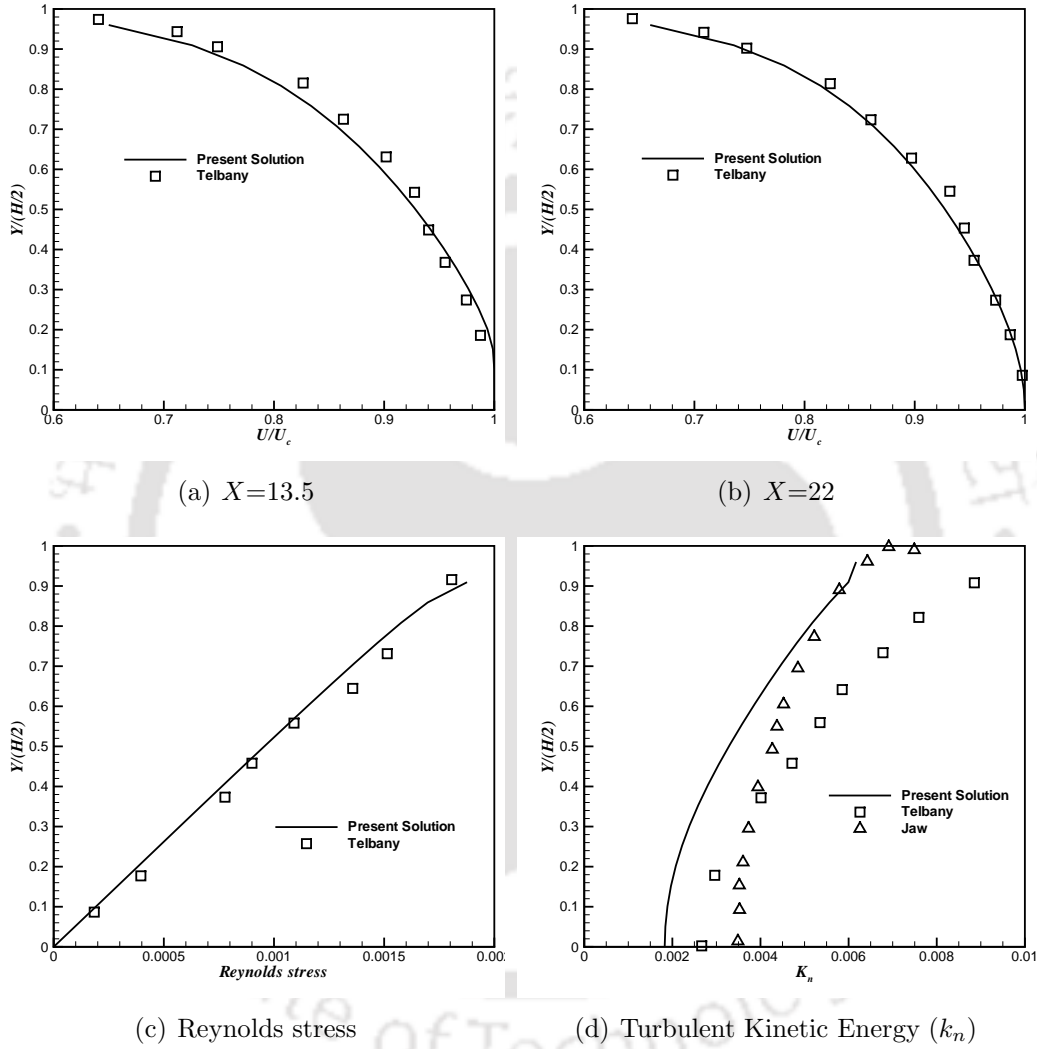
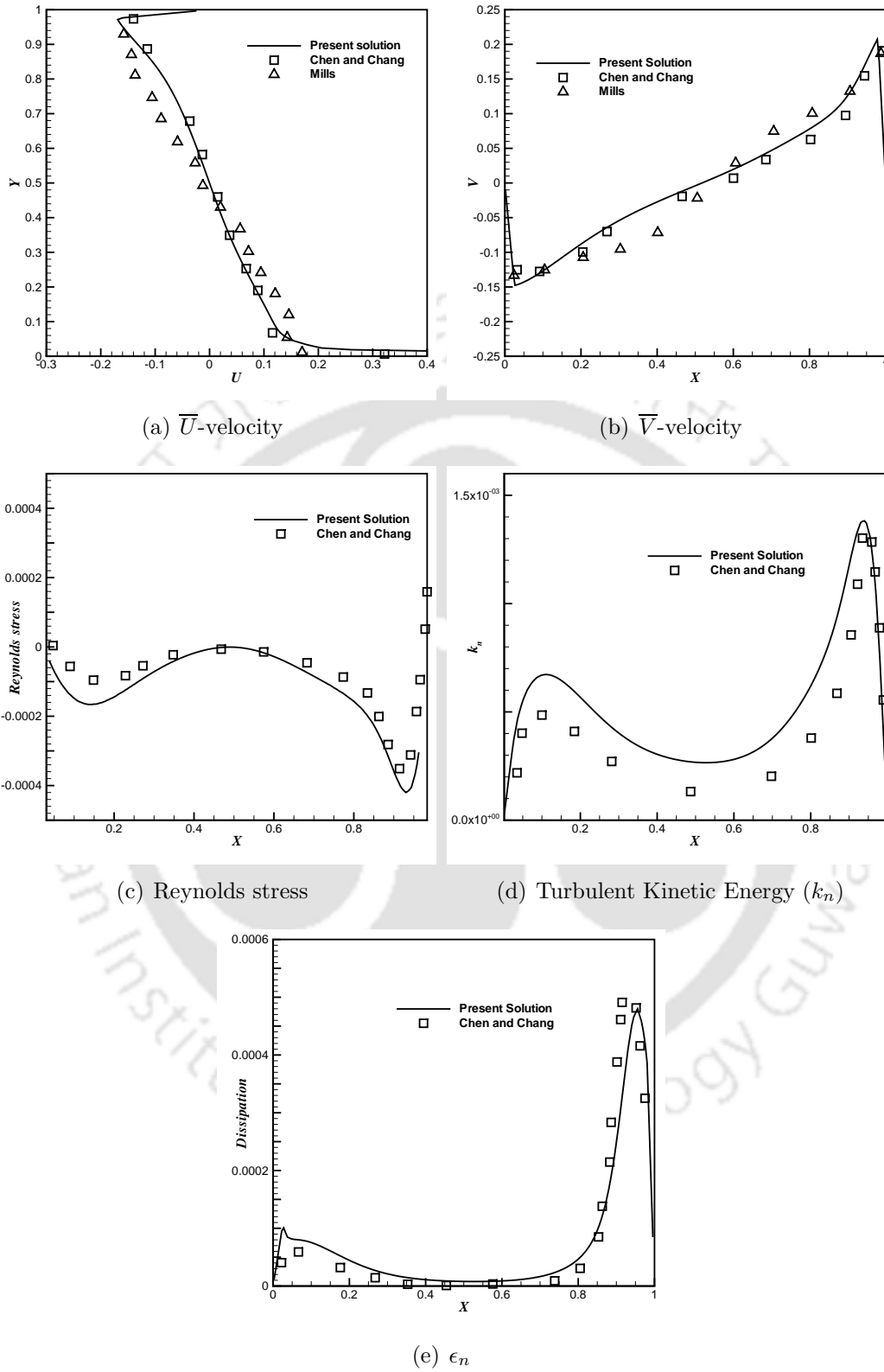
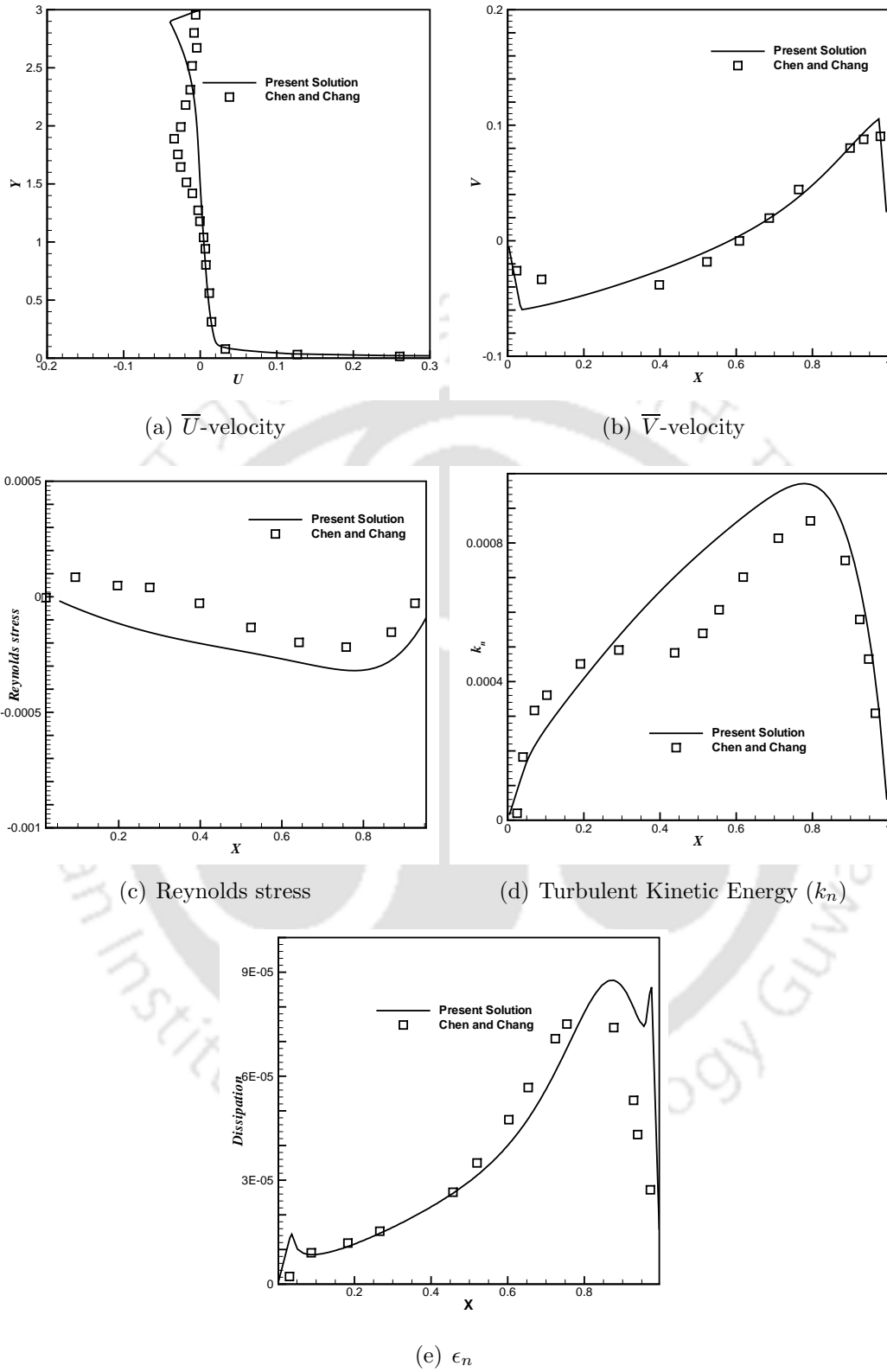


Figure D.1: Schematic diagram of square and rectangular cavities

cases bottom of the lid is moving at a constant velocity and  $Re$  is defined based on the width of the cavities.  $Re=4.8 \times 10^5$  and  $2 \times 10^5$  for square and rectangular cavities respectively. The non-dimensionalized boundary conditions are provided as input to the solution. Since the bottom of the wall is moving  $\bar{U}=1.0$  is taken. At the all walls of the cavities, no-slip boundary conditions are used for velocities.

Figure D.2: Validation study with channel flow at  $Re=65600$

Figure D.3: Validation study of square cavity flow at  $Re = 4.8 \times 10^5$

Figure D.4: Validation study of rectangular cavity flow at  $Re = 2.0 \times 10^5$

# Bibliography

- [1] M.B. Glauert. The wall jet. *Journal of Fluid Mechanics*, 1:625–643, 1956.
- [2] D.J. Tritton. *Physical Fluid Dynamics*, pages 284–286. Von Norstrand Reinhold, UK, 1977.
- [3] J. R. R. Pelfrey and J. A. Liburdy. Mean flow characteristics of a turbulent offset jet. *Transaction ASME: Journal of Fluids Engineering*, 108:82–88, 1986.
- [4] J. T. Holland and J. A. Liburdy. Measurements of the thermal characteristics of heated offset jets. *International Journal of Heat and Mass Transfer*, 33(1):69–78, 1990.
- [5] X. K. Wang and S. K. Tan. Experimental investigation of the interaction between a plane wall jet and a parallel offset jet. *Experiments in Fluids*, 42:551–562, 2007.
- [6] C. Bourque and B. G. Newman. Reattachment of two dimensional incompressible jet to an adjacent plate. *Aeronautical Quarterly*, 11:201–232, 1960.
- [7] R. A. Sawyer. The flow due to a two-dimensional jet issuing parallel to a flat plate. *Journal of Fluid Mechanics*, 9:543–560, 1960.
- [8] R. A. Sawyer. Two-dimesional reattachment jet flows including the effect of curvature on entrainment. *Journal of Fluid Mechanics*, 17:481–498, 1963.

- [9] R.A. Seban and L.H. Back. Velocity and temperature profiles in a wall jet. *International Journal of Heat and Mass Transfer*, 3:255–265, 1961.
- [10] N. Rajaratnam and N. Subramanya. Plane turbulent reattached wall jets. *ASCE J. of Hydraulics Div*, 94(1):95–112, 1968.
- [11] E. Gutmark and I. Wygnanski. The planar turbulent jet. *Journal of Fluid Mechanics*, 73:465–495, 1976.
- [12] J. Hoch and L.M. Jiji. Two-dimensional turbulent offset jet-boundary interaction. *Transaction ASME: Journal of Fluids Engineering*, 103:154–161, 1981.
- [13] J. Hoch and L.M. Jiji. Theoretical and experimental temperature distribution in two dimensional turbulent jet-boundary interaction. *Transaction ASME: Journal of Heat Transfer*, 103:331–335, 1981.
- [14] B.E. Launder and W. Rodi. The turbulent wall jet. *Progress in Aerospace Sciences*, 19(2-4):81–128, 1981.
- [15] B.E. Launder and W. Rodi. The turbulent wall jet-measurements and modeling. *Annual Review of Fluid Mechanics*, 15:429–459, 1983.
- [16] T. Dakos, C. A. Verriopoulos, and M. M. Gibson. Turbulent flow with heat transfer in plane and curved wall jets. *Journal of Fluid Mechanics*, 145:339–360, 1984.
- [17] I. Wygnanski, Y. Katz, and E. Horev. On the applicability of various scaling laws to the turbulent wall jet. *Journal of Fluid Mechanics*, 234:669–690, 1992.
- [18] M. D. Zhou and I. Wygnanski. Parameters governing the turbulent wall jet in an external stream. *AIAA journal*, 31(5):848–853, 1993.

- [19] D.S. Kim, S.H. Yoon, D.H. Lee, and K.C. Kim. Flow and heat transfer measurements of a wall attaching offset jets. *International Journal of Heat and Mass Transfer*, 39(14):2907–2913, 1996.
- [20] S.H. Yoon, S.E. Eun, and M.K. Chung. Numerical study on the two-dimensional stepped wall jet. *Transaction Korean Society of Mechanical Engineering*, 12:865–875, 1988.
- [21] H.-M. Koo and S. O. Park. Prediction of turbulent offset jet flows with an assessment of QUICKER scheme. *International Journal for Numerical Methods in Fluids*, 15:355–372, 1992.
- [22] A. Nasr and J. C. R. Lai. A turbulent plane offset jet with small offset ratio. *Experiments in Fluids*, 24:47–57, 1998.
- [23] N. W. M. Ko and K. K. Lau. Flow structures in initial region of two interacting parallel plane jets. *Experimental Thermal Fluid Sciences*, 2:431–449, 1989.
- [24] Y. F. Lin and M. J. Sheu. Investigation of two plane parallel unventilated jets. *Experiments in Fluids*, 10:17–22, 1990.
- [25] A. Nasr and J. C. S. Lai. Comparison of flow characteristics in the near field of two parallel plane jets and an offset jet. *Physics of Fluids*, 9:2919–2931, 1997.
- [26] C. S. Wang, Y. F. Lin, and M. J. Sheu. Measurements of turbulent inclined plane dual jets. *Experiments in Fluids*, 16:27–35, 1993.
- [27] C. Y. Soong, P. Y. Tzeng, and C. D. Hsieh. Numerical investigation of flow structure and bifurcation phenomena of confined plane twin-jet flows. *Physics of Fluids*, 10:2910–2921, 1998.

- [28] E. A. Anderson and R. E. Spall. Experimental and numerical investigation of two-dimensional parallel jets. *Transaction ASME: Journal of Fluids Engineering*, 123:401–406, 2001.
- [29] Y-T. Yang and C-H. Shyu. Numerical study of multiple impinging slot jets with an inclined confinement surface. *Numerical Heat Transfer: Part A*, 33(1):23–37, January 1998.
- [30] S.Z. Shuja, B.S. Yilbas, and M.O. Budair. Gas jet impingement on a surface having a limited constant flux area: various turbulence models. *Numerical Heat Transfer: Part A*, 36(2):171–200, August 1999.
- [31] L.B.Y. Aldabbagh and I. Sezai. Numerical simulation of three-dimensional laminar, square twin-jet impingement on a flat plate, flow structure and heat transfer. *Numerical Heat Transfer: Part A*, 41(8):835–850, June 2002.
- [32] B.S. Yilbas, S.Z. Shuja, and M.O. Budair. Jet impingement onto a cavity. *International Journal of Numerical Methods for Heat and Fluid Flow*, 12(7):817–838, 2002.
- [33] B.S. Yilbas, S.Z. Shuja, and M.O. Budair. Jet impingement onto a hole with constant wall temperature. *Numerical Heat Transfer: Part A*, 43(8):843–865, June 2003.
- [34] S.A. Salamah and D. A. Kaminski. modeling of turbulent heat transfer from an array of submerged jets impinging on a solid surface. *Numerical Heat Transfer: Part A*, 48(4):315–337, September 2005.
- [35] A.V. Luikov, V.A. Aleksashenko, and A.A. Aleksashenko. Analytical methods of solution of conjugated problems in convective heat transfer. *International Journal of Heat and Mass Transfer*, 14:1047–1056, 1971.

- [36] A. V. Luikov. Conjugate convective heat transfer problems. *International Journal of Heat and Mass Transfer*, 17:257–265, 1974.
- [37] P. Payvar. Convective heat transfer to laminar flow over a plate of finite thickness. *International Journal of Heat and Mass Transfer*, 20:431–433, 1977.
- [38] Y. Ould-Amer, S. Chikh, K. Bouhadeh, and G. Lauriat. Forced convection cooling enhancement by use of porous materials. *International Journal of Heat and Fluid Flow*, 19:251–258, 1998.
- [39] P.R. Kanna and M.K. Das. Conjugate forced convection heat transfer from a flat plate by laminar plane wall jet flow. *International Journal of Heat and Mass Transfer*, 48(14):2896–2910, July 2005.
- [40] A. Kassab, E. Divo, J. Heidmann, E. Steinthorsson, and F. Rodriguez. BEM/FVM conjugate heat transfer analysis of a three-dimensional film cooled turbine blade. 13:581–610, 2003.
- [41] G. Iaccarino, A. Ooi, P.A. Durbin, and M. Behnia. Conjugate heat transfer predictions in two-dimensional ribbed passages. *International Journal of Heat and Fluid Flow*, 23:340–345, 2002.
- [42] K.J. Hsieh and F.S. Lien. Conjugate turbulent forced convection in a channel with an array of ribs. *International Journal of Heat and Fluid Flow*, 15(5):462–482, 2005.
- [43] H-M Kim and K-Y Kim. Design optimization of rib-roughened channel to enhance turbulent heat transfer. *Numerical Heat Transfer: Part A*, 47:51595168, 2004.
- [44] P.R. Kanna and M.K. Das. Conjugate heat transfer study of two-dimensional laminar incompressible offset jet flows. *Numerical Heat Transfer: Part A*, 48(7):671 – 691, October 2005.

- [45] P.R. Kanna and M.K. Das. Heat transfer study of two-dimensional laminar incompressible wall jet over backward-facing step. *Numerical Heat Transfer: Part A*, 50(2):165–187, July 2006.
- [46] H. Tennekeys and J.L. Lumley. *A First Course in Turbulence*. The MIT Press, 1974.
- [47] Stephen B. Pope. *Turbulent Flows*. Cambridge University Press, 2000.
- [48] B.E. Launder and D.B. Spalding. The numerical computation of turbulent flows. *Computer Methods in Applied Mechanics and Engineering*, 3:269–289, 1974.
- [49] David C. Wilcox. *Turbulence Modelling for CFD*. DCW Industries, Inc. La Canada, California, 1994.
- [50] C-J. Chen and S-Y Jaw. *Fundamentals of Turbulence Modelling*. Taylor & Francis, 1997.
- [51] G. Biswas. The  $\kappa - \epsilon$  Model, the RNG  $\kappa - \epsilon$  Model and the Phase-Averaged Model. In G. Biswas and V. Eswaran, editors, *Turbulent Flows: Fundamentals, Experiments and Modeling*, chapter 11, pages 339–375. Narosa Publishing House, New Delhi, India, 2002.
- [52] G.C. Cheng and S. Farokhi. On turbulent flows dominated by curvature effects. *Transaction ASME: Journal of Fluids Engineering*, 114:52–57, 1992.
- [53] W. Rodi. A new algebraic relation for calculating the reynolds stresses. *Z. Angew. Math. Mech*, 56:T219–T221, 1976.
- [54] M. Pathak, A. Dewan, and A.K. Dass. An assessment of streamline curvature effects on the mixing region of a turbulent plane jet in a crossflow. *Applied Mathematical Modeling*, 29:711–725, 2005.

- [55] J. H. Ferziger and M. Peric. *Computational Methods for Fluid Dynamics*. Springer-Verlag, 2001.
- [56] S. V. Patankar. *Numerical Heat Transfer and Fluid Flow*. Hemisphere, New York, 1980.
- [57] H. K. Versteeg and W. Malalasekera. *An introduction to computational fluid dynamics. The finite volume method*. LONGMAN, 1996.
- [58] S. E. Norris. *A Parallel Navier-Stokes Solver for Natural Convection and Free Surface Flow*. PhD thesis, University of Sydney, September 2000.
- [59] T. J. Craft, A. V. Gerasimov, H. Iacovides, and B. E. lauder. Progress in the generalization of wall-function treatments. *International Journal of Heat and Fluid Flow*, 23:148–160, 2002.
- [60] M. M. M. Telbany and A. J. Reynolds. Turbulence in plane channel flows. *Journal of Fluid Mechanics*, 111:283–318, 1981.
- [61] S. Y. Jaw. *Development of an isotropic turbulence model for prediction of complex flow*. PhD thesis, University of Iowa, 1991.
- [62] R. D. Mills. On the closed motion of a fluid in a cavity. *Journal of Royal Aeronautical Society*, 69:116–120, 1965.
- [63] C-J. Chen and S. M. Chang. Prediction of turbulent flows in rectangular cavity with  $k - \epsilon$ -a and  $k - \epsilon$ -e models. *IN: Turbulence measurements and flow modeling; Proceedings of the International Symposium, Iowa City, IA, Sept. 16-18*, pages 611–620, 1985.
- [64] J.W. Goodrich, K. Gustafson, and K. Halasi. Hopf bifurcation in driven cavity. *Journal of Computational Physics*, 90:219–261, 1990.

# List of Publications from this thesis work

## Journals

1. Vishnuvardhanarao, E., and Das, M.K., Computation of Mean Flow and Thermal Characteristics of Incompressible Turbulent Offset Jet Flows, *Numerical Heat Transfer: Part A*, 53: 843-869, 2008.
2. Vishnuvardhanarao, E., and Das, M.K., Computational Study of Heat Transfer in a Conjugate Turbulent Wall Jet Flow at High Reynolds Number, *Journal of Heat Transfer*, JULY 2008, Vol. 130 / 072201-1-7.
3. Vishnuvardhanarao, E., and Das, M.K., Study of Conjugate Heat Transfer from a Flat Plate by Turbulent Offset Jet Flow, *Numerical Heat Transfer: Part A*, 53: 524-542, 2008.
4. Vishnuvardhanarao, E., and Das, M.K., Computational Study of Heat Transfer in a Conjugate Turbulent Wall Jet Flow with Constant Heat Flux. accepted for publication in *International Journal of Numerical Methods for Heat & Fluid Flow*.
5. Vishnuvardhanarao, E., and Das, M.K., Conjugate Heat Transfer Study of Incompressible Turbulent Offset Jet Flows, submitted to Heat and Mass Transfer (June 27, 2008).
6. Vishnuvardhanarao, E., and Das, M.K., Numerical simulation of the turbulent flow interaction between a plane wall jet and a parallel offset jet, submitted to Applied Mathematical Modelling (April 22, 2008).
7. Vishnuvardhanarao, E., and Das, M.K., Different Turbulent Flow Behaviors of a Combined Plane Wall Jet and a Parallel Offset Jet, submitted to En-

gineering Applications of Computational Fluid Mechanics. (resubmitted on June 16, 2008).

8. Vishnuvardhanarao, E., and Das, M.K., Study of the Heat Transfer Characteristics in a Turbulent Combined Wall and Offset Jet Flows, resubmitted to IJTS (September 29, 2008).

**Referred conferences:**

1. Vishnuvardhanarao, E., and Das, M.K., Computation of Mean Flow and Thermal Characteristics of Incompressible Turbulent Offset Jet Flows, 19<sup>th</sup> National and 8<sup>th</sup> ISHMT-ASME Heat and Mass Transfer Conference.



# curriculum vitae

Name: Elaprolu Vishnuvardhanarao  
D.O.B: 05-06-1978  
email: vishnu.kavuluru@gmail.com, elaprolu@iitg.ernet.in

## Permanent Address:

E. Vishnuvardhanarao,  
kavuluru post,  
kondapalli via,  
krishna district,  
Andhra Pradesh-521228

## Academic Qualification:

- **Diploma in ME:** Govt. Polytechnic, AP, India. Completed in 1997 with an aggregate of 69.9%
- **B.Tech:** Koneru Lakshmaiah College of Engineering, AP, India. Completed in 2001 with an aggregate of 67.04%
- **M.Tech:** Indian Institute of Technology Guwahati, AS, India. Completed in 2004 with an aggregate CGPI of 8.672.
- **Ph.D:** Indian Institute of Technology Guwahati, AS, India. Completed in November, 2008.